Abstract

Title of Dissertation: The Hot Atmospheres of X-Shaped Radio Galaxies

Edmund Hodges-Kluck, Doctor of Philosophy, 2011

Dissertation directed by: Professor Christopher Reynolds
Department of Astronomy

We present an observational and numerical study of X-shaped radio galaxies, a subset of the double-lobed radio galaxies with a second set of lobes or "wings." These sources have been proposed as the "smoking gun" of supermassive black hole mergers, in which case the secondary lobes would be fossil remnants following a black hole spin-flip jet reorientation. However, they may instead originate in the interplay between giant radio lobes and their hot plasma environments, since radio lobes can be considered as bubbles of light fluid in the heavier intracluster medium. Circumstantial evidence from studies of the host galaxies at optical wavelengths indicates that this may indeed be the case, leading to two important questions we attempt to answer in this work: (1) Does it appear that X-shaped radio galaxies are *aware* of their environments? (2) Can radio galaxies *respond* to their environments in such a way as to form X-shaped morphology?

We use radio, optical, and X-ray imaging data to investigate the first question, finding that, in general, X-shaped sources have jets co-aligned with the major axes of their hot (X-ray emitting) atmospheres and wings co-aligned with their minor axes. However, in at least one case (where the jet clearly does not follow this trend), a deep X-ray observation suggests that rapid reorientation of the jet axis is the best explanation. Moreover, despite the trend we discover, the hydrodynamic models of wing formation have significant theoretical problems.

Thus, the second major component of this thesis is concerned with using hydrodynamical simulations to determine whether X-shaped radio galaxies can be produced in response to asymmetries in the atmosphere. We inject jets as light fluids into a model cluster or galactic atmosphere previously in hydrostatic equilibrium, thereby forming bubbles similar to those observed in radio galaxies. Since we inject the jet along the major axis of an asymmetric atmosphere, distortions to the canonical double-lobed radio galaxy result from different responses to the local pressure gradient. With a significantly anisotropic atmosphere and a powerful but decaying jet, we find that X-shaped morphology indeed results for reasonable jet and cluster parameters. However, it is unclear whether our simulated mechanism would be effectual in nature because of the high degree of anisotropy required and the differences between some observed wings and our model wings. We make a number of predictions which we would expect to be observed in the future if the hydrodynamic model is at work.

The Hot Atmospheres of X-Shaped Radio Galaxies

by

Edmund Hodges-Kluck

Dissertation submitted to the Faculty of the Graduate School of the
University of Maryland at College Park in partial fulfillment
of the requirements for the degree of
Doctor of Philosophy
2011

Advisory Committee:

Professor Christopher Reynolds, chair
Doctor Teddy Cheung
Professor Kara Hoffman
Professor Richard Mushotzky
Professor Sylvain Veilleux

Preface

The contents of this thesis have been published in a series of three articles in *The Astrophysical Journal*. Brief supplementary material excluded from these articles for brevity has been included here when necessary for clarity. The bibliographic information of the published portions of this thesis follows:

- The *Chandra* View of Nearby X-shaped Radio Galaxies (Chapter 2)
  Hodges-Kluck, E., Reynolds, C. S., Cheung, C. C. & Miller, M. C. 2010, ApJ, 710, 1205
- A Deep *Chandra* Observation of the X-shaped Radio Galaxy 4C +00.58: A Candidate for Merger-induced Reorientation? (Chapter 3)
  Hodges-Kluck, E., Reynolds, C. S., Miller, M. C. & Cheung, C. C. 2010, ApJL, 717, 37
- Hydrodynamic Simulations of Radio Galaxies: Winged and X-shaped Sources (Chapter 4)
  Hodges-Kluck, E. & Reynolds, C. S. 2011, ApJ, 733, 58

The entirety of this work has been supervised by Prof. Christopher Reynolds and has been divided evenly between observational X-ray, optical, and radio studies and hydrodynamic simulations. Committee members Profs. Richard Mushotzky and Sylvain Veilleux bring substantial expertise in X-ray astronomy, active galactic nuclei, and the environments of galaxies. Dr. Teddy Cheung is intimately involved in discerning the origin of X-shaped radio galaxies and provides substantial expertise in radio astronomy, radio galaxies, and high energy astrophysics.

To Scott Paine, who had faith in me on Cerro Sairecabur.

Acknowledgements

My deepest gratitude is to my advisor, Chris Reynolds, for three years of guidance, assistance, and friendship. Chris is an exceptional scientist possessed of a remarkable clarity of explanation, and a wonderful resource for any aspiring astronomer. I am very fortunate to have had the chance to work with him, and look forward to continued collaboration. As a graduate student, it is easy to take an R.A. for granted, so I am especially grateful for all the work he has done to secure funding, data, and a postdoctoral position, and for the chance to visit Hawaii and Japan.

I also owe a debt of gratitude to my previous advisors: Andy Harris, supervisor of the Second Year Project that won't end, and Alex Brown and Tom Ayres at Colorado who introduced me to astrophysics. Andy has been a continual source of encouragement and guidance, and it has been through working with him over the past five years that I have learned the most about designing and carrying out an original astrophysical experiment from start to finish. Thanks to Andy, I can claim the coveted

title of "multiwavelength observer." To Alex, thanks for talking to me virtually every day through my first exposure to real astronomy.

Of course, I have not solely worked with my past advisors. I am indebted to Teddy Cheung for his careful attention to my work and motivating this dissertation, Marc Pound for his introduction to reducing CARMA data and ongoing participation in the Galactic Center project, and Cole Miller for his back-to-basics approach to work. Thanks to Richard Mushotzky for frequently providing a broader perspective on my interests. I have learned a great deal about how to be an effective astronomer from you all.

None of this work would be possible without the instrumentation and software built to do the science. I extend my thanks to the *Chandra*, VLA, SDSS, and CARMA teams, to the developers of ZEUS, and to John Vernaleo for working the bugs out of much of the code I use.

I would be remiss if I did not also acknowledge the important role the department administration has played in my life here, albeit usually behind the scenes. Thanks especially to Adrienne Newman and Susan Lehr for looking out for me, and to MaryAnn Phillips for guarding the sanctity of our work environment.

Virtually all of the interactions I've had at the University of Maryland have been positive, and for the culture of the department I am grateful. I would like to acknowledge the UMD grad students who make coming to work a pleasure: BAZ, DSJ-H, SRS, MJK, MED, KHP, HG, SK, MAM, DRP, RIH-C, MJA, and AML. Thanks for the many little adventures, trips to the Union, and late-night goofing around.

Thanks as well to friends outside of the campus. In particular, my church family and small group has made me feel at home in metro DC, and I thank Kevin Offner and the grads in InterVarsity for years of friendship. Thanks again to Ann Wion for friendship and hospitality, and to Helen McComas for the gift of so much furniture when I first arrived.

Last but certainly not least, I would like to thank my family for years of love and support. To my parents, who impressed upon me the importance of finding work you can love and working at it, thank you. To Stefan, thanks for putting up with me over the years, and for many fond childhood memories. Finally, to Jana, I can't express how grateful I am to you and for you. Knowing you has been one of the great joys of my life.

Contents

List of Tables

List of Figures

Chapter 1

Introduction

As a branch of applied physics, astrophysics is compelling because it unites processes on scales smaller than an atomic nucleus (10^{-13} cm) to larger than groups of galaxies (10^{24} cm). Radio galaxies—giant lobes of plasma emanating from the nuclei of elliptical galaxies—are a prime example of astrophysical phenomena with high dynamic range. The lobes of radio galaxies, which are often tens or hundreds of times larger than the host galaxy, are fed by a relativistic jet originating in the ergosphere of a supermassive black hole deep in the galaxy's nucleus. These jets have bulk motions of up to near the speed of light and can remain highly collimated along their length, thereby serving as conveyor belts transporting tremendous amounts of energy from scales smaller than our Solar System out to the vast spaces between the galaxies. Indeed, this connection has led to the proposal that radio galaxies are cosmologically significant in the evolution of galaxy groups and clusters, and radio galaxies are part of the surprisingly rich set of phenomena associated with accreting black holes.

This dissertation is concerned with probing the hot atmospheres of a subset of radio galaxies—the X-shaped radio galaxies—to gain insight into the formation of these and other radio galaxies through the interaction of a jet and the interstellar or

intergalactic medium (ISM/IGM). The prior sentence is packed with astronomical jargon with surprisingly specific definitions (*à la* "dark matter"). In this section, I will attempt to explain these concepts such that a graduate student in physics who has taken an introductory astronomy course can follow the main threads of this dissertation. As such, this thesis is accompanied by a glossary (Appendix A) of terms, units, and quantities used extensively in this work. Supplemental introductions to radiative processes relevant to the thesis are found in Appendix B. Equations and quantities in this work are given in the *cgs* system of units, which is standard in astronomy.

I begin by reviewing radio galaxies from an observational standpoint, then briefly explore their physical origin and importance in the context of their environments. I will then define the "X-shaped" radio galaxies (XRGs) and motivate this work.

1.1 Radio Galaxies

A *radio galaxy* is an "active" galaxy (Section 1.3) which is extremely luminous in the radio band of the electromagnetic spectrum with $L \sim 10^{40} - 10^{46}$ erg s^{-1} (for reference, the luminosity of the Sun is $L_\odot = 4 \times 10^{33}$ erg s^{-1}). Whereas all galaxies exhibit some continuum and spectral line radio emission (from synchrotron emission and molecular rotational energy-level transitions in the ISM respectively), radio galaxies refer to those galaxies where the radio image is dominated by large (kpc to Mpc scale) structures (Figure 1.1), typically a jet or giant lobes that are clearly different from the ISM. In almost every case, the host galaxy is an elliptical galaxy (Véron-Cetty & Véron 2001), but throughout this thesis and most of the astronomical literature, "radio galaxy" is used to indicate only the radio-emitting structures associated with the galaxy rather than the host galaxy itself. In fact, the relation-

ship between the host galaxy and the radio galaxy is incompletely understood, and there are some spiral galaxy hosts (e.g., 3C 120).

As seen in Figure 1.1, radio galaxies typically exhibit a double-lobed structure emanating from the nucleus of their host galaxy. Frequently, the radio galaxy contains a narrow, bright "jet" that originates in a bright core cospatial with the galactic nucleus and terminates in the more diffuse lobes. Sometimes, the jet is associated with radio-bright "hot spots," but other times the jet widens into a "plume" with no hot spot. These structures are visible in the radio band and are illuminated by synchrotron radiation (Appendix B) as determined by the spectral energy distribution (SED) and the high observed polarization of the radio emission. Thus, the radio galaxy contains both magnetic fields and highly relativistic electrons (electrons with Lorentz factors $\gamma \gg 1$). The jets themselves have bulk relativistic velocities as indicated by the "superluminal" motion of some jet knots when the jet is closely aligned with the line of sight. Indeed, the jets of more powerful radio galaxies are estimated to retain bulk velocities of $\gtrsim 0.5c$ out to the terminal hot spots. The jets typically propagate deep into the intergalactic or intracluster medium (ICM), with surrounding lobes spanning tens of kpc and occasionally up to a few Mpc (the host galaxy typically has a characteristic radius of about 10 kpc). Clearly, these are extremely energetic phenomena.

The components of the radio galaxy suggest a plausible phenomenological model for the formation of the observed morphology (Figure 1.2). To wit, the classical double-lobed morphology results from twin relativistic jets of material ejected from the nucleus of the host galaxy ramming into the tenuous plasma surrounding the galaxy. Since the shock front advances more slowly than the bulk motion of the jet, strong back-flows develop in which spent jet material which has passed through the shock (at the hot spot) streams away from the hot spot and forms the diffuse

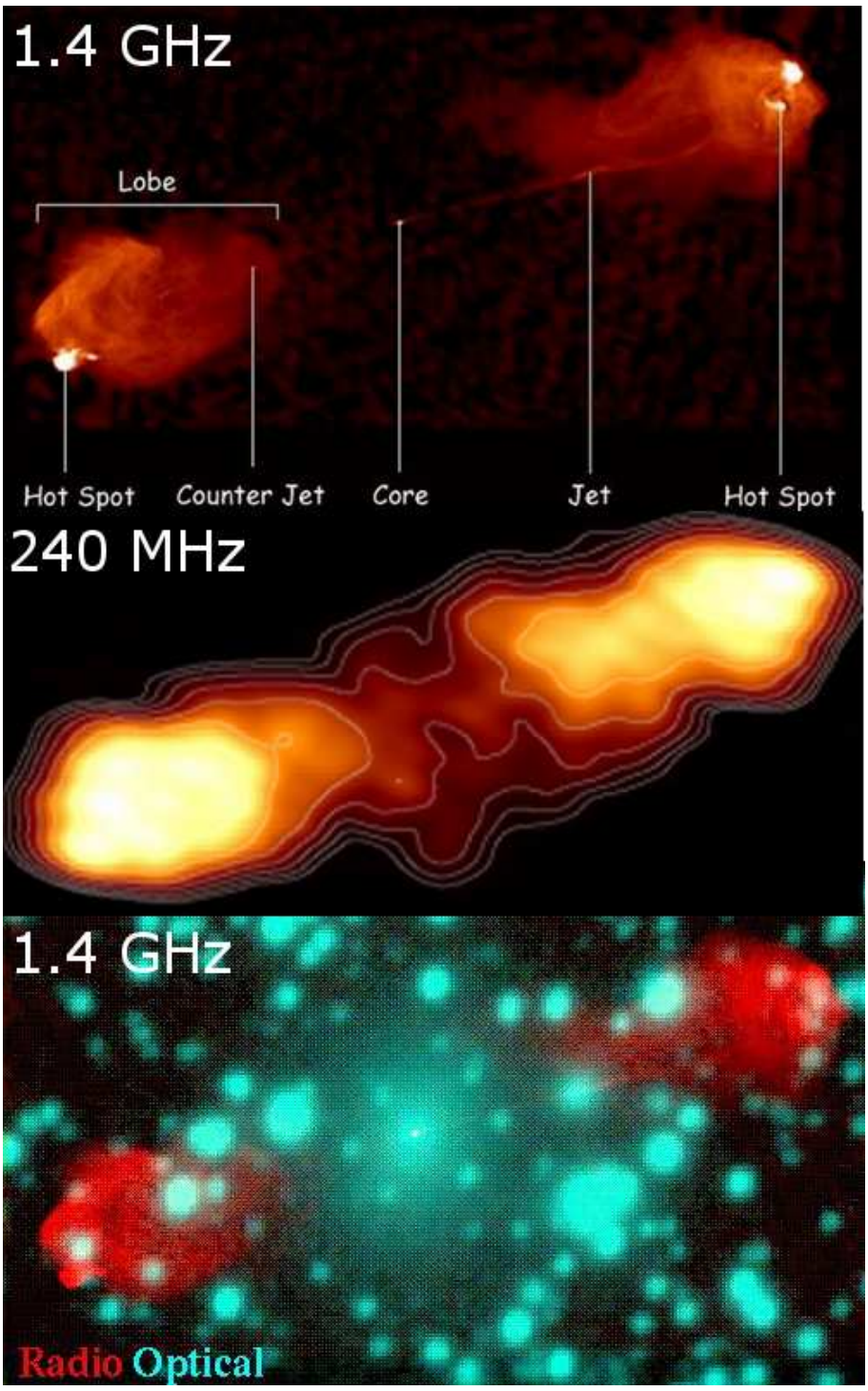

Figure 1.1 Cyg A, a powerful double-lobed radio galaxy showing the twin jets, hot spots, and associated lobes. *Top:* 1.4 GHz VLA image showing "hot" electrons in the lobes (labels from http://www.oulu.fi/astronomy/astrophysics/pr/dragnparts.jpg). *Center:* 240 MHz LOFAR image showing a bridge of lower-energy (but still relativistic) electrons (McKean et al. 2011). *Bottom:* 1.4 GHz image overlaid on optical image using data published in Owen et al. (1997).

lobes that sheath the jet. The bulk motion of the back-flows is directed towards the nucleus, so lateral (pressure driven) expansion is slow compared to the jet head advance speed and the radio galaxy becomes narrow. At higher radio frequencies, the lobes often appear to be truncated before reaching the nucleus rather than forming the contiguous cocoon visible in Figure 1.2. This is because the electrons cool via synchrotron emission, and electrons that radiate at the higher frequencies cool faster. At lower frequencies, the cocoon is often visible (e.g. Figure 1.1). A key piece of evidence in favor of this model is that the jets emanate from the *nuclei* of their host galaxies. At the center of each major galaxy there is a supermassive black hole (SMBH) that provides the relativistic potential required to accelerate the jets. We now believe that radio galaxies are one dramatic consequence of accretion of matter onto SMBHs (Section 1.3).

The formation and dynamics of radio galaxies are incompletely understood. The picture described above is a reasonable first approximation to keep in mind, and will suffice for the remainder of this Introduction. Before discussing the nuclear engine and the influence of the jet upon its environment (fields unto themselves), let us first flesh out this simple picture of radio galaxies.

1.2 Radio Galaxy Morphology

The classical double-lobed radio galaxy described above is a good baseline description of the radio galaxy phenomenon, but the morphology and emission of the radio galaxy is a function of age, environment, and possibly intrinsic jet properties.

The most prominent subdivision of double-lobed radio galaxies is a morphological dichotomy between "edge-darkened" and "edge-brightened" sources, known as Fanaroff-Riley (FR) class I and II respectively (Fanaroff & Riley 1974). The classi-

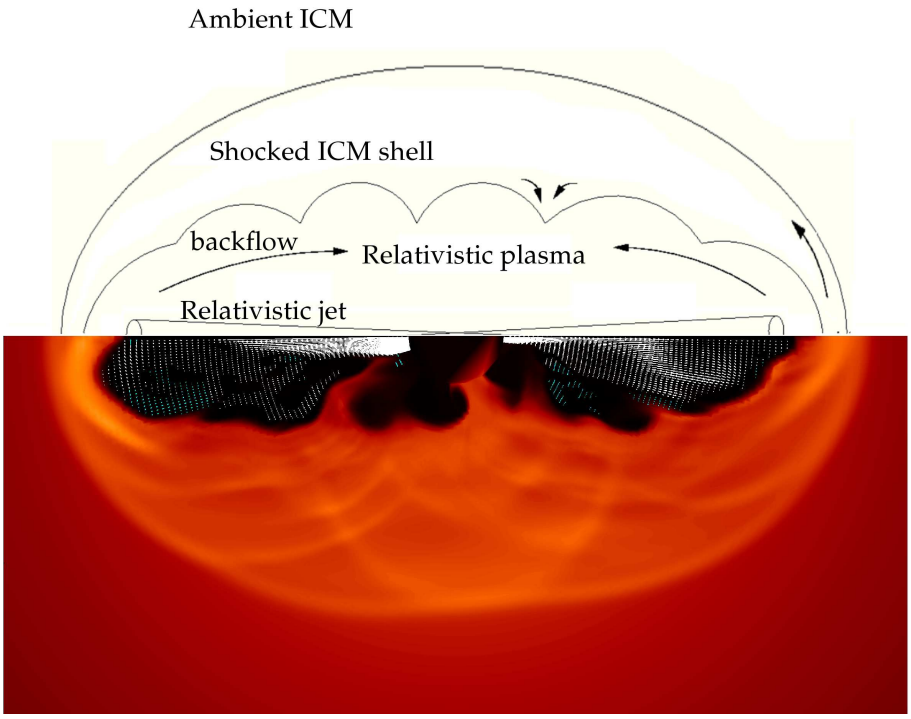

Figure 1.2 A schematic picture of a radio galaxy showing the phenomenological model for radio galaxy formation. A supermassive black hole drives a narrow relativistic jet into the surrounding medium, forming a cocoon and shocking the surrounding gas. Within the cocoon, the jets run into a terminal shock and drive backflows which create lobes. Rayleigh-Taylor and Kelvin-Helmholtz instabilities arise at the boundary between the jet plasma and the ambient plasma. The bottom half of the diagram shows a density slice through a 3D hydrodynamic simulation where this process is at work overlaid with jet velocity vectors.

fication of double-lobed radio sources into FR I and II classes is made on the basis of the distance between the brightest spots in the lobes (Figure 1.3). FR I sources are "edge-darkened" in that most of the bright emission occurs near the center; these sources also have lobes which are less well defined and are often described as "plumes." They rarely have hot spots, but often exhibit "warm" spots near where the jet decelerates to subsonic velocities and decollimates. Unlike the classical picture described above (Section 1.1), the edges of the lobes are not characterized by a shock front as the jet has already broken up. The jet deceleration is thought to

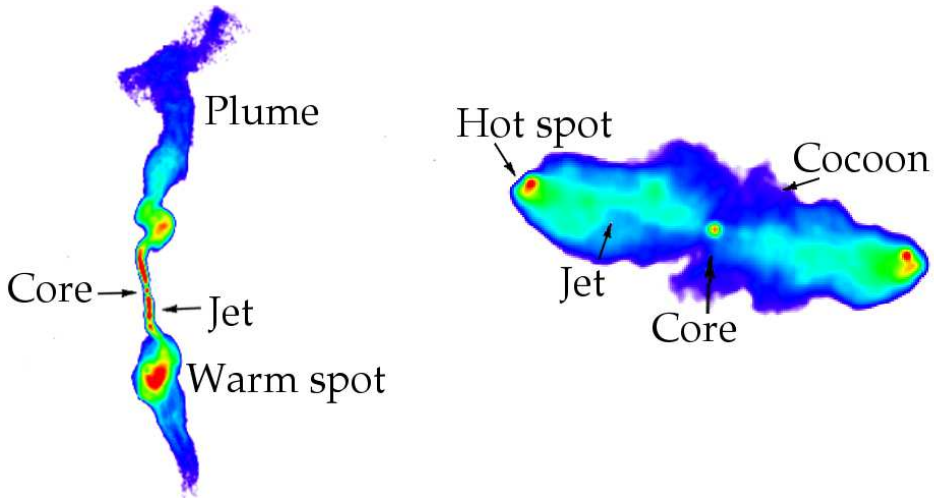

Figure 1.3 *Left*: FR I radio galaxy showing plumed structure, broken up jet, and edge-dimmed morphology. *Right*: FR II radio galaxy showing classical double-lobed edge-brightened morphology with a narrow jet and hot spots.

occur due to the entrainment of ambient material. FR II sources, on the other hand, are "edge-brightened" in that the hot spots and bright synchrotron emission occur at the leading edges of the lobes. The jets in these sources often remain collimated and relativistic along the entirely of their length, although in many cases more than one hot spot is observed (a "hot spot complex").

The origin of the morphological FR I/II dichotomy has been a controversial subject for decades. A study by Ledlow & Owen (1996) indicated that FR I and II sources are cleanly separated (Figure 1.4, often called a "Ledlow–Owen" plot) in radio power relative to host galaxy luminosity, with FR II sources being more powerful for a given galaxy luminosity. However, this result has been called into question by a more extensive study by Best (2009), who found a large overlap between FR I and II sources (Figure 1.4). While the most powerful radio galaxies are predominantly FR IIs, it is possible to have very "weak" FR IIs. (Parenthetically, we note that the FR I/II "dichotomy" has led to confusing terminology such as "low luminosity radio galaxy" to refer to low power FR I sources). On the other hand, the relatively low angular resolution of the radio survey used in Best (2009) makes

it difficult to cleanly distinguish FR I and II sources.

Indeed, complicating this picture further are those radio sources which are difficult to classify. Many radio galaxies appear to have FR II morphology but lack hot spots, and some radio sources have one edge-brightened lobe and one edge-darkened lobe (the hybrid-morphology HYMOR sources; Gopal-Krishna et al. 2003). Still, the basic morphological difference between classical FR I and II radio sources remains unexplained. Moreover, FR I radio galaxy hosts do not tend to have broad optical or UV emission lines from their nuclei whereas FR II hosts may have either broad or narrow lines (Section 1.3). This suggests that there is some real difference between the FR I and II sources other than morphology. The resolution of this debate is beyond the scope of this work, but it is important to mention the two possibilities: the dichotomy is due to intrinsic differences in jet structure related to the jet formation (e.g., higher kinetic luminosity or type of particles) or interaction between the jet and its environment (e.g., different ambient pressures or entrainment of ambient material). In either case, it is also possible that there is some evolutionary connection between FR I and II sources.

Beyond the major differentiation of radio galaxies into FR I and II sources, double-lobed radio galaxies have different morphologies that are a function of age, environment, or jet motion and run the gamut of interesting shapes (Figure 1.5). Some are more obviously the result of radio galaxies responding to their environments (e.g. distortion due to buoyant effects or asymmetric pressure gradients). These include the wide-angle tail radio sources, which often occur near cluster centers and are thought to be radio lobes buffeted by bulk motion in the intracluster medium due to "weather" or mergers (Sakelliou & Merrifield 2000). These sources have plumes like the FR I sources, but also contain features like hot spots associated with FR II sources (Hardcastle & Sakelliou 2004). The narrow-angle tail (or head–

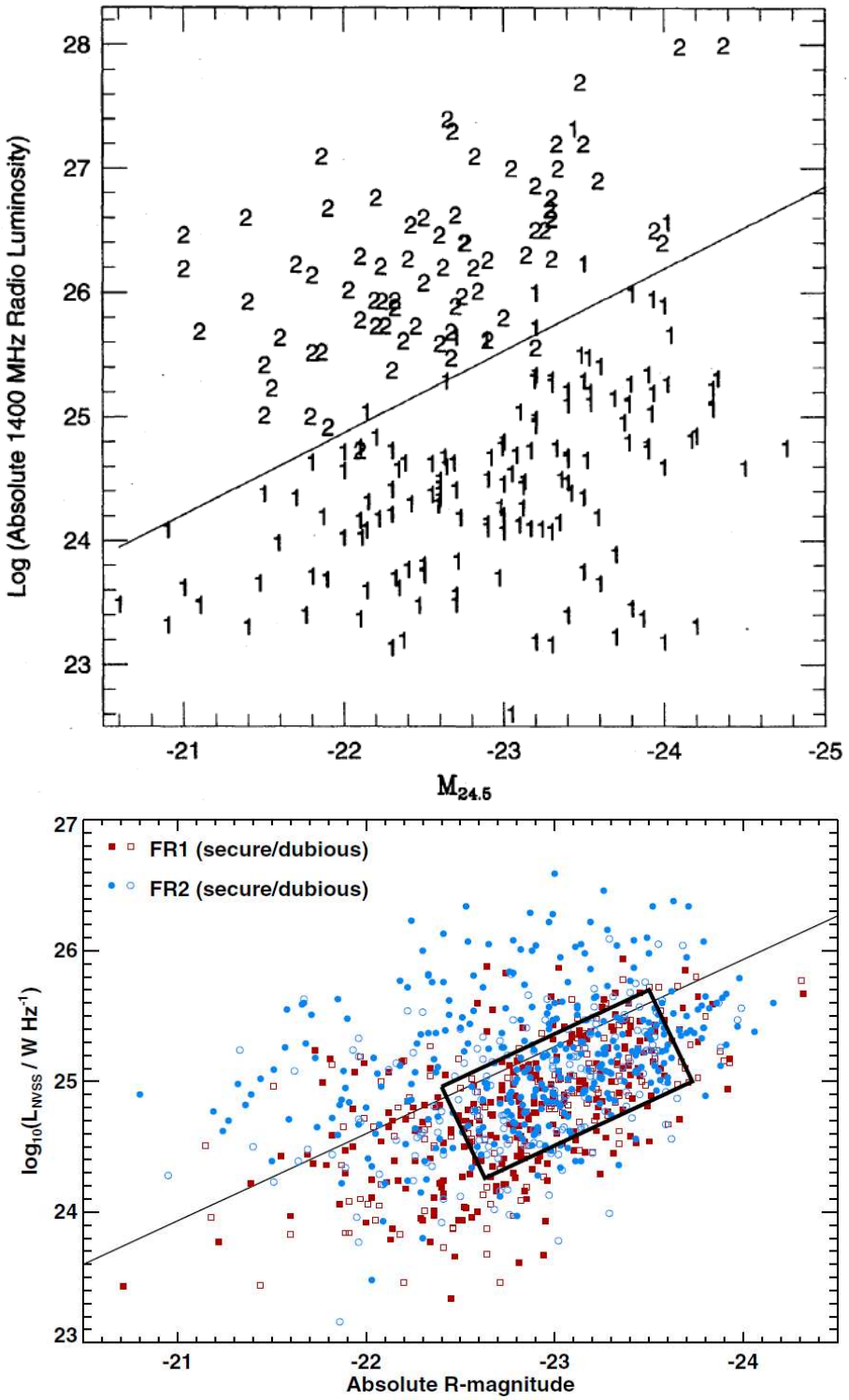

Figure 1.4 *Top*: Plot from (Ledlow & Owen 1996) indicating a correlation between radio power relative to host galaxy luminosity and the Fanaroff-Riley classification type. The x-axis is the luminosity of the galaxy (in magnitudes measured at an isophote at a surface brightness of 24.5 mag arcsec^{-1}) and the y-axis is the total radio power at 1.4 GHz. The FR type of each object is denoted by 1 and 2. *Bottom*: A more recent plot of the same quantities with more sources from Best (2009) showing that while FR I sources tend to be low-power, many FR II sources are as well.

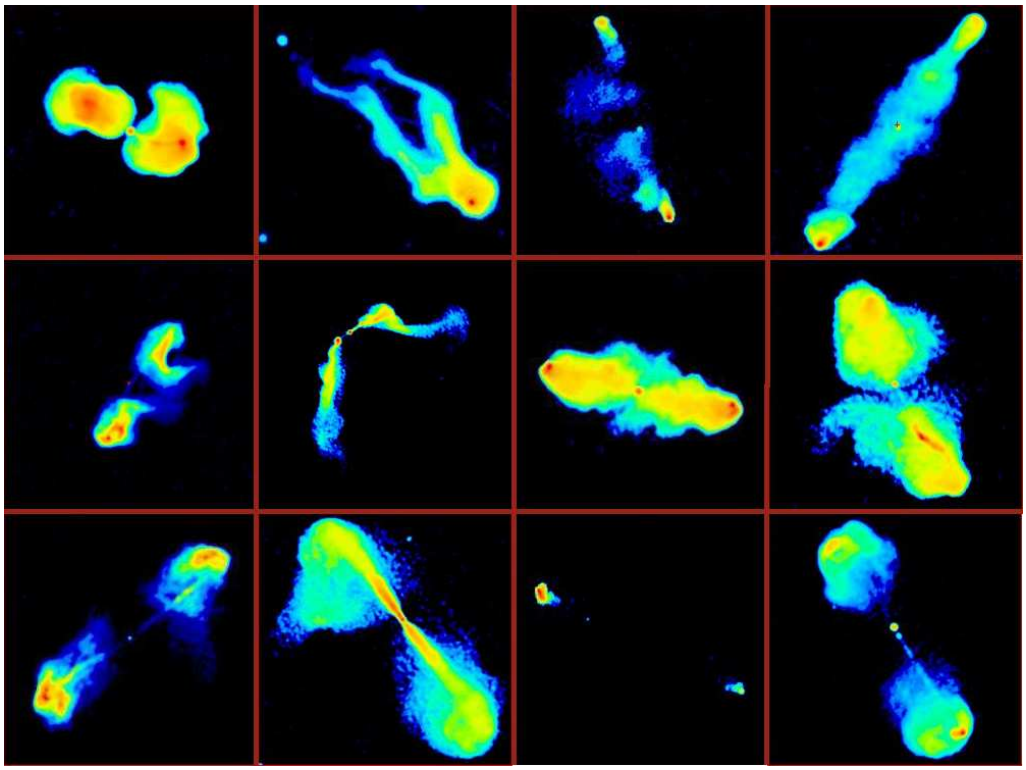

Figure 1.5 Gallery of radio galaxies showing the different morphologies encountered in the wild (images taken from the Atlas of DRAGNs at http://www.jb.man.ac.uk/atlas/dragns.html).

tail) radio sources, on the other hand, could be produced either by cluster mergers (Bliton et al. 1998) or radio lobes strung out behind a galaxy that is moving rapidly through the ICM (e.g. Sun et al. 2005). Some radio galaxies exhibit "S" or "Z"-shaped structures (point symmetry) which is thought to be caused in some cases by secular precession of the jet axis (Section 1.3) and by deflection of lobe material in a transverse direction due to asymmetric pressure gradients in others (e.g., near a place where the jet encounters a dense pocket of plasma). Finally, there are the X-shaped sources, to which we will return below.

Frequently, the lobes of radio galaxies are joined by a bridge (for a classification of different types of bridged sources, see Leahy & Williams 1984). This is the natural outcome of the lobe formation process in the phenomenological model above because the jet shock fronts evacuate space behind them which is filled by the radio plasma.

As mentioned above, even in sources with no apparent bridge at high frequencies, we expect (in the phenomenological model) that every radio source is bridged in the sense that they form a cylindrical cavity around the jet path. Indeed, many sources without bridges at 1.4 GHz have them at MHz frequencies near the synchrotron frequency of "cooler" electrons (Figure 1.1). Still, the presence of a bridge in GHz frequencies is revealing, since many edge-brightened FR II sources clearly lack one.

Radio galaxies also vary with age. Of course, the younger sources also tend to be smaller, but the degree of variation in intrinsic power (and therefore the speed at which the lobes can grow) makes it impossible to infer radio galaxy age from size alone. However, constraints may be placed. Simulations of radio galaxy formation suggest that the lobes undergo three distinct phases of life: *ignition*, *active*, and *passive* phases (e.g., Antonuccio-Delogu & Silk 2010; Hodges-Kluck & Reynolds 2011; Reynolds et al. 2002). The ignition phase occurs near the host galaxy's nucleus and involves the initial formation of a cocoon sheathing the nascent jet. Compact steep-spectrum and GHz-peaked radio sources may be identified with this stage. During the active phase, the jet drives forward and leaves the cocoon in its wake, thereby forming a double-lobed radio source (Figure 1.2). This is the phase most commonly observed, and essentially what is meant by our phenomenological description. Once the jet turns off, the lobes evolve as light fluids in a heavier one and rise buoyantly, begin to shred, and ultimately dissipate. Because of the finite synchrotron cooling time (Appendix B), radio galaxies in the passive phase ("dead") are not visible for long at higher frequencies such as 1.4 GHz, but may be seen as cavities in the X-ray emission from the hot atmosphere or at low MHz frequencies. Of course, as a radio galaxy ages its lobe morphology is increasingly influenced by its environment, but given the power of the jets some disturbed morphology must be caused by jet behavior.

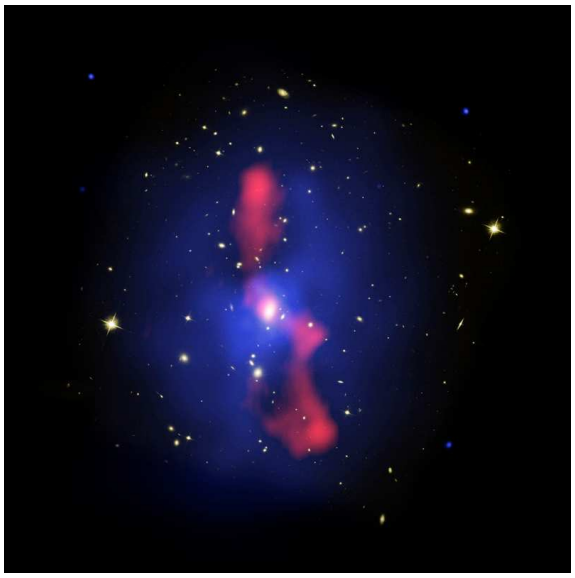

Figure 1.6 Radio (red) and X-ray (blue) composite image of the cluster MS0735.6+7421 showing the interaction between the radio lobes and the hot surroundings (McNamara et al. 2005). Note the correspondence between the decrements in the X-ray surface brightness and the radio emission.

1.3 Active Galactic Nuclei

About 1–10% of galaxies have an extremely bright, point-like radiation source at their center. This is called an *active galactic nucleus* (AGN), with AGN hosts called "active" galaxies. AGN are tremendously powerful, with isotropic bolometric luminosities between $10^{40} - 10^{47}$ erg s^{-1} ($10^{7} - 10^{14} L_{\odot}$). In the more powerful cases, the AGN outshines the entire host galaxy and may even be detected when the background galaxy is not (as is the case with some distant quasars). They must also be very small: not only do they always appear point-like to telescopes, but they exhibit variation on timescales of days, implying that their sizes cannot exceed a few light-days. Hence, AGN cannot be star clusters. Although supernovae (SNe) or gamma-ray bursts (GRBs) could account for such luminosities, AGN are long-lived whereas SNe and GRBs are transient phenomena with such high luminosities persisting only for days. Many AGN are also associated with highly collimated

relativistic jets which require some long-term particle acceleration mechanism; such ordered jets are seen down to very close to the nuclei of host galaxies and cannot plausibly be produced by star formation, SNe, or other mechanisms for producing the high luminosity associated with AGN.

It is now widely accepted that an AGN is powered by the accretion of material onto a SMBH at the center of the galaxy (for a textbook dedicated to AGN, see Krolik 1998). Each major galaxy has a central SMBH, and accretion onto it is a remarkably efficient way of producing energy. Indeed, the release of gravitational potential energy by infalling material is more efficient than nuclear fusion at liberating rest mass energy. Accretion can be sustained for long periods of time by the capture of gas near the black hole. The source of this gas may be ambient ISM, gas driven toward the center of the galaxy by dynamical processes (such as a galaxy merger or tidal interaction), or stellar mass loss from the winds of giant stars in the galaxy bulge. Gas entering the region where the black hole's gravity is dominant becomes trapped and forms a Keplerian disk from which the black hole accretes (Lynden-Bell 1969). Because there is an innermost stable circular orbit around a black hole, the accretion disk is truncated at some inner radius. Much of the radiation associated with AGN does not come directly from material inside this radius, but rather from the disk as viscosity or magnetic stresses transport angular momentum outwards, allowing material to slowly move inwards and liberate gravitational potential energy. Most of this binding energy is liberated near the inner edge of the accretion disk, heating and ionizing the disk and producing substantial amounts of ultraviolet and X-ray emission. One of the strongest pieces of evidences in support of this picture is that the ionized Fe Kα line is broadened (Tanaka et al. 1995) exactly in accordance with the effects of general relativity on light very close to the black hole. Some of the disk radiation may be boosted to even higher energies

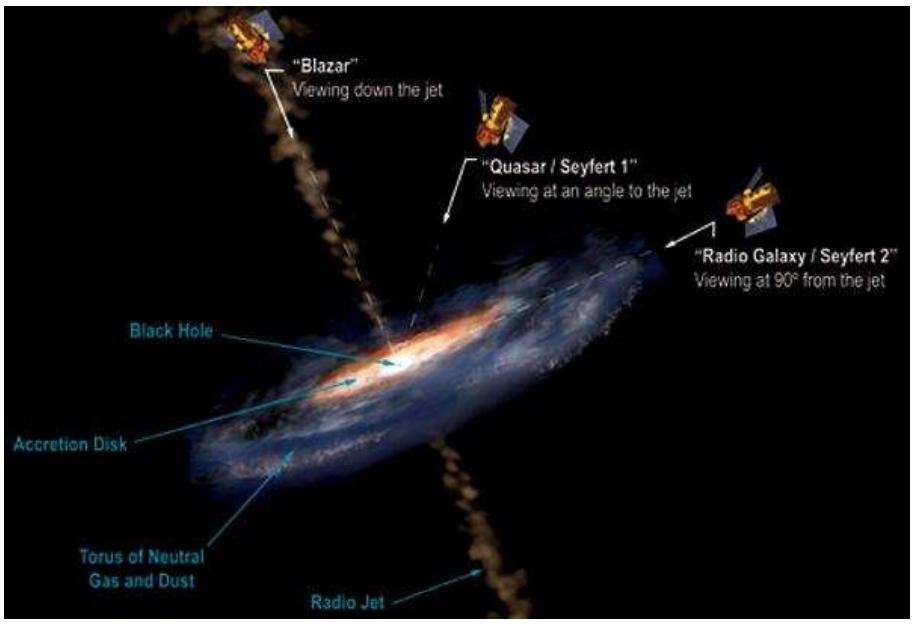

Figure 1.7 Schematic Model of AGN unification based on orientation (illustration by Aurore Simonnet). Radio galaxies are presumed to be seen edge-on, whereas "blazars" are presumed to be seen directly down the jet. Seyfert 1 or 2 galaxies are typically not radio loud, although they often have jets.

by inverse Compton scattering off a hot "corona" of electrons surrounding the black hole, causing the AGN to radiate in the hard X-rays and γ-rays ($h\nu \gtrsim 10$ keV).

This mechanism can both account for the spectrum of radiation seen from AGN as well as the small sizes implied by the variability timescales of the luminosity—the disk–SMBH system might only be about the size of our Solar System. Further, the different types of AGN can be unified (Antonucci 1993; Urry & Padovani 1995) in this model by considering the effects of orientation on the type of light observed (Figure 1.7). The AGN phenomenon is a rich and complex subject whose details are beyond the scope of this thesis, and indeed reviews of the field now must address narrow sections of the phenomenon (e.g. the hard X-ray view or the connection to the host galaxy) for brevity. For our purposes, we are only interested in the AGN as a power source for radio galaxies.

There are many different types of AGN, but the ones associated with radio

galaxies are the radio-loud AGN. About 10% of AGN are radio loud, and these are further categorized based on radio morphology and nuclear emission (in this work, as in much of the astronomical literature, "nuclear emission" refers to emission from the AGN and *not* to particle or photon radiation from interactions mediated by the strong force). These include radio galaxies, blazars, and radio-loud quasars. As we have seen, radio galaxies are further subdivided by morphology and power, and we believe that blazars–bright, highly variable continuum sources with extremely rapid variability–are radio galaxies in which the beam of the jet coincides with our line of sight. Radio-loud quasars are radio galaxies in which the continuum emission from the AGN vastly exceeds the luminosity of the radio lobes. Hence, radio-loud objects differ in power and orientation from one another.

They also differ from their radio-quiet cousins: for instance, radio-loud AGN tend to be hosted exclusively by large elliptical galaxies (Smith et al. 1986; Véron-Cetty & Véron 2001) and presumably have black holes with near-maximal spin. Regardless of spin, radio galaxies also seem to require black hole masses exceeding $10^8 M_\odot$, as black holes with smaller masses but high spin are not radio loud (Chiaberge & Marconi 2011). Thus, despite the basic similarity of accretion-powered AGN, the emergence of a radio jet must depend on local conditions. The reason for this apparent mass threshold is unknown, as is the precise mechanism by which the relativistic jets are formed (such jets may also exist in radio-quiet sources, but do not give rise to radio galaxies).

There are, however, two leading models for the generation of the relativistic jets: disk-wind jets and spin-driven jets. The radio jets are highly collimated with bulk relativistic speeds, implying confinement and acceleration through a relativistic potential. Although this potential is, in principle, supplied by an active SMBH, how exactly the confinement and acceleration occurs depends on the details.

In the spin-driven models, the rotational energy of the black hole itself is tapped to drive the jets, which are driven off the black hole's spin axis (the direction of its angular momentum vector). The "spin" of the black hole is defined as $a \equiv Jc/GM_{\rm BH}^2$ where J is the angular momentum and $M_{\rm BH}$ is the mass, and ranges from 0 to 1. Black holes with large spin (close to 1) have a large reservoir of rotational energy which may be extracted from the ergosphere, an ellipsoidal region of space surrounding the event horizon in which spacetime is frame-dragged at a velocity faster than the speed of light relative to the rest of the Universe. The most popular of these models is the Blandford–Znajek mechanism (Blandford & Znajek 1977) in which a rotating black hole (one with a non-zero spin; a "Kerr" hole) is threaded by magnetic fields. Field loops cannot partially fall into the black hole, so fields tied to accreting particles become trapped near the event horizon. Since the black hole is rotating (frame-dragging the space-time around the event horizon), the fields essentially become wound up akin to wrappers on hard candies. What happens next is incompletely understood, but one can treat the black hole as if it becomes *charged* because its lowest energy state becomes one where it has a charge dependent on the strength of the field and the angular momentum of the SMBH (Wald 1974). Thus, a strong electric field is generated parallel to the field lines. A charge falling into this configuration is accelerated by the potential, radiating and triggering a cascade of particle production and acceleration, where the energy required to accelerate the particles comes from the rotational energy of the black hole. This process is analogous to rotation-powered pulsars (Goldreich & Julian 1969). More generally, the Blandford–Znajek mechanism falls under the umbrella of Penrose processes (Penrose 1969) in which the rotational energy of the black hole is extracted due to orbits with "negative energy" which arise in the ergosphere. A particle which falls onto such an orbit (e.g. due to a collision) can

leave the ergosphere with more energy than when it entered, hence tapping the rotational energy of the black hole for particle acceleration. If the particles escape predominantly along the spin axis, a relativistic jet may be formed (Gariel et al. 2010; Williams 2004). All spin-driven models require a large rotational energy to power the jets, and this requirement is easily met for many holes because the SMBH is accreting from a *disk* with a certain orbital angular momentum. The black hole therefore acquires this momentum via accretion and is "spun up."

On the other hand, the jet may not be produced in the ergosphere but rather from hydromagnetic winds from the accretion disk. The earliest and one of the simplest models of disk-driven jets is the Blandford–Payne model (Blandford & Payne 1982), in which energy and angular momentum are transported from the disk surface out into space by magnetic field lines. At large distances (relative to the size of the disk), the large-scale toroidal structure of the field collimates the flow, thereby forming a jet. Consider a thin accretion disk threaded by magnetic fields frozen into the material. The poloidal fields (those with components perpendicular to the plane of the disk) can transport small bundles of charges out of the disk. These packets begin with some initial angular momentum appropriate to their radius in the disk, but must follow the field line, which spans more than a single radius and tends to bend towards the rotation axis. Depending on the angle between the disk and the poloidal field, material lifted from the disk will tend to be thrown outwards (at relativistic speeds) effectively by centrifugal force. At larger distances from the disk, the fields become more toroidal (with non-zero components in the plane of the disk), collimating this outflow into a jet. Such hydromagnetic winds are similar to those invoked to explain astrophysical jets observed from non-relativistic potentials where the Blandford–Znajek mechanism is irrelevant. The Blandford–Payne and other hydromagnetic wind models do not rely on black holes with high spin values

since the angular momentum and energy is derived directly from the disk, but are not inconsistent with large spin because the black hole accretes from the disk.

There are a large number of more complex models built on the foundation of these ideas, and naturally there are hybrid models as well which tap the angular momentum of both the disk and the hole. The detailed origin, collimation, and content of the jets (e.g. particles or Poynting flux) are unsolved problems well beyond the scope of this work. Moreover, the type of accretion flow is probably important: radio jets may be associated with radiatively inefficient accretion flows in which the black hole is accreting from a hot, tenuous torus (which can support magnetic fields) far below the maximum Eddington accretion rate (Narayan & Quataert 2005; Rees et al. 1982); because (in the Blandford–Znajek scheme) it is the energy of the black hole that is tapped to produce the jet (via particle creation cascades), very little accretion is required to drive an extremely powerful radio jet. For our purposes we consider the jet to form inside a black box on a scale much smaller than the radio galaxy. However, it is worth emphasizing that the "black box" is much larger than the AGN because we do not know what galactic conditions lead to the local conditions required for radio jets. Bearing this in mind, we leave behind the ergosphere and return to already-formed radio galaxies and their interaction with the hot intracluster medium on scales more than ten billion times larger.

1.4 The Hot Atmospheres of Radio Galaxies & Radio-Mode Feedback

Some of the first X-ray observations of clusters of galaxies revealed a surprising fact about the Universe: galaxies are but tiny islands in seas of hot ($\sim 10^7$ K) plasma. Thermal emission from galaxy groups and clusters as well as observed

inverse-Compton (up)scattering of cosmic background radiation light there (the *Sunyaev-Zeldovich effect*; for an early review, see Sunyaev & Zeldovich 1980) indicates that, in fact, the vast majority of the baryonic matter in clusters resides in between the galaxies (e.g. David et al. 1995). It is this material with which the radio jets and lobes interact, so it is worth briefly discussing the origin and characteristics of the hot plasma before describing the jet–atmosphere interaction in detail. For a more thorough review of X-ray emission from galaxy clusters, see Rosati et al. (2002). (Parenthetically, we note that X-ray astronomers frequently refer to the hot plasma in and out of galaxies as "hot gas" or "X-ray emitting gas" despite the fact that the material is in the plasma phase. The term "hot atmosphere" can refer to the ISM or the IGM/ICM.)

Galaxy groups and clusters are the largest known gravitationally bound structures in the Universe, and the galaxies in them are merely tracers of the large underlying dark matter potential. Moreover, there is a vast sea of hot plasma in between the galaxies in the potential well—the galaxies in the cluster contain only a tiny fraction of the total baryonic matter. The formation and evolution of galaxy clusters over cosmic time is the subject of intense study. There is broad agreement that clusters are essentially large regions of dark matter which have collapsed faster than the expansion of the Universe could separate them. Directly after the Big Bang, the Universe is thought to have been uniformly dense except for small perturbations on quantum scales. These perturbations were nearly instantaneously amplified during the inflationary epoch (in which the Universe is hypothesized to have increased its volume by more than a factor of 10^{75} within 10^{-32} s). After the end of inflation the Universe resumed steady expansion, and regions with sufficient density to collapse did so. In the most widely accepted cosmology (cold dark matter with a cosmological "constant," or ΛCDM for short), the smallest structures col-

lapsed first and merged to form larger structures. In this scheme, galaxy clusters are the largest and most recently formed associations of dark matter halos (with denser constituents inside making up the galaxies).

Trapped inside these regions are the baryons, whose temperature is largely a function of the dark matter potential. Since the dark matter is dynamically dominant, collisionless, and does not interact electromagnetically, to first approximation the distribution of the baryons is determined by the distribution of the dark matter. In fact, hydrostatic equilibrium is a remarkably good approximation for many clusters, so evidently the baryons have mostly relaxed, and they can be reasonably described as an isothermal gas with a King or β-model density profile (Cavaliere & Fusco-Femiano 1976), e.g.

$$\rho = \frac{\rho_0}{(1 + (r/r_0)^2)^{3\beta/2}} \text{ g cm}^{-3}, \tag{1.1}$$

where β is typically 0.5, r_0 is the core radius, and ρ_0 is the core density of the cluster. Typical values for a rich cluster might be $r_0 \sim 100$ kpc and $\rho_0 \sim 0.01 m_{\rm H}$ g cm^{-3}. Assuming hydrostatic equilibrium, the temperature of the plasma is roughly proportional to the cluster mass ($T \propto M^{2/3}$), and typical rich clusters range from $10^7 - 10^8$ K with sound speeds of $c_s \sim 1000$ km s^{-1}. In reality, cluster temperature profiles are not isothermal, but rather decline with radius after a certain point because the dark matter making up the cluster also tapers off. Toward the center, all else being equal, one expects the temperature to rise. Even for relaxed clusters, at large radii hydrostatic equilibrium is no longer a good approximation, but the work presented in this dissertation is concerned exclusively with the cluster gas within the virial radius where, by definition, a relaxed cluster is relaxed. Mergers, galaxy motions, and AGN activity can disrupt the relaxed state, and we shall return to this below.

Because of the depth of the potential, the plasma gets quite hot. It is initially

heated by supersonic infall into the cluster well, creating an accretion shock which helps to thermalize the kinetic energy. Cluster plasma typically reaches temperatures of a few $\times 10^7$ K, so virtually all of it is ionized. Hence, we observe it in X-rays. This X-ray emission cools the gas both via continuum emission (thermal bremsstrahlung) and line radiation from those atoms which are not completely ionized. However, cooling tends to be slow thanks to the small densities in the ICM. For instance, thermal bremsstrahlung (also called free-free emission because it involves a free electron decelerated by an ion and thereby emitting radiation) power depends weakly on temperature and strongly on density:

$$j = \frac{dE}{dtdV} = 1.4 \times 10^{-27} T^{1/2} g_{\rm ff} n_e n_i \text{ erg s}^{-1} \text{ cm}^{-3} \tag{1.2}$$

where j is the frequency-integrated plasma emissivity and n_e and n_i are the electron and ion densities respectively. $g_{\rm ff} \sim 1.1 - 1.5$ is the frequency-averaged Gaunt factor. Since the plasma is largely ionized hydrogen, we often assume $n = n_e = n_i$. The internal energy of the plasma is proportional to nkT, so the cooling time is inversely proportional to n:

$$t_{\rm ff} \sim \frac{5nkT}{2j} \propto \frac{nkT}{T^{1/2} n^2} \tag{1.3}$$

Computing numerical factors, this is

$$t_{\rm ff} \sim 1600 T_7^{1/2} n_{-3}^{-1} \text{ Myr} \tag{1.4}$$

where T_7 is the temperature in units of 10^7 K and n_{-3} is the density in units of 10^{-3} cm^{-3}. Since these are typical values, the free-free cooling time is on the order of a couple billion years.

However, when densities in the core are sufficiently high, the cooling time is substantially smaller. It turns out that clusters are divided along a dichotomy into "cool-core" and "non-cool-core" clusters , with cool-core clusters comprising up to $\sim$75% of clusters (Hudson et al. 2010). Apart from smaller central temperatures,

cool-core clusters have much greater X-ray surface brightnesses and measured densities than their non-cool-core cousins, implying rapid cooling. Since cooling increases n, cooling material sinks and cools faster, leading to runaway cooling. In many cases, the measured luminosities and densities of the cluster core imply that the cooling time of the gas is much shorter than the age of the cluster. We would therefore expect to see a large reservoir of cold gas (i.e., below X-ray emitting temperatures) deposited on the cluster core–between $100 - 1000 M_{\odot}$ yr^{-1} in rich clusters. However, much less cool gas than expected has been detected in these systems, corresponding to a deposition rate of $1 - 10 M_{\odot}$ yr^{-1} (Fabian 1994; Peterson & Fabian 2006). The discrepancy is the so-called "cooling flow problem," and it is one of the central mysteries of clusters.

The obvious solution to the cooling flow problem is ongoing heating, and it is generally accepted that some kind of balancing heating occurs. There are several sources of heating which must contribute at certain rates, and it is not clear which, if any, are dominant. For instance, conduction from the surrounding ICM (Narayan & Medvedev 2001; Voigt & Fabian 2004) may maintain a floor temperature in the cool cores, or merger shocks (Randall et al. 2002) and merger-induced gas sloshing (Zuhone & Markevitch 2009) may heat or disrupt the cores. Alternatively, the cooling gas may induce starburst (Peterson & Fabian 2006; Veilleux et al. 2005) or AGN activity which then provides radiative and mechanical feedback, heating the cool core. Some of these may be ruled out as general solutions: conduction heating depends on $T^{5/2}$ and therefore is inefficient in cool clusters, it is not clear how frequently cluster mergers occur or if their rate was significantly higher in the distant past than in the "present," and star formation and SNe activity is too inefficient to prevent the cooling catastrophe. We therefore turn to AGN feedback (for a short, accessible review of AGN feedback see Fabian 2010).

In the AGN feedback picture, a heating–cooling balance is reached where just enough gas condenses onto the central galaxy to trigger a heating event that prevents further cooling. AGN feedback has observational support: whenever the central galaxy in the cluster (the brightest cluster galaxy or BCG) hosts a radio-loud AGN, the cluster has a cool core (Sun et al. 2009), the energy required to inflate radio cavities meets the heating requirement to keep the gas X-ray bright (e.g. Blanton et al. 2009; Fabian et al. 2006; McNamara et al. 2005; Randall et al. 2011), and the tight correlation between the Bondi accretion rate onto the central SMBH in elliptical galaxies and the jet power (Allen et al. 2006) suggests that AGN feedback is tunable: a stronger cooling rate produces a larger heating rate to maintain the balance.

However, AGN feedback is not without its problems. One of the most significant is that no obvious way to isotropize the energy distribution has been discovered. A powerful quasar generates winds which can sweep out and heat the surrounding material isotropically, but a radio galaxy (as seen in cool core clusters) occupies a narrow solid angle in the cluster. Although the jet drives shock waves and sound waves which may dissipate roughly isotropically, it is not clear how the work done to inflate the radio lobes eventually makes it into the ICM. One way this may happen is through entrainment of ICM and lifting it to large radii (Reynolds et al. 2002); when the gas falls back, the gravitational potential energy is thermalized. Another possibility is that the radio galaxy bubbles do not directly heat the gas, but rather stir it up to allow more efficient conduction heating from the cluster outskirts (Ruszkowski & Oh 2010). Still, there is not yet observational confirmation of these hypotheses. Arguments for the viability of AGN feedback through radio galaxies ("radio-mode feedback") primarily rely on the ubiquitous detection of X-ray cavities in the ICM associated with the radio galaxy (Figure 1.6). Additionally, despite the

Allen et al. (2006) results showing that jet power scales with inferred accretion rate, how the cooling material actually makes it down into the central parsec of the central galaxy is unclear, and there are no tight measurements of the energy deposition rate relative to the cooling time. In part, this is because AGN feedback is—considering the simplicity of the premise—remarkably broad in the amount of physics and astrophysics required to connect the small scales to large ones in detail: cosmology, plasma physics, magnetohydrodynamics, special and general relativity, galactic kinematics, molecular chemistry, and radiative transfer. Still, because of its potential cosmological significance, the connection between radio galaxies and their environments is important to understand.

1.5 X-shaped Radio Galaxies

We are now in a position to introduce the X-shaped radio galaxies (XRGs; Figure 1.8). XRGs are a bizzare class of radio galaxy with (apparently) *two* pairs of lobes, both somewhat or highly collimated. XRGs have one "active" or "primary" pair of lobes which house an active jet, whereas the "secondary" pair or "wings" have no jet and are strikingly misaligned with the primary lobes. In fact, it is unclear that the "secondary lobes" are really lobe-like at all in that they may never have been excavated by a jet. In many cases, both pairs of lobes are centered on the host galaxy's nucleus, but in all cases the XRGs are centro-symmetric (i.e., secondary lobes may be largely attached to the primary ones offset from the nucleus).

XRGs make up about 5-10% of FR II radio galaxies (Leahy & Parma 1992). The consensus sample is fairly small, but Cheung (2007) identified 100 "candidate" sources through a systematic search of the Very Large Array (VLA) Faint Images of the Radio Sky at Twenty-cm (FIRST) survey (Becker et al. 1995). Hence, a search

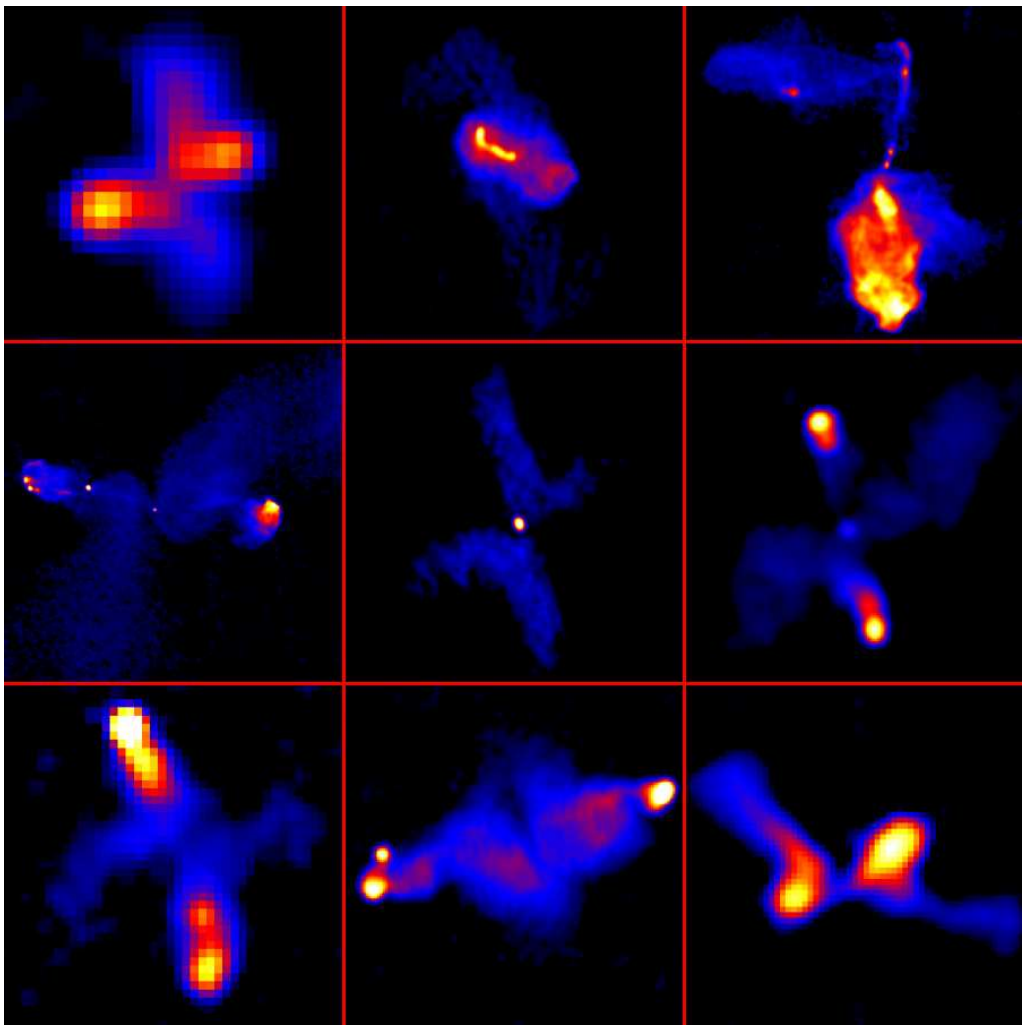

Figure 1.8 Some of the nearby X-shaped radio galaxies at 1.4 GHz.

for trends is now possible. XRGs are strongly bridged sources, but have powers commensurate with low-powered FR II sources or high-powered FR I sources near the FR I/II break, and have been proposed as a "transition" population (Cheung et al. 2009), although they may be consistent with the distribution of FR IIs in Best (2009). XRGs reside in elliptical galaxies with larger-than-average black hole masses (inferred from the $M-\sigma$ relation between black hole mass and stellar velocity dispersion and broad spectral lines from the AGN; Mezcua et al. 2011). XRGs do not seem to be in galaxies currently undergoing a merger based on an inferred starburst history (Mezcua et al. 2011) and a spectroscopic search for broad emission lines

and dusty nuclei (Landt et al. 2010), but the dynamic ages of their active lobes are younger than the age of the most recent starburst (Mezcua et al. 2011). XRG wings tend to be preferentially co-aligned with the minor axis of the host galaxy, whereas the primary lobes tend to be co-aligned with the major axis (Capetti et al. 2002; Saripalli & Subrahmanyan 2009). The radiative ages of the wings do not seem to follow a clear trend, as some wings have steeper spectral indices than the primary lobes (implying aging) whereas others do not (Lal & Rao 2005, for a brief explanation of spectral aging, see Appendix B).

The origin of XRGs is controversial, with three basic ideas discussed in the literature. The first is that XRGs are the result of a "spin-flip" in which the jet axis (which is identified with the spin axis of the black hole) is rapidly or instantaneously reoriented along a new direction, leaving the old lobes to decay while generating new ones along a new direction (Dennett-Thorpe et al. 2002; Ekers et al. 1978; Klein et al. 1995; Merritt & Ekers 2002; Rees 1978; Rottmann 2001; Zier & Biermann 2001). The second is that XRGs are simply formed by having two misaligned jets in the same galactic bulge (Lal & Rao 2005). Finally, there is a family of hydrodynamic models in which XRGs, like several other common distortions to the classical double-lobed radio galaxy, are shaped by pressure fronts and gradients in the ICM (Capetti et al. 2002; Leahy & Williams 1984; Worrall et al. 1995).

In the spin-flip model, the reorientation may occur as the result of secular precession in which the spin axis of the SMBH is quickly changed as a result of accretion torque (Dennett-Thorpe et al. 2002; Rees 1978). This may occur when a galaxy merger produces a disk of gas in the nuclear region with a significantly different orbital angular momentum than the black hole's spin. As the black hole accretes from this disk, its angular momentum shifts and it warps the disk into its equatorial plane (the Bardeen-Petterson effect; Bardeen & Petterson 1975). As a result of the

back-reaction of these torques, the spin axis shifts. While not instantaneous, this process might take only a few Myr (Dotti et al. 2010), which is small compared to the lifetime of the radio galaxy. A more intriguing possibility is that the XRGs are signatures of an approximately instantaneous spin-flip due to the final coalescence of a SMBH binary (Ekers et al. 1978). In this case, following a galactic merger, dynamical friction eventually brings the two nuclei and then SMBHs together. A binary SMBH forms, and hardens due to three-body interactions over an unknown period of time. Eventually, the binary separation is small enough that gravitational radiation becomes efficient and drives a rapid merger. If the angular momentum vectors of the SMBHs are misaligned, then upon merger the coalesced object will have a spin axis different from either of the binary components. If one of the black holes is driving a radio jet at the time of coalescence, an X-shaped source would result. XRGs may then be one of the few electromagnetic signatures of a massive black hole merger. Since the fossil lobes will decay rapidly due to radiative losses and adiabatic expansion, the frequency of XRGs could then be used to estimate SMBH merger rates.

This hypothesis is supported by the tendency of XRGs to be associated with higher-than-average mass SMBHs (Mezcua et al. 2011), but there are no signs of an ongoing merger (Landt et al. 2010; Mezcua et al. 2011). This is not necessarily a strike against the model, since black hole binaries may coalesce on much longer timescales than any starburst or AGN activity directly associated with the galaxy merger. However, Bogdanović et al. (2007) raise a significant objection to the black hole merger hypothesis. During coalescence, conservation of angular momentum can give the merged SMBH a significant "kick" of linear momentum. The strength of the kick depends on how misaligned the angular momenta of the binary components are, and in extreme cases they can reach ~ 3000 km s^{-1}. This is sufficient to eject a

fraction of SMBHs from their host galaxies entirely, which is inconsistent with our current understanding that every major galaxy has a central SMBH. Bogdanović et al. (2007) argue that, in fact, by the time of coalescence, most black holes will not have significantly misaligned angular momenta due to accretion during the binary phase from a common disk of material (with its own orbital angular momentum). Coalescence would then fail to produce an X-shaped source except in the case of "dry" mergers where the SMBH binary lacks significant material from which to accrete.

A second possibility for X-shaped morphology is simply that there are two misaligned jets within the same nucleus. In this scenario (Lal & Rao 2005), two SMBHs reside in the same bulge, each powering a jet and presumably accreting from different reservoirs of gas. The most plausible explanation for this configuration is a galactic merger in which the two galactic nuclei have sunk to the center of the system but have not yet completely relaxed. However, this scenario cannot explain some XRGs in which the wings are slightly offset from the nucleus and attached to the primary lobes, and XRGs are usually easily distinguishable into primary and secondary lobes. The primary lobes are frequently characterized by having jets or hot spots like their normal FR II counterparts, but such features are never seen in the wings. It is unclear in this scenario why a dual AGN would always consist of a powerful radio galaxy and a weak one with no apparent jet; it is conceivable that a dual AGN might consist of a radio-loud and radio-quiet AGN, but then the length of the wings (often comparable to or exceeding the primary lobes) could not be explained. In any event, this hypothesis is relatively easy to test with high-resolution radio images of XRG nuclei.

Finally, the wings may be produced by the preferential deflection of lobe plasma along a direction transverse to the jets by strongly asymmetric pressure gradients.

There is reason to believe jets respond to such gradients: the jets of XRGs are preferentially aligned along the major axis of their host galaxies and the wings along the minor axis (Capetti et al. 2002; Saripalli & Subrahmanyan 2009). Supposing that the hot ISM of the galaxy is roughly isothermal and in hydrostatic equilibrium, this means that the pressure falls off more rapidly along the minor axis while the atmosphere provides more resistance to the jet along the major axis. Hence, material in the radio lobes tends to flow along the minor axis, forming an X-shaped source.

In fact, there are several different proposals in the literature for how this might occur. The first is that the relativistic plasma flowing back from the jet head (*backflow*) which fills the lobes is diverted away from the jet axis by the pressure structure of the atmosphere (Kraft et al. 2005; Leahy & Williams 1984; Worrall et al. 1995). In this scenario (*buoyant backflow*), the backflow initially flows toward the nucleus antiparallel to the jet heads, but as the material is buoyant and does not occupy the same channel as the jet, it essentially flows around the high pressure zone of the central atmosphere. At this point, the flow is creating a new channel, so, like rivulets of water, it follows the path of least resistance and expands toward the minor axis. The buoyancy force prevents the material from moving closer to the galaxy, resulting in an X-shape. However, a significant objection to this scenario is that, even for light jets like the type we believe to power radio galaxies, the backflow speeds are a small fraction of the jet velocity (e.g., Antonuccio-Delogu & Silk 2010). Moreover, in the Worrall et al. (1995) picture, there is an underlying assumption that wings are free to form at the speed of the backflow whereas the lobes expand not at the speed of the jet but rather at the advance speed of the shock. If the wing plasma behaves at all like a fluid, it will instead evacuate cavities similar to the primary lobes as it expands into the cluster atmosphere. Even if the backflow is coherent to the ends of the wings, it will simply act as a much weaker

jet and the wing will expand at speeds much less than the backflow velocity. One might imagine overcoming this obstacle by invoking plasma physics: can a condition be found in which the relativistic electrons in the backflow simply free-stream into the surrounding atmosphere? It seems unlikely. First, although the mean free path might be very large for a given relativistic electron, the wings are identified as synchrotron-emitting features. The relativistic electrons are therefore confined to magnetic field lines and fill certain regions. This points to fluid-like behavior. Second, the buoyant backflow model relies on buoyancy to bend the lobes away from the jets. If electrons simply free-stream, buoyancy is not important. Since many wings are *longer* (in projection) than the lobes and spectral aging sometimes suggests lifetimes requiring highly supersonic expansion (e.g., 3C 403; Kraft et al. 2005), the buoyant backflow model is not obviously viable in all cases.

A second possibility proposed by Capetti et al. (2002) is that the resistance provided by the high pressure hot ISM laterally confines the nascent radio galaxy, i.e., in the "cocoon" phase where well developed radio lobes are absent. Of course, the atmosphere does not stop the jet, but if the jet is aligned along the major axis of the galaxy, the radio galaxy takes sufficiently long to escape the atmosphere that the spent jet plasma building up in the cocoon becomes overpressured relative to the ISM. As a result, the cocoon ruptures along the direction of the steepest pressure gradient (the minor axis), forming an XRG. The blow-out that forms the wings remains somewhat collimated by the tendency of the light radio-emitting plasma to follow the direction of least resistance, but pressure equilibrium is quickly re-established. Thus, the *overpressured cocoon* model requires XRGs to be formed near the inception of jet activity. As with the buoyant backflow model, wings longer than $\sim$100 kpc are difficult to explain with this model, since there is no driving force once the cocoon reaches pressure balance and it is difficult to imagine backflow driving

wings at relativistic speeds.

Other flavors of the hydrodynamic model propose that the jet itself is redirected, motivated by the observation that bent jets are fairly common. One such hypothesis is that dense clumps of gas left behind from a minor merger interfere with the jet, causing it to veer off in a transverse direction until the clump is ablated (Gopal-Krishna et al. 2010). Since jets appear to be able to turn at large angles while retaining their collimation, the radio galaxy would appear Z-shaped until the blockage in the original direction is removed, at which point it would return to its original path, thereby forming an XRG with wings slightly offset from the nucleus. The symmetry of the XRG in this scenario is attributed to the clumps of gas being associated with stellar shells, phase-wrapped remnants of a smaller merged galaxy distributed periodically across the galaxy (see, e.g. Quinn 1984).

Although each of these models finds some support in the data, the origin of XRGs is unknown (a critical review of the observational data and existing models is found in Gopal-Krishna et al. 2010). The strikingly different possibilities make XRGs an interesting class of objects on their own, as well as of interest for the gravitational wave community if the black hole merger hypothesis is correct. Further, regardless of the origin of XRGs, they offer a fascinating look at the processes which govern passive radio lobe evolution in the ICM: the wings are not jet-driven and therefore likely evolve as "dead" radio galaxies would despite the connection to the primary lobes (as we shall see, simulations indicate that synchrotron-emitting fluid flowing into the wings becomes turbulent and loses its memory and collimation). Whereas truly dead radio galaxies are rare (Worrall et al. 2007), and ghost bubbles associated with prior AGN activity are difficult to see in the radio and in the X-ray (although with sufficient telescope time it may be done, see a 1.4 Ms view of the Perseus cluster in Fabian et al. 2011), X-shaped sources keep the wings illuminated through

an influx of plasma. While the wings are not directly analogous to separate bubbles, they are subject to the same forces, often over similar distances. For this reason, XRGs are relevant to the AGN feedback community in terms of how the energy in radio lobes is ultimately transferred to the ICM.

1.6 Relevant Astronomical Instrumentation

Since radio galaxies are most easily detected in the radio band but their hot atmospheres can only be seen in the X-rays, both radio and X-ray observations are critical to this work. The X-ray observations presented in this thesis have been conducted exclusively with the *Chandra* X-ray Observatory whereas the radio data is primarily from the Very Large Array (VLA) radio interferometer. Much of the data we use in this work is publicly available, and in particular the optical Digital Sky Survey (DSS) and Sloan Digital Sky Survey (SDSS) data comes in final data product form with all calibrations applied.

1.6.1 *Chandra* X-ray Observatory

The *Chandra* X-ray Observatory is a NASA satellite comprised of a high resolution mirror assembly (HRMA) and detectors for imaging and high resolution spectroscopy. The HRMA consists of four concentric sets of grazing-incidence mirrors which focus the X-rays (through a parabolic–hyperbolic reflection) on to the detector array. Since X-rays have wavelengths short enough to interact with individual atoms, the mirrors are set up such that the incident X-rays hit the mirror almost edge-on (grazing incidence) and coated with iridium. At the focal plane, either the Advanced CCD Imaging Spectrometer (ACIS) array or the High Resolution Camera (HRC) detectors may be used. To obtain high resolution spectra of bright sources,

the High Energy Transmission Grating Spectrometer (HETGS) may be placed in front of the detector such that light dispersed by the grating falls onto different spatial locations on the detector, forming a bright "X" shape crossing at the zeroth order image (one arm is from the High Energy Grating while the other is from the Medium Energy Grating). *Chandra* is a soft X-ray instrument sensitive to photons with energies between $0.3 - 10$ keV (about 1–20 Å), and compared to other concurrent X-ray instruments has a relatively low effective area (energy-dependent light collecting area in cm^2, peaking near 1 keV) and high spatial resolution ($0.''5$). Hence, *Chandra* is the prime instrument for high-resolution X-ray imaging studies but requires more observing time to reach the same signal-to-noise ratio (S/N) as other X-ray observatories. Because X-ray observatories must be in space (X-ray photons are quickly absorbed in the upper atmosphere), further improvements to the instrument are impossible; slow degradation of the observatory requires occasional re-calibration.

Owing to its high spatial resolution, *Chandra* is the only X-ray instrument which can sufficiently resolve the ISM around radio galaxies. We use the ACIS array, made up of two focal plane arrays (ACIS-I and ACIS-S) shown in Figure 1.9. Apart from excellent spatial resolution, the aimpoint 80% encircled energy radius (a measure of the point spread function) is $0.''685$, allowing clean separation of the bright AGN from the surrounding hot ISM (this is not possible with the *XMM-Newton* X-ray mission whose angular resolution is approximately $6''$). Separating the ISM from the ICM is an important aspect of our project because we wish to test the Capetti et al. (2002) hypothesis that the jets in XRGs are preferentially co-aligned with the shallow pressure gradient along the major axis of the ISM.

Since (aside from the very brightest sources) X-ray events are recorded individually on the detector, it is easy to check the light curves for background flares.

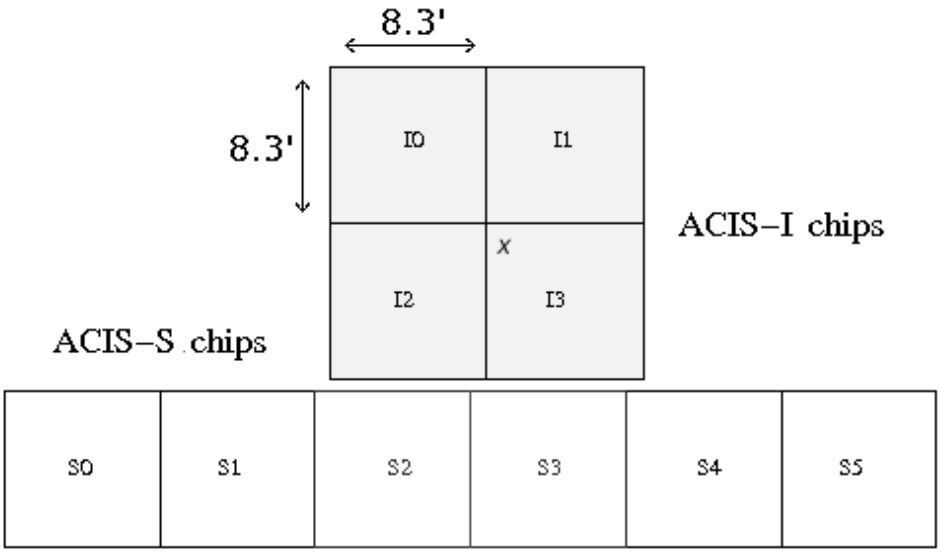

Figure 1.9 Schematic diagram of the ACIS detector array. The S3 chip is the usual aimpoint for *Chandra* observations and was used in all of our XRG observations. Some control sample radio galaxy data we used was obtained with the lower sensitivity ACIS-I array at top.

Moreover, because the ACIS pixels record energy information, detection of a hot atmosphere allows us to obtain its frequency spectrum, allowing us to determine whether it is thermal emission. Since nonthermal emission does not necessarily trace the morphology of the hot gas with which radio galaxies interact, it is important to be able to distinguish between thermal and nonthermal extended emission. While these spectra are low resolution ($\Delta E \sim 160$ eV) compared to grating spectra ($\Delta E \sim 0.4 - 77$ eV), the spectral shapes of thermal and nonthermal plasma in the energy range probed by *Chandra* ($0.3 - 10$ keV) are sufficiently different that even with tens of counts a distinction may be made.

1.6.2 The Very Large Array & Radio Interferometry

The radio images we use primarily come from the VLA interferometer in New Mexico. Interferometry is much more common at radio wavelengths than in other bands because the wavelengths are so long (at 1.4 GHz, a radio wavelength is 21 cm). Since the spatial resolution of a telescope θ is given by $\theta = \lambda/D$, where λ is the wavelength of light received and D is the telescope diameter, long wavelengths require very large telescopes to achieve high resolution. The sizes required are often impractical (the Arecibo Observatory is the largest single-dish telescope in the world at 305 m across but cannot be steered and is located in a natural bowl in Puerto Rico), so collecting area is sacrificed for spatial resolution.

In brief, the principle behind interferometry is that light from a given source arrives at slightly different times to two telescopes separated by some distance d. Supposing we pick out just one wavelength of light to observe, the phase of the light is slightly different by the time it reaches the second detector. When the two waves are combined (after first being converted into some electronic signal), the resultant wave has an interference pattern dependent on this phase difference. This process is sketched in Figure 1.10. The phase difference information corresponds to information about distribution on the sky; a single pair of telescopes (baseline) is sensitive only to emission on scales corresponding to the separation distance d and follows a predictable pattern known as the complex visibility (measured source amplitude as a function of d akin to a sinc function). Hence, changing the distance of a baseline until a strong detection is achieved yields information about the angular size of the source on the sky.

Imagine now that instead of just two telescopes, one has an array of many telescopes, each with a different separation from one another. The maximum baseline is

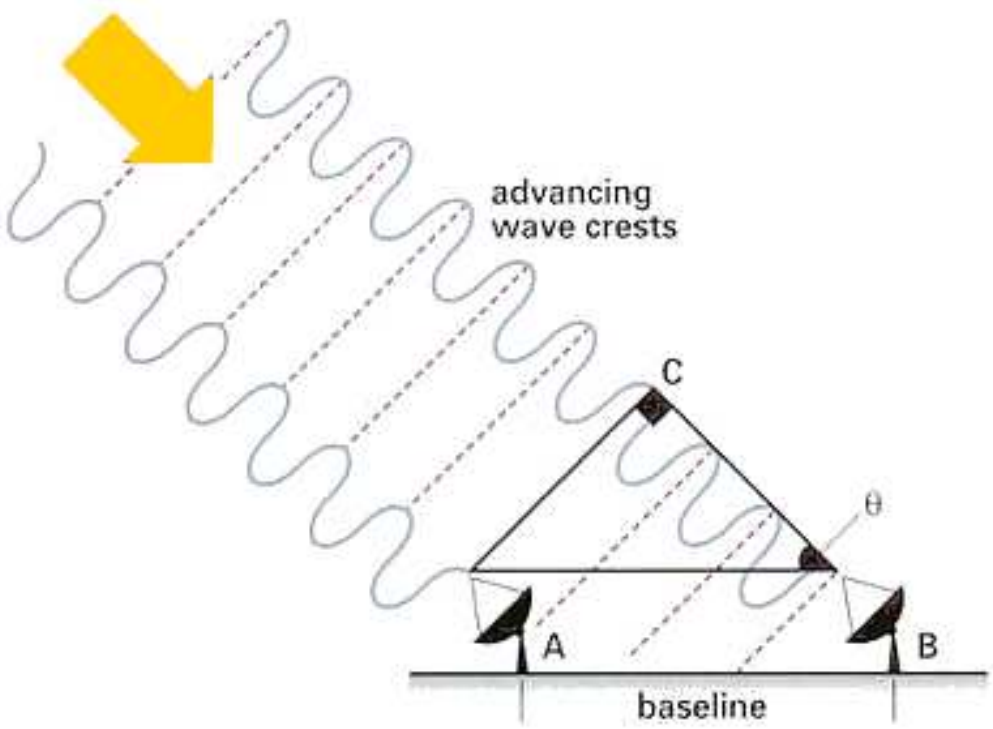

Figure 1.10 Schematic diagram of a single interferometer arm, showing the geometry and phase difference incurred in light from a given source.

the longest distance between any two telescopes, and likewise the minimum baseline is the shortest distance between any two telescopes. The array therefore functions as a giant aperture made up more of empty space than telescope. Instead of directly imaging (because interferometry relies on differencing of incoming waves to find phase changes), the interferometer maps the sky it sees in Fourier space, with a field of view equivalent to the size of an individual telescope. In other words, one must take the inverse Fourier transform of the observed pattern on the sky in order to recover an image. One might imagine that this is not particularly useful when the array is static (the Fourier space would be extremely sparsely sampled), but radio interferometers take advantage of the rotation of the Earth to move the sky across the field while essentially observing continuously. Hence, *arcs* are traced in Fourier space (called the uv plane in contrast to the familiar xy plane), and the

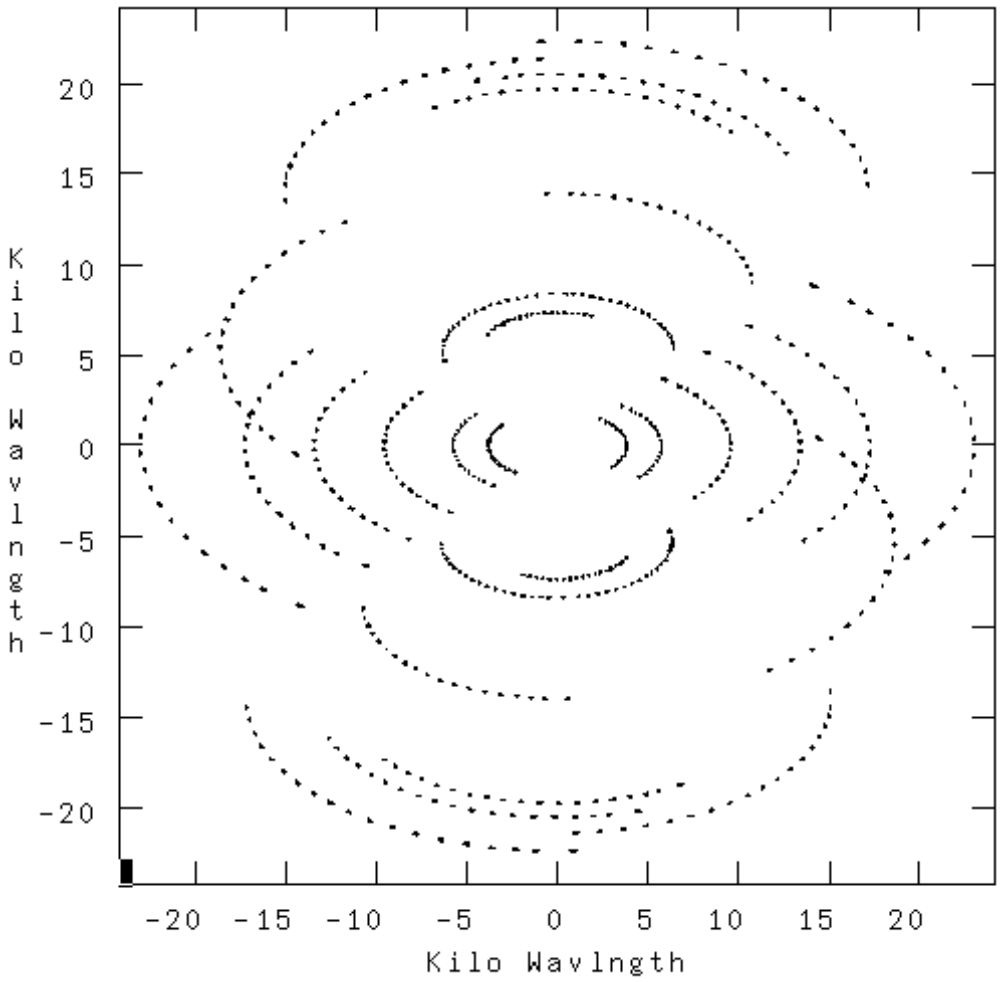

Figure 1.11 Arcs in the *uv* plane showing the effect of the rotation of the Earth on the projected baselines. Taking the Fourier transform of this map would produce an image. A complete image would have a completely filled *uv* plane (entirely black). Note the shortest and longest scales probed.

density of these arcs determines the quality of the image (Figure 1.11). In an array with no redundant baselines, each telescope forms an interferometer with each other telescope. To process the large amount of phase difference data coming in, radio telescopes use a *correlator* in which the signals from each interferometer arm are combined.

The VLA is a radio interferometer made up of 27 antennas. The spatial resolution depends on the array configuration and the spectral coverage ranges from 74 MHz

to 50 GHz. The radio galaxy images used in this thesis are primarily at 1.4 GHz (about 21 cm, coinciding with an atmospheric window of high transmission and the famous spin-flip spectral line from neutral atomic hydrogen), but we also present 5 GHz data where it is better. We use primarily archival data obtained in the A or B configurations with beamsizes (full width at half maximum [FWHM] of the point spread function) of $1 - 5''$. The VLA has recently been upgraded to the expanded VLA (EVLA), but none of the data presented in this work is from the EVLA.

None of the images we present were obtained below 1 GHz, so it is possible that some low-frequency emission has been missed (as is often the case with non-bridged radio galaxies). However, since the XRGs are strongly bridged sources, we deem this unlikely. Many of the consensus XRGs have been observed with low-frequency radio interferometers and corroborate this assumption (Lal & Rao 2005). Still, low-frequency observations are of interest to search for spectral ageing of the radio plasma and thereby gain insight into what makes wings and keeps them bright.

1.7 Dissertation Outline

As may be guessed from the title, this dissertation concerns the *hot atmospheres* of X-shaped radio galaxies. The formation models for XRGs are remarkably different, and heretofore the hot environments of XRGs have not been systematically studied despite being claimed as the source of XRG morphology in the hydrodynamic models. Although the preferential orientation of the radio jet along the major axis of its host galaxy is suggestive, it is not the starlight with which the radio galaxy interacts, but rather the hot ISM. Beyond the galaxy, the structure of the ICM to which the morphology of some XRGs is attributed is unclear. Hence, a major goal of this thesis is determining the viability of the hydrodynamic models.

To remedy this obvious gap, we conduct two simple experiments to answer two major questions: (1) Do XRGs appear to be aware of their hot environments, and (2) Can hot environments actually produce X-shaped morphology as proposed in the literature?

The first is addressed in Chapter 2 (adapted from Hodges-Kluck et al. 2010a), where we present the results of an X-ray survey of nearby XRGs and demonstrate that the jet–major axis alignment exists in the hot gas as well. Just as importantly, we demonstrate that this is not the case in a control sample of FR I and II radio galaxies with archival *Chandra* data.

As part of our observational X-ray study, we obtained a deep (100 ks) *Chandra* pointing toward the XRG 4C +00.58, an XRG whose jet is, unusually, aligned with the *minor* axis of the host galaxy. This study, presented in Chapter 3 and adapted from Hodges-Kluck et al. (2010b), concludes that the hydrodynamic models are not good explanations for the X-shaped morphology and that accretion torque or a black hole merger is the most likely scenario. Indeed, our study proves that X-ray observations are crucial for testing models beyond the hydrodynamic scenarios.

To address the second major question, we conduct a numerical hydrodynamic experiment to determine how the underlying ISM/ICM morphology influences the classical double-lobed radio galaxy morphology. This experiment is described in Chapter 4 (adapted from Hodges-Kluck & Reynolds 2011) and demonstrates that some mixture of the buoyant backflow and overpressured cocoon models may produce X-shaped morphology when a powerful, but decaying, radio jet is driven along the major axis of a highly eccentric or triaxial host galaxy.

Finally, in Chapter 5 we summarize the results of this work, address outstanding issues, and discuss potential ways forward. We also motivate XRGs as a way to probe AGN feedback in detail, something that has little to do with their origin but

has broader relevance for the AGN and galaxy clusters fields.

Chapter 2

The *Chandra* View of Nearby X-shaped Radio Galaxies

2.1 Introduction

"Winged" and X-shaped radio galaxies (XRGs) are centro-symmetric subclasses of Fanaroff-Riley (FR) type I and II radio galaxies (Fanaroff & Riley 1974) which exhibit a second, fainter pair of wings lacking terminal hot spots in addition to the symmetric double lobe structure seen in ordinary FR II galaxies (Leahy & Williams 1984). A broader introduction is given in Chapter 1. The X-shaped morphology is of interest because two remarkably disparate classes of models have been invoked to explain it. The first class is predicated on the reorientation of the jets either by realignment of the supermassive black hole (SMBH) spin or the accretion disk, whereas the second purports to explain the distorted morphology as the result of hydrodynamic interaction between the radio lobe and its surrounding gaseous environment on kiloparsec scales.

In the first case, the most common explanation for the X-shaped morphology is

that the SMBH has its spin axis realigned, either via merger or precession (Chapter 1).

In contrast to the rapid-realignment models, hydrodynamic models propose that the wings of XRGs were never directly inflated by a jet. These models argue that XRGs form due to backflow (plasma flowing back towards the AGN from the hot spot shocks) that interacts with the surrounding gas. As presently conceived, backflow models require FR II morphlogy to drive the strong backflows. The existence of FR I XRGs challenges these hypotheses, but Saripalli & Subrahmanyan (2009) argue that, since several of the FR I XRGs appear to be restarted AGN with inner FR II morphology, the FR I XRGs could have had edge-brightened morphology when the wings were inflated, implying an evolution of FR II to FR I sources (Cheung et al. 2009). In this Chapter, we consider the backflow models as a unified class. The two most prominent backflow scenarios include the "buoyant backflow" model (Leahy & Williams 1984; Worrall et al. 1995) and the "overpressured cocoon" model (Capetti et al. 2002). The buoyant backflow model supposes that the buoyancy of the relativistic plasma cocoon in the interstellar or intragroup/intracluster medium (ISM or IGM/ICM) produces the additional wings. Because of the collimation seen in the more dramatic XRG wings, we refer to them hereafter as "secondary lobes" even though, if the hydrodynamic premise is correct, they are not of the same character as the primary lobes.

Capetti et al. (2002) propose a variant model in which backflowing plasma confined by an envelope of hot gas continues to aggregate until the cocoon of radio plasma is significantly overpressured, at which point it blows out of the confining medium at its weakest point. Supposing that the confining medium is the ISM of an elliptical galaxy, if the jet is aligned along the *major* axis of the galaxy, then the cocoon may become overpressured before the jet bores through the ISM, and

the radio plasma will blow out along the *minor* axis of the galaxy, forming the secondary lobes. Conversely, if the jet is oriented along the minor axis of the galaxy, then backflow will either escape along the same axis or the jet will escape the ISM before the cocoon can become overpressured. Capetti et al. (2002) cite an intriguing correlation between the orientation of the secondary lobes in XRGs and the minor axis of the stellar light of the host galaxy as evidence for their model, which they further support with two-dimensional hydrodynamic simulations. In a follow-up study including "normal" radio galaxies, Saripalli & Subrahmanyan (2009) find that the primary lobes of giant radio galaxies are preferentially aligned along the minor axis of the host, whereas they extend the original Capetti et al. (2002) result to a larger XRG sample. Although the observed geometric correlation is strong, much of the potentially relevant physics is absent in the Capetti et al. (2002) simulations, and Kraft et al. (2005) note that the buoyant backflow model can explain the observed correlation by assuming an anisotropic medium to divert the backflow. Moreover, it is unclear whether real radio lobes are actually overpressured. Reynolds et al. (2002) argue that an overpressured cocoon is inflated early on, but in the buoyant backflow model, the secondary lobes are formed later. In either case, the geometric correlation favors a hydrodynamic origin for the secondary lobes in the absence of an explanation for a relationship between the angular momenta of two merging SMBHs and large-scale structure of the galaxy. For the remainder of this Chapter, we refer to the "Capetti et al. (2002) geometry" to describe the correlation noted in XRGs and the proposed geometry of jet alignment that would produce them.

There are additional XRG formation models which are similar to the ones presented above in that they rely solely on either the black hole(s) involved or jet–gas interaction. These include the hypothesis that X- and Z-shaped distortions arise via gravitational interaction with another galaxy (van Breugel et al. 1983; Wirth et al.

1982), the idea that the jets are diverted by the ISM of a smaller merging galaxy (Gopal-Krishna et al. 2003; Zier 2005), and the aforementioned Lal & Rao (2007) proposal that both lobes are powered by active jets. Because these models are not as easily probed by the hot gas, we focus on the backflow models hereafter.

In this Chapter, we seek to characterize the properties of the hot gas which makes up the confining medium in these systems and determine whether the Capetti et al. (2002) optical–radio geometric correlation also exists in the X-ray band. One assumption of the Capetti et al. (2002) proposal is that the stellar distribution traces the hot gas which makes up the confining medium. We will test this assumption directly by determining the extent to which optical and X-ray morphology are correlated. As a parallel study, we present the results from new and archival *Chandra X-ray Observatory* observations of XRGs and investigate whether the hot gas in XRG systems differs from that in a comparison sample of archival *Chandra* observations of "normal" FR I and II galaxies (taken largely from the 3CRR catalog; Laing et al. 1983).

Any observational study of XRGs is necessarily limited by the small number of known and candidate sources. Our study is further limited by two important factors: (1) the hot gas surrounding radio galaxies becomes increasingly difficult to characterize at higher redshift, and (2) useful X-ray data do not exist for most XRGs. These considerations strongly constrain our conclusions. We therefore discuss in detail our target selection criteria in Section 2.2, as well as the observational parameters and reduction techniques applied to the data. In Section 2.3 we discuss our primary analysis of the morphology of the hot gas, and in Section 2.4 we discuss the X-ray spectra of the AGN. In Section 2.5 we summarize our results and interpretations.

Throughout this Chapter, we adopt the *Wilkinson Microwave Anisotropy Probe*

(WMAP) values of $H_0 = 71$ km s^{-1} Mpc^{-1}, $\Omega_M = 0.27$, and $\Omega_{vac} = 0.73$ with flat geometry. We calculate equivalent angular scale and distances at redshift using the online calculator provided by Wright (2006), and for Galactic absorption, we use the online HEASARC N_H calculator with values from the Leiden/Argentine/Bonn survey (Kalberla et al. 2005)[1].

2.2 *Chandra* Observations

Chandra is well suited to a study of the hot environments of radio galaxies thanks to its high sensitivity, 0.5″ spatial resolution, and 0.3-10 keV bandwidth. *Chandra* has also been able to resolve X-ray emission associated with the radio lobes into hot spots and jets (Hardcastle et al. 2004); distinguishing this emission from the gaseous halos is especially important for our purposes.

Our analysis sample of *Chandra* data consists of eighteen comparison sample galaxies and eight XRGs (Figure 2.1 & 2.2 with observational parameters in Table 2.1). In this section, we describe how we arrived at this sample, starting with the preliminary selection criteria for the XRG and comparison samples from radio data and availability in the *Chandra* archive (Section 2.2.1). After reducing these data, we rejected a number of galaxies due to low quality or pile-up (Section 2.2.2), then used spectral fitting to find those galaxies where the diffuse gas dominates the photon count in the relevant regions (Section 2.2.3). These are the galaxies we include in our final sample (Table 2.1); Figures 2.1 & 2.2 are discussed along with the radio and optical data we use in Section 22.4.

We note that many of the archival data sets have been published, and references are provided in Table 2.1 where available. Our goal is not to exhaustively study any

[1]See http://heasarc.gsfc.nasa.gov/cgi-bin/Tools/w3nh/w3nh.pl

Table 2.1. *Chandra* Observational Parameters

Name	Secondary Identifier	z	Ang. Scale (kpc/″)	obs. IDs	Exp. Time (ks)	CCD Array	FR Type	Selected *Chandra* Refs.	Radio Refs.
				XRGs					
B2 1040+31A	J1043+3131	0.036	0.706	9272	10	ACIS-S	I/II	this work	AM221+AM222
PKS 1422+26	J1424+2637	0.037	0.725	3983	10	ACIS-S	I/II	this work	AM364
NGC 326	J0058+2651	0.048	0.928	6830	94	ACIS-S	I/II	1,2,9,10	a
3C 403	J1952+0230	0.059	1.127	2968	49	ACIS-S	II	3,4,5	b
4C +00.58	J1606+0000	0.059	1.127	9274	10	ACIS-S	II	this work	AC818
3C 192	J0805+2409	0.060	1.144	9270	10	ACIS-S	II	6	c
3C 433	J2123+2504	0.102	1.855	7881	38	ACIS-S	I/II	7	b
3C 315	J1513+2607	0.108	1.951	9313	10	ACIS-S	I	this work	AM364
				Comparison Sample					
3C 449	J2229+3921	0.017	0.341	4057	30	ACIS-S	I	4,5,8,9,10,26	AK319
3C 31	J0107+3224	0.017	0.341	2147	45	ACIS-S	I	4,5,9,11,26	a
3C 83.1B	J0318+4151	0.018	0.361	3237	95	ACIS-S	I	4,5,12	AK403
3C 264	J1145+1936	0.021	0.419	4916	38	ACIS-S	I	4,8	d
3C 66B	J0223+4259	0.022	0.439	828	45	ACIS-S	I	4,5,8,13	e
3C 296	J1417+1048	0.024	0.477	3968	50	ACIS-S	I	4,5	f
NGC 6251	J1632+8232	0.024	0.477	4130	50	ACIS-S	I/II	4,14	g
PKS 2153−69	J2157−6941	0.028	0.554	1627	14	ACIS-S	II	15,16	h
3C 338	J1628+3933	0.030	0.593	497+498	20+20	ACIS-S	I	4,5,8,9,14,17	i
3C 98	J0358+1026	0.030	0.593	10234	32	ACIS-I	II	this work	j
3C 465	J2338+2702	0.031	0.612	4816	50	ACIS-S	I	4,8,9,27	a
3C 293	J1352+3126	0.045	0.873	9310	8	ACIS-S	II	25	k
Cyg A	J1959+5044	0.056	1.073	360+5831	35+51	ACIS-S	II	18,19	j
3C 445	J2223−0206	0.056	1.073	7869	46	ACIS-S	II	26	l
3C 285	J1321+4235	0.079	1.474	6911	40	ACIS-S	II	20	k
3C 452	J2245+3941	0.081	1.508	2195	81	ACIS-S	II	4,21	b
3C 227	J0947+0725	0.087	1.609	6842+7265	30+20	ACIS-S	II	22	b
3C 388	J1844+4533	0.091	1.675	4756+5295	8+31	ACIS-I	II	23	m

Note. — Observational parameters for archival and proprietary *Chandra* datasets with significant thermal emission (see Table 2.3). Redshifts are obtained either from SIMBAD or compilation of Cheung (2007). X-ray references with more detail on the particular data set are provided above; not all references are provided. VLA program codes are provided where we processed data ourselves.

References. — **X-ray:** (1) Worrall et al. (1995); (2) Murgia et al. (2001); (3) Kraft et al. (2005); (4) Evans et al. (2006); (5) Balmaverde et al. (2006); (6) Hardcastle et al. (2006); (7) Miller & Brandt (2009); (8) Donato et al. (2004); (9) Canosa et al. (1999); (10) Worrall & Birkinshaw (2000); (11) Jeltema et al. (2008); (12) Sun et al. (2005); (13) Hardcastle et al. (2001); (14) Evans et al. (2005); (15) Ly et al. (2005); (16) Young et al. (2005); (17) Johnstone et al. (2002); (18) Young et al. (2002); (19) Smith et al. (2002); (20) Hardcastle et al. (2007b); (21) Isobe et al. (2002); (22) Hardcastle et al. (2007a); (23) Kraft et al. (2006); (24) Sun et al. (2009); (25) Massaro et al. (2008); (26) Perlman et al. (2010); (27) Hardcastle et al. (2005)
Radio: (a) Condon et al. (1991); (b) Black et al. (1992); (c) Baum et al. (1988); (d) NRAO VLA Archive Survey; (e) Hardcastle et al. (1996); (f) Leahy & Perley (1991); (g) Sambruna et al. (2004); (h) Fosbury et al. (1998); (i) Ge & Owen (1994); (j) Perley et al. (1984); (k) Alexander & Leahy (1987); (l) Leahy et al. (1997); (m) Roettiger et al. (1994)

individual source. Notes on individual sources are found in Appendix C.

2.2.1 Preliminary Target Selection

The most complete compilation of known and candidate X-shaped sources in the literature is that of Cheung (2007), who used the NRAO[2] *Very Large Array* (VLA; Thompson et al. 1980) Faint Images of the Radio Sky at Twenty cm (FIRST; Becker et al. 1995) data to identify the candidate XRGs. For this Chapter, we define XRGs as comprising all radio galaxies in Cheung (2007) that have a wing length exceeding 80% of the active lobes (Leahy & Parma 1992, the "classical" XRGS) and those "winged" sources in Cheung (2007) which have obvious X-shaped morphology in the angle between the active lobes and the wings. Assuming the projected lengths on the sky are the real lengths of the wings, in the backflow models these may be "classical" XRGs at an earlier stage.

We wish to study the hot gas surrounding the radio galaxy. The rapid decline in surface brightness and reduction in angular size with increased redshift makes a cutoff redshift of $z \sim 0.1$ practical for typical *Chandra* exposure times (even in this scheme, our sample is biased towards high pressure systems). Nineteen XRGs fall within this cutoff; the highest redshift in this group is $z = 0.108$. However, we have *Chandra* data for only thirteen of these sources, and these comprise our preliminary sample. These sources include 3C 315, 3C 223.1, NGC 326, PKS 1422+26, 3C 433, 3C 403, 3C 192, B2 1040+31A, Abell 1145, 4C +00.58, 3C 136.1, 4C +32.25, and 4C +48.29.

This sample is heterogenous in its radio properties and morphology. A few of the galaxies may be described as Z-shaped (Gopal-Krishna et al. 2003; Zier 2005).

[2]The National Radio Astronomy Observatory is a facility of the National Science Foundation operated under cooperative agreement by Associated Universities, Inc.

NGC 326, for instance, has long secondary lobes that do not seem to meet at a common center. Others (e.g. B2 1040+31A) have obviously X-shaped lobe axes, but the lobes are not as well collimated as in NGC 326 or 3C 315. Lastly, PKS 1422+26, B2 1040+31A and 3C 433 appear to be hybrid FR I/II radio galaxies with one FR I lobe and one FR II lobe (A "HYMOR"; see Gopal-Krishna & Wiita 2000). It is unknown whether these distinctions are signatures of any formation model, and we note that XRGs tend to lie close to the FR I/II break in other observables (Cheung et al. 2009). In this Chapter we use the definitions of Cheung (2007) and so consider the XRG sample as a unified whole, and we caution that our results are interpreted within this framework. In particular, there is no consensus in the literature on what constitutes an "X"-shaped galaxy. In their optical study, for example, Saripalli & Subrahmanyan (2009) classify 3C 76.1 ($z = 0.032$) as an XRG, whereas we do not. They also classify several higher redshift galaxies as XRGs which do not appear in the Cheung (2007) list (e.g. 3C 401 or 3C 438); in this respect our sample is conservative. At least one high redshift XRG from the Cheung (2007) list—3C 52 ($z = 0.285$)—has a *Chandra* exposure, and 3C 197.1 ($z = 0.128$) may be an XRG and is also in the *Chandra* archive. We choose not to use these exposures, although we note them in Appendix C.3.

Within the same redshift cutoff, we identify normal FR I and II galaxies in the *Chandra* archive as a comparison sample. The aim of this sample is to determine whether XRGs systematically differ in X-ray properties from normal radio galaxies. It is not obvious what constitutes an appropriate comparison sample because although FR II lobes are deemed necessary to produce X-shaped morphology in the backflow scenario, FR I XRGs exist (Saripalli & Subrahmanyan (2009)). In the Saripalli & Subrahmanyan (2009) interpretation of FR I XRGs, the FR I lobes must have had FR II morphology at the time the wings were generated. Supposing

that both the Capetti et al. (2002) model and Saripalli & Subrahmanyan (2009) interpretation are correct, the "old" FR I lobes must obey the same geometry as their "active" FR II counterparts. A comparison of the XRG sample to both types is therefore useful. The combined sample also provides a larger reservoir of sources for measuring the correlation between optical and X-ray isophotes in the ISM. We adopt a preliminary comparison sample consisting of (1) all FR II galaxies within $z \sim 0.1$ with data in the *Chandra* archive and (2) FR I galaxies from the DRAGN catalog [3] with the same conditions. There are 41 sources meeting these criteria.

2.2.2 Data Reduction

Thirteen XRGs and 41 normal radio galaxies comprise our preliminary samples, but the data for many of these are not of sufficient quality for our analysis. Both the archival data and our new data use Advanced CCD Imaging Spectrometer[4] (ACIS) chips with no transmission grating in place; we immediately rejected sources which have only grating spectrometer observations due to severe pile-up in the zeroth order image (only the brightest sources have grating data). Most of the data sets use the nominal aim point on the ACIS-S3 chip, but we consider several ACIS-I archival observations.

We reprocessed the *Chandra* data sets to generate 0.3–10 keV level=2 files using the *Chandra* Interactive Analysis of Observations (CIAO v4.0) data processing recipes ("threads")[5] with the most recent CALDB release (3.5.0). Times with noticeable background flares were excised by inspecting 0.3–10 keV lightcurves. A

[3]Leahy, J.P., Bridle, A.H. & Strom, R.G., editors "An Atlas of DRAGNs" (http:/wwww/jb.man.ac.uk/atlas/)

[4]See http://cxc.harvard.edu/proposer/POG/pdf/ACIS.pdf

[5] See http://cxc.harvard.edu/ciao/threads/index.html

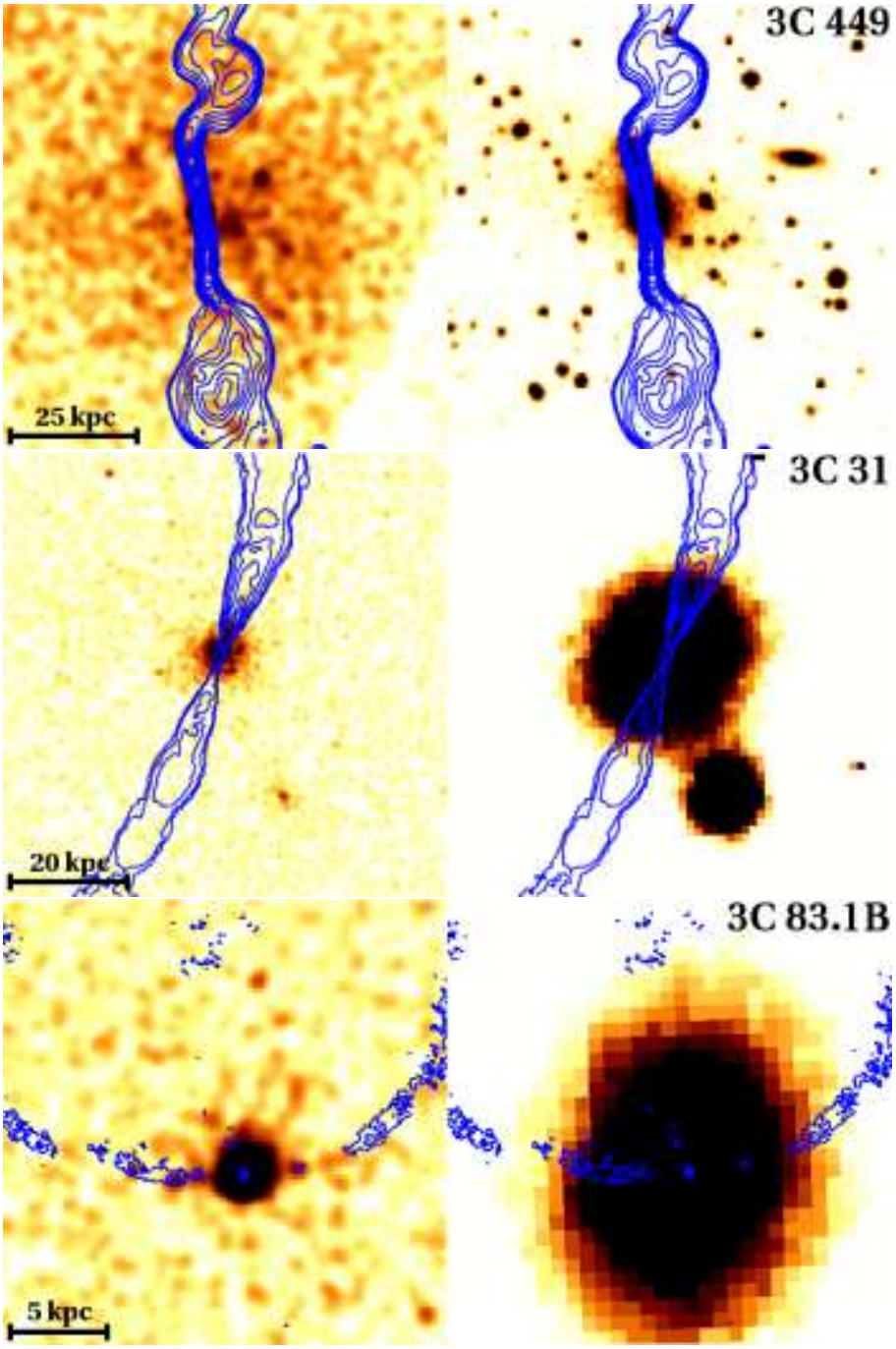

Figure 2.1 *Chandra* and optical images of our control sample galaxies with significant thermal emission. The left panel in each case is an image of the *Chandra* ACIS-S3 chip with uniform Gaussian smoothing and point sources removed. The right image is an optical image from DSS or SDSS. Overlaid in blue are VLA radio map contours. The images are sorted by ascending redshift. Note that for 3C 98 and 3C 388 the chip image is of the ACIS-I chip(s) instead of ACIS-S3.

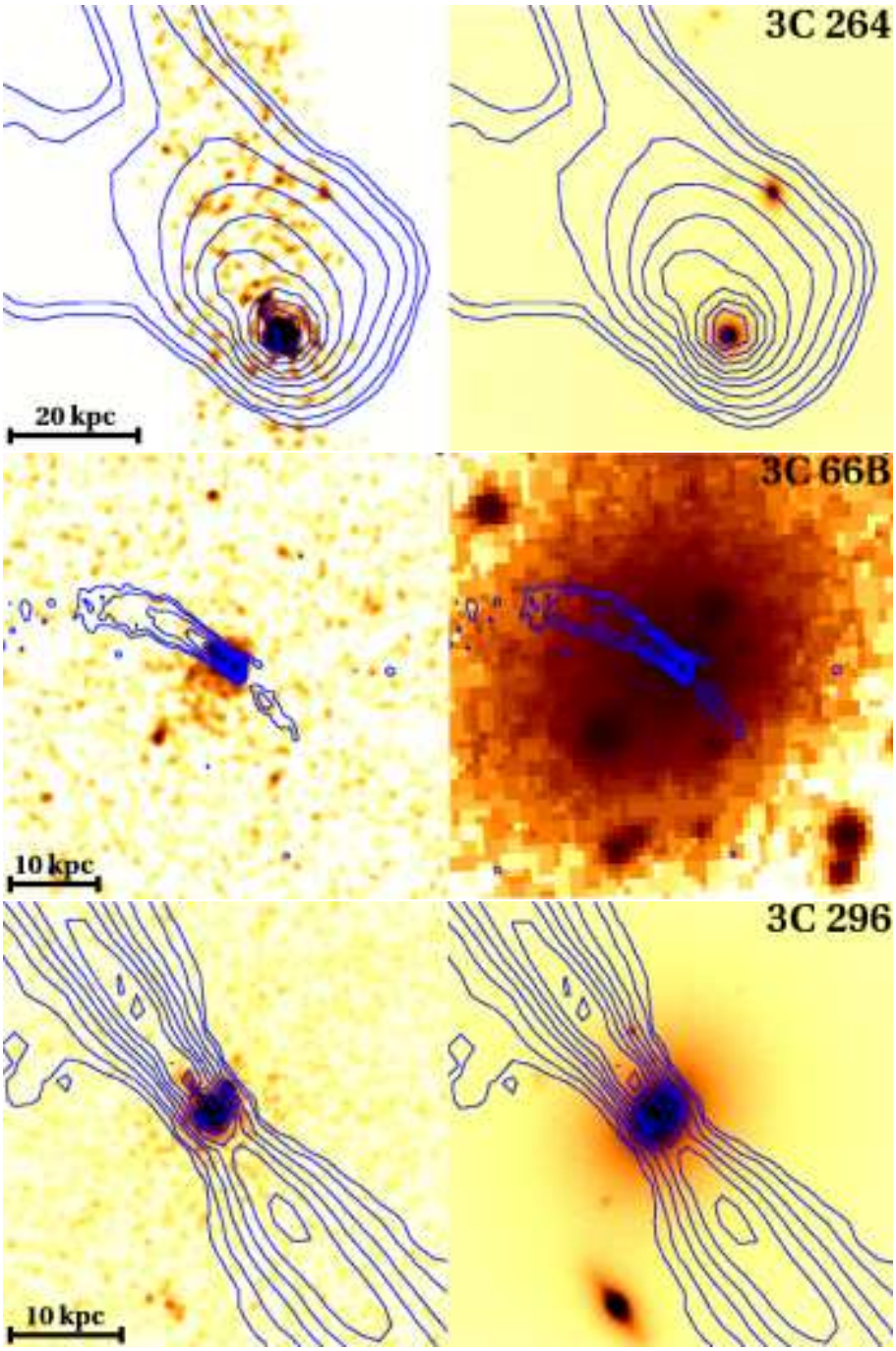

Figure 2.1 continued

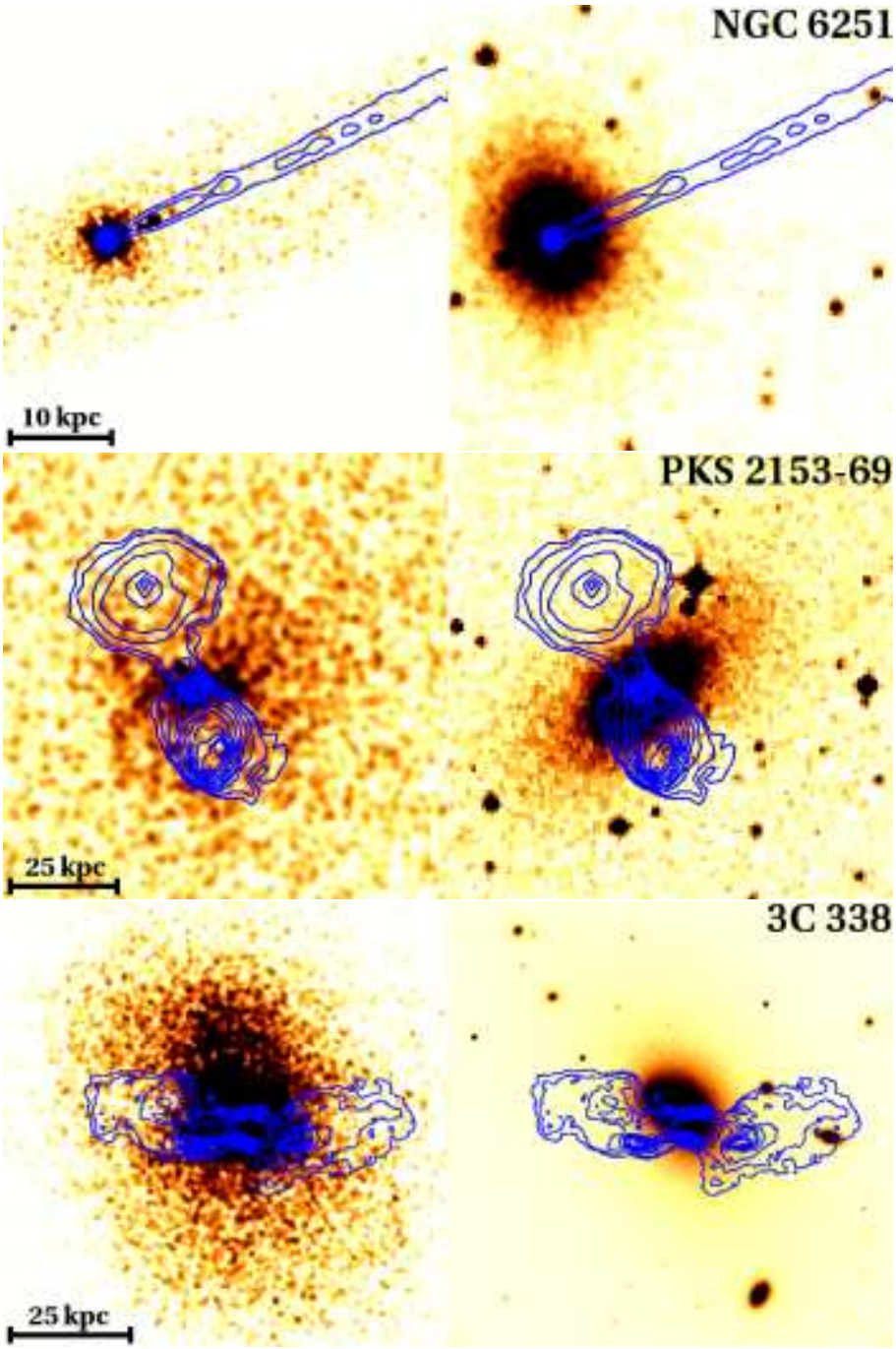

Figure 2.1 continued

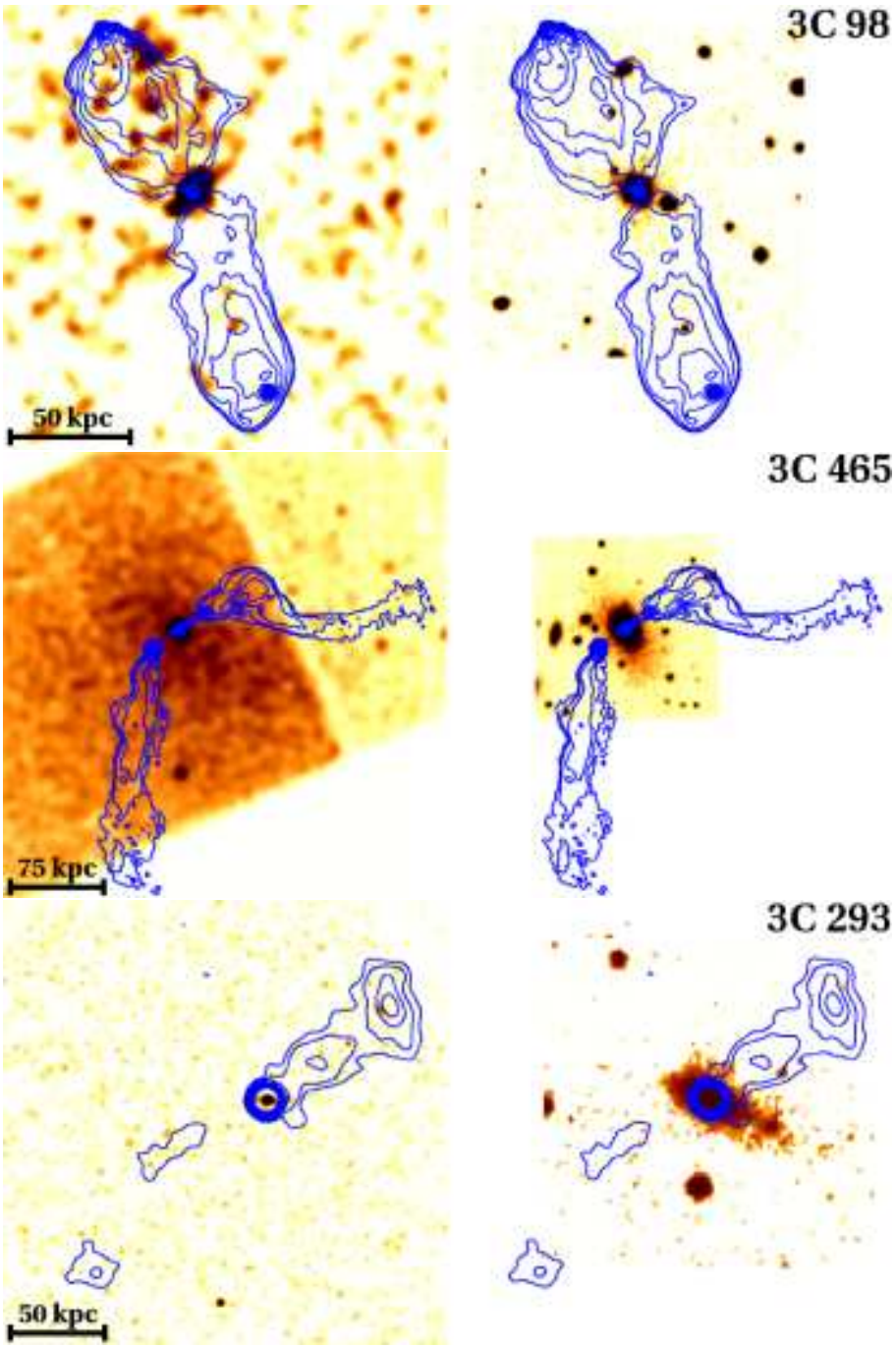

Figure 2.1 continued

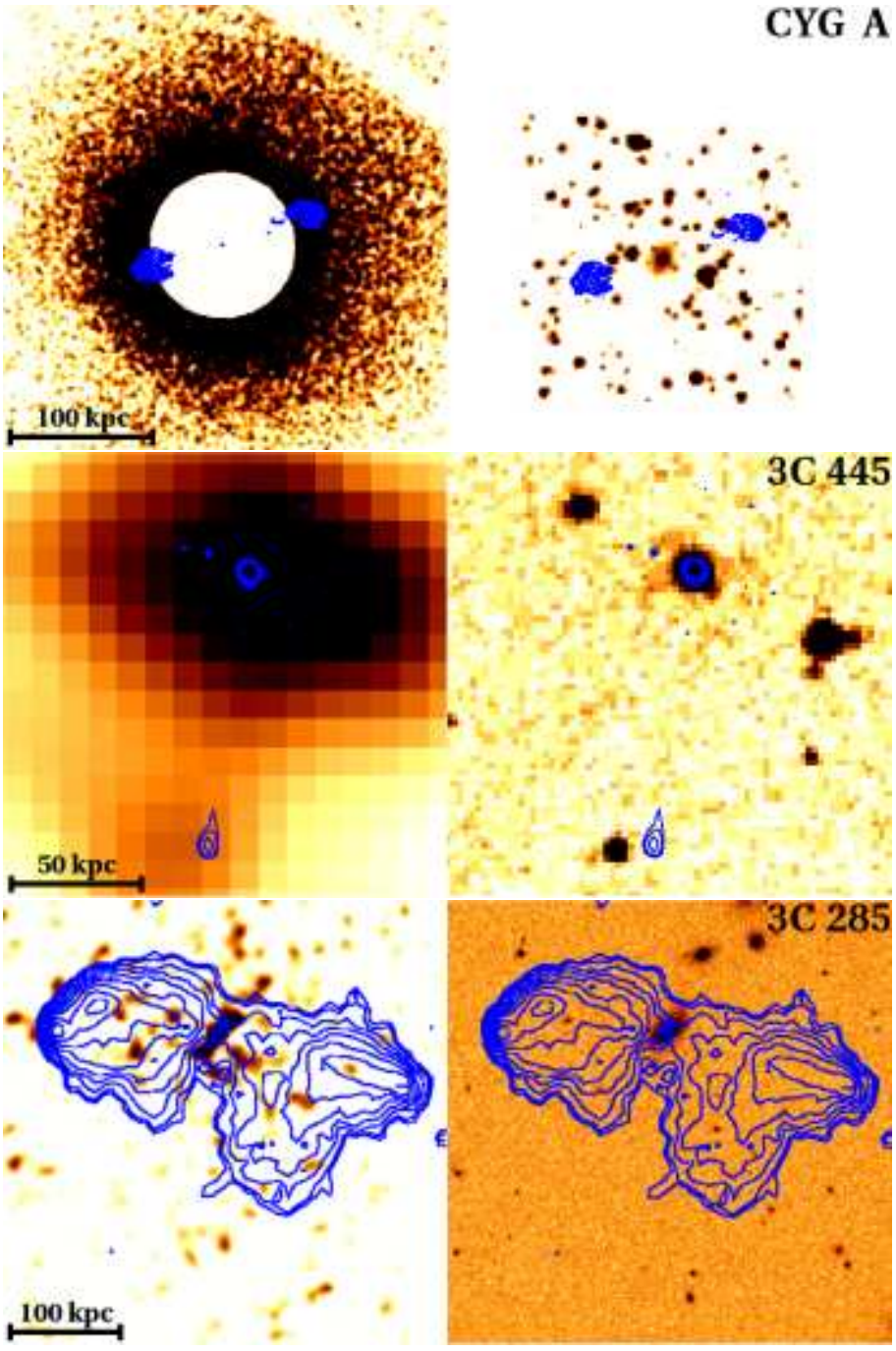

Figure 2.1 continued

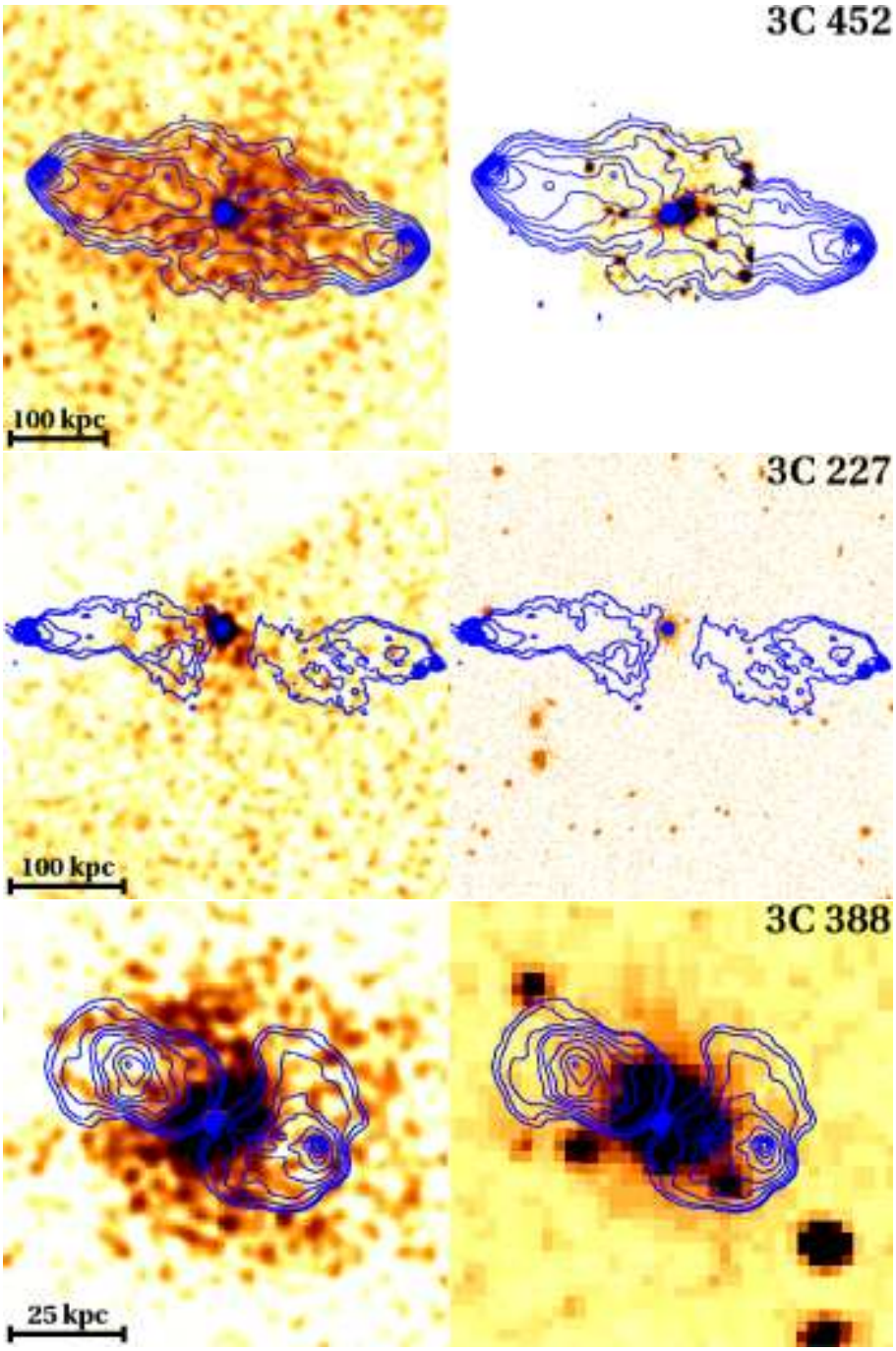

Figure 2.1 continued

few comparison sample data sets contained the readout streak produced by bright sources, which we replaced, following the CIAO thread, with a strip of nearby background on either side of the central point source. The bright sources NGC 6251 and 3C 264 were observed in a 1/8-size subarray mode of the ACIS-S3 chip, but still produced a readout streak. Exposure-corrected final images were then produced from the energy-filtered level=2 files following the standard CIAO thread, using the aspect solution file associated with each observation.

The core AGN X-ray emission was identified by matching the position of the X-ray source with the optical counterpart on the sky. More accurate positions were determined by binning the X-ray image and calculating the centroid.

2.2.3 Spectral Extraction

Our analysis (Section 2.3) is based on the properties and morphology of the ISM and IGM/ICM. Therefore, we reject galaxies from our preliminary sample where we do not detect strong extended thermal plasma. We determine the final sample in two steps: (1) We use radial profile fitting to reject sources with no extended emission and distinguish between multiple components of extended emission in the remainder. We extract spectra from regions corresponding to these extended components, then (2) reject sources whose extended emission is not fit well by strong thermal components. We describe the first step presently and the second in Section 2.2.4.

Extended emission on the chip may be made up of multiple sources. We use surface brightness profile fitting to distinguish between these sources, and based on these fits, define regions for spectral extraction to isolate each source as much as possible. We excised point sources from the level=2 file, then extracted and fit radial profiles from annuli surrounding the AGN out to many kpc (scale depends on z). In many cases, no diffuse emission was detected above background. Where

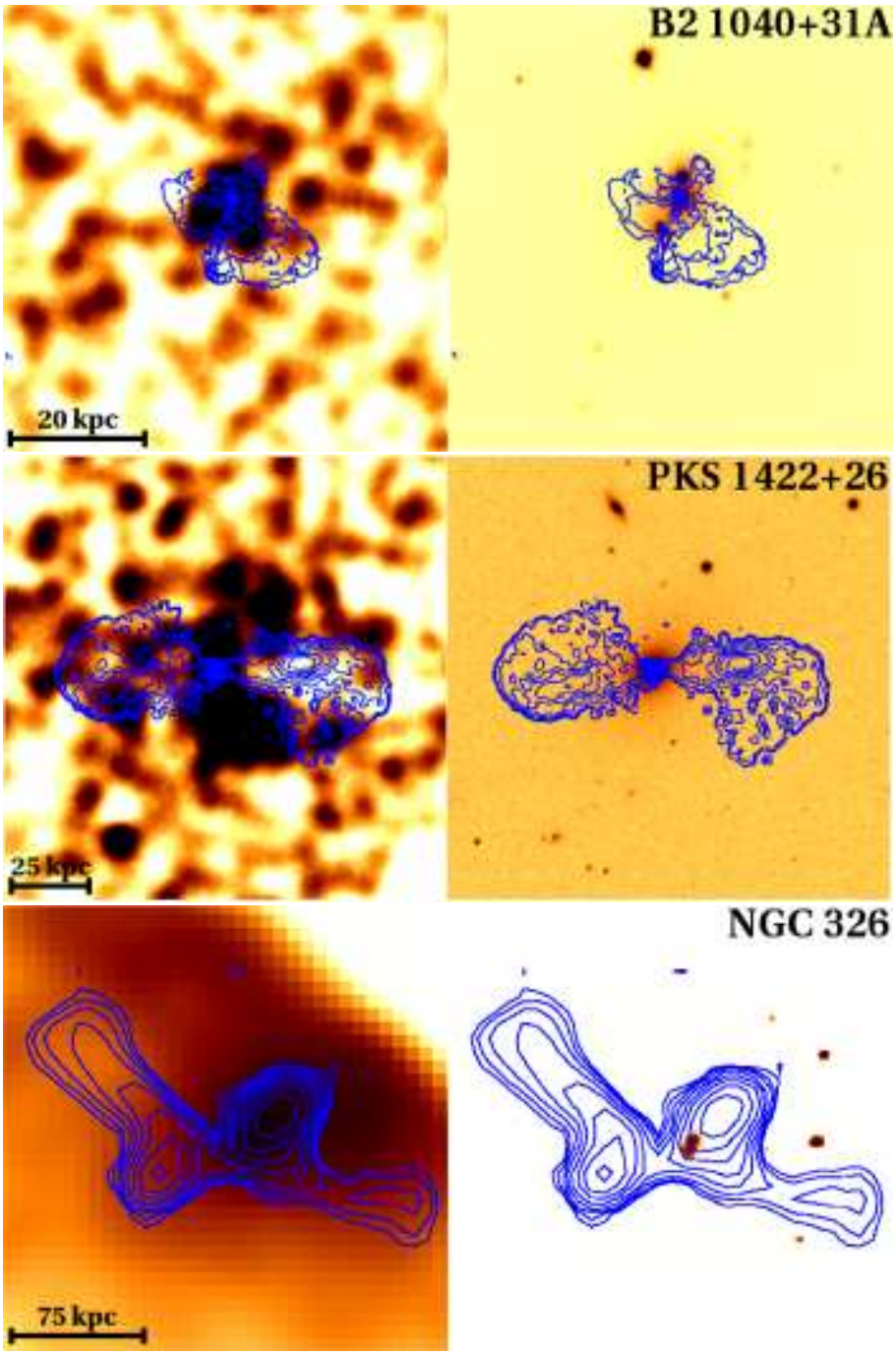

Figure 2.2 *Chandra* and optical images of our XRG sample galaxies with significant thermal emission. The left panel in each case is an image of the *Chandra* ACIS-S3 chip with uniform Gaussian smoothing and point sources removed. The right image is an optical image from DSS or SDSS. Overlaid in blue are VLA radio map contours. The images are sorted by ascending redshift.

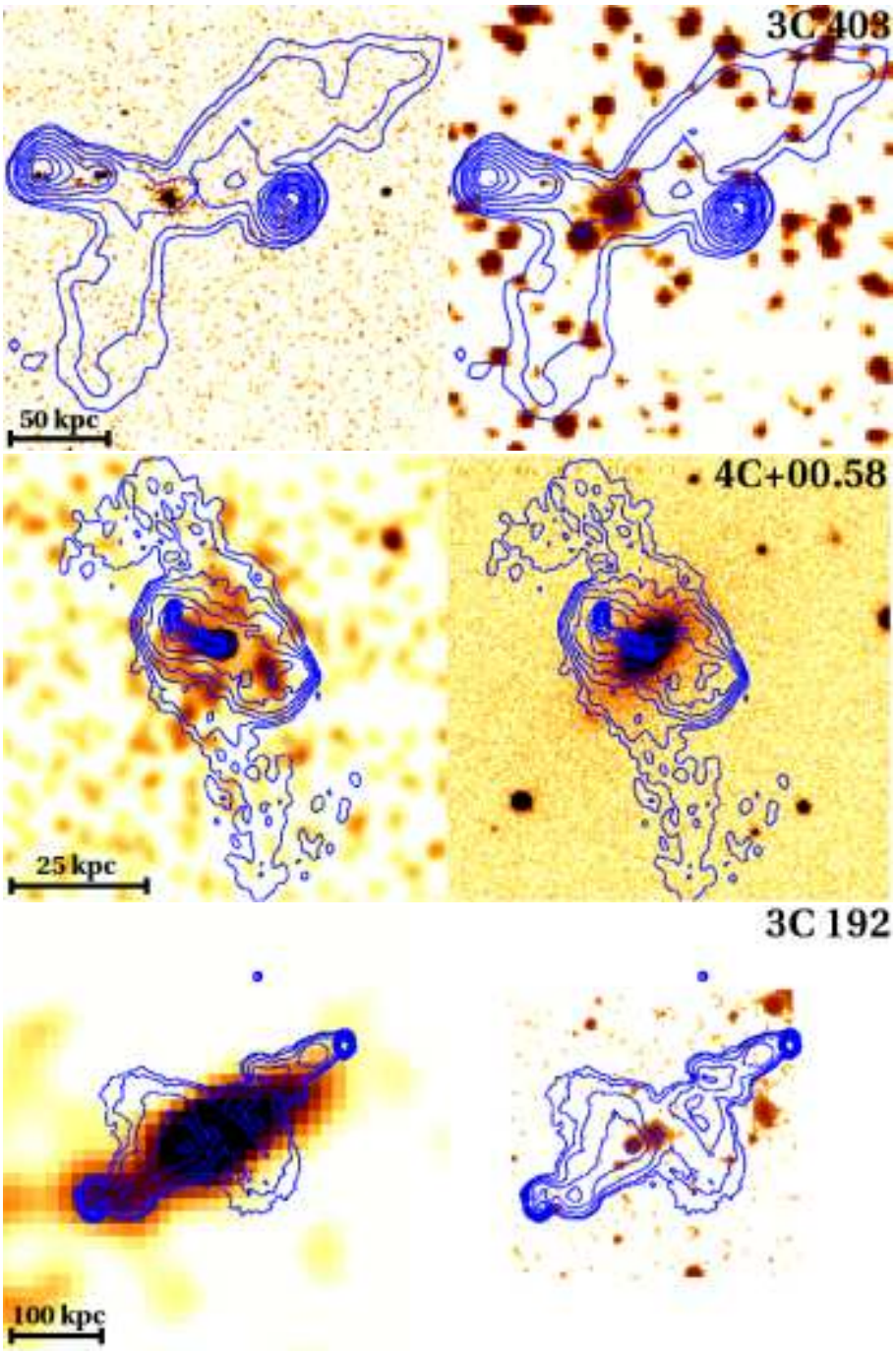

Figure 2.2 continued

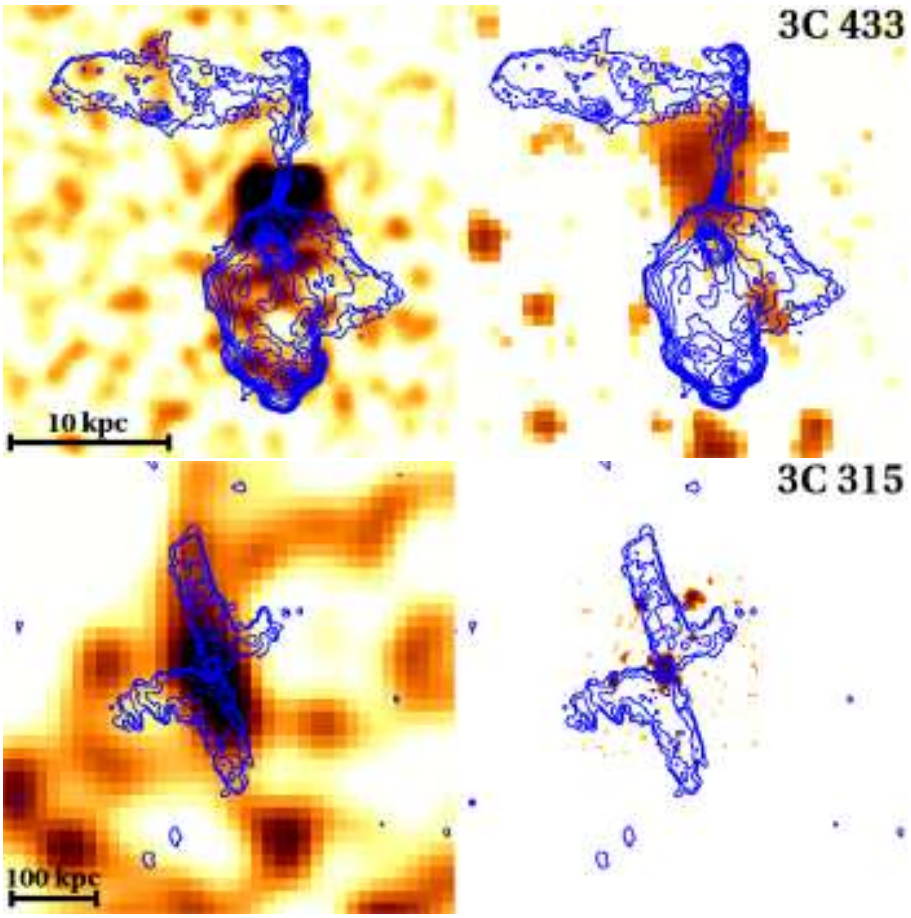

Figure 2.2 continued

multiple components were found, we defined spectral extraction apertures based on the characteristic radii (r_0 from a β model) for each region. Compact emission centered on the AGN with r_0 smaller than the host galaxy we identified as "ISM", whereas very broad emission which declines slowly in surface brightness we identified with the "IGM/ICM". These are the labels used in Table 2.3; we note that the only sources included in Table 2.3 are those in which thermal emission has been verified. At the present stage, the purpose of these regions is solely to isolate different sources for spectral fitting.

For the larger, dimmer extended sources, the fits (and hence r_0) were less reliable. However, the slow decline of the "IGM" surface brightness means the spectra

we extract are relatively insensitive to the size and shape of the region. Crucially, the spectral extraction apertures are *not* the same as those we use for our analysis in Section 2.3 and are defined only to isolate different sources. Spectra were extracted from these regions and were binned to at least 15 photons/bin to ensure the reliability of the χ^2 statistic; in high-quality spectra, the binning was as high as 100. In addition, we extract spectra for the unresolved AGN emission from detection cells using the 90% encircled energy radius as determined by the CIAO *mkpsf* tool. We return to the AGN spectra in Section 2.4.

2.2.4 Detection of Diffuse Gas

We fit models to the spectra we extracted (Section 2.2.3) to determine whether the emission is dominated by thermal plasma. Specifically, our sample consists of those galaxies in which the thermal emission surrounding the AGN appears dominant in number of photons, a point we return to below. We first ascertain the presence of hot gas by fitting the spectra extracted from each source using XSPEC v.12.5.0j (Arnaud 1996). In this Chapter we exclusively use the `apec` model. This step is required since extended emission need not be thermal in origin—plausible nonthermal sources include power law emission from the boundary shock of the cocoon inflated by the radio jets or from X-ray binaries (XRBs) in the host galaxy. Our fits all use a frozen Galactic N_H absorption component. After thermal emission is established, we then require the thermal component to be dominant at low energies. This ensures that the main contribution to the (energy-filtered) surface brightness is the thermal plasma. Of course, the hot atmospheres of many galaxies in our sample have been well studied (e.g. by *Chandra*; Table 2.1), but we wish to apply a uniform standard to all our sources including ones which have low signal.

For each spectrum, we first determine whether a single power law or thermal

model is a better baseline fit based on the χ^2 statistic, then add complexity as the degrees of freedom allow. In the case of thermal models we begin by freezing the abundances with an isothermal model (there exists an abundance—normalization degeneracy in the absence of strong emission lines). 2-temperature (2-T) or multi-T models are invoked if an isothermal model is insufficient to fit the spectrum and the additional thermal component produces a better fit than a power law component. It is worth asking whether a spectrum fit well by a single thermal model is better fit by a blend of power law and thermal components. The answer is almost invariably "no". In very low signal spectra with few degrees of freedom we conclude hot gas is present if a thermal model with reasonable parameters ($kT < 5.0$ keV and $0.1 < Z < 1.0 Z_{\odot}$) is a better fit than a power law model. We justify this assumption by the slopes of soft spectra: unabsorbed power law emission tends not to fall off at the lowest energies, whereas thermal emission peaks near 1.0 keV. A "peaky" spectrum, even a low-signal one, is fit better by a thermal model. As described in Section 2.2.3, we have attempted to isolate different sources, but we see the ISM and IGM in projection. We usually lack the signal for a deprojection analysis, so we first extract and fit a spectrum from the larger IGM region, then add the resultant models as frozen components in the ISM spectrum (keeping the normalization thawed). We find this produces better results than using a ring of IGM as background for the ISM spectra. It is possible that the power law models are in fact describing thermal continua, but the thermal models which fit these spectra have inordinately high temperatures and often require suspiciously low abundances.

For a galaxy to be included in our final sample we required the thermal component to be dominant between $0.3 < E < 2$ keV. Due to *Chandra*'s energy-dependent effective area, even components with higher *luminosity* (e.g. an absorbed power law) may have many fewer photons in this range. This criterion allows us to characterize

the morphology of only the hot plasma.

Up to this point we have treated our sources as uniformly as possible. Our analysis sample consists of the galaxies whose extended emission is dominated by thermal plasma, but we also reject sources with very complex morphology (3C 321, M84, M87, and 3C 305; Cyg A was retained after excising the inner cocoon). We remind the reader that we began with an XRG sample comprising those 13 galaxies within $z \sim 0.1$ with data in the *Chandra* archive. Of these, we have 8 in our analysis sample. The preliminary comparison sample included 41 normal radio galaxies within the same cutoff, and of these we retain 18 (ten of which are FR II galaxies). Unfortunately, in many of the shorter XRG observations, we failed to detect significant diffuse emission. Notes on individual galaxies are in Appendix C, including those XRGs not included in our analysis sample (Appendix C.3). Sources we considered but rejected are listed in Table 2.2.

For those galaxies in our analysis sample, we provide the model fit parameters in Table 2.3. We also present the emission-weighted density $\bar{n}$ and average pressure $\bar{P} = \bar{n}kT_{\rm fit}$. $\bar{n}$ was computed by assuming the minor axis of the extraction region on the sky is the true minor axis and that the ellipsoid is axisymmetric in the minor axis (i.e. the axis along the line of sight is the minor axis). We report errors in Table 2.3 for one parameter of interest at $\Delta\chi^2 = 2.7$ (90%), but we do not report errors on $\bar{n}$ or $\bar{P}$ since there are unquantifiable sources of systematic error from our assumptions on the volume. The average densities and pressures are not particularly useful for studying any one system because profile information has been discarded; for most of our sources we cannot use deprojection. Our spectra with folded model fits are shown in Figure 2.3 (ISM), Figure 2.4 (IGM), and Figure 2.5 (AGN).

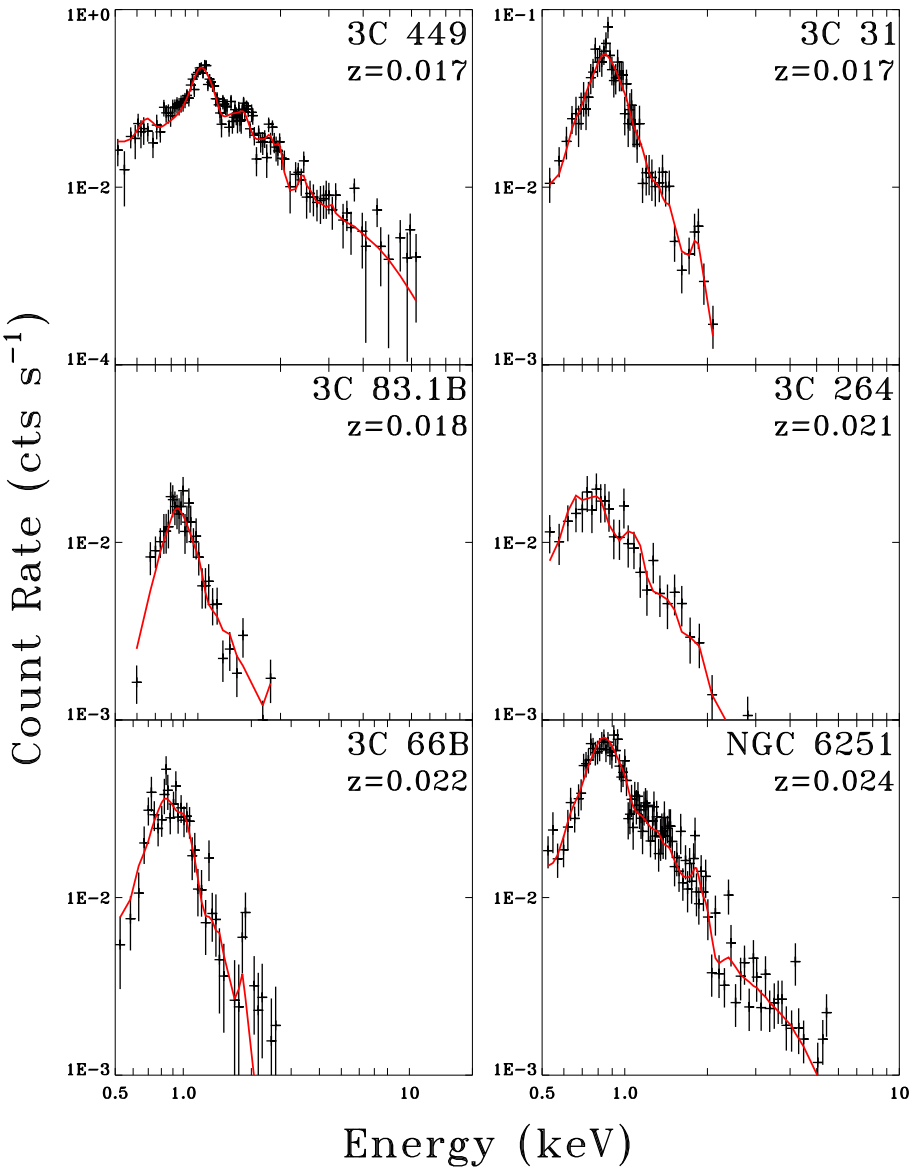

Figure 2.3 Spectra of the X-ray ISM we use in our morphology comparison (Table 2.5). The XRG sample is shown with galaxy names in green and the total model fit has been plotted over the data in red. The values can be found in Table 2.3. Note that 3C 403 is shown in Figure 2.5 since the ISM is small compared to the PSF and is isolated via energy filtering (Kraft et al. 2005).

Table 2.2. Rejected *Chandra* Observations

Name	z	Obs. IDs	Exp. Time (ks)	Obs. Type	Reason
		XRGs			
4C +32.25	0.052	9271	10	ACIS-S	a
4C +48.29	0.053	9327	10	ACIS-S	a
3C 136.1	0.064	9326	10	ACIS-S	a
J1101+1640	0.068	9273	10	ACIS-S	mispointing
3C 223.1	0.107	9308	8	ACIS-S	a
		Archival Normal Radio Galaxies			
M84	0.003	803+5908+6131	29+47+41	ACIS-S	b
M87	0.004	352+1808	38+14	ACIS-S	b
3C 84	0.018	333+428	27+25	HETGS	b+pileup
3C 442A	0.026	5635+6353+6359+6392	29+14+20+33	ACIS-I	b
3C 353	0.030	7886+8565	72+18	ACIS-S	c
3C 120	0.033	3015+5693	58+67	HETGS+ACIS-I	c
DA 240	0.036	10237	24	ACIS-I	a
3C 305	0.042	9330	8	ACIS-S	b
3C 390.3	0.056	830	34	ACIS-S	c
3C 382	0.058	4910+6151	55+65	HETGS	c+pileup
3C 33	0.059	6910+7200	20+20	ACIS-S	c
3C 35	0.067	10240	26	ACIS-I	a
0313-192	0.067	4874	19	ACIS-S	c
3C 105	0.089	9299	8	ACIS-S	a
3C 326	0.090	10242+10908	19+28	ACIS-I	target not on chip
3C 321	0.096	3138	48	ACIS-S	b
3C 236	0.099	10246+10249	30+41	ACIS-I	c
3C 327	0.104	6841	40	ACIS-S	c
4C +74.26	0.104	4000+5195	38+32	HETGS	c
3C 184.1	0.118	9305	8	ACIS-S	a

[a]No diffuse emission detected

[b]Complex morphology

[c]No diffuse thermal emission detected

Note. — Galaxies were selected for the preliminary sample as described in Section 2.2.1 and rejected for lack of diffuse gas or prohibitively complex morphology for our analysis (e.g. obvious multiple bubbles).

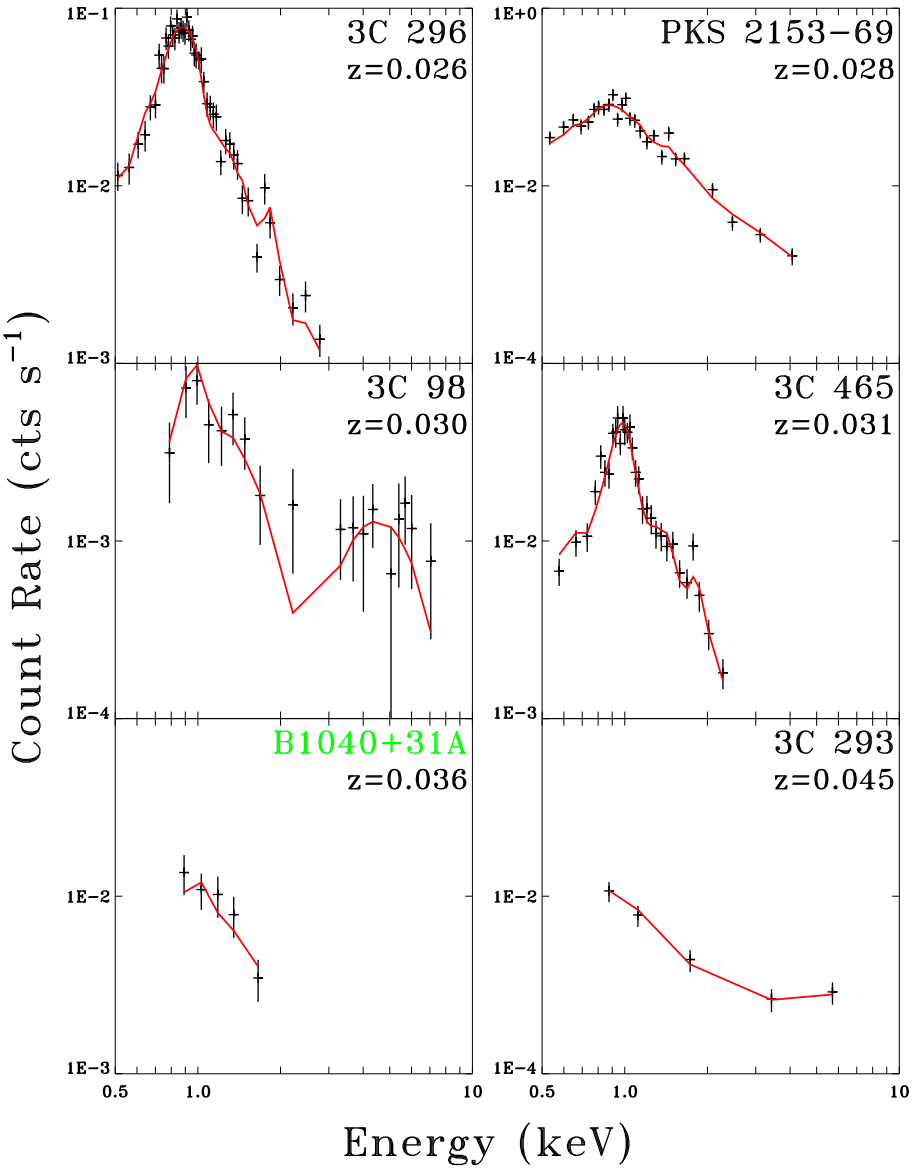

Figure 2.3 continued

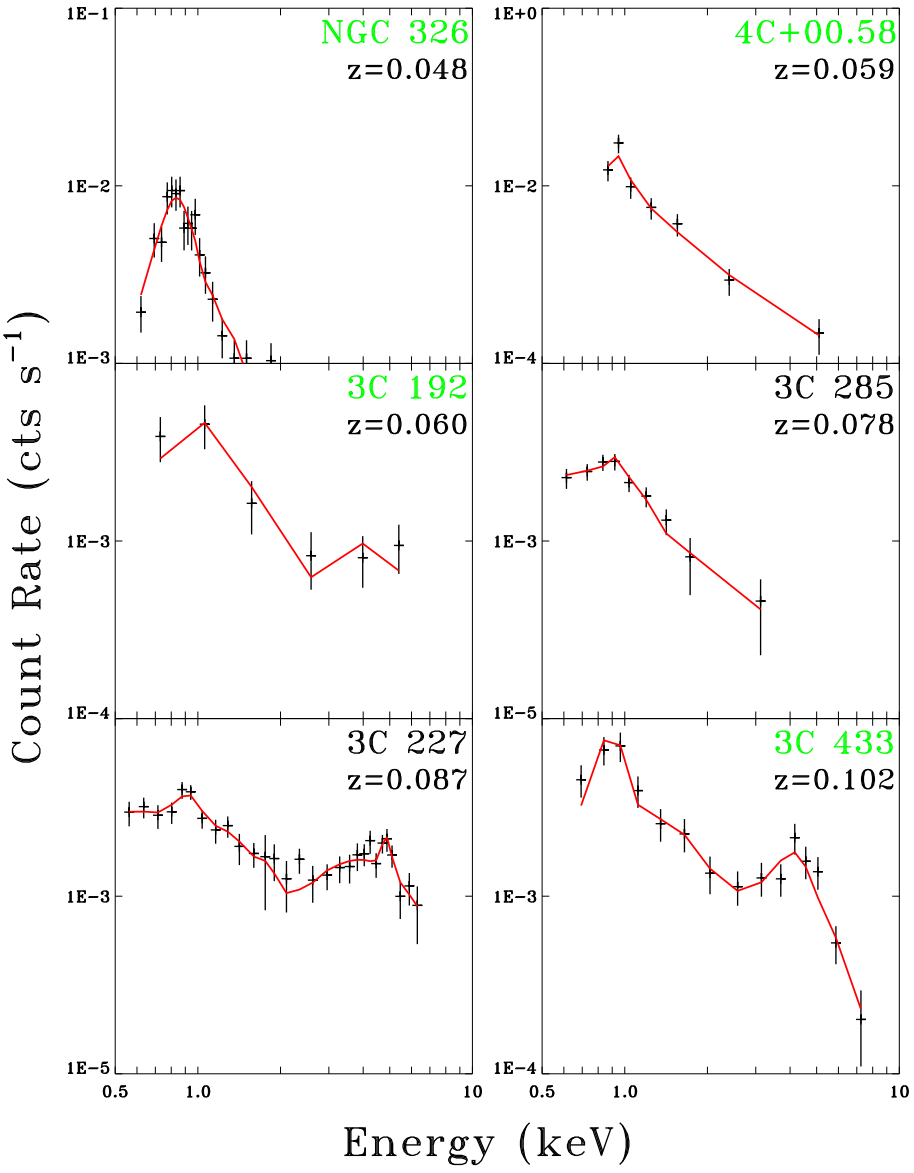

Figure 2.3 continued

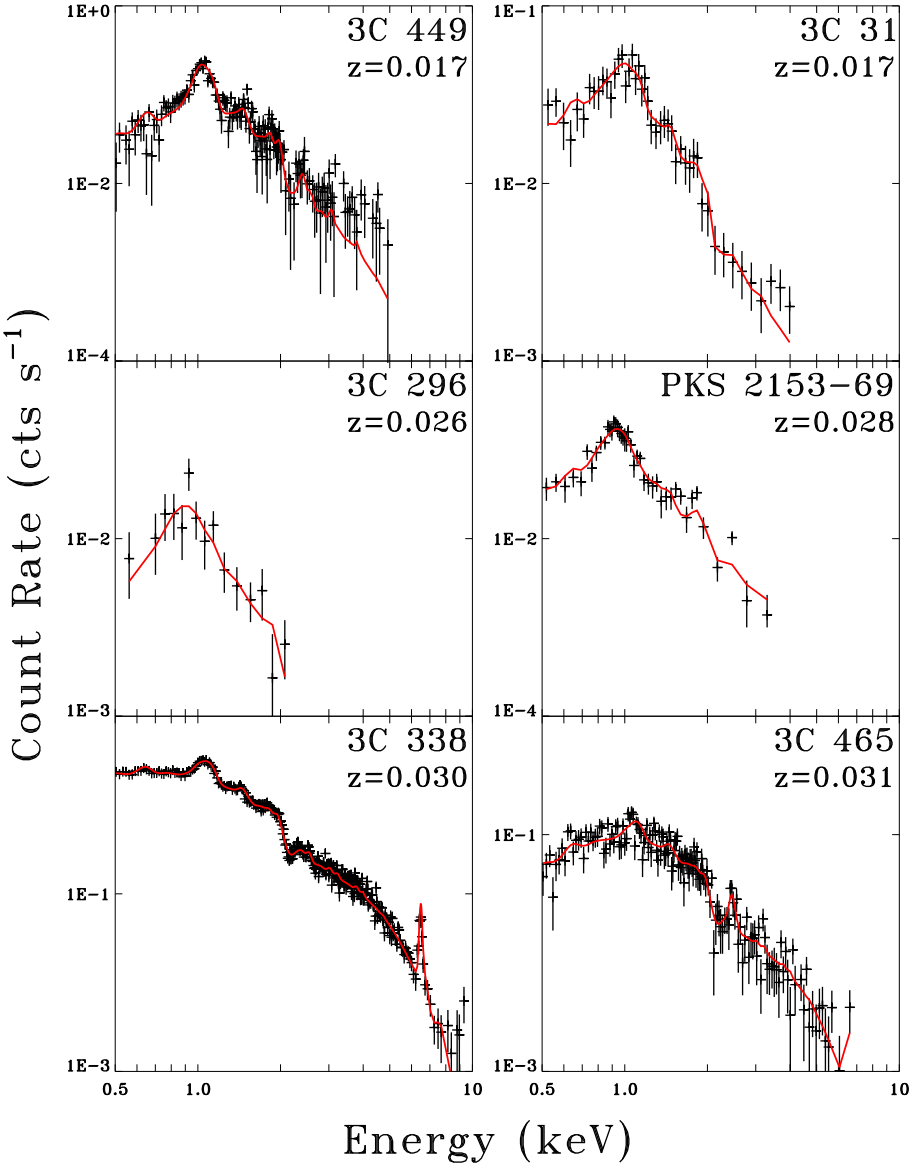

Figure 2.4 Spectra of the X-ray IGM we use in our morphology comparison (Table 2.6). The XRG sample is shown with galaxy names in green and the total model fit has been plotted over the data in red. The values can be found in Table 2.3.

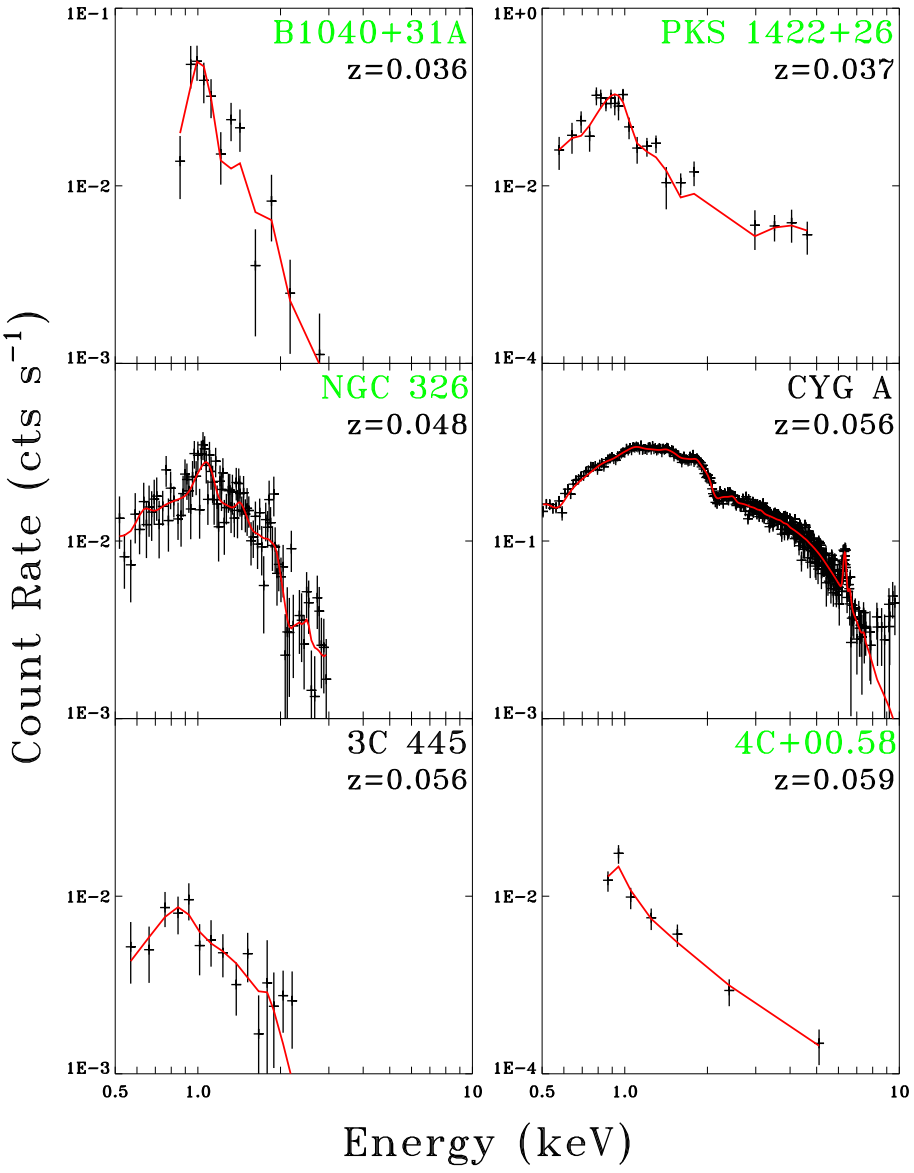

Figure 2.4 continued

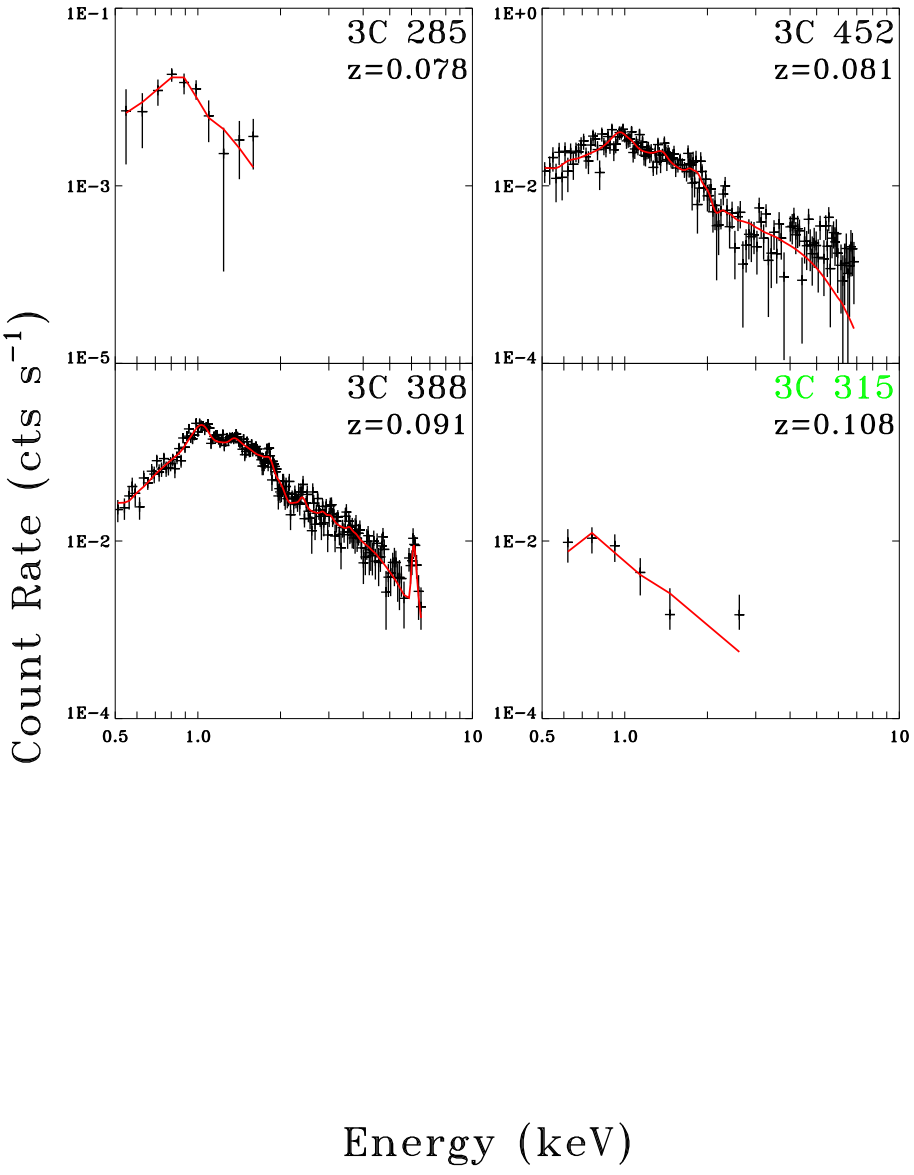

Figure 2.4 continued

Table 2.3. Thermal X-ray Spectral Parameters

Galaxy	Region	a (kpc)	b (kpc)	z	Gal. N_H (10^{20} cm^{-2})	kT (keV)	Z	$\bar{n}$ (10^{-3} cm^{-3})	P (10^{-11} dyne cm^{-2})	Models	$L_{X,\rm th}$ (10^{41} erg s^{-1})	χ^2/d.o.f.
XRGs												
B2 1040+31A	ISM	5	5	0.036	1.67	1.6 ± 0.4	0.3 (f)	38.	9.7	apec	1.6	4.66/5
···	IGM (s)	25	25	···	···	1.8 ± 0.2	1.0 (f)	3.8	1.1	apec	3.2	10.9/11
···	IGM (l)	75	75	···	···	$1.3^{+0.3}_{-0.1}$	$0.3^{+0.4}_{-0.2}$	1.1	0.24	apec	4.7	20.2/23
PKS 1422+26	IGM	85	40	0.037	1.54	0.89 ± 0.09	$0.3^{+0.2}_{-0.1}$	2.0	0.29	apec+PL	5.2	23.1/20
NGC 326	ISM	6	6	0.048	5.86	0.68 ± 0.05	1.0 (f)	28.	3.0	apec(+IGM)	5.4	13.3/17
···	IGM	166	94	···	···	3.6 ± 0.4	0.8 (f)	1.9	1.1	apec	10.	94.1/100
3C 403	ISM	9	6	0.059	12.2	0.24 ± 0.03	1.0 (f)	23.	0.89	apec+PL+N_H(gauss+PL)	1.0	100.7/94
···	IGM	97	40	···	···	0.6 ± 0.2	1.0 (f)	0.37	0.04	apec	0.9	34.3/36
4C +00.58	ISM	17	17	0.059	7.14	1.2 ± 0.2	1.0 (f)	7.3	2.0	apec	3.0	5.8/6
3C 192	ISM+IGM	19	19	0.060	4.08	$1.0^{+2.2}_{-0.2}$	1.0 (f)	4.9	0.79	apec+N_H(PL)	2.5	3.9/5
3C 433	ISM+IGM	44	26	0.102	7.77	0.96 ± 0.1	1.0 (f)	2.8	1.1	apec+PL+gauss	4.0	16.2/12
3C 315	IGM	200	110	0.108	4.28	$0.6^{+0.4}_{-0.1}$	1.0 (f)	1.0	0.1	apec+PL	8.2	4.5/10
Comparison Sample												
3C 449	ISM	5	5	0.017	8.99	0.77 ± 0.09	1.0 (f)	15.	1.9	apec(+IGM)	0.22	21.1/19
···	IGM	32	32	···	···	1.58 ± 0.06	0.8 ± 0.2	2.9	0.73	apec	3.9	179.8/169
3C 31	ISM	4	4	0.017	5.36	$0.68^{+0.04}_{-0.03}$	1.0 (f)	22.	2.4	apec(+IGM)	0.34	47.0/58
···	IGM	30	30	···	···	$2.0^{+0.5}_{-0.2}$	$0.4^{+0.2}_{-0.1}$	2.0	0.69	apec	1.3	143.1/138
3C 83.1B	ISM	3	3	0.018	13.4	0.65 ± 0.04	1.0 (f)	34.	3.6	apec(+IGM)	0.13	30.1/35
···	ICM	56	30	···	···	$8.^{+6}_{-3}$	1.0 (f)	1.2	1.6	apec	1.7	80.9/86
3C 264	ISM	5	5	0.021	1.83	0.34 ± 0.04	1.0 (f)	6.6	0.37	apec(+IGM)	0.18	19.7/30
3C 66B	ISM	9	9	0.022	7.67	$0.61^{+0.06}_{-0.04}$	$0.3^{+1.}_{-0.1}$	7.2	0.71	apec(+IGM)	0.36	49.8/42
3C 296	ISM	9	7	0.024	1.92	0.76 ± 0.02	1.0 (f)	9.0	1.1	apec(+IGM)	1.3	49.0/46
···	IGM	75	75	···	···	$4.^{+4}_{-1}$	1.0 (f)	0.8	0.5	apec	0.8	18.2/19
NGC 6251	ISM	6	6	0.024	5.59	0.66 ± 0.03	1.0 (f)	14.	1.5	apec(+IGM)	1.0	110./111
PKS 2153-69	ISM	7	7	0.028	5.59	0.77 ± 0.07	1.0 (f)	10.	1.2	apec(+hot IGM)	1.4	26.0/24
···	IGM	32	32	···	···	$T_1 = 3.0^{+2.}_{-1.}$	1.0 (f)	2.6	1.3	apec+apec	6.8	41.8/42
···	···	···	···	···	···	$T_2 = 0.9 \pm 0.06$	1.0 (f)					
3C 338	ICM	30	30	0.030	0.89	$T_1 = 1.8^{+0.2}_{-0.1}$	0.7±0.05	28.	17.	apec+apec	434.	432.5/390
···	···	···	···	···	···	$T_2 = 5.0^{+1.}_{-0.5}$	0.7±0.05					
3C 98	IGM	46	31	0.030	10.8	$1.1^{+0.3}_{-0.2}$	$0.2^{+0.4}_{-0.1}$	1.8	0.32	apec	0.8	8.5/11

2.2.5 Radio & Optical Maps

We require high signal and high resolution radio data in order to study the interaction between the radio lobes and the X-ray emitting gas. As the secondary lobes of XRGs and ZRGs are typically much fainter than the hot spots demarcating the terminal shocks of the active lobes, deep radio observations are often required to accurately determine their extent and angular offset from the active pair. The VLA is ideal for continuum band observations. Reduced VLA data for many of the sources are available through the NASA/IPAC Extragalactic Database (NED); references are provided in Table 2.1 where available. In some cases, we have reprocessed archival VLA data ourselves, and these are noted in Table 2.1.

In contrast to the requirement for high quality radio data (needed to constrain the orientation of the radio jets and lobes), images from the (Palomar or UK Schmidt Telescope) Digitized Sky Survey (DSS) are usually sufficient for comparing the extent and alignment of the diffuse X-ray emitting gas to the distribution of optical light. Except in the case of B2 1040+31A, a close triple system, the optical emission on the relevant scales does not have significant contamination from companion sources. We note that the DSS spans our entire sample, whereas the higher resolution Sloan Digital Sky Survey (SDSS; Adelman-McCarthy et al. 2008) data are available for fewer than half of our sources. However, we compare the DSS images to the SDSS images where available, and note that good agreement is found in most cases for our model parameters (Section 2.3.2; Table 2.5). We also use published *Hubble Space Telescope* (HST) images, in particular those of Martel et al. (1999) for 3CR galaxies within $z < 0.1$. However, this survey is not sufficiently complete to replace the DSS data.

The images in Figure 2.1 & 2.2 show the data, using the higher quality SDSS im-

Table 2.3 (cont'd)

Galaxy	Region	a (kpc)	b (kpc)	z	Gal. N_H (10^{20} cm^{-2})	kT (keV)	Z	$\bar{n}$ (10^{-3} cm^{-3})	P (10^{-11} dyne cm^{-2})	Models	$L_{X,\rm th}$ (10^{41} erg s^{-1})	χ^2/d.o.f.
3C 465	ISM	6	6	0.031	4.82	1.12±0.08	1.0 (f)	20.	3.6	apec(+IGM)	1.4	30.4/32
···	IGM	80	56	···	···	$4.2^{+0.5}_{-0.3}$	1.0 (f)	2.3	1.6	apec+gauss	25.	176.8/164
3C 293	ISM	8	5	0.045	1.27	1.0 ± 0.3	0.2 (f)	28.	4.4	apec(+IGM)	1.6	0.7/4
Cyg A	ICM	140	140	0.056	30.2	$T_{\rm low} = 3.2^{+1.3}_{-0.1}$	0.6 (f)	4.8	6.0	cflow	1600	433.1/403
···	···	···	···	···	···	$T_{\rm high} = 18. \pm 7.$						
3C 445	IGM	73	54	0.056	4.51	$0.7^{+0.3}_{-0.4}$	1.0 (f)	0.26	0.03	apec+PL	0.6	9.38/14
3C 285[a]	ISM+IGM	30	30	0.079	1.27	$T_1 = 1.2^{+0.4}_{-0.2}$	1.0 (f)	2.3	0.13	apec+apec	2.9	6.9/7
···	···	···	···	···	···	$T_2 = 0.33^{+0.3}_{-0.05}$	1.0 (f)					
3C 452	IGM	201	82	0.081	9.64	3.8 ± 0.1	1.0 (f)	1.3	0.79	apec+PL	5.0	148.7/155.
3C 227	ISM+IGM	28	28	0.087	2.11	$T_1 = 0.2$ (f)	1.0 (f)	5.9	1.0	apec+apec+gauss	7.4	12.7/29
···	···	···	···	···	···	$T_2 = 1.2^{+0.3}_{-0.2}$	1.0 (f)					
3C 388	ICM(bar)	16	16	0.091	5.58	2.4 ± 0.2	1.0 (f)	24.	9.2	apec	41.	38.9/40
···	ICM(big)	130	130	···	···	3.3 ± 0.1	1.0 (f)	3.1	1.7	apec	425.	174.9/200

[a]3C 285 is difficult to disentangle, but the larger IGM values agree with those coincident with the ISM.

Note. — Diffuse atmosphere spectral parameters for targets in Table 2.1. (f) denotes a frozen parameter. In calculating $\bar{n}$, we assume axisymmetry and use a volume $V = ab^2$. Unabsorbed luminosities are reported for the thermal component only; in the case of the ISM, this is the cooler component. The notation (+IGM) indicates that a thermal model with all parameters except the normalization frozen was used in the fit; these parameters are based on fits to the IGM.

ages for the optical band where possible. Because of the differences in scale between radio galaxies and the different media which are important for lobe–gas interaction, the chip images we show are all processed slightly differently. In most cases, they have been smoothed with a Gaussian kernel of fixed σ (per galaxy) to enhance diffuse emission. Adaptive smoothing sometimes produces artificial structure in our images and is not used. Overlaid on the images of the ACIS chips are radio contours, and accompanying each X-ray image of the optical field on the same spatial scale. Figures 2.1 & 2.2 have been processed to represent the appearance of the sources and distribution of surface brightness on the sky, but we did not use these images directly in our analysis. In addition, the varying signal-to-noise ratios (S/N) in X-ray images do not necessarily correspond to real variation in source luminosity because the data sets come from observations of varying depth and redshift. Because some of the observations are shallow ($\leq$ 10 ks) or use the ACIS-I array, a non-detection of diffuse emission is not conclusive.

2.3 Thermal Atmosphere Properties

The models which assert that XRGs result from the interaction of the radio lobes with anisotropic gaseous environments (Capetti et al. 2002; Kraft et al. 2005) must ultimately be tested by direct observations of these environments. In particular, we wish to know whether the correlation described in Capetti et al. (2002) exists in the X-ray band, i.e. whether XRGs are preferentially found in systems where the jets are directed along the major axis of the gas distribution.

This objective can be distilled into two distinct questions. First, the observed correlation between the XRG secondary lobes and the minor axis of the host galaxy was taken by Capetti et al. (2002) to imply that the minor axis of the ISM in these

galaxies was similarly aligned. But how well does the X-ray gas trace the optical isophotes? Second, is there a systematic difference between the orientation of the radio lobes and the X-ray gas distribution in XRGs and normal radio galaxies? In other words, does the Capetti et al. (2002) correlation exist in the media which interact with the radio lobes? These questions are distinct in part because the medium responsible for shaping the XRGs in the backflow models is not necessarily the inter*stellar* medium, but may be the IGM/ICM. Because these questions rely on our measurement of gas morphology, we first describe our image fitting method, which consists of fitting ellipses to measure ellipticity ($\epsilon \equiv 1 - b/a$) and position angle (PA) of the X-ray emission on the sky.

2.3.1 Ellipse Fitting

We determine the gross morphology of the hot gas by fitting ellipses to the X-ray emission and finding the characteristic ϵ and PA—gross elongation and orientation—of the surface brightness. We treat the surface brightness as a two-dimensional "mass" distribution and compute the moment of inertia tensor within an aperture chosen by the scale of the medium (a point we return to below). From this we measure the principal axes corresponding to the characteristic major and minor axes of the distribution. Of course, the gas distribution may well have complexity beyond that captured by a simple elliptical model—however, most of our data do not justify higher-order models. We describe our method presently.

Our generic ellipse-fitting routine takes as input a processed surface brightness distribution on the chip (see below). To determine the principal axes, we use the QL method with implicit shifts (Press et al. 1992) to find the eigenvalues of the tensor, whereas the position angle is determined by the orientation of one of the eigenvectors.

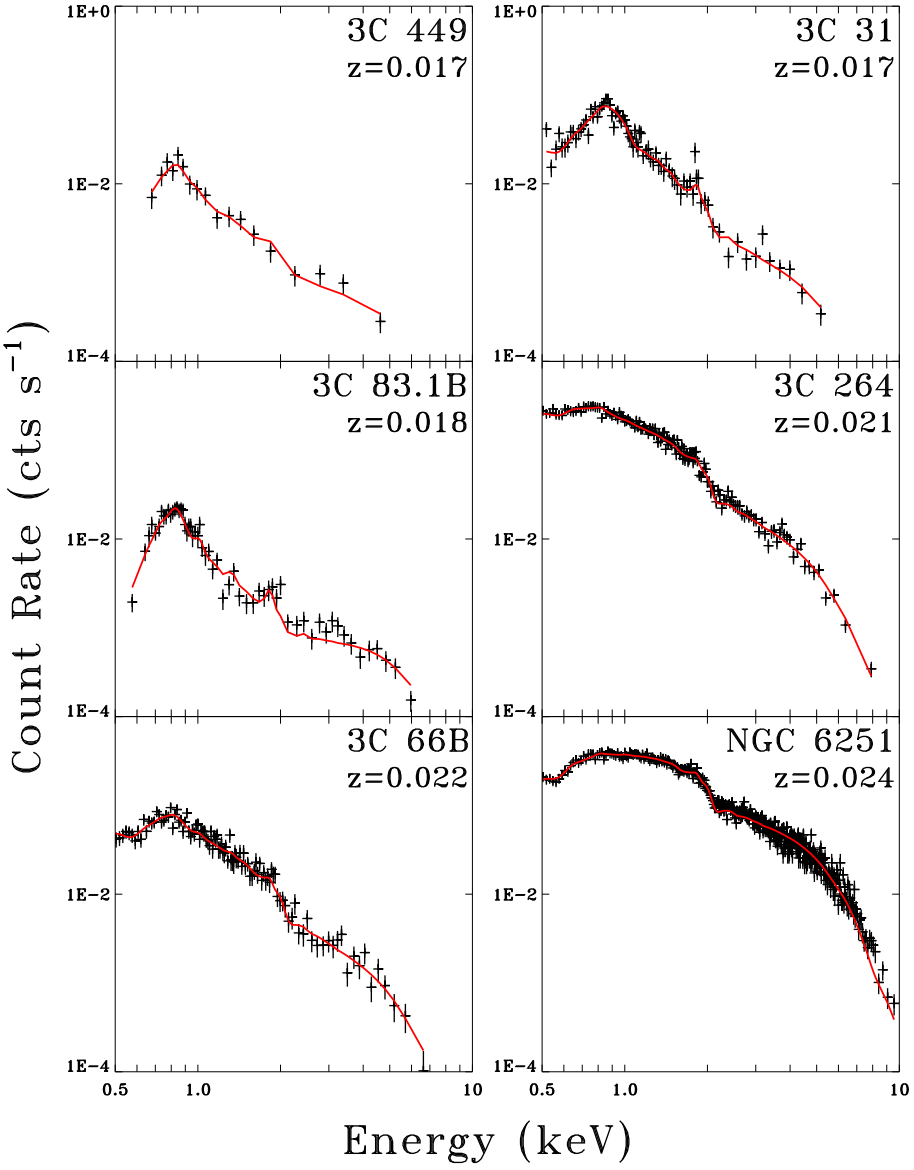

Figure 2.5 Spectra extracted from the central PSF of the host galaxy; emission may come from either the parsec-scale jet or accretion disk region. The total model fit has been plotted over the data in red and XRG galaxies have their names in green. The spectra are essentially broken into absorbed and unabsorbed spectra; some of the unabsorbed spectra require thermal components. Note that 3C 338 has no detected AGN emission and 3C 403 has a small ISM represented in the spectrum of the area near the AGN.

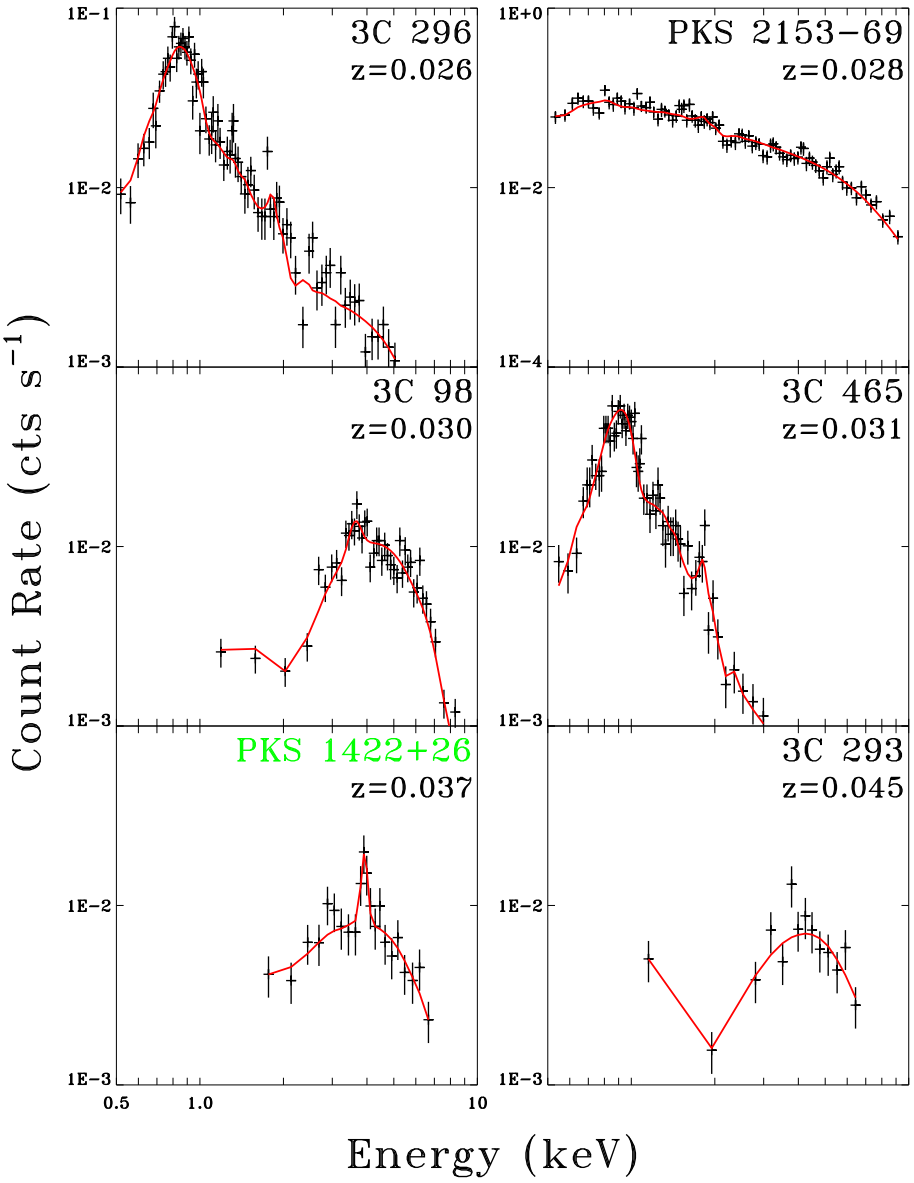

Figure 2.5 continued

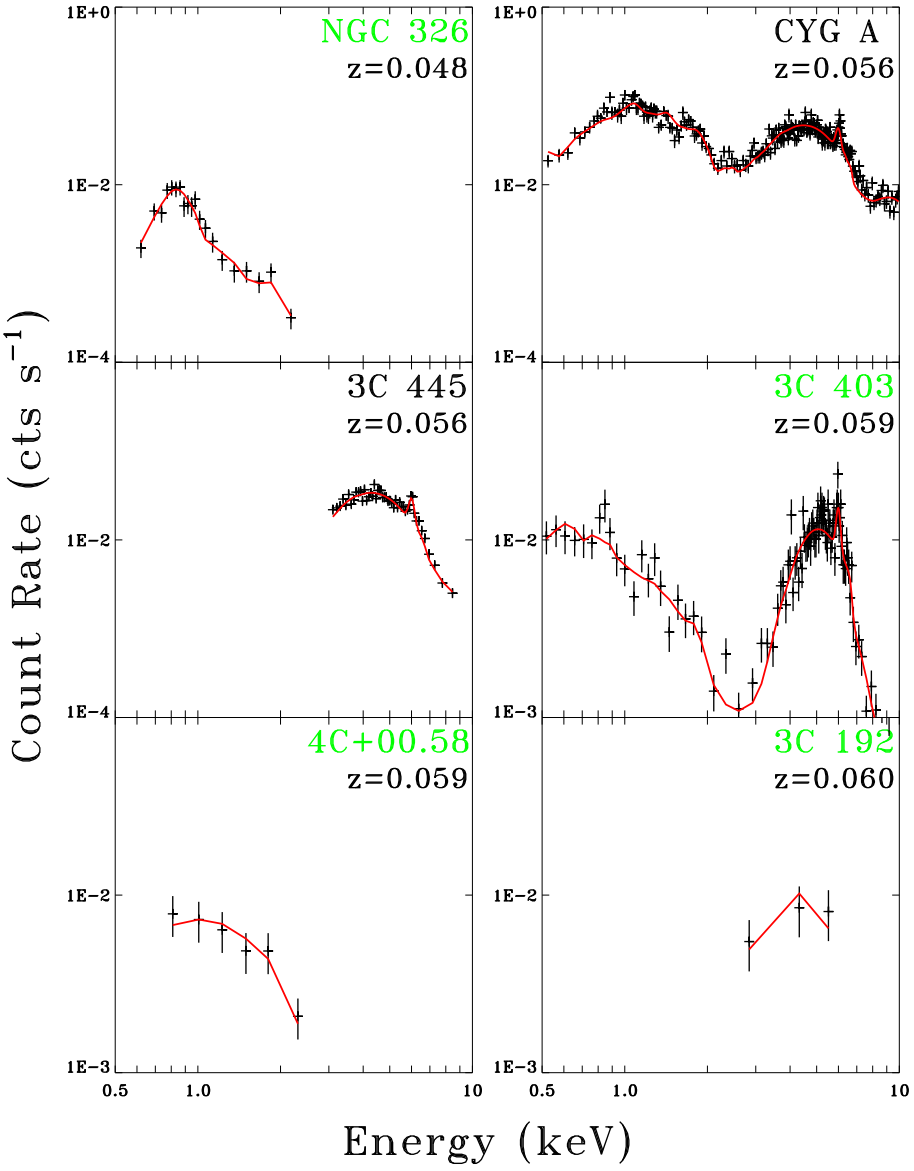

Figure 2.5 continued

We use the *Interactive Data Language* `eigenql` function[6] realization of this method. The QL method with implicit shifts is a method for finding the eigenvalues of a matrix by decomposing it into a rotation matrix "Q" and a lower triangular matrix "L"; by virtue of the decomposition, the eigenvalues of the original matrix appear on the diagonal of the lower triangular matrix at the end. To determine the 2σ

[6]Source code available from http://imac-252a.stanford.edu/programs/IDL/lib/eigenql.pro

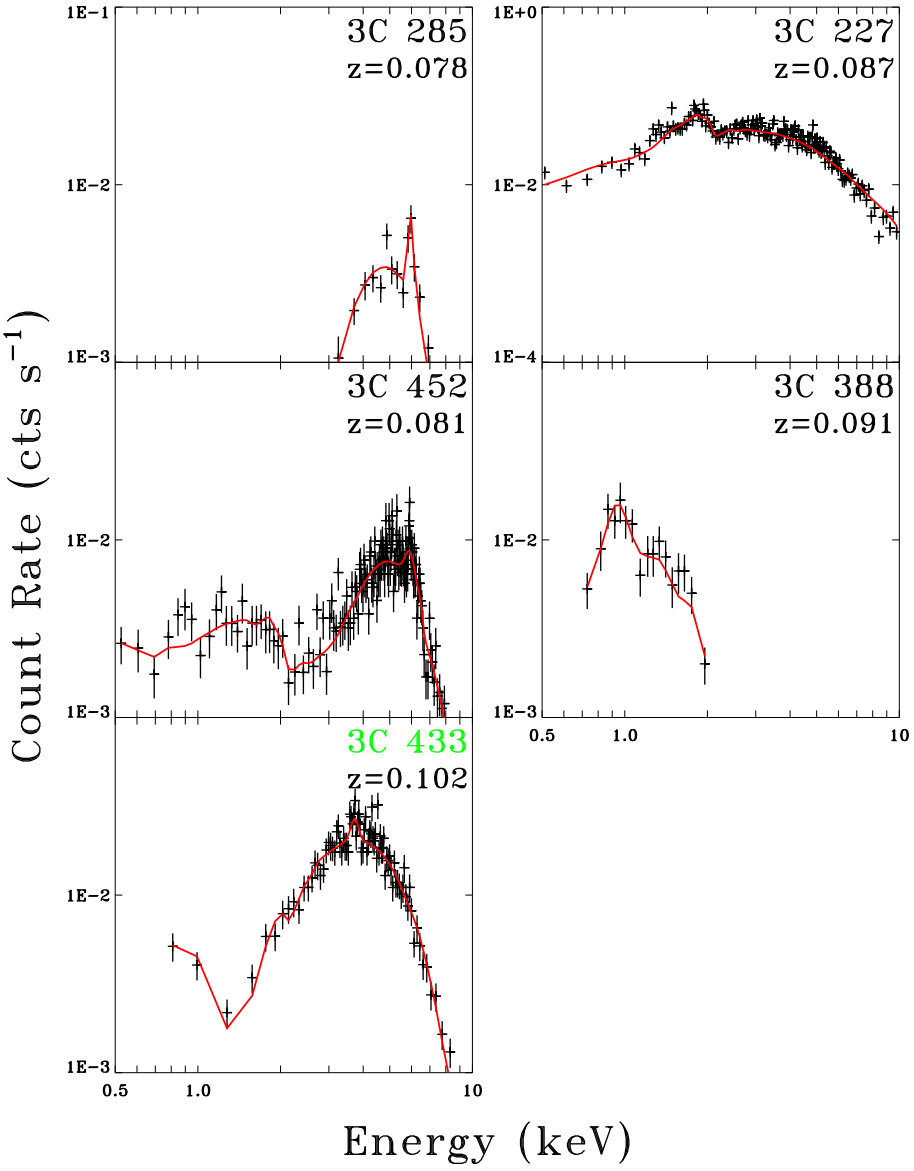

Figure 2.5 continued

error bars reported in Table 2.5, we use the bootstrap resampling method over 10^4 iterations (Efron 1982). We adopt this method since it is better suited to low count rate images than the standard *Sherpa*[7] 2D fitting routines.

Our treatment of the surface brightness prior to the fitting described above differs slightly between the bright and compact ISM and the faint, extended IGM/ICM.

[7]See http://cxc.harvard.edu/sherpa

Within each regime we attempt to treat each data set uniformly; any additional processing is noted in Appendix C.

1. *Interstellar Medium*

   For the ISM, we use no additional binning beyond the *Chandra* resolution (and thus cannot subtract a constant background). This choice is motivated by the desire to minimize artificial smoothing due to the relatively small scales of the ISM. However, we do apply the exposure correction across the medium as an adjustment to the brightness of each pixel, and we energy filter the image based on the spectrum. The radius of the (circular) aperture we use is straightforwardly determined from a 1D radial profile extracted from annuli centered on the AGN. We excise the AGN emission through energy filtering and masking a point spread function (PSF) we created at the location of the AGN using the CIAO tool *mkpsf*. We mask the region corresponding to the 95% encircled energy ellipse. One might worry that (especially with very bright AGN) this procedure would bias our measured ϵ or PA, but this appears not to be the case; the AGN is also usually centered on the nominal aim point, so $\epsilon_{\rm PSF}$ is usually small. The remaining counts within the aperture are fed into our ellipse-fitting routine. Because background is not subtracted, the bootstrap method is likely more accurate, but our measured ϵ values are systematically low (though not *very* low thanks to the high contrast of the compact ISM). We note that toggling pixel randomization appears to have no effect on our results.

2. *Intragroup/Intracluster Medium*

   Because the IGM is typically quite faint and extended, we must bin the chip quite coarsely to see the enhanced surface brightness. We mask the ISM and all other point sources, then bin to 16×16 pixels and apply a similarly binned ex-

posure correction. Energy filtering is applied based on the spectrum. Finally, we smooth the image with a Gaussian kernel ($\sigma = 2$ coarsely binned pixels). We subtract background levels using either empty regions on the chip (if the visible extent of the IGM is small) or blank sky files if the medium fills the chip. The background files are similarly energy filtered and binned/smoothed. We choose circular apertures motivated by the idea that all our radio galaxies have escaped the ISM, but only some have escaped the "local" IGM (Section 2.3.3). By "local" IGM we specifically mean we use an aperture guided by the characteristic radius r_0 determined in 1D radial profile fitting centered on the radio galaxy. Where r_0 is not well constrained, we take an aperture roughly bounding the "2σ" isophote (where "1σ" is taken to be the background level in the binned, smoothed image). We then fit the IGM assuming it is a smooth ellipsoid on the scales of interest (i.e. no internal structure) so the range in plate scale is not important between galaxies. A brief inspection of the isophotes indicates that this is a good first-order description on large scales, but wrong near the center. Inside our chosen aperture, the bootstrap method essentially tracks the contrast of structure against noise, so the uncertainty is also a function of the background level we subtract. Nonetheless, the position angles are reasonably constrained. Notably, there are a few cases where there is strong IGM/ICM not centered on the galaxy (NGC 326 and 3C 83.1B), but we ignore the emission that cannot be "seen" by the radio galaxy. Additionally, in B2 1040+31A, the most significant IGM is a smaller structure centered on the radio galaxy's host system enveloped in a larger, much dimmer atmosphere with a different PA. Using the methods above, we take the smaller structure to be the local IGM.

We treat the optical DSS data similarly. We do not further bin the images

and we measure the background near the host galaxy (but away from companions, which we mask). We use an aperture corresponding to the extent of the hot ISM emission. We wish to use similar apertures in the X-ray and optical images because ϵ may (physically) vary with r. In the inner optical isophotes, both ϵ and P.A. may be (artificially) radially dependent due to convolution with the PSF and viewing a triaxial object (isophotal "twists") respectively (Binney & Merrifield 1998). Inner isophotes have dramatically lower values of ϵ than the outer "real" values (as in Tremblay et al. 2007). The isophotal twists, on the other hand, are a consequence of viewing a triaxial object at a viewing angle not aligned with any of its axes. Either is potentially a problem for our optical fitting when the X-ray ISM aperture is small, but usually the X-ray emission is extended sufficiently that most of the optical light in our aperture comes from regions where $d\epsilon/dR$ is small; isophotal twists are only seen in the very central regions of a few nearby galaxies in our DSS data. None of our sources are quasars or appear to be saturated.

2.3.2 Optical—X-ray Correlation

Because long ($50-100$ ks) exposures are often required to see the diffuse X-ray gas even in nearby galaxies, it is plainly attractive to adopt the optical light as a proxy for the hot ISM. To zeroth order the stars and ISM should coincide, but the ISM may not be in hydrostatic equilibrium with the host (Diehl & Statler 2007), and may be disturbed by recent mergers presumed to power the AGN. In fact, Diehl & Statler (2007) find (in an analysis of 54 *Chandra* detections of hot ISM) that the gas ellipticity and morphology differs significantly from the starlight, although their sample only overlaps our own by a small amount. Acknowledging that a detailed view of the inner ISM shows significant differences from the starlight, we ask whether the starlight is a sufficient proxy for the ISM in gross morphology (i.e.

we are interested in the outer X-ray "isophotes") or whether it is of such different character that it weakens the Capetti et al. (2002) and Saripalli & Subrahmanyan (2009) analyses.

In fact, our work supports the identification of the optical light as an appropriate proxy for the hot ISM. However, in contrast to Capetti et al. (2002), we do not find that XRGs are preferentially in galaxies with higher ϵ, although we note that our X-ray ϵ values are probably underestimated. For the subset of our combined sample with strong ISM emission (19 of 26 galaxies), we find a correlation coefficient of $R = 0.60$ (Figure 2.6) between the ellipticity of the X-ray light ($\epsilon_{\text{X-ray}}$) and the ellipticity of the host galaxy in the DSS images (ϵ_{DSS}). The correlation between the position angles of the best-fit ellipses is even stronger ($R = 0.96$), but this is not meaningful because we expect a positive correlation even if the ellipses are misaligned. This is because an ellipse may have a P.A. anywhere between $0^\circ < \text{PA} < 180^\circ$, but when considering the angular separation of the PAs of two superimposed ellipses, one of the angles of separation must be acute. Therefore, a better measurement of the agreement between the optical and X-ray position angles is shown in Figure 2.6 where the distribution of $\Delta\text{PA} = \text{PA}_{\text{ISM}} - \text{PA}_{\text{optical}}$ is shown. The values in Figure 2.6 are presented in Table 2.5. The uncertainties are given at the 2σ level from the bootstrap method. For $N = 21$ our results are significant at the 95% level. The values we use are given in Table 2.5 along with a comparison of DSS to SDSS values (and our ISM values to the best-fit AGN PSF values).

We check our results for the optical values against the literature, where profile and isophotal fitting is standard. Our distribution of optical ϵ peaks slightly below $\epsilon = 0.2$ and falls off quickly at higher values. This is in agreement with the *HST* study by Martel et al. (1999), but is slightly rounder than the reported distributions in the ground-based studies of radio galaxies by Smith & Heckman (1989) and

Table 2.4. Optical Hosts Comparison

Name	ϵ_{DSS}			PA_{DSS}			PA_{radio}		
	This work	C02	SS09	This work	C02	SS09	This work	C02	SS09
Working Sample									
B2 1040+31A	0.15	-	-	153	-	-	159	-	-
PKS 1422+26	0.16	-	-	118	-	-	92	-	-
NGC 326	0.04	-	0	153	-	b	120	-	135
3C 403	0.27	a	0.25	39	35	39	72	85	79
4C +00.58	0.51	-	-	139	-	-	65	-	-
3C 192	0.02	a	0	119	95	b	123	125	123
3C 433	0.30	-	0.47	167	-	145	169	-	164
3C 315	0.37	a	0.46	44	35	33	12	10	8
Unused XRGs									
4C +32.25	0.12	a	0.15	90	90	84	61	60	64
4C +48.29	0.03	-	0	127	-	b	179	-	170
3C 136.1	0.39	a	0.37	101	100	117	106	110	139
J1101+1640	0.34	-	0.29	62	-	64	113	-	114
3C 223.1	0.42	a	0.45	43	40	40	7	15	15

[a]Capetti et al. (2002) do not provide ϵ values in their paper.

[b]Saripalli & Subrahmanyan (2009) do not report an optical P.A. if ϵ is "0".

Note. — A "-" signifies no data exist in the literature for comparison. C02 and SS09 refer to Capetti et al. (2002) and Saripalli & Subrahmanyan (2009) respectively. Note that while radio position angles are generally in agreement, large discrepancies exist (attributable to where the jet/lobe P.A. is measured). Uncertainties are not quoted in C02 or SS09.

Lambas et al. (1992), whose distributions peak at $\epsilon = 0.2$ and 0.25 respectively. The small excess of very round hosts may be real (it persists even when ϵ is measured at larger radii than reported) but our method may also underestimate ϵ. The ϵ measurement has been made for far fewer sources in the X-ray band so a systematic comparison is difficult. In addition, we compare our optical ϵ and P.A. values for the XRG sample specifically to any matching sources in the Capetti et al. (2002) and Saripalli & Subrahmanyan (2009) studies (Table 2.4) and find generally good agreement. In other words, in the X-ray band we (to some extent) reproduce the Capetti et al. (2002) and Saripalli & Subrahmanyan (2009) results.

Additionally, we note here a few caveats. First, we do not take into account the possible XRB contamination of the ISM. We do not consider this a significant

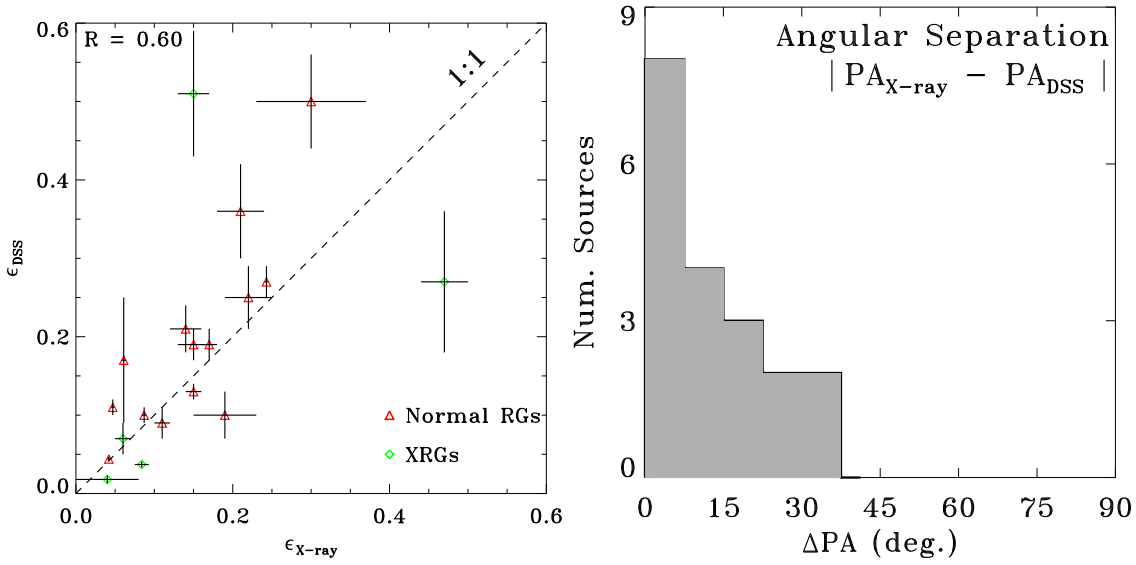

Figure 2.6 LEFT: A comparison of the ellipticities of the diffuse ISM to the optical light where ϵ in each case has been generated by our ellipse-fitting method (Section 2.3.1). The dashed line represents a 1:1 correlation rather than a best-fit line. RIGHT: Comparison of the position angles of the best-fit ellipses for the diffuse ISM to those of the optical light where the values are determined by our ellipse-fitting method (Section 2.3.1).

problem based on our spectroscopic analysis—even though LMXB spectra are often stronger at lower energies, the thermal models are much better able to fit the peaks in the ISM spectra, and are often sufficient for an adequate fit without requiring a power law. This is consistent with Sun et al. (2005) who demonstrate that the XRB contribution to the emission is usually less than 10% of the luminosity; in many of our spectra we lack the signal to distinguish a $< 10\%$ contribution. Second, as noted in Section 2.3.1, our X-ray ϵ values tend to be systematically underestimated. This makes a comparison with, for example, the Diehl & Statler (2007) work difficult. Notably there is one strong outlier in 3C 403, whose $\epsilon_{\text{X-ray}} = 0.47 \pm 0.03$ is much higher than its optical ellipticity $\epsilon_{\text{opt}} = 0.27$. Kraft et al. (2005) find an even higher value of $\epsilon_{\text{X-ray}} = 0.57 \pm 0.04$ using a profile fitting technique (they also compare $\epsilon_{\text{X-ray}}$ to *HST* $\epsilon_{\text{optical}}$), so it appears likely that the 3C 403 ISM is indeed out of

equilibrium. However, the case of 3C 403 is noteworthy in that the small extent of the ISM relative to the AGN emission makes energy filtering a more effective way to remove the AGN prior to fitting. Kraft et al. (2005) use a $0.3-1.0$ keV window, but it is difficult to conclude with certainty that this emission is "dominated" by the hot gas because it is possible to obtain a good fit to the spectrum (shown in Figure 2.5) using an unabsorbed power law between $0.3-2.0$ keV. If 3C 403 is indeed badly out of equilibrium, it appears to be an isolated case in our sample.

2.3.3 X-ray—Radio Correlation

We now measure the correlation between the position angles of the X-ray media and the radio jets by asking whether the quantity $\Delta\mathrm{PA} = |\mathrm{PA}_{\mathrm{radio}} - \mathrm{PA}_{\mathrm{X\text{-}ray}}|$ is uniformly distributed for the XRGs and normal radio galaxies. A uniform distribution means that for a given sample there is no preferred alignment between the radio jets and the P.A. of the surrounding hot gas. The radio jets are highly collimated and their orientation is determined "by eye"; we believe the values are accurate to within 10°. The ellipticity and P.A. of the X-ray emission are determined as described in Section 2.3.1, but to which medium shall we compare the alignment of the jets? Our goal is to determine whether XRGs reside preferentially in media elongated along the jet axis. In the overpressured cocoon model, this medium is assumed to be the ISM, but there are a few XRGS (NGC 326 and PKS 1422+26) for which the ISM cannot be the "confining" medium because the wings are produced outside the ISM. Therefore we must consider how to deal with the IGM/ICM. We describe the process of IGM/ICM aperture selection after our ISM comparison. In our discussion, the "relevant" medium is the one which could potentially confine the radio galaxy.

1. *Interstellar Medium*

   All of our radio galaxies have escaped the ISM, but it must have been the

Table 2.5. Ellipse Parameters for the ISM

Name	$\epsilon_{\text{X-ray}}$	$\text{PA}_{\text{X-ray}}$ (°)	$\epsilon_{\text{X-ray PSF}}$	$\text{PA}_{\text{X-ray PSF}}$ (°)	ϵ_{DSS}	PA_{DSS} (°)	ϵ_{SDSS}	PA_{SDSS} (°)	PA_{jets} (°)	PA_{wings} (°)
XRGs										
B2 1040+31A	0.21±0.07	158±11	0.07	58	-	-	0.15±0.02	153±22	159	58
NGC 326	0.084±0.009	130±37	0.09	134	0.037±0.004	153±33	-	-	120	42
3C 403	0.47±0.03	35±5	0.11	108	0.27±0.09	39±35	-	-	72	133
4C +00.58	0.15±0.02	138±17	0.07	161	0.51±0.08	139±6	0.44±0.02	138±3	65	14
3C 192	0.04±0.01	126±22	0.06	146	0.018±0.005	119±40	0.018±0.002	132±38	123	54
3C 433	0.09±0.02	156±40	0.04	172	0.3±0.1	172±21	-	-	169	84
Comparison Sample										
3C 449	0.14±0.02	6±15	0.16	30	0.21±0.03	8±6	-	-	9	
3C 31	0.087±0.003	112±16	0.18	159	0.10±0.01	142±12	-	-	160	
3C 83.1B	0.17±0.01	166±16	0.12	1	0.19±0.02	161±17	-	-	96	
3C 264	0.042±0.002	129±27	0.17	148	0.044±0.003	129±27	0.011±0.005	160±32	30	
3C 66B	0.15±0.01	128±9	0.15	13	0.13±0.01	131±15	-	-	60	
3C 296	0.15±0.02	137±6	0.17	147	0.19±0.02	151±13	0.23±0.01	147±6	35	
PKS 2153-69	0.22±0.03	106±8	0.17	34	0.25±0.04	126±12	-	-	136	
NGC 6251	0.047±0.002	25±23	0.15	72	0.11±0.01	24±13	-	-	115	
3C 98	0.19±0.04	92±24	0.13	90	0.10±0.03	62±20	-	-	10	
3C 465	0.061±0.003	51±29	0.17	74	0.17±0.08	33±25	-	-	126	
3C 293	0.30±0.07	84±18	0.05	110	0.50±0.06	64±7	0.29±0.05	60±10	126	
3C 285	0.21±0.03	141±18	0.19	96	0.36±0.06	133±13	0.36±0.05	125±9	73	
3C 227	0.11±0.01	19±20	0.33	98	0.09±0.02	27±17	-	-	65	

Note. — Position angles are reported counter-clockwise from North (0°) and chosen to reflect the acute angle between the major axes of the X-ray, optical, and radio ellipses. The error bars are reported at 95% using our ellipse-fitting method (Section 2.3.1). Radio position angles are estimated visually and have an estimated error of ΔP.A. $\sim 10°$. The PSF values are reported for the best-fit PSF used to mask the AGN emission.

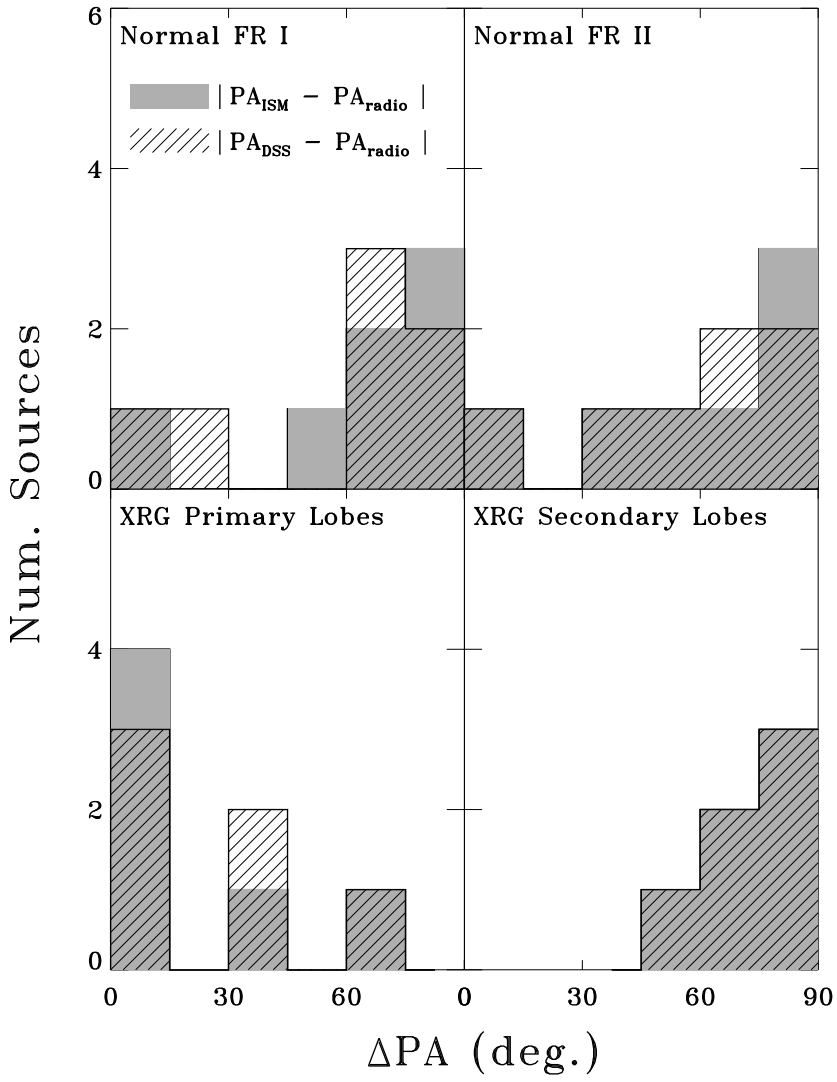

Figure 2.7 Comparison of the alignment of the radio jets with the interstellar medium (filled) and the optical light (hashed). ΔP.A. is the acute angle between the major axes of the best-fit ellipses (Section 2.3.1) and the orientation of the radio jets. ΔP.A. $\sim 0^\circ$ indicates alignment of the *major* axis of the medium with the radio lobes, whereas ΔP.A. $\sim 90^\circ$ indicates alignment with the *minor* axis. Note not all galaxies are represented here.

relevant medium for all of them at early stages. Assuming that the jet orientation relative to the ISM has not changed over the life of the radio galaxy, it is straightforward to compare ΔP.A. for the normal radio galaxies and the XRGs using the ISM. In the Capetti et al. (2002) model, we expect that the XRGs would have a small angular separation between the ISM major axis and the radio jets, i.e. ΔP.A. ~ 0. Figure 2.7 bears this expectation out (values reported in Table 2.5). The aperture for the ISM was the same as described in Section 2.3.2 and we exclude the same five galaxies. Figure 2.7 includes 6 XRGs and shows the distributions of both the active and secondary lobes. As noted in Section 2.3.2, the agreement between the gas and the starlight is good. Neither XRG distribution is consistent with a uniform distribution ($P = 0.04$ for the primary lobes and 0.01 for the secondary lobes) despite the small sample size, whereas the normal radio galaxies are consistent with uniform distributions ($P \sim 10\%$). The normal FR I ΔP.A. distribution is only marginally consistent with uniform (although dramatically different from the XRGs) and may be influenced by the giant radio galaxies which Saripalli & Subrahmanyan (2009) noted tend to have jets aligned along the *minor* axis of the host. This result is, in our view, strong evidence for the Capetti et al. (2002) model, although it was anticipated from Section 2.3.2. The IGM may be the confining medium for several XRGs, but the strong agreement with the Capetti et al. (2002) geometry in the ISM suggests that the ISM—jet orientation may be intrinsically important. The overpressured cocoon model put forth to explain this geometry should not be confused with the observed result.

2. *Intragroup/Intracluster Medium*

   Because the XRGs exist whose wings could not have been produced by the

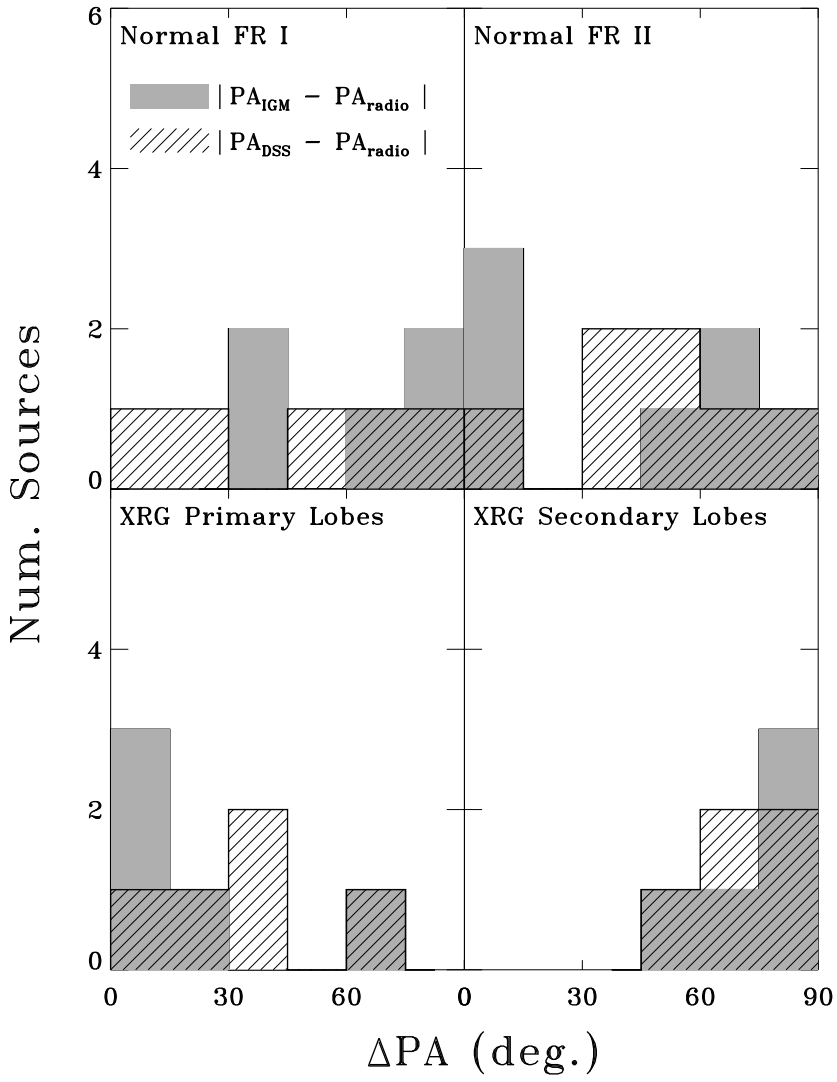

Figure 2.8 Comparison of the alignment of the radio jets with the local IGM (filled, see text) and the optical light (hashed). ΔP.A. is the acute angle between the major axes of the best-fit ellipses (Section 2.3.1) and the orientation of the radio jets. ΔP.A. $\sim 0^\circ$ indicates alignment of the *major* axis of the medium with the radio lobes, whereas ΔP.A. $\sim 90^\circ$ indicates alignment with the *minor* axis. Not all galaxies are represented here.

ISM in the Capetti et al. (2002) model, we want to see if the Capetti et al. (2002) geometry exists among IGM atmospheres as well. We thus have to consider how to choose apertures in the IGM/ICM for the comparison sample as well. There is no obvious way to compare these media for various radio galaxies, especially since some of our control sample radio sources extend far beyond the chip boundaries.

However, using the same logic as above, we can measure the elongation and orientation of the "local" IGM/ICM (Section 2.3.1). All sources larger than the local IGM/ICM must have passed through it at one point, and it is the relevant medium for all sources enclosed by it and outside the ISM. As mentioned in Section 2.3.1, we assume that the IGM/ICM is described by a smooth ellipsoid so the position angles are comparable between sources of vastly different scale (the gradients are more important). We therefore expect the ΔP.A. values to be uniformly distributed in the control sample.

We detect IGM/ICM emission in fewer galaxies, but we include the five galaxies with IGM/ICM but no clearly distinguishable ISM (3C 338, 3C 388, 3C 445, 3C 452, and Cyg A). We thus have 5 normal FR I galaxies, 7 normal FR II galaxies, and 5 XRGs. Of the XRGs, the IGM/ICM is the relevant medium for NGC 326 and PKS 1422+26, and may be the relevant medium in 3C 315, 4C +00.58 and B2 1040+31A. Although the sample sizes are smaller, the ΔP.A. distributions for the FR I and II galaxies are consistent with uniform ($P = 0.3$ and 0.4 respectively; Figure 2.8). The XRG sample, on the other hand, is not consistent with a uniform distribution ($P = 0.02$ for both the primary and secondary lobes). Our values are found in Table 2.6.

In 3C 452, the X-ray emission traces the radio emission so well that the geometry of the extended emission probably represents the radio galaxy cocoon

Table 2.6. Ellipse Parameters for the Local IGM/ICM

Name	ϵ_{IGM}	PA_{IGM} (°)	PA_{jets} (°)	PA_{wings} (°)
XRGs				
B2 1040+31A	0.18±0.08	130±30	159	58
PKS 1422+26	0.13±0.03	88±14	92	179
NGC 326	0.20±0.04	128±20	120	42
4C +00.58[a]	0.15±0.02	138±17	65	14
3C 315	0.38±0.06	23± 7	12	120
Comparison Sample				
3C 449	0.3±0.1	41±12	9	-
3C 31	0.18±0.01	123±4	160	-
3C 296	0.23±0.04	121±8	35	-
PKS 2153-69	0.13±0.03	140±10	136	-
3C 338	0.243±0.002	65±6	90	-
3C 465	0.37±0.02	53±3	126	-
Cyg A	0.2±0.1	22±4	115	-
3C 445	0.3±0.1	77±8	169	-
3C 285	0.28±0.06	163±9	73	-
3C 452	0.43±0.03	83±2	78	-
3C 388 (l)	0.13±0.02	65±6	55	-
3C 388 (s)	0.088±0.005	133±18	55	-

[a]The same values for 4C +00.58 are used in the ISM ellipse table. The identity of the medium we fit is ambiguous.

Note. — The error bars are reported at 95% using our ellipse-fitting method but are likely underestimates. Images are processed before fits (Section 2.3.1) by binning and smoothing due to the extended faint emission. For 3C 388 we use the large (l) ICM value, but note the smaller ICM has a distinct position angle (Section 2.3.3).

or a bounding shock and not the actual IGM (even when a purely "thermal" image is reconstructed; Appendix C.1). Similarly, the radio lobes of 3C 388 may be responsible for the geometry of the surrounding medium and the inner isophotes of the surrounding ICM are elongated perpendicular to the jet. If we exclude 3C 452 and use a smaller aperture in 3C 388 as the "local" ICM, our results for the IGM/ICM comparison outlined above are unchanged (the normal FR II galaxies still look uniformly distributed).

We cannot easily compare a mix of ISM and IGM/ICM relevant media in the XRG sample to the comparison sample. However, we can do this for the XRG

sample because we have the additional spatial information of the secondary lobes. When we use the IGM values for NGC 326 and PKS 1422+26, the distribution of ΔP.A. obeys the Capetti et al. (2002) correlation even more strongly than for the ISM or IGM alone. The probability that the ΔP.A. distribution for this "best guess" sample is $P = 0.006$ for the primary lobes and $P = 0.001$ for the secondary ones. Regardless, the samples individually are distinguishable from normal radio galaxies by their jet—medium geometry.

Does this geometry necessarily implicate the overpressured cocoon model? NGC 326, and 3C 433 obey the Capetti et al. (2002) geometry but would be difficult to form in the overpressured cocoon model alone. NGC 326, for example, is a well studied XRG which has longer secondary lobes than primary ones. This poses a problem for the overpressured cocoon model, since we expect the jets to expand supersonically and the wings to be (at most) transonic. The long secondary lobes may therefore imply buoyant evolution of the backflow (Worrall et al. 1995), although subsonic expansion of the primary lobes is possible. 3C 433 is an especially odd case since the southern radio lobes are of qualitatively different character than the northern counterparts. Miller & Brandt (2009) argue that the difference between the northern (FR I) and southern (FR II) lobes is due to propagating into a very asymmetric medium. The secondary lobes are close to the ISM, so it is ambiguous which medium is relevant for XRG formation. Lastly, 4C +00.58 appears to violate the Capetti et al. (2002) geometry as the jet appears to come out of the minor axis of the ISM. 4C +00.58 almost certainly disagrees with the Capetti et al. (2002) geometry in the optical image (due to the high ϵ the major axis is likely to be close to the plane of the sky) and we detect an X-ray jet cospatial with the northern radio jet. However, it is unclear that the extended X-ray emission comes entirely from the ISM. Deeper followup observations are required to assess the role of the IGM in this source and establish

whether it is actually a counterexample to the Capetti et al. (2002) geometry; this study is presented in Chapter 3. 3C 192 is an ambiguous case because although it obeys the Capetti et al. (2002) geometry, the eccentricity of the ISM is small. For 3C 192 to be produced in the overpressured cocoon model, small differences in pressure gradients must be important.

2.4 Properties of the Central Engine

In the backflow models, FR II morphology is thought to be necessary to drive strong backflows. Although the backflows begin at the hot spots, edge-brightened FR II morphology is strongly associated with absorbed power law AGN emission. We note that several galaxies in our XRG sample are not unambiguously FR type II (some of the galaxies with poor data are FR I), so we attempt to characterize the XRG sample in terms of absorbed or unabsorbed AGN spectra. Highly absorbed spectra tend to have higher L_X for a given flux than unabsorbed spectra owing to the large amount of "absorption" blocking the low-energy photons, whereas unabsorbed spectra tend to be lower energy with small X-ray luminosities above ~ 2 keV.

Our model fitting of the AGN spectra started by fitting a single power law (either absorbed or unabsorbed depending on the appearance of the spectrum). Additional complexity was added as the degrees of freedom allowed until an acceptable fit was achieved. We note that N_H and Γ are often degenerate and require one of the two to be frozen (to values ranging from $\Gamma = 1.0 - 2.0$; Table 2.7). All the fits also incorporated Galactic N_H. Our model parameters and luminosities are given in Table 2.7 and are largely in accordance with previous studies of the 3CRR *Chandra* sample (Balmaverde et al. 2006; Evans et al. 2006). These papers have also conducted a more exhaustive study of the AGN X-ray emission, whereas our

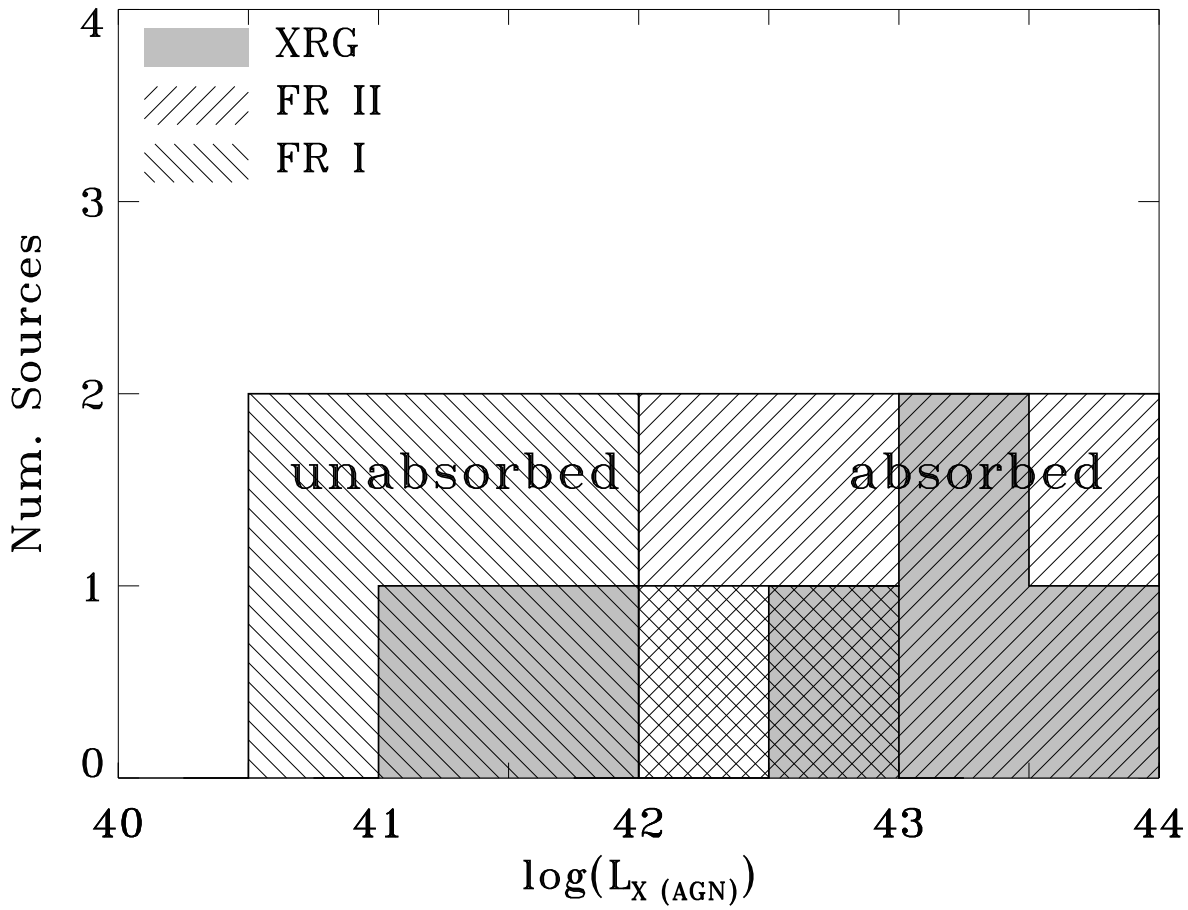

Figure 2.9 Distribution of the XRG and comparison sample model luminosities for spectra extracted from the central PSF. The luminosities are calculated for the full model fit. FR II galaxies tend to have highly absorbed spectra with corresponding high luminosities, whereas FR I galaxies tend to have unabsorbed spectra. XRGs have both absorbed and unabsorbed spectra.

purpose is to determine whether this emission lends insight to the XRG sample.

In fact, the XRG sample cannot neatly be classified in terms of asorbed or unabsorbed spectra (Figure 2.9). This is in agreement with other evidence (e.g. optical data from Cheung et al. 2009), although the highly absorbed XRGs do not tend to have a smaller L_X than the normal FR II galaxies. Indeed, the XRG sample, while small, is consistent with the distribution of L_X between 10^{40} and 10^{44} erg s^{-1} for the full comparison sample, and not with either the normal FR I or II galaxies

by themselves. We note that we detect X-ray jets in some of our systems, but we find no evidence for misaligned jets in any of the XRGs. The sample size is too small to rule out the Lal & Rao (2007) model on this basis, but we might expect to see misaligned jets in their scheme.

2.5 Discussion & Summary

We present new and archival *Chandra* data of XRGs alongside normal FR I and II galaxies within $z \leq 0.1$. We extend the Capetti et al. (2002) and Saripalli & Subrahmanyan (2009) geometric correlation between the orientation of the secondary lobes in XRGs and the minor axis of the interacting medium to the X-ray band, including the intragroup/intracluster medium. We find that this geometry strongly distinguishes the XRGs from normal radio galaxies (although we are unable to strongly distinguish between XRGs and normal radio galaxies using only the local IGM/ICM values), and that XRGs may be produced in galaxies with both absorbed and unabsorbed AGN. Our results in the X-ray band are consistent with Cheung et al. (2009) who find that XRGs lie close to the FR I/II division in a comparison of radio—optical luminosity. We note that in properties of the hot atmospheres (temperature, density, and pressure), the XRG sample appears indistinguishable from the comparison sample (Table 2.3) but that these parameters are spatial averages of profiles and may not be directly comparable.

The remarkable geometric distinction between the normal and X-shaped radio galaxies may be an important clue to the genesis of the secondary lobes. We cannot rigorously examine the formation models in our data, but identify potential problems for the backflow models in several galaxies. The backflow schemes naturally explain the observed geometry, but also have yet to explain other features of XRGs in

Table 2.7. Radio Galaxy Nuclei X-ray Spectral Parameters

Galaxy	z	Galactic N_H (10^{20} cm^{-2})	Models	Local N_H (10^{22} cm^{-2})	Γ	kT (keV)	Luminosity (10^{42} erg s^{-1})	χ^2/d.o.f
XRGs								
PKS 1422+26	0.037	1.54	N_H(PL+Gauss)	4. ± 1.	0.5 ± 0.4	-	3.8	8.2/16
NGC 326	0.048	5.86	N_H(PL)+apec	0.5 (f)	1.3 ± 0.4	0.68 ± 0.06	0.15	11.1/16
3C 403	0.059	12.2	N_H(PL+Gauss)+PL+apec	46.± 5.	$\Gamma_1 = 1.9 \pm 0.1$ $\Gamma_2 = 2.0$ (f)	0.24 ± 0.03	16.6	100.7/94
4C +00.58	0.059	7.14	PL	-	1.3 ± 0.6	-	1.1	1.6/4
3C 192	0.060	4.08	N_H(PL)	16 (f)	2.0 (f)	-	3.1	0.9/2
3C 433	0.102	7.77	N_H(PL+Gauss)+apec	8. ± 1.	1.1 ± 0.1	1.0 ± 0.2	59	72.5/77
Comparison Sample								
3C 449	0.017	8.99	N_H(PL)+apec	0.5 (f)	1.6 ± 0.2	0.59 ± 0.08	0.05	7.6/14
3C 31	0.017	5.36	PL+apec	-	1.9 ± 0.1	0.70 ± 0.03	0.13	81./83
3C 83.1B	0.018	13.4	N_H(PL)+apec	2.2± 0.9	2.0 ± 0.3	0.48 ± 0.08	0.05	22.7/36
3C 264	0.021	1.83	PL+apec	-	2.13± 0.03	0.34 ± 0.06	1.7	152.7/154
3C 66B	0.022	7.67	PL+apec	-	2.17± 0.06	0.52 ± 0.08	0.33	90.6/114
3C 296	0.026	1.92	N_H(PL)+apec	0.10 (f)	1.1 ± 0.1	0.68 ± 0.02	0.38	91.8/81
NGC 6251	0.024	5.59	N_H(PL)+apec	0.05±0.01	1.5 ± 0.03	0.35 ± 0.05	8.0	391/386
PKS 2153-69	0.028	2.67	pileup(PL)+apec	-	1.49± 0.05	0.4 ± 0.2	12.2	73.1/86
3C 98	0.030	10.8	N_H(PL)+gauss+PL	9. ± 1.	$\Gamma_1 = 1.2$ (f) $\Gamma_2 = 1.5$ (f)	-	3.1	47.4/35
3C 465	0.031	4.82	N_H(PL)+apec	0.3 (f)	2.4 ± 0.2	0.83 ± 0.06	0.31	62.0/62
3C 293	0.045	1.27	N_H(PL)+apec	11 ± 4	1.5 (f)	1.55 (f)	4.5	9.3/10
Cyg A	0.056	30.2	pileup(N_H(PL))+gauss+cflow	25 ± 2	2.0 (f)	-	87.6	294.3/217
3C 445	0.056	4.51	pileup(N_H(PL))+gauss[1]	16 ± 1	1.7 (f)	-	47.	62.4/44
3C 285	0.079	1.27	N_H(PL)+gauss	28 ± 4	1.2 (f)	-	8.7	12.6/9
3C 452	0.081	9.64	N_H(PL)+gauss+apec+PEXRAV[2]	38 ± 9	1.65 (f)	0.8 ± 0.2	25	156.6/145
3C 227	0.087	2.11	pileup(N_H(PL))+PL	3.3 ± 0.1	$\Gamma_1 = 1.75$ (f) $\Gamma_2 = 1.0 \pm 0.2$	-	155	248.9/167
3C 388	0.091	5.58	PL+apec	-	2.3 ± 0.3	1.2 ± 0.2	1.9	14.1/16

[1]Complex emission between $0.5 - 3.0$ keV is ignored; see Appendix C

[2]PEXRAV is a reflection model from Magdziarz (1995)

Note. — Reported errors for Γ are the *smaller* of the values given by 90% confidence intervals determined in XSPEC; if there is significant asymmetry about the best-fit value, the larger error bar is ill defined. (f) denotes a frozen parameter, and complex model components are discussed in Appendix C with the relevant galaxy. The "fits" to low-count spectra (e.g. 3C 192 or 4C +00.58) are not reliable, but they do constrain well whether the spectrum is absorbed or unabsorbed, so we report them only for an order-of-magnitude luminosity estimate.

detailed modeling (e.g. the flat spectral indices of the secondary lobes Lal & Rao 2007). However, the models are presently immature: the Capetti et al. (2002) overpressured cocoon model has only been modeled in a highly elliptical 2D ISM, whereas the Kraft et al. (2005) suggestion that the buoyant backflow mechanism can produce X-shaped wings in the presence of an anisotropic buoyant medium has not been rigorously modeled. 3D modeling and deeper observations of the relevant media in XRGs are required to make a convincing case for either of these models. Notably, the rapid reorientation models have yet to present a reason for the Capetti et al. (2002) correlation. Any successful model must account for it. Lastly, deeper observations of the XRGs in our sample for which no diffuse emission was detected are required. The total sample of nearby XRGs is quite small, so every member is important.

Chapter 3

A Deep *Chandra* Observation of the X-shaped Radio Galaxy 4C +00.58

3.1 Introduction

X-shaped radio galaxies (XRGs) are double-lobed radio galaxies (Leahy & Williams 1984) which also possess a pair of long, faint, centro-symmetric "wings" (for a broader introduction, see Chapter 1). They have gained notoriety as a possible signature of a rapid (within a few Myr) reorientation of the supermassive black hole (SMBH) spin axis, conceivably induced by galaxy mergers in which either accretion torque or a SMBH merger causes a spin-flip (Merritt & Ekers 2002; Rottmann 2001). In this scenario, wings are "fossils" tracing the prior jet axis which radiatively decay.

However, no convincing case for reorientation has been made in any individual XRG, whereas several lines of evidence support a hydrodynamic origin for the wings. For instance, in most XRGs, the wings are coaligned with the minor axis of

the host galaxy and the jet with the major axis (Capetti et al. 2002; Saripalli & Subrahmanyan 2009). A similar major-axis—radio alignment trend exists in the X-rays (Chapter 2). These results have been interpreted to favor models in which the wings are produced by radio-lobe—gas interaction (Capetti et al. 2002; Leahy & Williams 1984; Worrall et al. 1995). Additionally, no clear signs of mergers have been found in a spectroscopic study of XRG hosts, whereas they may be overpressured (Landt et al. 2010).

In this Chapter, we identify 4C +00.58 (Figure 3.1, classified as a candidate XRG by Cheung 2007) as one of the best candidates for a merger-induced reorientation based on quantities derived from a deep *Chandra X-ray Observatory* observation and publicly available data. Unlike other XRGs, the 4C +00.58 jet is coaligned with the *minor* axis of its host. Even if only a fraction of XRGs are produced by reorientation, their frequency may be important for estimating *Laser Interferometer Space Antenna* detection rates.

We use a Galactic absorption of $N_H = 7.14 \times 10^{20}$ cm^{-2} (Kalberla et al. 2005), as well as the *Wilkinson Microwave Anisotropy Probe* cosmology ($H_0 = 71$ km s^{-1} Mpc^{-1}, $\Omega_\Lambda = 0.73$, and $\Omega_m = 0.27$; Spergel et al. 2007). At a redshift of $z = 0.059$, $1'' = 1.13$ kpc.

3.2 Observations

We obtained a 93 ks *Chandra* exposure toward 4C +00.58 using the Advanced CCD Imaging Spectrometer[1] (ACIS) and combined it with a 10 ks archival observation (obs. IDs 10304 and 9274; latter published in Hodges-Kluck et al. 2010a). The source is centered at the nominal aim point on the ACIS-S3 chip. The data were

[1]See http://cxc.harvard.edu/proposer/POG/pdf/ACIS.pdf

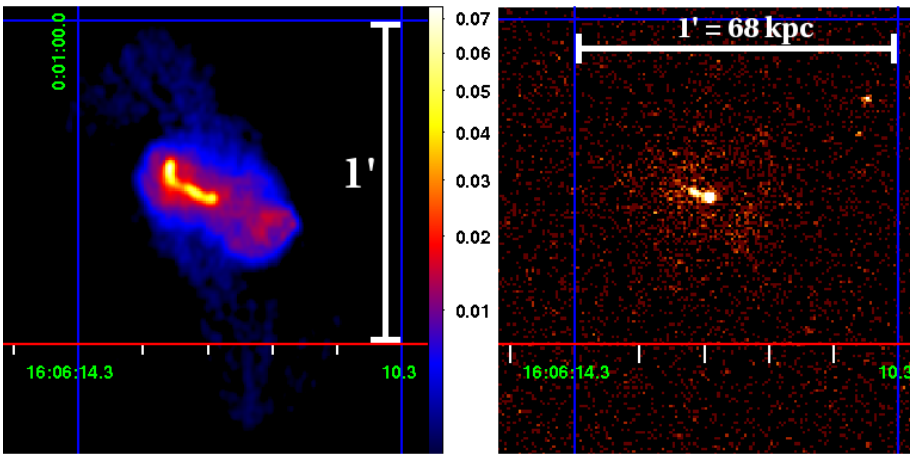

Figure 3.1 LEFT: 1.4 GHz VLA A-array map ($1.''6 \times 1.''3$ beam, units in Jy/beam). RIGHT: Raw *Chandra* image ($0.3 - 10$ keV). The brightest pixel in the AGN has 282 counts.

reduced with the *Chandra* Interactive Analysis of Observations (CIAO v4.0) software, and spectral fitting was performed with XSPEC (Arnaud 1996). We extracted a $0.3 - 10$ keV bandpass lightcurve (binned to 600 s) from empty regions to check for background flares, but found no 3σ deviations. The extended emission around 4C +00.58 is less than $45''$ in radius, so we use local background for spectral extraction.

We also use the NRAO[2] *Very Large Array* (VLA; Thompson et al. 1980) 1.4 GHz map (Chapter 2) and a 4.9 GHz map produced by combining archival snapshot A-array data from Best et al. (1999) and C-array data from program AC406. We use Sloan Digital Sky Survey (SDSS; Adelman-McCarthy et al. 2008) red (623.1 nm) and green (477.0 nm) images from two 54 s exposures of the host (SDSS J160612.68+000027.1) to measure color and magnitude, correcting for the smaller point spread function of the green images as well as sky background, the 1000-count software bias, and Galactic extinction.

[2]The National Radio Astronomy Observatory is a facility of the National Science Foundation operated under cooperative agreement by Associated Universities, Inc.

The 1.4 GHz map is shown in the left panel of Figure 1. The primary lobes of the radio galaxy lie nearly on an east–west axis and have a well defined boundary, whereas the faint wings are oriented in a north–south direction. The jet experiences a dramatic bend (by 60°) just before terminating, and the cocoon in the 1.4 GHz map is notable for a well defined edge with a surface brightness about five times that of the wings. The 5 GHz map resolves the jet into a string of knots (§3.3). We detect no counterjet.

The X-ray emission (Figure 3.1) is made up of two components: bright emission spatially associated with the jet/AGN and a compact diffuse atmosphere. To isolate the atmosphere, we mask point-like sources and restrict the energy bandpass to $0.3 - 3$ keV (Figure 3.2); this energy range contains 80% of the photons within $45''$. On the basis of an unsharp mask image and a weighted Voronoi tessellation adapatively binned image (Cappellari & Copin 2003; Diehl & Statler 2006), we have identified several X-ray cavities (Figure 3.2). These cavities, labeled C_{NE}, C_{NW}, C_{SE}, and C_{SW}, are low surface brightness regions in the hot atmosphere bounded by "spurs" of greater surface brightness. The cavities are deep negatives in an unsharp mask image in which a heavily smoothed map (40 px) is subtracted from a lightly smoothed (3 px) map. The residuals are shown in Figure 3.2.

The SDSS image (Figure 3.3) reveals a dim, resolved extension to the southeast of the host galaxy. The elliptical host shows no obvious internal structure, but the extension may be a stellar shell from a prior minor merger (for a discussion of shells see Quinn 1984). The extension is red ($g - r \sim 0.7$), but bluer than the host ($g - r \sim 1.0$). The apparent magnitude of the entire extension is $m_r \sim 20$.

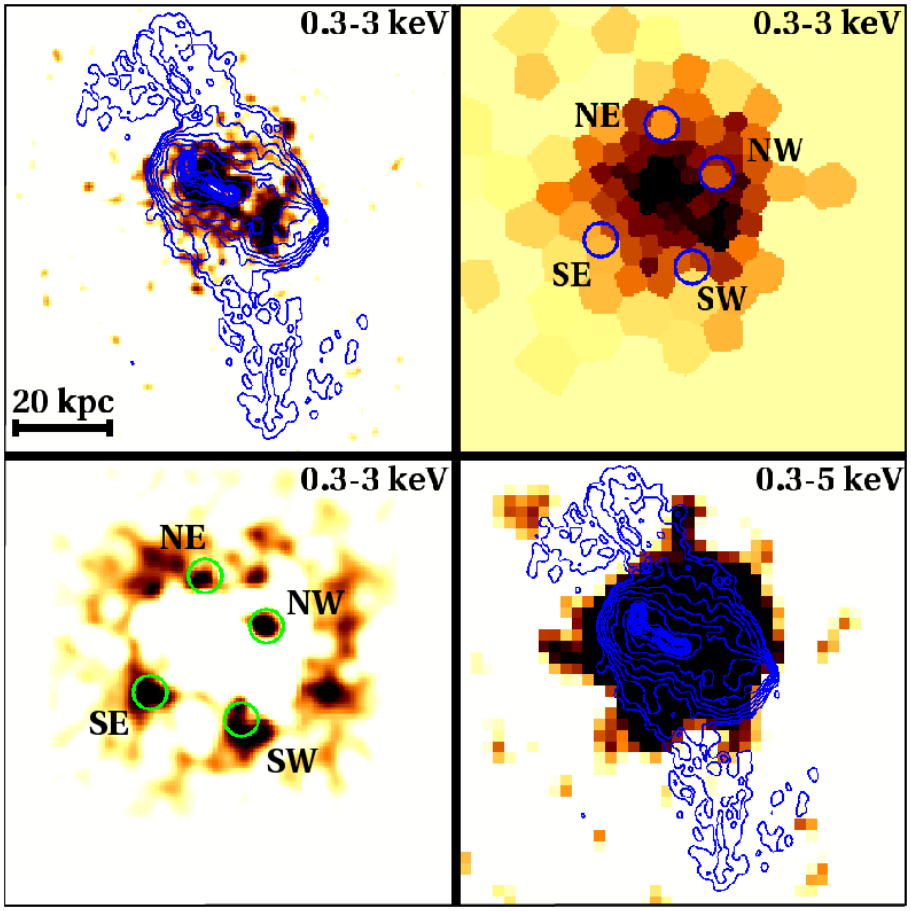

Figure 3.2 Top Left: 1.4 GHz contours overlaid on smoothed (σ = 3 pixels) X-ray image with point-like sources excised, clipped at twice the mean background. Top Right: A weighted Voronoi tessellation image (S/N = 5.0 in each tile) of the $0.3-3$ keV events with cavities identified. Bottom Left: Negative of an unsharp mask image of top left (using a smoothing length of 40 px for subtraction) showing cavities. Bottom Right: Coarsely-binned (4× native pixels) image from $0.3-5$ keV showing extended structures beyond 20 kpc from the AGN.

3.3 Results

3.3.1 Hot Atmosphere

The bright X-ray emission immediately near the jet is nonthermal, otherwise the extended emission is consistent with isothermal plasma out to 50 kpc from the

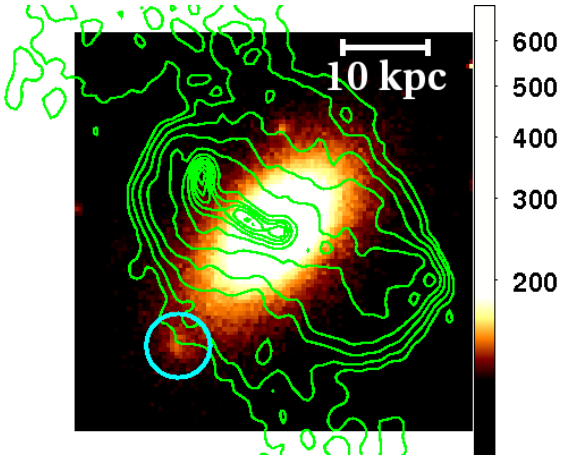

Figure 3.3 1.46 GHz contours overlaid on a combined red+green SDSS image of the host galaxy of 4C +00.58. The cyan circle encloses a 20th magnitude resolved "extension" to the elliptical galaxy which is slightly bluer.

AGN, with $kT = 1.1 \pm 0.2$ keV within 25 kpc and $kT = 0.9 \pm 0.1$ keV outside. Thus, we adopt a sound speed $c_s \approx 400$ km s^{-1} throughout the region. The photon statistics preclude a deprojection analysis. On the basis of the resulting emission measures, densities within 25 kpc are a few$\times 10^{-3}$ cm^{-3}, implying pressures $P = 10^{-12}$ to 10^{-11} dyne cm^{-2}. The total luminosity of the hot atmosphere is $L_X \sim 3 \times 10^{41}$ erg s^{-1}.

The gross morphology of the X-ray emission does not coincide with the host galaxy. Using only the 10 ks exposure, we argued Chapter 2 that the orientation agreed with the host although the ellipticity did not. With deeper data it is evident that while we correctly excluded nonthermal emission to the southwest, we could not exclude nonthermal emission to the northeast.

The most notable feature of the diffuse X-ray map is C_{NW} (Figure 3.2), which is collinear with C_{SE} and the AGN. C_{NW} is enclosed by emission and cospatial with a spur in the radio cocoon, suggesting that C_{NW} and C_{SE} are jet-blown cavities. C_{NE} and C_{SW} are also collinear with the AGN and are associated with the bases of the

wings, with walls extending into the surrounding medium.

The free-free cooling time of the C_{NW} and C_{SE} bounding material places an upper limit on their ages:

$$t_{\rm ff} \sim \frac{5}{2}\frac{nkT}{\Lambda_{\rm ff}(T)} \approx 1.6 \times 10^9 T_7^{1/2} n_{-3}^{-1} \text{ yr} \sim 500 \text{ Myr} \tag{3.1}$$

where $T_7 \sim 1.4$ is the temperature in units of 10^7 K and $n_{-3} \sim 4$ is the density in units of 10^{-3} cm^{-3}. If C_{NW} is a spherical bubble (of radius 5 kpc) inflated at a locally estimated pressure $P = 5 \times 10^{-12}$ dyne cm^{-2}, the work done to inflate it is $W \sim 7 \times 10^{55}$ erg. Since the transonic expansion time is 10 Myr, the minimum average kinetic luminosity of the jet during that period is 2×10^{41} erg s^{-1} if C_{NW} is jet-blown.

3.3.2 Wings

The long wings are associated with low-signal X-ray structure (Figure 3.2, bottom right). The approximate wing symmetry implies coherent formation, but the southern wing is slightly longer.

If the wings expanded transonically, their length ($\sim$ 36 kpc) implies an age of 90 Myr, although this is a minimum age since the wings are seen in projection and may expand subsonically. Conversely, the synchrotron decay time $t_{\rm sync}$ provides a maximum wing lifetime assuming the radio emission traces the entire wing volume and the wings were inflated by the radiating plasma. To estimate $t_{\rm sync}$, we follow Tavecchio et al. (2006) and use the 1.4 GHz map to estimate the equipartition field $B_{\rm eq}$. We take the spectral index, $\alpha = 0.7$ ($S_\nu \propto \nu^{-\alpha}$), from low-resolution radio photometry and assume $\gamma_{\rm min} \sim 10$. For cylindrical wings of $r = 6$ kpc and $h = 36$ kpc, we obtain $B_{\rm eq} \sim 10$ μG. We then find the electron Lorentz factor

$\gamma \sim 5600$ from $\nu_{s[1.4\ \mathrm{GHz}]} = 4 \times 10^{-3} B\gamma^2 = 1.4$ GHz, and thus find

$$t_{\mathrm{sync}} \approx 2.4 \times 10^9 \gamma_4^{-1} B_{\mu\mathrm{G}}^{-2}\ \mathrm{yr} \sim 40\ \mathrm{Myr} \tag{3.2}$$

where γ_4 is in units of 10^4 and $B_{\mu\mathrm{G}}$ is in μG. This value represents the cooling time of the 1.4 GHz electrons; we emphasize our assumption that this is "first-generation" plasma occupying the wings. t_{sync} is insensitive to projection effects relative to the transonic expansion time: if the wings are longer by a factor of 2, B_{eq} decreases by a factor $2^{1/(3+\alpha)} \sim 1.2$ and t_{sync} increases by a factor ~ 1.4. The disagreement between t_{sync} and the expansion time suggests either supersonic expansion (i.e. like a jet-blown cocoon) or wing replenishment by supersonic inflowing lobe plasma.

The work required to inflate the wings, assuming the cylinders above, is $PdV \sim 10^{57}$ erg. An age of 40 Myr implies an average kinetic luminosity of $L_{\mathrm{kin}} \sim 8 \times 10^{41}$ erg s^{-1} applied to the wings alone.

3.3.3 Nucleus and Jet

The strong central X-ray point source corresponds to the AGN and contains 1100 counts. The spectrum is fit well by a model consisting of an unabsorbed power law with spectral index $\alpha = 0.7 \pm 0.1$ and a weak thermal model frozen at $kT = 1.0$ keV. The nonthermal luminosity is $L_X \sim 7 \times 10^{41}$ erg s^{-1} between $0.3 - 10$ keV.

The X-ray jet is the next brightest feature and traces the radio jet well, including several X-ray knots (Figure 3.4). A super-sampled X-ray image reveals that two of these knots coincide with more compact knots visible in the 5 GHz image and a bright region in the 1.4 GHz jet. There is a modest radio ($1.4 - 5$ GHz) spectral gradient between the inner and outer jet (Table 3.1), and the outer jet does not appear in the X-rays. Along the inner jet, we measure a broad-band radio to X-ray spectral index, $\alpha_{rx} \sim 1.0$, which is consistent with the X-ray spectrum ($\alpha_x \sim$

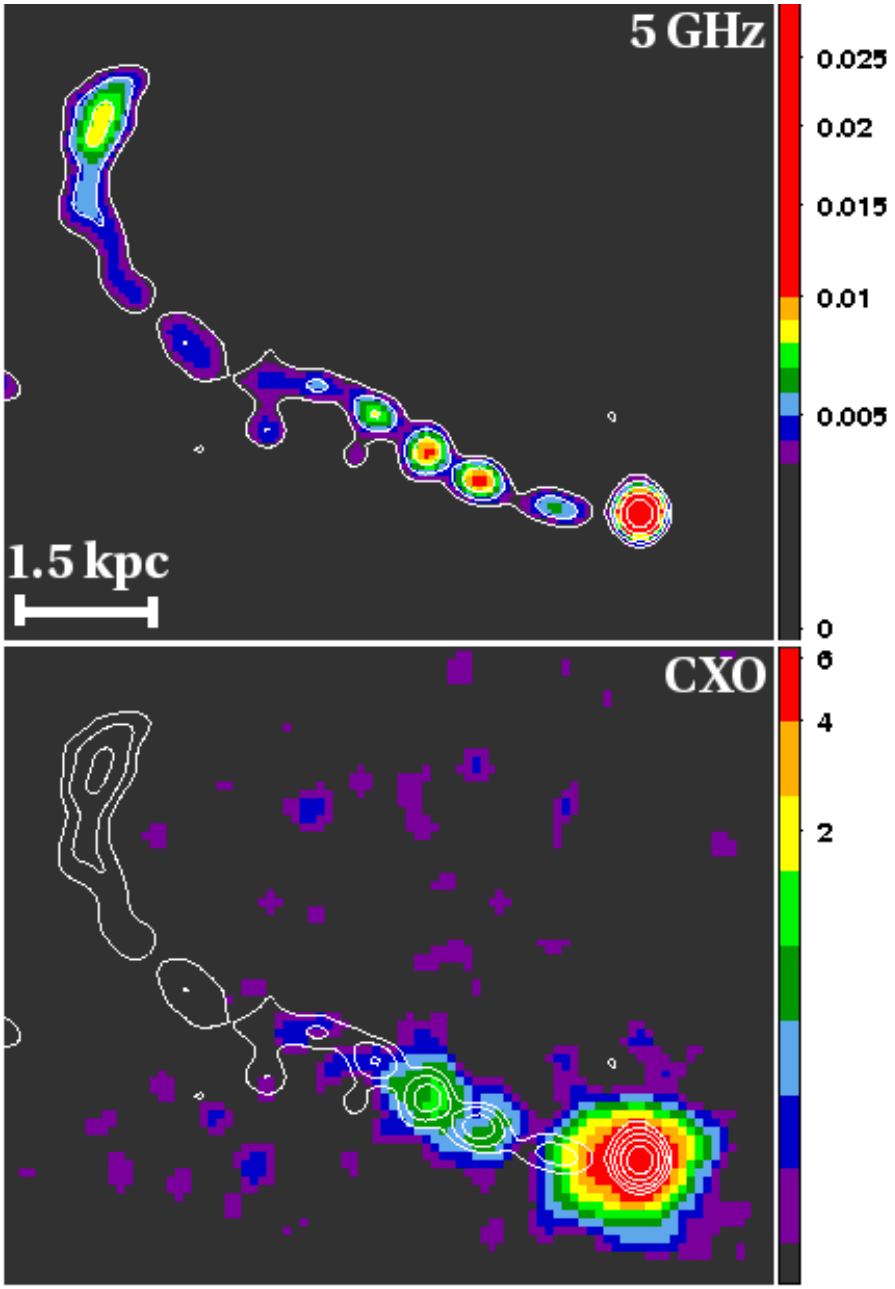

Figure 3.4 Top: 5 GHz VLA image of the jet with contours (beamsize $0.5 \times 0.5''$, units in Jy/beam). Bottom: Smoothed X-ray image with pixel randomization turned off (superbinned to 1/4-original pixel size) with 5 GHz contours overlaid.

Table 3.1. Core and Jet Parameters

Designation	Distance ($''$)	$F_{1.4\ \mathrm{GHz}}$ (mJy)	$F_{4.9\ \mathrm{GHz}}$ (mJy)	$F_{\mathrm{X\text{-}ray}}$ (nJy)	α_r	α_{rx}	α_x	δ	B_{eq} (μG)
Core	0.0	41±4	30±3	$8.3^{+0.7}_{-0.1}$	0.25	0.8	0.7±0.1	-	-
Inner jet	0.6−6.0	180±20	88±9	1.0 ± 0.3	0.6	1.0	1.1±0.4	< 7	7
Inner Knot 1	2.5	-	14±1	0.3 ± 0.2	0.6[a]	1.0	1.0±0.7	< 8	9
Inner Knot 2	3.3	-	15±1	0.9 ± 0.3	0.6[a]	0.9	1.5±0.6	< 10	7
Outer jet	6.0−10.	220±20	70±7	< 0.1	0.9	>1.1	-	-	$120/\delta$

[a]It is not possible to separate the knots at 1.4 GHz, so we use the average value instead of measuring a flux.

Note. — Most of the jet X-ray emission comes from knot 2 and the outer jet has no X-ray emission. The distance is measured radially from the core in arcsec. We report a model X-ray flux from the best-fit power-law model with errors reported at 90% confidence.

1.1±0.4). Thus, the X-ray emission is consistent with a synchrotron origin (requiring a concave-down spectral energy distribution). Alternatively, assuming an inverse Compton origin for the X-rays, we follow Tavecchio et al. (2006) to estimate the jet Doppler factor $\delta = [\gamma(1 - \beta\cos\theta)]^{-1}$ in the knots by finding B such that $B_{\mathrm{eq}}\delta = B_{\mathrm{IC}}/\delta$. This results in $\delta \sim 10$ (Table 3.1) and $B_{\mathrm{knot}} \sim 10$ μG. As the jet X-ray emission may not be dominated by inverse-Compton emission, δ is formally an upper limit. B_{eq} is derived with no knowledge of the X-ray emission and predicts $P \sim 3 \times 10^{-12}$ dyne cm^{-2}, in agreement with spectral fitting estimate.

Although no counterjet is visible, the 1.4 GHz emission suggests the jet has point symmetry. If the jet tail is dragged, the tail will cool radiatively with its length set by the cooling time (i.e. no additional plasma influx). We derive an upper $B_{\mathrm{eq}}\delta \sim 120$ μG at $\nu_s = 5$ GHz and thus find $t_{\mathrm{sync}} \sim 0.5 - 15$ Myr for $\delta = 1 - 10$. We assume δ declines along the jet, so for $\delta \sim 5$, $t_{\mathrm{sync}} \sim 6$ Myr.

The projected length of the radio cocoon gives a transonic expansion time of 35 Myr. The work done to excavate a cocoon with semimajor axis $a = 17$ kpc and semiminor axes $b = c = 8$ kpc is $PdV \sim 7 \times 10^{56}$ erg, so the minimum average kinetic luminosity while inflating the cocoon is $L_{\mathrm{kin}} \sim 7 \times 10^{40}$ erg s^{-1}.

3.4 Wing Formation Models

We consider three wing formation scenarios: an overpressured outburst, conical precession of the jet axis, and merger-induced reorientation of the jet axis.

In the backflow models, wings are produced by pressure- or buoyancy-driven back-flowing plasma from the terminal shocks evolving in the hot medium. Since we see no obvious evidence for a plumed jet *directly* feeding the wings, the most plausible of these models is a "blow-out" from an overpressured cocoon early in the source's life (Capetti et al. 2002). In this model, the native atmosphere confining the young jets is aspherical with a preferential direction along which the cocoon ruptures.

The backflow model suffers from several difficulties when applied to 4C +00.58. First, the wings must expand at most transonically. The long projected length of the wings in 4C +00.58 (requiring an AGN lifetime of at least 90 Myr) is difficult to reconcile with the cocoon length unless the cocoon inclination angle from the line of sight $\theta_{\rm LOS}$ is less than 30°. The equivalent widths of O II (3727Å) and O III (5007Å) measured by Landt et al. (2010) argue against a steep inclination (Landt et al. 2004). Furthermore, the maximum wing lifetime $t_{\rm sync}$ disagrees with the transonic expansion time, although the wing plasma may be continuously replenished. Second, the model relies on strong backflows typically associated with Fanaroff & Riley (1974, FR) type II sources. 4C +00.58 is not easily classified as FR I or II, but at $M_R \sim -22.7$ and $\log L_r(1.4\ {\rm GHz}) \sim 25.3$ W Hz^{-1} falls very close to the Ledlow & Owen (1996) boundary between FR I and II radio galaxies ($L_{\rm radio} \propto L_{\rm opt}^{1.8}$). Since XRGs generally lie near this boundary, they may be a transition population (Cheung et al. 2009; Landt et al. 2010). Finally, the radio emission is misaligned with its host, so the Capetti et al. (2002) model cannot produce wings until the jet escapes

the interstellar medium.

Conical precession is a simple model in which the jet axis swings around, so the wing extensions and post-bend jet are equidistant from the AGN. This requires a steep inclination angle of $\theta_{\rm LOS} < 30°$. In this model, the wings trace the jet history, and the oldest plasma can be no older than the synchrotron cooling time. To obtain the precession rate $\dot{\phi}$, we compare the projected length of the post-bend jet to its cooling time (about 6 Myr) and obtain $\dot{\phi} \sim 4°$ Myr^{-1} (corresponding to a mildly supersonic $v \sim 460$ km s^{-1}). A 180° rotation takes ~ 45 Myr and implies supersonic expansion for the cocoon. The timescale is consistent with the wing $t_{\rm sync}$, but the model must also explain the larger far-side cone, as both the far-side cocoon and wing have longer projected lengths. Notably, precession does not explain the presence of $C_{\rm NW}$ and $C_{\rm SE}$, and numerical simulations (e.g. Falceta-Gonçalves et al. 2010) indicate that it would not preserve obvious cocoon structure.

In the reorientation (spin-flip) scenario, the wings are fossil lobes of a jet whose direction rapidly changed, either due to accretion torque or coalescence of a SMBH binary. There is circumstantial evidence for such a spin-flip: a possible stellar shell indicating a minor merger, and the cavities $C_{\rm NW}$ and $C_{\rm SE}$ with overlapping cocoon extensions implying somewhat recent jet–gas interaction along an old axis. We describe a reorientation scenario for 4C +00.58 presently.

Given the small size of $C_{\rm NW}$ and $C_{\rm SE}$, the jet was in a weak or "off" state prior to the minor merger, but the SMBH spin axis was aligned with the major axis of the host. Upon ignition, the jet quickly formed $C_{\rm NW}$ and $C_{\rm SE}$. However, since the angular momentum axis of the accreting gas is generally misaligned with that of the SMBH, accretion torque will reorient the black hole's spin within a few Myr (Dotti et al. 2010). Hence, $C_{\rm NW}$ must have expanded at $v_{\rm exp} > 2c_s$ if no prior cavity existed.

Once accretion torque moved the jet to the wing axis, it inflated the wings as active lobes. The transonic lateral expansion time of the wings is 10 Myr, implying $v_{\rm exp} < 8c_s$ during wing inflation. The "Z-shaped" wing extensions (covering 30°) could be explained either as post-reorientation "wiggles" from a hot disk (Dotti et al. 2010, show that a thermally hot disk is required for wiggles of this magnitude) or interaction between the lobes and merging ISM swirling into the host (Gopal-Krishna et al. 2003; Zier 2005). These Z-shaped extensions then evolve buoyantly, and may be replenished by the primary lobes once the jet axis has moved (Gopal-Krishna et al. 2003). We suppose the jet moved to its current position due to coalescence of the SMBH binary or ongoing accretion torque, then formed the present cocoon. Since the jet may have experienced small realignments during the wing inflation phase, we infer a reorientation timescale of fewer than 50 Myr since jet ignition, well within the free-free cooling time of the $C_{\rm NW}$ walls and constrained by the wing $t_{\rm sync}$. Although it is possible that the system represents only a single spin-flip from the wings to the present location, this hypothesis does not not explain $C_{\rm NW}$ or $C_{\rm SE}$.

The presence of a stellar shell must be confirmed, and it is possible that $C_{\rm NW}$ and $C_{\rm SE}$ are not jet-blown cavities but rather part of a cocoon-evacuated shell (with bounding material describing a ring perpendicular to the jet) produced by a jet-ignition shockwave. The overlap of $C_{\rm NW}$ by the radio cocoon is then due to backflow filling the cavity. Assuming a circular ring, the eccentricity of the ring implies $\theta_{\rm LOS} \sim 60°$, far above the 30° required to reconcile the cocoon and wing lengths.

3.5 Context and Summary

There are few deep X-ray observations of XRGs. Apart from 4C +00.58, there is a $\sim$ 100 ks *Chandra* observation of NGC 326 and a 50 ks exposure of 3C 403 (Kraft et al. 2005). These data show X-ray emission on different scales and of differing surface brightness, forcing the hydrodynamic hypothesis to contend with a variety of environments. The cavities in 4C +00.58 also demonstrate that X-ray observations are useful beyond studying backflow models. Our prior survey Chapter 2 and this study suggest exposure times of at least 100 ks are required to examine detailed structure.

We know of no clean evidence for merger-induced reorientation. Even in our toy model, the wings are produced by merger-induced accretion rather than an instantaneous spin-flip, so the black hole merger itself would involve mostly-aligned spins (Bogdanović et al. 2007). Nonetheless, the presence of an apparent stellar shell suggests that searching for structure in the hosts of XRGs may provide strong indirect evidence for such mergers in a subclass of these objects.

We have presented a deep *Chandra* observation of the XRG 4C +00.58. The hot atmosphere is roughly co-spatial with the radio galaxy and has a temperature of $kT \approx 1.0 \pm 0.2$ keV. An X-ray jet of about 5 kpc is detected, overlapping well with the 5 GHz knots. We synthesize information from the radio and X-ray maps to assess three wing-formation models based on approximate limiting timescales and argue that the hydrodynamic scenario faces several difficulties whereas circumstantial evidence favors the reorientation model. Although 4C +00.58 does not obey the optical–radio correlation of XRGs (Capetti et al. 2002; Saripalli & Subrahmanyan 2009), confirmation of any of the wing formation scenarios would bear on XRG formation generally.

Chapter 4

Hydrodynamic Models of Radio Galaxy Morphology: Winged and X-shaped Sources

4.1 Introduction

Recently, X-shaped radio galaxies (XRGs)—a peculiar class of radio galaxies with two pairs of misaligned lobes (Ekers et al. 1978; Leahy & Parma 1992)—have received significant attention as new observations have explored and critiqued the competing models for the origin of their odd morphology. The distinctive "X" shape occurs due to the intersection of two centro-symmetric synchrotron-emitting structures at a common nucleus (e.g. Figure 4.1). One of these structures is associated with an active relativistic jet (the "primary" lobes) whereas the other is fainter, more ragged, and does not appear to harbor a jet (the "secondary" lobes or "wings"). The wings can be long, collimated, and symmetric about the nucleus, and may even exhibit Z-shaped morphology of their own (Gopal-Krishna et al. 2003). The origin of

the wings is not presently understood, but XRGs share other characteristics which indicate a common origin (Chapter 1).

A critical review of the observational data and existing models is found in Gopal-Krishna et al. (2010); here we briefly summarize the main threads. The origin of the secondary lobes has been attributed to (i) a rapid reorientation of the spin axis of the supermassive black hole (SMBH) powering the jet (i.e., the wings are fossils), either due to a SMBH merger (e.g. Merritt & Ekers 2002; Rottmann 2001; Zier & Biermann 2001) or rapid precession (e.g. Dennett-Thorpe et al. 2002); (ii) redirection and collimation of "backflow" (spent jet plasma flowing back from the terminal shocks) (Capetti et al. 2002; Kraft et al. 2005; Leahy & Williams 1984; Worrall et al. 1995); (iii) a binary AGN (Lal & Rao 2007); and (iv) interaction of the jet with disturbed morphology (e.g. stellar shells, phase-wrapped remnants of a merged disk galaxy; Gopal-Krishna et al. 2010). Since XRGs are usually strongly bridged sources and are apparently aware of their environments, it is worth examining closely the hypothesis that the X-shaped morphology originates from an interaction between the radio galaxy and its environment. In this Chapter, we seek to test the viability of the *backflow model* with three-dimensional hydrodynamic simulations in elliptical atmospheres.

In the backflow model, wings are produced by a single AGN outburst with powerful jets as the backflow is diverted along the steepest pressure gradient of the surrounding atmosphere (i.e., the minor axis). The wings either rise buoyantly or are driven in this direction (Kraft et al. 2005; Leahy & Williams 1984; Worrall et al. 1995) or form as supersonic outflows along the direction of least resistance from a ruptured overpressured cocoon (Capetti et al. 2002; Zanni et al. 2003). These scenarios naturally explain the observed correlation between the wings and the minor

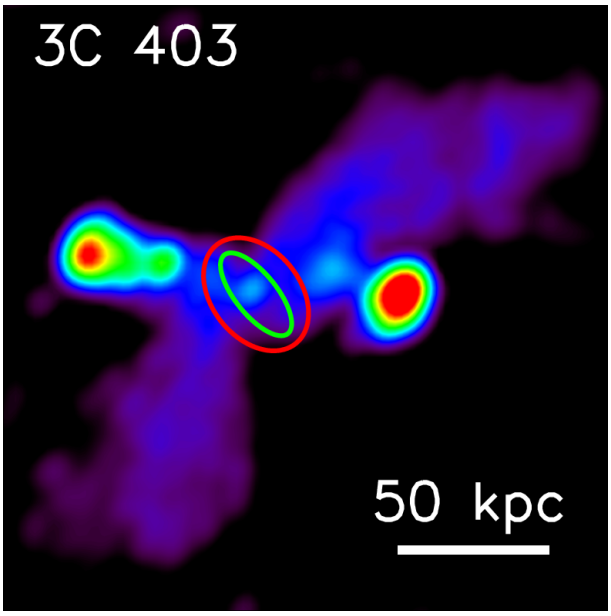

Figure 4.1 3C 403, a typical XRG showing long, faint wings emanating from the same core as the edge-brightened lobes (east–west axis). The red and green ellipses have the ellipticity and position angle of the host galaxy and ISM (from Kraft et al. 2005) respectively (not to scale).

axis of the host galaxy as well as the dearth of strictly FR I XRGs (the weaker FR I sources do not produce powerful back-flows). However, the backflow model faces significant challenges, most notably the very long wings in many XRGs (often longer than the primary lobes). Whereas powerful jets are expected to drive through the surrounding medium supersonically, wings which expand buoyantly would do so at most transonically for most of their lives (Leahy & Parma 1992).

Because, in this model, fluid effects are primarily responsible for the "X" shape, hydrodynamic simulations are an ideal proving ground. Although recent hydrodynamic simulations of radio galaxy morphology exist in the literature, (e.g. Falceta-Gonçalves et al. 2010; Gaibler et al. 2011; Sutherland & Bicknell 2007), most are not concerned with the formation of lateral asymmetries such as wings. In view of advances in simulating radio galaxies in the past decade, the mounting evidence that XRGs constitute a population demands a critical look at the backflow model

with new simulations. In this Chapter, we discuss 3D hydrodynamic models of radio galaxies ignited in initially relaxed, elliptical atmospheres and examine how wings form.

We begin by discussing our simulation setup and strategy for exploring wing production in Section 4.2, then present our model runs and describe the evolution of a generic winged source in Section 4.3. In particular, we find that favorable pressure gradients are necessary but not sufficient to produce an X-shaped source; the character and time evolution of the jet is equally important. In Section 4.4, we briefly discuss the missing and artificial physics in our simulations, and in Section 4.5 we assess the backflow model in view of our results as well as discuss the implications for the broader picture of radio lobe morphology. Finally, in Section 4.6 we summarize our main results and conclusions.

Throughout this Chapter we use the terms "secondary lobes" and "wings" interchangeably. We also use the term "winged" source to refer to any radio source with substantial symmetric off-axis distortions whereas "X-shaped" sources are a subset of winged sources with an axial wing-to-lobe length ratio of more than 0.8. This nomenclature reflects the view of the hydrodynamic model in which XRGs are indeed a subset of a broader category of distortions. Finally, we use the term "backflows" to refer specifically to actual fluid flows heading back to the nucleus from the jet heads, whereas we use "backflow" to refer to the material in these flows.

4.2 Hydrodynamic Simulations

We use a parallelized version of the ZEUS code (Stone & Norman 1992a,b) for our hydrodynamic simulations. ZEUS is a second-order (spatial accuracy) Eulerian finite-differencing magnetohydrodynamic (MHD) code which solves the standard

equations of hydrodynamics,

$$\frac{\partial \rho}{\partial t} + \nabla \cdot (\rho \mathbf{v}) = 0 \tag{4.1}$$

$$\frac{\partial \mathbf{v}}{\partial t} + \mathbf{v} \cdot \nabla \mathbf{v} = -\frac{\nabla P}{\rho} - \nabla \Phi \tag{4.2}$$

$$\frac{\partial}{\partial t}(\rho e) + \nabla \cdot (\rho \mathbf{v} e) = -P \nabla \cdot \mathbf{v}, \tag{4.3}$$

for an ideal compressible fluid and introduces artificial viscosity for shocks, where ρ is the fluid density, v is its velocity, P its pressure, e is the internal energy of the fluid, and Φ is the (external) gravitational potential. The version we use, ZEUS-MPv2, is based on the National Center for Supercomputing Applications (NCSA) code described in Hayes et al. (2006). We use spherical polar coordinates (r,θ,ϕ) in the purely hydrodynamical mode for all our runs; the jets are therefore injected from an inner boundary sphere with some small, but finite, radius $r_{\rm inner}$. We outline our basic simulation setup below, followed by our strategy for exploring winged sources and a description of the evolution of a standard double-lobed source for comparison.

4.2.1 Simulation Setup

Hydrodynamic and MHD simulations of radio galaxies interacting with their surroundings are common due to the possibility that energy deposited by the lobes is a mode of heating in AGN feedback scenarios. We do not incorporate relativistic jet physics since we are primarily concerned with lobe mixing and evolution, but the robustness of this assumption is explored in Section 4.4.1. We note here that non-relativistic, light, hypersonic hydrodynamic jets reproduce several essential features of jets. These include recollimation shocks, terminal shocks at the jet head (associated with radio "hot spots") and back-flows of spent material from the terminal shocks which sheath the jet and produce lobes. Since we are interested in the evolution of back-flowing fluid in anisotropic environments, we adopt a non-relativistic

purely hydrodynamic scheme.

We inject the jets as bi-directional flows into an initially hydrostatic, ellipsoidal atmosphere. The atmospheres we set up are ellipsoids with a polytropic equation of state ($\gamma = 5/3$) and a 3D β-model density profile (Cavaliere & Fusco-Femiano 1976) given by

$$\rho = \frac{\rho_0}{(1 + (r/r_0)^2)^{3\beta/2}}, \tag{4.4}$$

where $\beta = 0.5$, r_0 is the core radius, and ρ_0 is the core density. To adapt this model for elliptical atmospheres, we make the radial density profile dependent on angle by adding a major-axis position angle P.A. and ellipticity ϵ to the atmosphere, which we denote as r_e for an elliptical atmosphere. To easily allow for triaxial atmospheres, we define the ellipsoid in Cartesian space (x_e, y_e, z_e) and break up ϵ along each axis, then transform back to spherical coordinates to obtain the radius r_e using the grid coordinates (r, θ, ϕ):

$$r_e = \frac{\sqrt{x_e^2(1-\epsilon_x)^2 + y_e^2(1-\epsilon_y)^2 + z_e^2(1-\epsilon_z)^2}}{(1-\epsilon_{\max})} \tag{4.5}$$

$$x_e = r\sin(\theta)\Big[\cos(\phi)cos(\text{P.A.}) + \sin(\phi)\sin(\text{P.A.})\Big] \tag{4.6}$$

$$y_e = r\sin(\theta)\Big[\sin(\phi)cos(\text{P.A.}) - \cos(\phi)\sin(\text{P.A.})\Big] \tag{4.7}$$

$$z_e = r\cos(\theta)\Big[\cos(\text{P.A.}) + \sin(\text{P.A.})\Big], \tag{4.8}$$

where P.A. is nominally measured counter-clockwise from the z-axis (in practice, it is only the difference between the jet axis and the major axis of the ellipsoid that matters). To normalize the size of the atmosphere, $\epsilon_{\max}$ in Equation 4.5 is defined as the largest value of ϵ along each axis. For example, an atmosphere with large ϵ_z is elongated along the z-axis. Equations 4 and 5 may be understood as saying that introducing ϵ changes the effective core radius along a given axis: $r_{0,\text{eff}} = r_0(1-\epsilon_{\max})/(1-\epsilon)$. For example, if $\epsilon_{\max} = \epsilon_z = 0.75$, $\epsilon_x = 0.0$, and $r_0 = 1.0$,

then along the z-axis $r_{0,\rm eff} = 1.0$ and along the x-axis $r_{0,\rm eff} = 0.25$. This phrasing is convenient when comparing the major and minor axes rather than the quantities along the full range of angles θ and ϕ and we use it hereafter.

The atmospheres are initially set up in hydrostatic equilibrium,

$$\nabla\Phi = \frac{1}{\rho}\nabla p, \tag{4.9}$$

assuming that the background dark matter potential is static and dominant so that the gas self-gravity is not important. We define the adiabatic sound speed $c_s \equiv 1.0$ in code units and set up an isothermal atmosphere so the potential Φ is

$$\Phi = \frac{c_s^2}{\gamma}\ln(\rho). \tag{4.10}$$

Since XRGs are powerful radio galaxies and exist at low redshift, we assume a smooth intergalactic/intracluster medium (IGM/ICM) and gas-poor systems, i.e., no disk of colder (i.e., atomic or molecular) material in the host (cf. Sutherland & Bicknell 2007). We note that in several exploratory runs, additional atmospheric complexity is overlaid onto a smooth atmosphere with no change in the gravitational potential Φ, i.e., not initially in hydrostatic equilibrium.

The jets in our simulations are hypersonic ($\sim 100 c_s$) light ($\rho_{\rm jet} \sim 0.01\rho_0$) flows injected in pressure equilibrium with the ambient material from back-to-back circular footpoints on the small inner boundary sphere at the origin. Ignoring higher-order contributions from the gravitational energy or thermal flux, the kinetic luminosity of the jets is given by

$$L_{kin} \sim \tfrac{1}{2}\rho_{\rm jet} v_{\rm jet}^3 A_{\rm jet} \tag{4.11}$$

where $A_{\rm jet}$ is the area of the footpoint at $r_{\rm inner}$. To tune $L_{\rm kin}$ we primarily vary $v_{\rm jet}$ because (i) $L_{\rm kin}$ is most sensitive to changes in $v_{\rm jet}$, (ii) the jets must be "light" to ensure that the Kelvin-Helmholtz instability growth rate at the boundary of the cocoon is approximately the same as in the relativistic case (Reynolds et al. 2002),

and (iii) jets are highly collimated. The maximum jet width is constrained by high-resolution X-ray observations of jet knots (e.g. Perlman & Wilson 2005) and very long baseline interferometry observations of transverse structures (e.g. Gabuzda et al. 2004). However, we note that in Section 4.3.2 we vary $\rho_{\rm jet}$ and $A_{\rm jet}$ in a limited range.

We insist that the jet cover enough grid zones ($\sim$ 30) to resolve transverse structures such as the oblique shocks which collimate the jet. The jet is rapidly precessed around a small angle ($\alpha < \theta_{\rm jet}$) at 20π rad s^{-1} (code time) to break the axisymmetry of the simulation setup and approximate the action of helical instabilities, thus spreading the thrust out over a larger working surface (cf. Heinz et al. 2006; O'Neill & Jones 2010; Sutherland & Bicknell 2007; Vernaleo & Reynolds 2006). The location of the jet on the inflow sphere is thus given by $(\theta, \phi) = (\alpha, \Omega_{\rm jet} \cdot t)$. Although the angular quantities are free parameters, they are constrained by the observed collimation of jets. Typical values are $\theta_{\rm jet} = \pi/7.5$ and $\alpha = \pi/60$ for $r_{\rm inner} = 0.05$. In agreement with other work, these jets develop a cylindrical core of fast-moving material sheathed in a slower concentric shell continuous at the boundaries with the surrounding material and core.

We use a grid with zones spaced according to a geometric series in r and θ (256 bins each) and uniformly in ϕ (64 bins). This grid resolves the internal jet structure and important processes near the injection footpoints. We choose $r \in [0.05, 5.0]$ and $\theta \in [0.01, 3.13]$ to avoid the polar singularity and begin with reasonably sized grid zones. The θ grid is broken into two symmetric 128-bin components with the smallest zones near the poles where the jets are injected. The adequacy of our grid is demonstrated by a run with double the resolution in each direction which produces similar internal jet structure and mixing which is not substantially different at the lobe boundaries.

We use periodic boundary conditions in the ϕ direction and reflecting boundary conditions in θ. The outer r boundary at $r = 5.0$ has outflow conditions (material leaving the grid); likewise, outflow conditions exist for all $r_{\rm inner}$ zones except where the jets are injected. The outer boundary is far from the jet activity so negligible material leaves the grid there. We discuss the importance of the inner boundary sphere in Section 4.4.

Code units are transformed to physical units by choosing appropriate values for r_0, c_s, and ρ_0. For instance, Reynolds et al. (2002) defined $r_0 = 100$ kpc, $c_s = 1000$ km s^{-1} and $\rho_0 = 0.01 m_{\rm H}$ g cm^{-3} for a rich cluster and $r_0 = 10$ kpc, $c_s = 500$ km s^{-1} and $\rho_0 = 0.1 m_{\rm H}$ g cm^{-3} for a group or poor cluster. In the former scheme a code unit of time (derived from the crossing time) corresponds to 50 Myr and in the latter 10 Myr. In our runs, we vary r_0 and ρ_0 but fix c_s; a value of $c_s \sim 500$ km s^{-1} appears appropriate for XRGs based on temperatures derived from spectral fitting (Hodges-Kluck et al. 2010a; Landt et al. 2010). A jet injected at $100 c_s$ would then have a physical speed between $0.17c - 0.35c$ (a Lorentz factor of $\gamma \sim 1.01 - 1.05$). However, as noted by Komissarov & Falle (1996), comparing classical and relativistic jet simulations requires careful matching of parameters, in particular the mass-energy density content of the jet. Hence, the jet velocities chosen should not be taken directly as assumptions of true jet velocity.

Our runs were parallelized and used variety of processors. Many of the runs were conducted on quad-core Intel® Core™ 2.4 and 2.83 GHz workstations.

4.2.2 Strategy

We now outline our guiding strategy to determine whether X-shaped sources can result from the interaction of radio galaxy lobes with their environment.

First, we only model powerful FR II sources which produce strong back-flows. Neither the physical origin of the FR I/II dichotomy nor the differences between jets in radio loud and radio quiet sources are understood, but the higher luminosity FR IIs exhibit the hot spots, well defined lobes, and bridges exploited by the backflow model.

In accordance with the observations (Capetti et al. 2002; Hodges-Kluck et al. 2010a; Saripalli & Subrahmanyan 2009), we inject jets along the major axis of the surrounding atmosphere. We first use unrealistic atmospheres with very favorable pressure gradients for wing production (as in Capetti et al. 2002), then explore jet and atmosphere parameters to study the production and characteristics of XRGs. In particular, we explore the dependence of wing formation on jet width, density, and kinetic luminosity as a function of time, and initial atmosphere parameters (core radius, density, ellipticity, and position angle). Although some parameter combinations are degenerate, this is a very large parameter space because the $L_{\rm kin}(t)$ may include dead time and intermittency. Compared to 2D modeling, our 3D simulations eliminate the requirement of axisymmetry which enhances the jet head advance speed (Bodo et al. 1998) and the coherence of the back-flows. The effect of turbulence is also more realistically explored in three dimensions.

Motivated by the expectation that pressure gradients affect the wings fundamentally the same way in different systems, we start from the ansatz that jet and atmospheric parameters are orthogonal. In other words, the jet parameters may be tuned in some fiducial atmosphere and the atmosphere parameters may be tuned

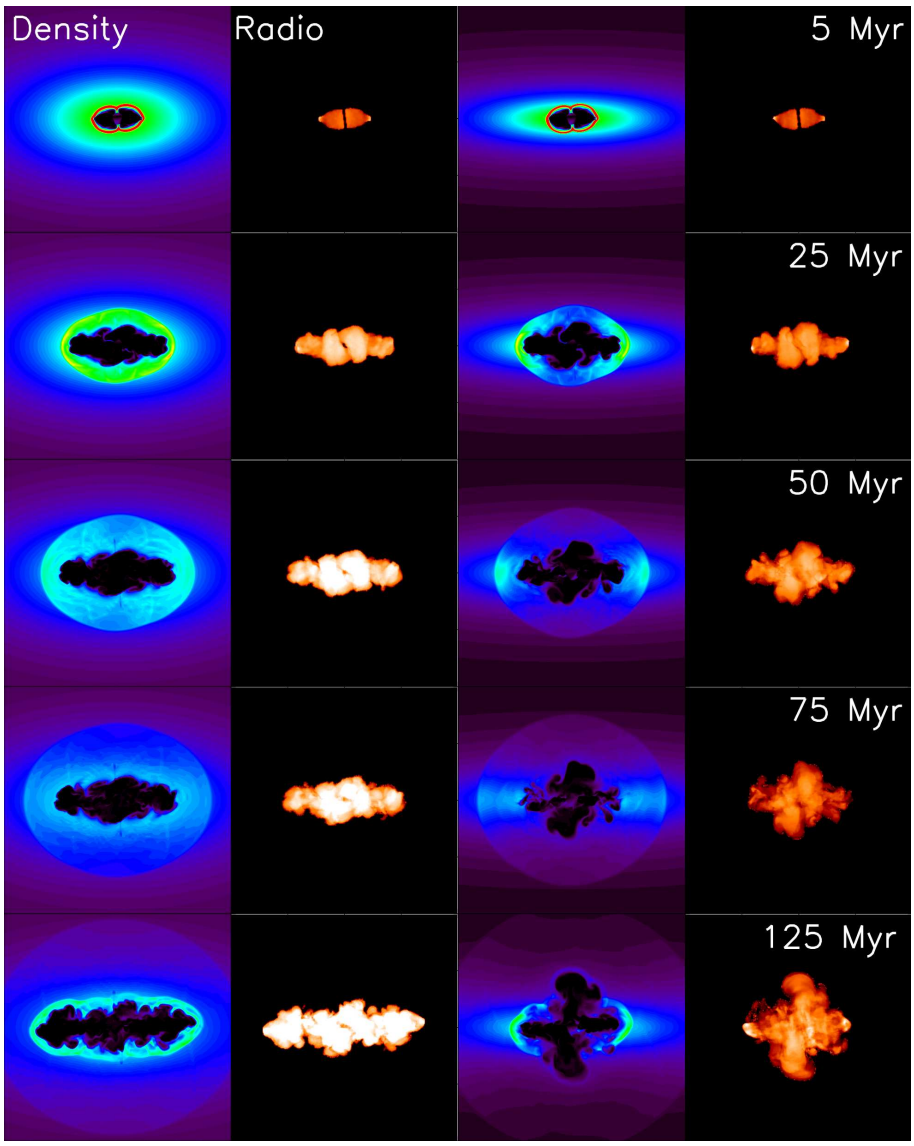

Figure 4.2 Comparison of a normal (left panels) and winged (right panels) radio source using the same jet ($v_{\rm jet} = 100\exp[-3t]$) in atmospheres differentiated only by ϵ. Note the size of the overpressured cocoon relative to the size of the atmosphere in the top panels. At a code time of 1.0 (100 Myr) the jet was restarted ($v_{\rm jet} = 100\exp[-3(t-1.0)]$). The colorbars are the same in each image; the integrated radio is brighter for the normal source because the winged source has the same amount of material spread out over more volume.

with some fiducial jet such that the behavior of an arbitrary jet in an arbitrary atmosphere can be inferred. On the basis of this method we will evaluate the factors key to wing prominence and the viability of the backflow models.

4.2.3 Hydrodynamic Models of Powerful Double-Lobed Radio Galaxies

If wings are distortions to a generic double-lobed source, we expect our simulated radio galaxies to strongly resemble the double-lobed sources produced by earlier models. Hydrodynamic and MHD models of jets are commonly employed to study either the phenomenology of the jets and lobes (with relativistic and nonrelativistic fluids) or the energy deposited by the lobes into their environment. Hence, a large body of work concerned with phenomenological models of these sources exists and has produced key insights into the life of a powerful radio source.

These studies include work on early jet/lobe evolution in a relaxed atmosphere (e.g. Antonuccio-Delogu & Silk 2010; Krause 2005), the influence of the $\rho_{\rm jet}/\rho_0$ density contrast and internal Mach number (e.g. Carvalho & O'Dea 2002a; Krause 2003; Vernaleo & Reynolds 2007), jet stability in nonrelativistic and relativistic conditions (e.g. Keppens et al. 2008; Mignone et al. 2010; O'Neill & Jones 2010; Rosen et al. 1999), the importance of intermittency (O'Neill & Jones 2010) or intrinsically spreading out the jet thrust to slow the advance of simulated jets (e.g. Heinz et al. 2006), the importance of the jet environment to morphology or energy deposition (e.g. Capetti et al. 2002; Carvalho & O'Dea 2002b; Falceta-Gonçalves et al. 2010; Gaibler et al. 2011; Kawakatu et al. 2009; Krause 2005; Simionescu et al. 2009; Vernaleo & Reynolds 2007; Zier 2005), and physics beyond MHD (e.g. Saxton et al. 2010). Naturally, there is overlap between the phenomenological studies and those motivated by the challenge to produce jets which prevent a cooling catastrophe in the ICM of a host galaxy cluster by isotropizing energy distribution. The viability of radio galaxies as AGN feedback mechanisms is beyond the scope of this work, but jet lifetime and the passive evolution of "dead" radio galaxies (Reynolds et al. 2002) place important constraints on wing prominence.

Based on this work, we understand a powerful double-lobed source to have three distinct phases of evolution: (i) *ignition*, in which a spheroidal cocoon of relativistic plasma is formed around the nascent jets, (ii) the *active phase*, wherein the jet produces the cigar-shaped lobes associated with FR II radio galaxies, and (iii) the *passive phase* where lobes evolve after the jet is turned off. Below we outline these phases for a preliminary hydrodynamical simulation of a fast ($v_{\rm jet} = 100c_s \exp(-3t)$), light jet with large $L_{\rm kin}$ (a "FR II" source) to provide a framework for discussing the evolution of winged sources (left-hand panels of Figure 4.2). We note that Belan et al. (2011) have recently found good agreement between the structures observed in hydrodynamic simulations of hypersonic jets and laboratory experiment.

Ignition The jet is injected in pressure equilibrium with the initially relaxed surrounding medium. The flow quickly forms and drives a spheroidal bow shock into the surrounding medium (Figure 4.2, top left panel). At the location where the jet impacts the shock, back-flows develop which fill the space evacuated by the bow shock with light, hot spent jet plasma. This plasma forms a cocoon which sheaths the jet. At very early times the jet expands laterally, since it is unconfined by the cocoon plasma (in part due to the initially conical shape of the jet) and the expansion of the nascent radio galaxy is nearly self-similar (Carvalho & O'Dea 2002a; Krause 2005). However, as a result, the early back-flows acquire a circulatory motion and flow along the inner edge of the bow shock (Figure 4.3, top panel). By the time these flows reach the midplane between the two jets, they have velocity vectors pointing radially inwards and do not collide with back-flows from the counter-jet (Antonuccio-Delogu & Silk 2010). In our models, the back-flows are also prevented from interacting with their counterparts from the counter-jet because our jets are injected into pristine atmospheres such that at very early times, each jet inflates its

own cocoon. The two cocoons are both bounded by a bow shock, and the two shocks meet at the midplane between the jets and form an interstice of dense material that prevents early mixing (Figure 4.3, top panel). Whether such an interstice is present in real sources is not clear (we do not resolve the very earliest jet stages such as the "flood-and-channel" phase seen in a clumpy, warm disk in Sutherland & Bicknell 2007), but the interstice is ablated and the cocoon is unified by the active phase.

As the cocoon pressure builds due to backflow confined by the bow shocks, the jet becomes azimuthally confined and a recollimation shock appears near the injection point; by the end of the ignition phase, the cocoon is strongly overpressured relative to its environment. At the same time, the terminal shock becomes increasingly distinct from the bow shock, and the jet head takes on the characteristic double-pronged appearance of a 3D hydrodynamical jet. While the back-flows still follow the bow shocks during the late ignition phase, they are increasingly straight. We note that this early evolution is seen in all our runs and does not depend much on atmosphere or jet parameters, nor on the boundary conditions (as long as the core radius of the atmosphere r_0 is much larger than $r_{\rm inner}$).

Active Phase When the jet head overtakes and pierces the initial bow shocks (driving a bow shock contiguous with the initial burst; Krause 2005), the active phase begins and a classical radio galaxy develops, with a cigar-shaped cocoon, hot spots, bow shocks (middle-left panels of Figure 4.2), and straight back-flows (Figure 4.3, bottom panel). At this point, the cocoon ceases to be substantially overpressured and the cocoon's lateral expansion falls close to the sound speed of the ambient medium, lagging behind the bow shock (the cocoon expands due to buoyancy, Kelvin-Helmholtz, and Rayleigh-Taylor instabilities). This weak shock ($v_{\rm shock} \sim 1.5 c_s$) sweeps up a large amount of material as it expands and becomes

better described as a strong sound wave (Figure 4.2). Meanwhile, the jet develops internal oblique collimating shocks along its length, retaining a high velocity out to the terminal shock at the jet head (i.e., the angular size of the jet decreases with increasing radius) where the cocoon becomes momentum-driven. Less powerful jets do not produce cocoons (Vernaleo & Reynolds 2007), but we focus on the cocoon-bounded case (the cocoon pressure also depends on the internal Mach number; Carvalho & O'Dea 2002a).

Passive Phase Once the jets are turned off, the back-flows cease and the "dead" radio lobes rise buoyantly in the atmosphere, lifting large amounts of material to great heights and mixing with the surrounding medium (Reynolds et al. 2002). Although the radio galaxy is relatively efficient at depositing its energy irreversibly in the surrounding medium, it is difficult to isotropize this energy deposition on short enough timescales to avoid cooling catastrophes (e.g. De Young 2010; Omma & Binney 2004; Omma et al. 2004; O'Neill & Jones 2010; O'Neill et al. 2005; Ostriker et al. 2010; Reynolds et al. 2002; Vernaleo & Reynolds 2006, 2007). The cocoon separates into bubbles which pinch off along the direction of the jets and rise in opposite directions; the evolution of these bubbles may be quite complex (e.g. Begelman 2001; Braithwaite 2010; Churazov et al. 2001; Dong & Stone 2009; O'Neill et al. 2009; Pope et al. 2010; Ruszkowski et al. 2007). This very late stage evolution is unlikely to be important for winged radio galaxy evolution, as winged galaxies appear to be related to sources with strong bridges (Leahy & Williams 1984), and is not shown in Figure 4.2.

4.3 Results

With the scheme described in Section 4.2, we produce winged radio galaxies by the deflection of backflow into channels perpendicular to the jets. In our models, wings are produced in strongly asymmetric atmospheres when the jet is driven near the major axis; the wings are produced along the minor axis as cocoon material escapes the central regions of the atmosphere and evolve buoyantly, collimated by the surrounding stratified atmosphere which promotes expansion along the steepest pressure gradient. Hence, these wings are similar to those produced by Capetti et al. (2002) and Zanni et al. (2003). Without introducing additional complexity to the atmosphere, hydrodynamic wings are formed in two stages. First, during the ignition phase (Section 4.2.3), the overpressured cocoon expands faster along the minor axis due to the steeper pressure gradient and forms small channels ("proto-wings") perpendicular to the jet into which back-flowing plasma flows. The proto-wings produced in this way can account for 20–40% of wing length at the end of the active phase depending on the gradient. Second, during the active phase, the wings rise buoyantly, fed by turbulent flows near the midplane. Although the back-flows near the jet heads are initially laminar and supersonic (relative to the lobe material), they quickly decelerate and do not enter the wings as coherent flows; the wings expand subsonically.

During the active phase the wings evolve almost independently of the cocoon. Hence, once wings have developed, their length depends only on the properties of the native atmosphere whereas the length of the jet-fed primary lobes is dominated by the properties of the jet (in particular the kinetic luminosity as a function of time) for powerful jets. Therefore, *decaying* jets produce prominent wings (i.e., wings that are long compared to the primary lobes).

In this section, we explore these ideas in detail, first comparing the life of a winged source to a canonical double-lobed one (Figure 4.2) and then looking at the dependence of wing prominence and longevity on various tunable parameters in our models.

4.3.1 Evolution of a Winged Source

Winged galaxies experience the same life stages outlined in Section 4.2.3. We describe how wings fit into this process in detail below, referencing our standard (extremal) atmosphere (Run `STANDARD`, Tables 4.1 and 4.2). While unrealistic in terms of ellipticity and relaxation, this atmosphere provides important insights into the backflow model and can be directly compared to prior work (Capetti et al. 2002; Zanni et al. 2003).

Ignition During the ignition phase of a winged source, the anisotropic expansion of the overpressured cocoon in an aspherical atmosphere produces channels which will later become the wings (the proto-wings). This pressure-driven expansion is supersonic but brief, since the cocoon quickly reaches pressure equilibrium. Although these channels need not be produced by an overpressured cocoon, some channels must exist for wings to form.

The degree of cocoon expansion in a given direction depends on the pressure gradient experienced in that direction, and hence on the atmospheric parameters. In particular, the eccentricity of the atmosphere effectively changes the core radius r_0 seen by the cocoon in different directions. For example, along the x-axis ($r\hat{x}$; the jet is driven along $\hat{z}$) Equation 4.4 gives:

$$\frac{\partial p}{\partial x} = -\frac{3}{2}\frac{c_s^2}{\gamma}\rho_0 r_{0,\mathrm{eff}}^{3/2}\frac{x}{(x^2 + r_{0,\mathrm{eff}}^2)^{7/4}}. \tag{4.12}$$

Since the pressure gradient is steeper for smaller $r_{0,\mathrm{eff}}$, higher ellipticity along other

axes promotes wing expansion: for $\epsilon_x = 0.0$ and $\epsilon_z = \epsilon_{\rm max} = 0.75$, $r_{0,\rm eff} = 0.25 r_0$ along the x-axis. Conversely, if $\epsilon_x = \epsilon_{\rm max} = 0.75$ and $\epsilon_z = 0.0$ (the jet is pointed along the minor axis), $r_{0,\rm eff} = r_0$ and wings are suppressed. Of course, wing expansion depends on the actual pressure gradients rather than just the ratio along different axes; the base values r_0 and ρ_0 determine whether wings can form (i.e., a highly elliptical atmosphere can have shallow pressure gradients along the minor axis if it is very large). Note that at very small radii $r \ll r_{0,\rm eff}$ (i.e., during the ignition phase), the pressure gradient steepens linearly with increasing r and at large radii (during the active phase, see below) the pressure gradient becomes shallower as $r^{-1/2}$. Hence, the ignition phase is the time at which atmospheric asymmetry has the strongest effect on the ultimate morphology of the source.

Active Phase Once the cocoon has reached pressure equilibrium, the proto-wings are no longer pressure-driven. As the back-flows become straight, they merge and fill the channels (Figure 4.3, bottom panel) to form structures more closely resembling observed wings. However, the flows into the wings are turbulent and transonic or subsonic (relative to the internal lobe sound speed $c_{s,\rm lobe} = 10 c_s$). In other words, wings are not *driven* during the active phase. Rather, because they are structures filled with light fluid, they rise buoyantly in the atmosphere, collimated by the stratified elliptical atmosphere.

Since the wings rise buoyantly, their growth rate is subsonic. To see this, it is instructive to look at the simplified case of a spherical bubble (of fixed radius) rising buoyantly in a dense fluid. The (terminal) buoyant velocity at a given height for such a bubble is

$$v_{\rm buoy} = \sqrt{\frac{2 g V_{\rm b}}{C_D A_{\rm b}}} = c_s \sqrt{\frac{16}{3\gamma} \frac{r_{\rm b}}{r_{0,\rm eff}^2} \frac{r}{1 + (r/r_{0,\rm eff})^2}} \tag{4.13}$$

where $V_{\rm b}$, $A_{\rm b}$, and $r_{\rm b}$ are the volume, cross-sectional area, and radius of the bubble

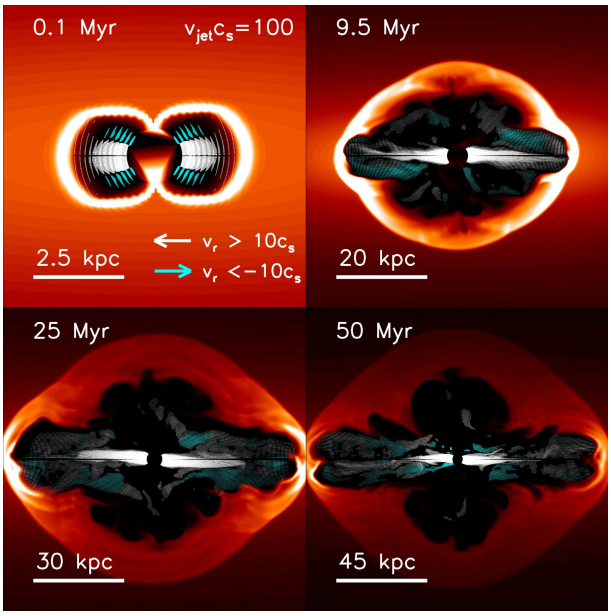

Figure 4.3 We show here v_x and v_y velocity vectors overlaid on density slices (taken at $\phi = 0$) at different times for the simulation TX_E75_VE3_B5.0 (Table 3). We have chosen (arbitrarily) $c_s = 500$ km s^{-1} and $r_0 = 50$ kpc (corresponding to a code $r_0 = 2.0$) to represent a large elliptical galaxy. White vectors point radially outwards and cyan vectors point radially inwards (i.e., the back-flows). Vectors are only shown when the magnitude of v exceeds the sound speed of the lobe material ($c_{s,\mathrm{lobe}} = 10c_s$). Note that early on, the back-flows follow the contact discontinuity and are directed towards the inner boundary, but later become straight as in Antonuccio-Delogu & Silk (2010).

respectively, $C_D = 0.75$ is the "drag" coefficient, and we have used the background dark matter potential Φ to compute g in terms of r and effective core radius $r_{0,\mathrm{eff}} = r_0(1-\epsilon_{\mathrm{max}})/(1-\epsilon)$. Naturally, this follows the pressure gradient (Equation 4.12), so when the bubble is at very small radii its velocity *increases* as $r^{1/2}$, whereas outside $r_{0,\mathrm{eff}}$ it *decreases* as $r^{-1/2}$. For typical values in our simulations, the peak value of v_{buoy} is approximately c_s. Hence, in a highly elliptical atmosphere, a bubble rising along the minor axis will rise subsonically with decreasing velocity for most of its lifetime.

The simulated wings do not fit this simplified case because they are large relative to $r_{0,\mathrm{eff}}$, variable in size, aspherical, and connected to the cocoon. Nonetheless,

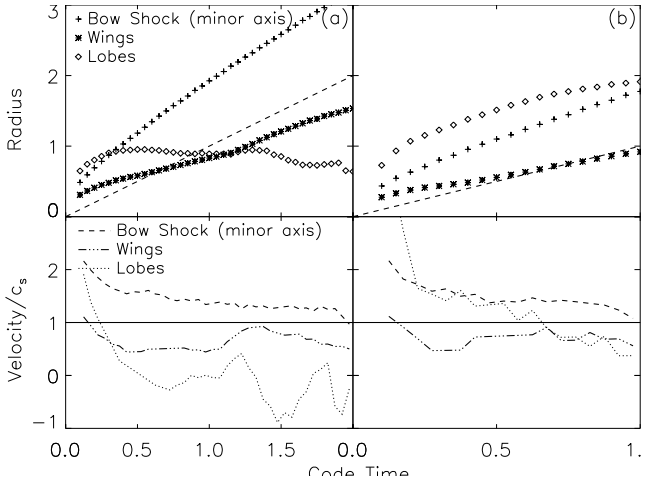

Figure 4.4 Positions and velocities of the leading edges of the bow shock, wings, and lobes shown for (a) the standard simulation and (b) a triaxial simulation. The dashed line in the top panel shows the position of a point moving radially outwards at the sound speed. Note the different x-axes; at $t = 1.0$ in the left panels, a new jet is reinjected. *Negative* growth for the lobes indicates collapse during the passive phase.

their expansion is subsonic for the same reason: the wings exceed $r_{0,\mathrm{eff}}$ early on when their growth is pressure-driven rather than buoyant, and v_{buoy} monotonically declines thereafter. This transition from supersonic to subsonic wing expansion is plainly seen in Figure 4.4.

Therefore, wings in our models may not intrinsically exceed the length of the primary lobes unless the primary lobes advance at some average speed $\bar{v}_h < c_s$. Since powerful jets are required to produce the proto-wings in an overpressured cocoon phase, prominent wings require decaying jets, intermittent jets, or jets which deposit their thrust over an increasingly large area with time. The profile of the fiducial run is shown along with its wing prominence in Figure 4.5 and compared to a triaxial atmosphere in Figure 4.4. Note that in the fiducial run (left panel of Figure 4.4) the wings eventually overtake the lobes (in part due to the collapse of the lobes when the jet is very weak), but clearly move into a subsonic regime early and remain there. The bow shock remains mildly supersonic through most of both simulations.

In Figure 4.6 we show wings produced by decaying jets during the active phase in several environments (the fiducial run is shown in the top row).

Passive Phase Once the jets are turned off, the cocoon disintegrates as the lobes either rise buoyantly as bubbles or collapse under the relaxing atmosphere. If the radio galaxy is within a few r_0 in a dense atmosphere, the fall-back of displaced material shreds the lobes into small bubbles. In either case, the wings pinch off and rise. These bubbles do not survive long, but their behavior might be substantially altered in the presence of magnetic fields (e.g. Braithwaite 2010; O'Neill et al. 2005; Pope et al. 2010). Because observed winged sources have strong bridges, we expect them to be in the active phase.

Reinjection A powerful jet reignited during the passive phase before the cocoon has disintegrated may significantly enhance the wings. If the old jet channel is somewhat broken up, the reinjected jet forms a new terminal shock and bow shocks *inside* the old cocoon. These new shocks do not form spheroidal structures (as in a relaxed atmosphere) but instead produce strong, straight back-flows near the midplane. Hence, the wings receive a large influx of fresh supersonic plasma directly after reinjection (Figure 4.2, bottom panels). This brightens the wings substantially and reinforces their structures.

There is a relatively narrow window of time where this process is effective. If the reinjection occurs while the jet channels are largely intact (i.e., during the active phase), the jet simply follows these channels. On the other hand, if the reinjection occurs when the wings have already separated from the lobes as individual bubbles, the new jet cannot feed them. Even if the reinjection occurs at the "right" time, the efficacy of the restarted jet at promoting wings is short-lived. However, this mechanism can produce wings that are intrinsically *longer* than the jet-driven lobes

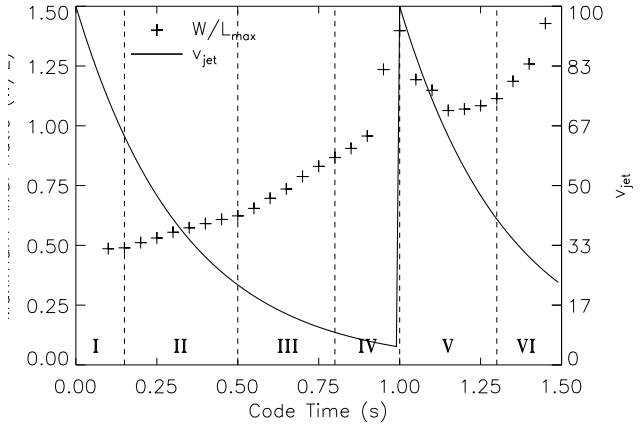

Figure 4.5 Plot of $W/L_{\max}$ (crosses) in timestep intervals of $\delta t = 0.05$ for the standard simulation with a reinjection at $t = 1.0$. We have overplotted the velocity of the jet as the black line (right y-axis). The Roman numerals indicate (I) the overpressured cocoon phase, (II) the active phase (powerful jet), (III) the active phase (weak jet), (IV) the passive phase (with cocoon collapse), (V) a second active phase due to the reinjected jet, and (VI) the second passive phase with further cocoon collapse. During cocoon collapse, the source does not resemble a winged source (instead it is a "dead" radio galaxy). A source appears winged during the active phase when the jet is most like a weak FR II or strong FR I.

(Figure 4.2, bottom panels). If the reinjected jet decays, this extreme axial ratio can be maintained for most of the lifetime of the restarted radio galaxy and a bona-fide X-shaped source results, although this source would only have the "FR II" primary lobes for a short period of time (~ 5 Myr for a source 40 kpc across).

4.3.2 Ecology of Winged Sources

In Section 4.3.1, we describe the life stages of a winged radio source. We now describe the dependence of wing prominence on our tunable parameters. Following the strategy laid out in Section 4.2.2, we begin with the fiducial simulation `STANDARD` which is characterized by an atmosphere with a large ellipticity ϵ and a jet with a

velocity profile $v_{\rm jet} = 100 c_s \exp[-3t]$ (Figures 4.2 and 4.4). Taking the jet from the fiducial run, we individually vary parameters in the atmosphere in order to see their influence on wings (Figure 4.7, Table 4.1), and then vary jet parameters in the fiducial atmosphere (Figure 4.8, Table 4.2). We then synthesize the information gleaned from these single-parameter curves to attempt to find atmospheres and jets which can explain real winged sources, including more complex behavior as well (Table 4.3). All of the runs proceed to a code time of 1.0 or more, where most have entered the passive phase. Reinjections, where used, occur near the beginning of the passive phase.

To quantify wing prominence we use the wing-to-lobe axial ratio (W/L). This quantity is an imperfect measure because W/L intrinsically varies with azimuthal

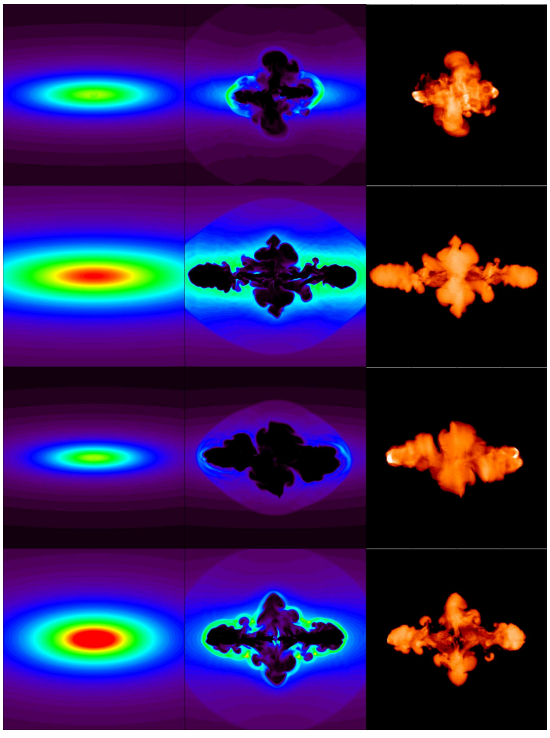

Figure 4.6 Examples of different intrinsic wing morphology. Left: Initial relaxed atmosphere density. Center: Winged sources during the late active phase. Right: False synchrotron maps ($j_\nu \propto p/\rho^{7/4}$ assuming equipartition) of these sources.

angle ϕ and time, and observable sources are seen in projection so the observed W/L will differ from the intrinsic value. W/L is also essentially meaningless during ignition or the passive phase, but a source in one of these stages would not be classified as "winged." For the parameter exploration in Figures 4.7 and 4.8 (values in Tables 4.1 and 4.2), we adopt as a fiducial value $(W/L)_{0.5}$: the maximum intrinsic W/L for any pair of azimuthal angles $[\phi,\phi+\pi]$ at a code time $t = 0.5$. For the standard jet ($v_{\rm jet} = 100c_s \exp[-3t]$), $t = 0.5$ represents the transition from a powerful to weak jet in the active phase, and by this time the wings have begun to grow buoyantly. Hence, a code time of $t = 0.5$ is a reasonable place to measure the influence of the atmosphere on wings. We also use $(W/L)_{0.5}$ in varying the jet parameters, noting that while $t = 0.5$ is no longer special, all of the runs in Table 4.2 are in the active phase at this time. $(W/L)_{0.5}$ is not predictive of wing length later in the same simulation, but is a good measure of relative wing prominence between simulations due to the subsonic growth of wings.

From Figure 4.7 one can get a broad sense of the dependence of wing prominence on the size and shape of the atmosphere. It is immediately obvious that there is a strong dependence on the ellipticity ϵ of the atmosphere, and that smaller, denser atmospheres are the most conducive to wing formation (although "small" could be physically quite large depending on the jet). It is also notable that relatively high values of W/L can be achieved by $t = 0.5$; because we use a decaying jet, the wings will only become more prominent during the later active phase. While these results are not surprising (Equation 4.12), the particular form of the curves depends on both the jet and the atmosphere. As anticipated from the observational results of Capetti et al. (2002), Saripalli & Subrahmanyan (2009), and Chapter 2, long wings require jets co-aligned close to the major axis.

The trends are less clear when varying jet parameters (Figure 4.8). In the top

panels, the jet velocity is allowed to vary freely without conserving integrated kinetic luminosity between runs. If the jet is injected at constant velocity throughout the simulation (Figure 4.8a), a faster jet is slightly better than a slower one at making wings. However, a decaying jet (Figure 4.8b) is better still, with pure exponential decay more effective at increasing $(W/L)_{0.5}$ than "Gaussian" jets of the form $v_{\rm jet} = v_0 \exp[-at^2]$. In the bottom panels of Figure 4.8, we hold the kinetic luminosity constant between runs by modifying v_0. From Figure 4.8c, it is evident that increasing the width of the jet (at the cost of a slower jet) is important. Changing the density of the jet material has an extreme effect on $(W/L)_{0.5}$ (Figure 4.8d); above $\rho_{\rm jet} \sim 0.01$, the jet ceases to be "light" relative to the background and no longer forms lobes resembling radio galaxies (Reynolds et al. 2002). At very low densities, mixing becomes very efficient at disrupting the radio galaxy.

We now discuss these results in detail, beginning with the properties of the fiducial run.

Fiducial Run Our fiducial run (`STANDARD`, Tables 4.1 and 4.2) is the combination of our fiducial atmosphere ($r_0 = 1.0$, $\rho_0 = 3.0$, $\epsilon_x = \epsilon_y = 0.0$, $\epsilon_z = 0.75$) with our fiducial jet ($v_{\rm jet} = 100 c_s \exp[-3t]$, $\theta_{\rm jet} = \pi/15$, $\alpha = \pi/35$, aligned along the z-axis). Like most of our runs, this simulation proceeds to a code time of 1.0, at which point the radio galaxy is in the early passive phase. Unsurprisingly, this run produces some of the most prominent wings of our suite (Figure 4.6); the shallow pressure gradient along the z-axis and declining velocity profile combine to produce stalled lobes which begin to collapse at the end of the active phase. At the same time, wings quickly escape the core region, and by $t = 0.4$ are easily recognizable (right-hand panels of Figure 4.2). After reaching $W/L = 0.83$ at $t = 0.75$, the cocoon collapse leaves the wings as the most notable features (Figure 4.5).

Table 4.1. Varying the Atmosphere using the Standard Jet

Name	Wings?	r_0	ρ_0	ϵ_x	ϵ_z	ΔPA (deg.)	W/L ($t = 0.5$)
Standard Atmosphere							
STANDARD	Y	1.0	3.0	0.0	0.75	0.0	0.62
Ellipticity							
SJ_E20	N	1.0	3.0	0.0	0.20	0.0	0.42
SJ_E30	N	1.0	3.0	0.0	0.30	0.0	0.43
SJ_E50	N	1.0	3.0	0.0	0.50	0.0	0.49
SJ_E60	Y	1.0	3.0	0.0	0.60	0.0	0.54
Core Radius							
SJ_R0.5	Y	0.5	3.0	0.0	0.75	0.0	0.73
SJ_R0.75	Y	0.75	3.0	0.0	0.75	0.0	0.61
SJ_R2.0	N	2.0	3.0	0.0	0.75	0.0	0.45
Core Density							
SJ_D1.5	Y	1.0	1.5	0.0	0.75	0.0	0.52
SJ_D2.0	Y	1.0	2.0	0.0	0.75	0.0	0.57
SJ_D4.0	Y	1.0	4.0	0.0	0.75	0.0	0.65
SJ_D5.0	Y	1.0	5.0	0.0	0.75	0.0	0.68
ΔPA							
SJ_PA5	Y	1.0	3.0	0.0	0.75	5.0	0.62
SJ_PA10	Y	1.0	3.0	0.0	0.75	10.0	0.60
SJ_PA15	Y	1.0	3.0	0.0	0.75	15.0	0.58
SJ_PA20	Y	1.0	3.0	0.0	0.75	20.0	0.51
Triaxial Atmospheres							
TX_E75_1	Y	1.0	3.0	0.375	0.75	0.0	0.65
TX_E75_2	Y	1.0	3.0	0.50	0.75	0.0	0.72

Note. — Runs in which the standard atmosphere was varied one parameter at a time, holding the standard jet ($v_{\rm jet} = 100c_s \exp[-3t]$, $\alpha = \pi/35$ rad and $\beta = \pi/15$ rad for $r_{\rm inner} = 0.1$) constant. The `STANDARD` run uses the standard jet and atmosphere and hence is a data point in each category. The "wings" column denotes whether a run produced noticeable wings at any point during its active lifetime. W/L at $t = 0.5$, on the other hand, is a way to directly compare different runs. At $t = 0.5$, $v_{\rm jet} \sim 20c_s$, i.e., twice the lobe material sound speed and a transition point during the active phase between a powerful and weak jet. The time of this transition depends on the velocity profile of the jet; $t = 0.5$ is only correct for the standard jet. ΔP.A. is the angular distance between the jet and the major axis.

At $t = 1.0$, we re-inject a jet with $v_{\rm jet} = 100 c_s \exp[3(t-1.0)]$ (Figure 4.5 and bottom panel of Figure 4.2). Since the jet is expanding into tenuous material from the old cocoon, the expansion quickly re-establishes a cocoon. However, the reinjection also drives a bow shock inside the collapsing cocoon, allowing initially strong back-flows to feed the wings directly. Hence, between $t = 1.10$ and $t = 1.35$, an X-shaped radio galaxy is apparent ($W/L \sim 1.2$). After $t = 1.35$, the jet again weakens to the point where collapse begins. If the jet is instead reinjected at the inception of the passive phase at $t \sim 0.75$, the end result is very similar ($W/L \sim 1.2$ at $t = 0.95$).

The atmosphere in this run is similar to the 2D simulations presented in Capetti et al. (2002) and 3D simulations in Zanni et al. (2003). Striking asymmetries develop despite the axisymmetric atmosphere because of turbulent mixing between different slices in ϕ and because the back-flows form three-dimensional structures within the lobes. If these flows are slightly misaligned on opposite sides of the midplane, asymmetries develop.

Atmosphere In our exploration of different atmosphere properties (Figure 4.7; Table 4.1), we vary ϵ, ρ_0, r_0, and ΔP.A. individually while keeping the other atmosphere parameters steady and using the standard jet ($v_{\rm jet} = 100 c_s \exp[-3t]$, $\rho_{\rm jet} = 0.01$, $\alpha = \pi/35$, and $\beta = \pi/15$). Except when we vary ΔP.A., the jet is coaligned with the major axis.

It is clear from Figure 4.7 that wing prominence depends strongly on the core radius r_0, core density ρ_0, and ellipticity ϵ. Because the lobes and wings evolve almost independently, these dependencies can be understood by breaking the axial ratio W/L into its constituent parts: the wing length W and lobe length L. For the purposes of this discussion, W and L are both taken to be measured at $t = 0.5$ (Table 4.1).

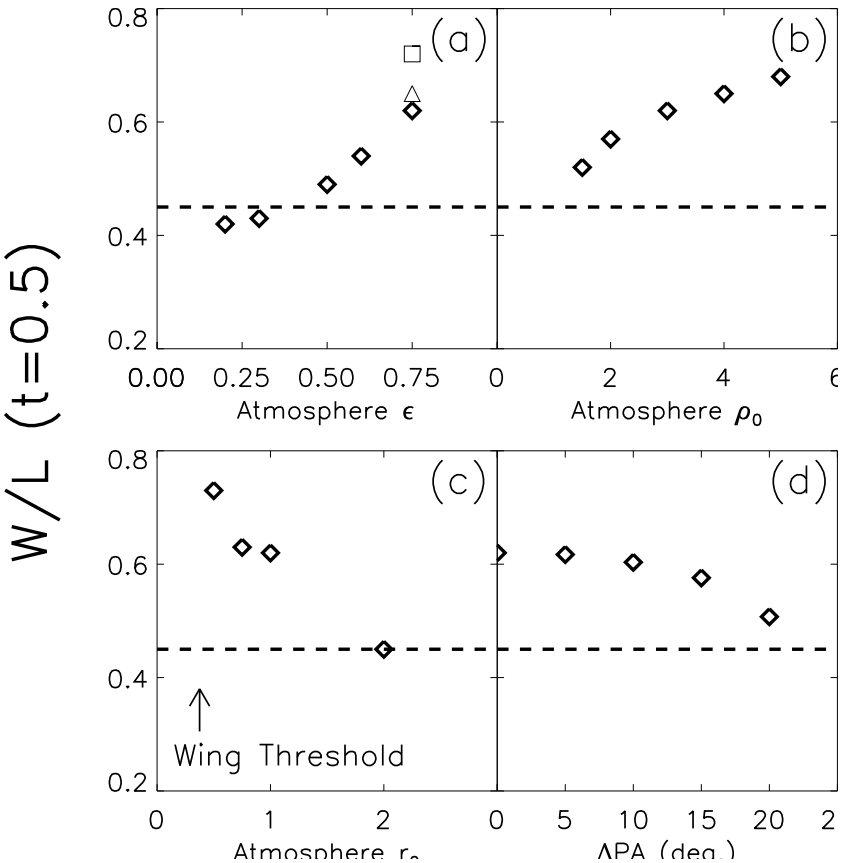

Figure 4.7 These plots show the dependence of axial ratio W/L on (a) the ellipticity of the atmosphere ϵ, (b) the core density ρ_0, (c) the core radius r_0, and (d) the angle between the jet and the major axis ΔP.A.. Each plot represents varying one parameter while holding the other standard atmosphere parameters ($\epsilon = 0.75$, $\rho_0 = 3.0$, $r_0 = 1.0$, and ΔP.A. $= 0$) steady and using the standard jet. In panel (a) the square and triangle represent runs with different ϵ_x for $\epsilon_z = 0.75$, demonstrating the effect of triaxiality on W/L (Table 4.1). W/L is measured at $t = 0.5$ for all cases; for the standard jet, this represents the transition during the active phase from a powerful to a weak jet (this time and the "wing threshold" vary with choice of jet). Values taken from Table 4.1.

We find that L varies only slightly as a function of r_0 (less than 10%) but does peak between $r_0 = 0.5$ and $r_0 = 2.0$. At very low r_0, the lobes are not confined by the atmosphere and spread out laterally, causing more turbulent mixing and dissipating the thrust of the jet. At very high r_0, the lobes are completely confined by the atmosphere and the density gradient is so shallow that as the jet weakens

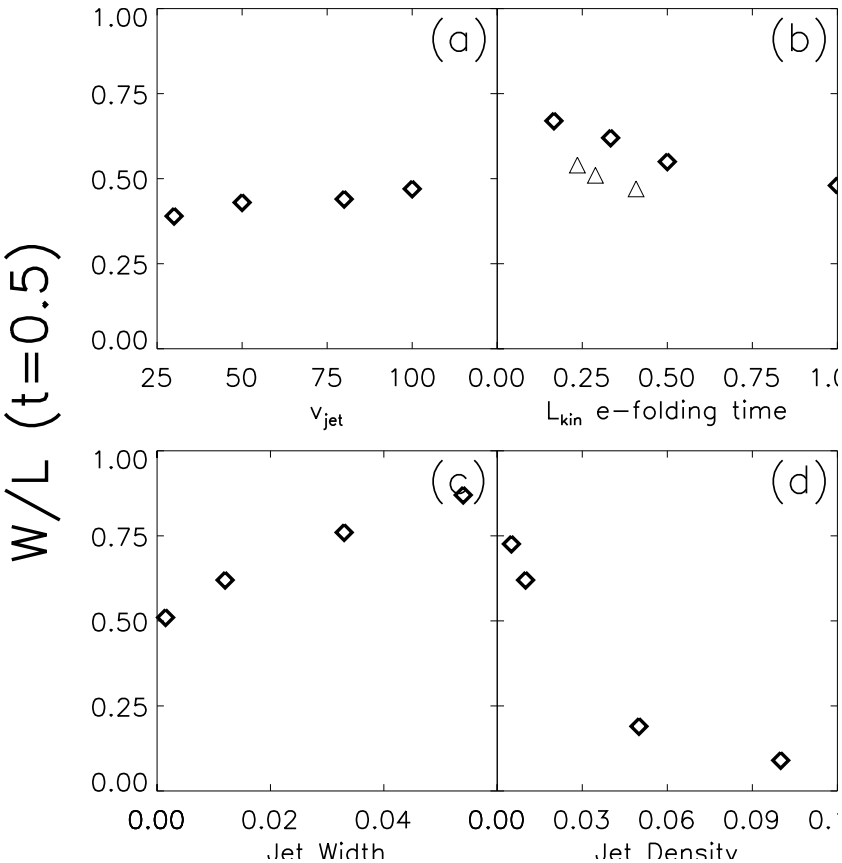

Figure 4.8 These plots show the dependence of axial ratio W/L on (a) jet velocity for a constant-velocity jet, (b) e-folding time for a decaying jet (diamonds represent jets of the form $v_{\rm jet} = 100\exp[-at]$ and triangles $v_{\rm jet} = 100\exp[-at^2]$), (c) area of the jet nozzle, and (d) density of the jet material. All runs are conducted in the standard atmosphere (Table 4.2). In (a) and (b), the jet kinetic luminosity is *not* conserved between runs, whereas in (c) and (d) we adjust the initial velocity v_0 to conserve $L_{\rm kin}$. As in Figure 4.7, we show W/L as measured at a code time $t = 0.5$; all sources are in the active phase but not at the same place.

it is increasingly resisted by the atmosphere. The importance of this effect on the lobes is more pronounced in a comparison between L and ρ_0 where the lobe length declines by 50% between $\rho_0 = 1.5$ and $\rho_0 = 5.0$.

On the other hand, the wing length W depends much more strongly on the core radius r_0 (declining precipitously with increasing r_0) and only weakly on the core density. This behavior occurs because the wings respond primarily to the

pressure gradient along the minor axis (Equation 4.12) which depends on r_0 and ρ_0 as $\nabla P \propto \rho_0 r_0^{-2}$. Thus, a large W/L requires small, dense atmospheres.

In this context, the importance of ellipticity is clear: ϵ determines the ratio of core radii along the major and minor axes. For high ϵ, the lobes expand into material which does not vary much in density during the active phase whereas the wings quickly escape the core region. This behavior is unsurprising; Capetti et al. (2002) and Kraft et al. (2005) make the same basic argument for wings produced when the jet is coaligned with the major axis of the atmosphere. However, the interplay between the parameters rules out predicting the wing length from first principles. For instance, one might imagine that we could produce wings in an atmosphere with $\epsilon \sim 0.3$ (Figure 4.7) by making r_0 tiny and ρ_0 large. Although this *does* increase the wing length, the radio galaxy expands beyond the dense part of the atmosphere during the ignition phase so the jet does not face as much resistance as might be expected.

It is possible to produce wings in atmospheres with smaller ϵ by making the atmospheres triaxial (using prolate ellipsoids) instead of axisymmetric. Zanni et al. (2003) expect triaxial atmospheres (as opposed to the axisymmetric simulations of Capetti et al. 2002) to produce longer wings because the backflow is collimated along a single minor axis as opposed to forming a torus at the midplane. We find that while a triaxial atmosphere does collimate the wings, it does not by itself make them substantially longer relative to an axisymmetric atmosphere with the same maximum ϵ because the backflow in our simulations is a compressible fluid and wing growth is driven by buoyancy (the pressure gradient is the same along the minor axis). Rather, triaxial atmospheres produce better-defined proto-wing channels during the ignition phase. These channels are then reinforced during the active phase. In other words, triaxiality increases $(W/L)_{0.5}$ at smaller values of ϵ

because the ignition cocoon is less axisymmetric.

Finally, we test the sensitivity of wing formation to the degree of alignment between the jet and major axis ΔP.A. (Figure 4.7d). Long wings are difficult to produce when the jet is misaligned with the major axis, and the wings produced differ in character. This is because the ignition cocoon produces proto-wings perpendicular to the jet instead of along the atmosphere's minor axis. Therefore, the longer wings which develop during the active phase do not benefit as much from the initial supersonic expansion. Wings also become increasingly associated with the lobe on their side of the major axis as ΔP.A. increases because the lobes are bent by the atmosphere and the back-flows no longer make it all the way to the midplane before flowing into the wings. Hence, the lobe-wing pairs are mirror-symmetric about the midplane. The angle between the lobe and the wing in each pair is also largely determined by ΔP.A..

Jet In contrast to the atmosphere parameter exploration, determining the dependence of $(W/L)_{0.5}$ on the character of the jet is difficult because of the potential for time dependence in the jet power. This time dependence, along with the small width of the jets, also makes it more difficult to test our findings observationally. We insist that the jets be light, hypersonic flows (Section 4.2) which produce sources which resemble double-lobed radio galaxies, and within these constraints test the dependence of $(W/L)_{0.5}$ on jet power as a function of time, jet width, and density of jet material (Figure 4.8). For each of the simulations in Figure 4.8 we use the standard atmosphere with $r_0 = 1.0$, $\rho_0 = 3.0$, $\epsilon = 0.75$, and ΔP.A. $= 0.0°$. Note that Figure 4.8a and Figure 4.8b do *not* conserve kinetic luminosity between runs, whereas Figure 4.8c and Figure 4.8d do. The exploration of jet velocity is conducted with jets with the standard width of $\beta = \pi/15$ (~ 0.01 code units wide) and density

Table 4.2. Varying the Jet in the Standard Atmosphere

Name	Wings?	$\rho_{\rm jet}$	$v_{\rm jet}(t)/c_s$	α	β	W/L ($t = 0.5$)
			Standard Jet			
STANDARD	Y	0.01	$100\exp[-3t]$	$\pi/35$	$\pi/15$	0.62
			Velocity Profiles			
SA_V30	N	0.01	30	$\pi/35$	$\pi/15$	0.39
SA_V50	Y	0.01	50	$\pi/35$	$\pi/15$	0.43
SA_V80	Y	0.01	80	$\pi/35$	$\pi/15$	0.44
SA_V100	Y	0.01	100	$\pi/35$	$\pi/15$	0.47
SA_VE1	Y	0.01	$100\exp[-t]$	$\pi/35$	$\pi/15$	0.48
SA_VE6	Y	0.01	$100\exp[-6t]$	$\pi/35$	$\pi/15$	0.67
SA_VG3	Y	0.01	$100\exp[-3t^2]$	$\pi/35$	$\pi/15$	0.47
SA_VG6	Y	0.01	$100\exp[-6t^2]$	$\pi/35$	$\pi/15$	0.51
			Jet Density			
SA_D0.005	Y	0.005	$100f\exp[-3t]$	$\pi/35$	$\pi/15$	0.73
SA_D0.05	N	0.05	$100f\exp[-3t]$	$\pi/35$	$\pi/15$	0.19
SA_D0.10	N	0.10	$100f\exp[-3t]$	$\pi/35$	$\pi/15$	0.09
			Jet Width			
SA_B30	Y	0.01	$100f\exp[-3t]$	$\pi/35$	$\pi/30$	0.51
SA_B7.5	Y	0.01	$100f\exp[-3t]$	$\pi/35$	$\pi/7.5$	0.76
SA_B5.0	Y	0.01	$100f\exp[-3t]$	$\pi/35$	$\pi/5.0$	0.87

Note. — The standard atmosphere is a relaxed, isothermal β-model with core radius $r_0 = 1.0$, core density $\rho_0 = 3.0$, ellipticity $\epsilon = 0.75$, and with the jet oriented along the major axis. Few runs are needed to deduce the dependence of the morphology on jet parameters other than the kinetic luminosity as a function of time, but in these cases we vary v_0 by some factor f such that $L_{\rm kin}(t)$ is the same as in the standard atmosphere; see text for caveats of this approach.

of $\rho_{\rm jet} = 0.01$.

Figures 4.8a and 4.8b demonstrate the importance of decaying jets to long wings. In Figure 4.8a, we use jets with differing velocities but no time dependence, finding that none produce a large $(W/L)_{0.5}$. $(W/L)_{0.5}$ actually *increases* with increasing $v_{\rm jet}$ even though the faster jets also punch through the atmosphere more quickly. This is because the overpressured cocoon produced by a weaker jet during the ignition phase is less overpressured and thus produces smaller proto-wings. Below $v_{\rm jet} \sim 20c_s$, the sources are not cocoon-bounded at all. Since the jets do not decay, W/L obviously

decreases with time.

Powerful jets which decay (Figure 4.8b) are effective at producing wings because the proto-wings form during the ignition phase and the jet generates strong backflows early on when the jet head is close to the midplane. Since the lobes grow increasingly slowly, the subsonically expanding wings keep pace with the active lobes more easily. As is clear in Figure 4.8b, the slower the decay, the smaller $(W/L)_{0.5}$ (diamonds represent exponentially decaying jets and triangles jets with $v_{\rm jet} = v_0 \exp[-at^2]$). Jets with *increasing* velocity do not produce long wings because a powerful jet is necessary at the inception of activity to produce proto-wings.

In Figures 4.8c and Figures 4.8d we investigate the dependence of $(W/L)_{0.5}$ on jet width and density. We vary β and $\rho_{\rm jet}$ while conserving $L_{\rm kin}$ by varying the initial velocity of the jet v_0, using the standard form of $v_{\rm jet} = v_0 \exp[-3t]$. We limit these runs to those with v_0 capable of producing an overpressured cocoon that seeds proto-wings.

The nozzle width of the jet clearly has a strong effect on $(W/L)_{0.5}$ (Figure 4.8c). Increasing the jet width makes the ignition cocoon larger and more overpressured during the ignition phase, promoting expansion along the minor axis. The lobe width during the active phase increases with increasing β, dissipating the jet thrust over a larger solid angle. Short, fat lobes attached to fat wings result. On the other hand, if β is tiny, the jet drills through the surrounding atmosphere quickly, and thin, long lobes result. It is not clear whether jet widths actually vary substantially between sources and what determines the width of the jet; all jets are very narrow. Thus, our results are more generally a statement that jets which dissipate their thrust over a wider area produce longer wings.

Figure 4.8d shows $(W/L)_{0.5}$ as a function of $\rho_{\rm jet}$. The sharp decline with increasing $\rho_{\rm jet}$ is due to the thrust carried by the jet. Even at moderate velocities, denser

material drives the lobes forward much faster than light material while at the same time driving weaker back-flows. Hence, wing formation is not favored. We note that when $\rho_{\rm jet} > 0.05$, the sound speed of the lobe material is not much greater than that of the ambient medium and the jet does not develop the usual KH instabilities. These jets are therefore not "light" as required to reproduce realistic radio sources with non-relativistic hydrodynamics (Section 4.2). However, these runs are shown along with the light ones to illustrate the importance of dissipating jet thrust to long wings.

Synthesis Runs We have used the insights gained from examining the dependence of wing prominence on various atmosphere and jet parameters to new runs with complex atmospheres and jets in an attempt to produce long, realistic wings. These simulations (listed in Table 4.3) are not a systematic exploration of any phenomenon. We offer a few brief observations here.

Triaxial atmospheres offer the best hope of making long wings at lower ϵ (e.g. Figure 4.6), but still cannot produce substantial wings in our simulations for $\epsilon \lesssim 0.45$. Several runs from a large suite of such simulations are listed in Table 4.3 with the prefix `TX`. Generally, they follow the same trends as described in above; the importance of both favorable atmosphere and jet parameters to wings is obvious in the simulation with $\epsilon_z = 0.45$ (`TX_E45_D5.0_WIDE`), where a wide, decaying jet in a small, dense atmosphere is required to produce wings comparable to that in the standard atmosphere at lower ellipticity. Embedded disks of hot material (i.e., a thick disk; runs `DISK_VE1` and `DISK_VE3`), however, alleviate the problem, allowing prominent wings to grow in atmospheres with globally small ϵ. These disks are somewhat denser than the larger ISM, so the ignition cocoon effectively encounters a small, dense, highly elliptical atmosphere during the ignition stage. The disks are

Table 4.3. Synthesis Runs

Name	r_0	ρ_0	ϵ_x	ϵ_z	$\rho_{\rm jet}$	$v_{\rm jet}/c_s$	α	β	$W/L_{\rm max}$
Interpolation									
WIDE_VE1	1.5	4.0	0.0	0.75	0.01	$100\exp[-t]$	$\pi/90$	$\pi/7.5$	0.58
WIDE_VE3	1.5	4.0	0.0	0.75	0.01	$100\exp[-3t]$	$\pi/90$	$\pi/7.5$	0.73
TX_E75_VE1	1.0	3.0	0.375	0.75	0.01	$100\exp[-t]$	$\pi/90$	$\pi/7.5$	0.63
TX_E75_VE1_BIG	1.5	4.0	0.375	0.75	0.01	$100\exp[-t]$	$\pi/90$	$\pi/7.5$	0.68
(restart at $t = 1.0$)									0.78
TX_E75_VE1_B7.5	0.75	3.0	0.375	0.75	0.01	$100\exp[-t]$	$\pi/90$	$\pi/7.5$	1.02
TX_E75_VE3_B5.0	1.5	4.0	0.375	0.75	0.01	$100\exp[-3t]$	$\pi/90$	$\pi/5$	0.82
TX_E60	0.75	3.0	0.30	0.60	0.01	$100\exp[-t]$	$\pi/90$	$\pi/7.5$	0.44
TX_E60_WIDE	0.75	3.0	0.30	0.60	0.01	$100\exp[-t]$	$\pi/90$	$\pi/5$	0.67
(restart at $t = 1.0$)									0.97
TX_E60_D5.0	0.75	5.0	0.30	0.60	0.01	$100\exp[-t]$	$\pi/90$	$\pi/7.5$	0.71
TX_E45_D5.0_WIDE	0.75	5.0	0.225	0.45	0.01	$100\exp[-3t]$	$\pi/90$	$\pi/5$	0.58
Other									
DISK_VE1	2.0	3.0	0.25	0.50	0.01	$100\exp[-t]$	$\pi/90$	$\pi/7.5$	0.60
	0.25	8.0	0.0	0.90					
DISK_VE3	2.0	3.0	0.25	0.50	0.01	$100\exp[-3t]$	$\pi/90$	$\pi/7.5$	0.83
	0.25	8.0	0.0	0.90					
TURBULENT[a]	1.0	3.0	0.0	0.75	0.01	$100\exp[-3t]$	$\pi/90$	$\pi/7.5$	0.64
SHELL_VE1[b]	1.0	3.0	0.0	0.75	0.01	$100\exp[-t]$	$\pi/90$	$\pi/7.5$	0.53
SHELL_VE3[b]	1.0	3.0	0.0	0.75	0.01	$100\exp[-3t]$	$\pi/90$	$\pi/7.5$	0.71
INTERMITTENT	2.0	2.0	0.0	0.75	0.01	$100\sin^2[50t]$	$\pi/90$	$\pi/7.5$	0.44
INTERMITTENT2	1.0	3.0	0.0	0.75	0.01	$100\sin^2[6t]$	$\pi/90$	$\pi/7.5$	0.47
SLOW_START_1[c]	1.0	1.5	0.0	0.75	0.01	20 *to* $100\exp[-t]$	$\pi/90$	$\pi/7.5$	0.42
SLOW_START_2[c]	1.0	1.5	0.0	0.75	0.01	20 *to* $100\exp[-t]$	$\pi/90$	$\pi/5$	0.45
SLOW_START_3[c]	1.0	5.0	0.0	0.75	0.01	20 *to* $100\exp[-t]$	$\pi/90$	$\pi/5$	0.55

[a]This is the standard run with axisymmetric Kolmogorov spectrum density perturbations introduced to the atmosphere.

[b]Shells of material with a peak amplitude $\rho = 3.0$ were superimposed on the standard atmosphere; shells are generated along the z-axis by using 2D sine or sinc functions with a period of $z \sim 0.5$.

[c]$v_{\rm jet} = 20c_s$ from $t = 0.0$ to $t = 0.25$ and $v_{\rm jet} = 100\exp[-(t - 0.25)]$ thereafter.

Note. — A representative sample of our non-systematic exploration of parameter space; not all runs attempted are included. "Interpolation" runs refer to those runs which are a natural extension of Tables 4.1 and 4.2 whereas "other" runs include substantially different atmospheres and jet behaviors. See text in Section 4.3.2 for discussion.

blown apart by the blast wave from the ignition stage and might not be observable once the radio galaxy has turned on.

In most of our models, the ignition stage occurs in a smooth, relaxed medium. In real galaxies, the ignition stage would occur in the galactic center where mergers, dynamical effects, and other phenomena associated with AGN can significantly disturb the ISM. We do not attempt to model real galaxies, but find that adding Kolmogorov spectrum turbulence to our atmospheres or small bar-like perturbations to the underlying gravitational potential near the nucleus does not have a large effect on the ignition stage. As long as there is a sufficient amount of ISM distributed around the nucleus, an overpressured cocoon can form. On the other hand, in runs where we begin with a weak jet of $v_{\rm jet} = 20c_s$ (twice the sound speed of the lobe material), and no cocoon is formed, wings do not form (the `SLOW_START` runs in Table 4.3). The backflow model has difficulty producing wings when a weak AGN suddenly becomes more powerful because an overpressured cocoon only forms when the jet is completely confined by the atmosphere. These runs can, however, produce something akin to Z-shaped morphology by virtue of the lobes escaping the densest regions of the atmosphere before the powerful jet turns on.

We have briefly investigated the potential for gas-rich "stellar shells" from minor mergers located periodically along the major axis to produce wings (motivated by Gopal-Krishna & Wiita 2010). We use a simple model in which only the positive peaks of two-dimensional sine/sinc waves are added to the density of an underlying elliptical atmosphere; the center is cut out. The amplitudes are set at a maximum of ρ_0. The shells do not significantly impact the formation of wings emanating from the center of the galaxy, although they do resist the jet, allowing for a higher W/L (the `SHELL` runs in Table 4.3). In the model of Gopal-Krishna & Wiita (2010), wings are instead produced near the site of the shell, and we cannot reproduce this.

Obviously, these runs are not a thorough exploration of the effect of stellar shells, especially if they actually bend jets (in which case they are beyond the scope of our models).

Motivated by the importance of a reinjected jet (Section 4.3.1), we examine the role of rapid intermittency (runs `INTERMITTENT` in Table 4.3). By this we mean jets which experience multiple outbursts during the run and which are essentially in an "on" state or an "off" state. Generally, we find that rapid intermittency has the effect of suppressing wing formation and results in much more regular cocoons (in terms of their projected morphology) than single outbursts. On the other hand, ragged cocoons are produced by long periods of dead time. In neither case are wings promoted, as each successive brief outburst deposits most of its thrust at the ends of the lobes, far from the midplane. The chief reason why such intermittency does not produce prominent wings is that wings expand subsonically. Since the duty cycles of the intermittent jets are much shorter than the crossing time, the cocoon expands as if a moderately powerful jet of constant velocity were powering it. Unlike in single decaying outbursts, the intermittent jets deposit most of their thrust far from the midplane. On the other hand, intermittency on the timescale of an e-folding time of a decaying jet can be effective at making wings.

4.4 Simulation Limitations

Because we have only solved the equations of hydrodynamics in evolving our simple models, it is worth considering the impact of additional complexity.

4.4.1 Missing Physics

Our models do not include magnetic fields, special relativity, or radiative losses, and our simple setup does not take into account complex jet or atmospheric structure, feedback, and other processes that may be important to radio galaxy morphology. In practice, we do not believe these omissions invalidate our results. For example, special relativity and magnetic fields must play crucial roles in determining the character and transverse structure of the jet, but we only insist that our simulated jets reproduce the collimation, hot spots, and back-flows of FR II sources. In other respects (e.g. radiative efficiency), the jet and AGN are inside a "black box." Because we are concerned with the behavior of lobe material, we believe these omissions are justified.

Likewise, radiative losses (depleting of lobe energy via synchrotron emission and inverse Compton scattering) only become important relative to adiabatic losses at late times and are not in a position to influence the formation of wings. Radiative losses from the ICM are also irrelevant on the timescales of AGN outbursts, so feedback (the connection of jet power to the amount of material crossing the inner boundary) resulting from cluster cooling is unimportant on these timescales. As to feedback from *backflow* (Antonuccio-Delogu & Silk 2010), there is no obvious recipe to describe what happens to the mass flowing across the inner boundary, since the inner boundary radius is much larger than the nuclear engine, but as the back-flows straighten, less material will have velocity vectors pointing towards the origin and eventually the AGN would cease to be "fed" by backflow. This is consistent with our entirely artificial recipe for decaying jets.

On the other hand, magnetic fields (that must be injected with the jet) and relativistic jets (which have a higher thrust for a given mass-energy density) may

strongly influence the behavior of lobe material.

Toroidal magnetic fields may help collimate the backflow and retard its mixing (e.g. Braithwaite 2010). The apparent continuity of fields in some wings (e.g. NGC 326 in Murgia et al. 2001) is suggestive, especially considering that in our models the lack of collimation leads to wide wings. However, Huarte-Espinosa et al. (2011) find in simulations of FR II sources that turbulence sets in within the cocoon even when ordered fields existed earlier, so it is unclear that the magnetic fields in the wings are actually toroidal. As to the realism of the *jet*, it is not our goal to understand the jet physics in detail, but we note the persistence of experimental hypersonic fluid jets in recent work by Belan et al. (2011), which the authors use to argue that magnetic collimation is only required near the base of the jet.

The importance of relativistic jets to the cocooon morphology is unclear. Komissarov & Falle (1996) find that, for jets matched by velocity, pressure, radius and power, relativistic jets produce preferentially wider cocoons than non-relativistic ones. The authors suggest that this effect may be accounted for by the higher thrust in the relativistic case. However, Rosen et al. (1999) find the opposite when using the same matching conditions: relativistic jets tend to produce narrower cocoons compared to non-relativistic jets (more specifically, jets with a higher Lorentz factor have smaller cocoons). Without matched relativistic simulations it is impossible to directly test the importance of special relativity on our cocoon sizes, but it is remarkable that Rosen et al. (1999) and Komissarov & Falle (1996) agree that the qualitative nature of the cocoon is unchanged. Including relativity may modify W/L but would not fundamentally change the appearance of our winged sources because relativistic physics in the lobes would not change the processes which produce wings. In other words, we believe that special relativity is a second-order effect akin to magnetic fields.

4.4.2 Initial Conditions

It is worth asking whether wings form only because our atmospheres are "smooth", i.e., because we have not included turbulence in the ICM or structure near the center (where the environment is presumably complex). This question is particularly important given the observed interactions between jets and molecular clouds (e.g. Ly et al. 2005), stellar shells (e.g. Gopal-Krishna & Wiita 2010), gas in companion galaxies (Evans et al. 2008), and more generally the complex nuclear environments of active galaxies (e.g. Rosario et al. 2010). To this end, we have introduced density perturbations mimicking stellar shells along the major axis at various intervals, tested the impact of a single ring near the nucleus, and introduced Kolmogorov-spectrum turbulence to the ICM. None of these structures alter the same basic evolution of winged sources. Additional jet physics would need to be in place in order to determine whether the jet itself can be bent by interaction with high density pockets (Gopal-Krishna & Wiita 2010). All of these tests use density perturbations with a maximum amplitude of the core density ρ_0. Finally, bulk flows in clusters are clearly important to radio galaxy structure (Morsony et al. 2010), although most XRGs are large, strongly bridged sources in which this may not be a defining effect.

4.4.3 Artifacts

It is encouraging that our simulated radio galaxies reproduce the basic features of other simulations in the literature (e.g. Antonuccio-Delogu & Silk 2010; Heinz et al. 2006; Reynolds et al. 2002; Vernaleo & Reynolds 2007), but it is worth considering the impact of boundary conditions and the jet structure on the morphology of the lobes—our setup is designed to produce lobes like those of radio galaxies with physics and conditions inherently different from those encountered in nature. The mixing

experienced by the lobes is also artificial (naturally set by the size of the grid zones, which vary along r and θ), but mixing is too slow a process to suppress the formation of wings.

The inner boundary is the most significant artifact of our simulation because it represents no physical analog but rather allows us to hide the AGN and the jet collimation mechanism. In addition, backflow crossing the boundary slows down and disappears. This has two consequences: not all the backflow can be harnessed, and flows may be effectively directed around the boundary by eddies as slowing backflow crosses the boundary. In the first case, the amount of material is too small to influence the wings. In the second, we find that the inner boundary must be small compared to r_0 (keeping the physical size of the jets fixed) in order to prevent the initial cocoon from being unduly influenced by the sphere. Inner boundary spheres which are too large tend to promote material flowing around them, hence promoting early wings, but suppress midplane mergers and hence the prominence of later wings. The initial interstices also survive for longer for oversized $r_{\rm inner}$. For typical atmospheres ($0.5 < r_0 < 1.0$), $r_{\rm inner}$ must be somewhat smaller than 0.1 code units; $r_{\rm inner} = 0.05$ is a compromise between a small impact on the initial cocoon and reasonably sized grid zones. Runs with $r_{\rm inner} = 0.01$ do not appear substantially different from those with $r_{\rm inner} = 0.05$, and the timestep is unreasonably small for general use.

We precess the jet injection footpoints rapidly (20π Hz) in a very tight circle around the poles in order to break up the jet symmetry and spread its thrust out over a larger working surface. We only require that our jet reproduce internal features seen in other hydrodynamic simulations along with the terminal shocks that give rise to the back-flows and lobes. Without breaking up the jets, axisymmetry is preserved and the jet head travels very quickly and produces unrealistic lobes (e.g.

Vernaleo & Reynolds 2006); in MHD simulations we would expect helical instabilities to break up the jet. Our precession scheme is thus an artifice that is motivated by observables but whose recipe is not an attempt to model a physical process (cf. Heinz et al. 2006). However, one might worry about its influence on backflow and wings because the precession angle is a free parameter (subject to the condition that $\alpha < \theta_{\rm jet}$). In other words, we can tune the width of the lobes and the rate of growth of the radio galaxy within some narrow range of parameters. Since stalling the jet head contributes to wing prominence via shortening the active lobes, is the axial ratio W/L artificially high? We do not believe so. Even with tiny precession angles, we form long wings in highly eccentric atmospheres (the only atmospheres where long wings form). Moreover, the jet head advance speed also depends on the kinetic luminosity as a function of time.

4.5 Properties and Predictions of the Backflow Model

We have successfully produced winged and X-shaped sources solely by redirecting back-flow with static environmental pressure gradients, and are now in a position to compare our simulated sources to observed XRGs (Figure 4.9) in order to critique proposed wing formation mechanisms involving back-flows. In these models, wings are produced as plasma flowing back from the jet heads is deflected into a direction misaligned with the jets. How this deflection occurs is uncertain (Capetti et al. 2002; Gopal-Krishna & Wiita 2010; Kraft et al. 2005; Leahy & Williams 1984; Worrall et al. 1995), and until now the backflow model has not been rigorously investigated with three-dimensional simulations.

Here we outline a series of predictions (expectations) for properties which are,

at least in principle, observable if our simulations are an adequate representation of wing formation. These predictions are also summarized in Table 4.4. We then assess the backflow model in light of these predictions and briefly discuss the implications of our work for the wider sample of distortions to the canonical double-lobed morphology of bridged radio galaxies.

4.5.1 Predictions

X-shaped and winged sources are one family The most natural consequence of the backflow model is that short and long wings are produced in the same way. Short wings should then be more common than long ones since the long wings are harder to produce. Although this is an obvious point, we note it as a potential observational test because sources with shorter wings and the candidate X-shaped sources (Cheung 2007) have not been tested for several of the trends seen in XRGs (most importantly, the jet–major axis correlation: Capetti et al. 2002; Saripalli & Subrahmanyan 2009). Our simulated sources predict that winged sources will fall in line, albeit with a greater spread in parameter space.

Projection almost always enhances W/L Wings in our models (even those produced by triaxial atmospheres) tend to be wider than the lobes and hold their shape better in rotation and projection. Hence, we predict that projection almost always enhances W/L. In other words, some observed sources with high $W/L_{\rm obs}$ probably have an intrinsically smaller aspect ratio (e.g. Figure 4.9). If the projection angle can be worked out for a sufficient number of XRGs and winged sources, we expect the lobes in a number of XRGs to be shortened via projection, i.e., the intrinsic distribution of W/L is shifted from the observed distribution (an idea of the observed distribution may be found in Saripalli & Subrahmanyan 2009). If this does

Table 4.4. Model Predictions

	Expectation	Observed?	Reference
1.	Short wings common; (intrinsically) long wings rare	No in SS09 sample (yes including C07?)	SS09
2.	Projection tends to enhance W/L	Undetermined	
3.	W/L correlated with $\epsilon_{\rm ISM}$	Sample size too small	HK10
	(weaker correlation with host ϵ)	No?	C02,SS09
4.	Wings require a jet aligned near the major axis	Yes	C02,SS09,HK10
5.	W/L enhanced by higher pressure, small atmospheres	Yes?	L10
		Yes?	SS09
6.	Most XRGs should be weak FR IIs	Yes	C09,L10
	(and hence strongly bridged sources)	Yes	LW84
7.	Intermittency on scales of 3–10 Myr produces longer wings	Undetermined	
8.	Wings are fainter than lobes	Yes	LW84
9.	Wings have flat spectral indices	Mixed results	LR07
10.	Backflow follows existing channels (collimation requires existing channels)	Yes?	SS09
11.	Wings grow subsonically	No? (large wings)	
	(hence wing AGN outbursts are old)	No?	DT02
12.	Flow speeds in wings should be transonic for lobe material	Undetermined	
	Backflow model piggybacks on other hydrodynamic models	Yes?	SS09

Note. — Predictions for XRG properties if our model is accurate; note that these may not hold for the "backflow model" generally as phrased in prior work. Predictions correspond to arguments made in Section 4.4.

References. — C02: Capetti et al. (2002); C07: Cheung (2007); C09: Cheung et al. (2009); DT02: Dennett-Thorpe et al. (2002); HK10: Chapter 2; L10: Landt et al. (2010); LW84: Leahy & Williams (1984); LR07: Lal & Rao (2007); SS09: Saripalli & Subrahmanyan (2009)

not turn out to be the case, the backflow model would need a collimation mechanism (see subsonic expansion below) to be consistent with observations. Unfortunately, this prediction makes it difficult to quantitatively compare the simulated population to the observed on because in most XRGs the projection angle is unknown.

Long wings require high ellipticity Our simulations predict that intrinsically long wings can only be produced in very elliptical atmospheres (Figure 4.7). The lowest ϵ for which we can make convincing wings is $\epsilon \sim 0.45$, and very long wings require $\epsilon > 0.55$. These values are much higher than the average powerful radio galaxy host ($\epsilon_{\rm peak} \sim 0.2$ in Smith & Heckman 1989, although 23% of the galaxies

in their study have $\epsilon > 0.35$) and even most XRGs. A high initial atmospheric ellipticity (or higher order asymmetry) is a clear prediction of our models, but confirming this behavior in observed sources is difficult.

For instance, a few sources with very small host ϵ and large W/L (the best example is NGC 326) appear to have wings originating *outside* the ISM, so it is not evident that the ellipticity of the ISM is always the relevant value for comparison. Further, the ellipticity of the ISM may differ substantially from that of the host galaxy on small scales (Diehl & Statler 2007) even when in broad agreement on galactic scales (Chapter 2). In this case, the best example in the literature is 3C 403 (Figure 4.1, where $\epsilon_{\rm ISM} = 0.059$ and $\epsilon_{\rm optical} = 0.25$ (Kraft et al. 2005). Indeed, we find that elliptical atmospheres of moderate ϵ with embedded disks are as effective at producing wings as single-component atmospheres with extreme ϵ, but the disks are largely destroyed by the radio galaxy. High resolution optical imaging may be required to see any disk remnants. The triaxiality of elliptical galaxies also plays a role, since we may not measure a true ellipticity. Finally, because projection tends to enhance W/L, extreme values of $\epsilon \sim 0.75$ (as we use in the standard atmosphere) are not required to produce observed long wings. All else being equal, we still expect the intrinsic W/L to be correlated with ϵ, but the caveats outlined above make it a difficult proposal to test presently.

Wings require a jet pointed nearly along the major axis of an anisotropic environment ($\Delta P.A. \sim 0$) As expected (based on the studies in Capetti et al. 2002; Hodges-Kluck et al. 2010a; Saripalli & Subrahmanyan 2009), wings require a strongly asymmetric environment in which the jet is stalled by progression along the long axis (Figure 4.7). The wings grow in the favorable pressure gradients along the minor axis or axes. Our models expect a fairly strict requirement for the jet

to be within $\sim 15^\circ$ of the major axis for substantial wings to be produced via the overpressured cocoon channel (the usual method for seeding wings in our models). The requirement is even more stringent in the event that a disk is present, indicating that disks are likely to be important only in a minority of cases.

As ΔP.A. increases, the wings become shorter (Figure 4.7) as well as increasingly associated with the lobe on the same side of the major axis. These lobe-wing pairs thus have mirror symmetry about the midplane. This is in agreement with radio maps of such sources. Since wings long enough to qualify the source as "winged" can be produced for a $\sim 15^\circ$ range of major axis–jet separation and truly X-shaped sources are only (intrinsically) produced for ΔP.A. $< 5^\circ$, we would expect $\sim 2/3$ of winged sources to have lobe-wing pairs, with acute angles between a lobe and its wing produced for smaller angles and obtuse angles for larger ones. Thus, we suggest that the existence of a large number of sources with lobe-wing pairs rather than true X-shaped morphology is consistent with the backflow model. However, we would also expect that wing length would decrease with increasing ΔP.A.; this has not yet been measured.

Longer wings are produced in higher pressure, smaller atmospheres

Steeper pressure gradients occur for smaller core radius and higher core density/pressure (Equation 4.12). Since the steepness of the pressure gradient influences the rate at which wings grow, these small, dense atmospheres (e.g. the ISM) are better at producing wings. Moreover, wings can only form via the overpressured cocoon channel if the cocoon can escape the central core region and its high density before it comes into pressure equilibrium. The top panels of Figure 4.2 demonstrate this point (see also Figure 4.7). Finally, a high core density also resists the jet advance along the major axis, allowing the wings to grow longer. Thus, our models expect that the

hosts of XRGs (where the jet is presumably pointed along the major axis) have higher pressure, on average, than those normal radio galaxies with jet geometry favorable to wings. Landt et al. (2010) find that the nuclear regions of XRGs have high temperatures ($T \sim 15000$ K) indicating that these regions may be overpressured. Although this does not directly correspond to our models of relaxed, isothermal atmospheres, our requirement for a small, high pressure environment is in agreement with their work.

Most XRGs should be weak FR IIs Another key ingredient in our models is a decaying jet that begins as a powerful FR II source and decays to luminosities more typical of FR I sources. A powerful jet is required to produce the overpressured cocoon and drive wings early on, whereas once wings begin expanding subsonically, a weakening jet (which advances increasingly slowly along the major axis of the atmosphere) allows the wings to become quite prominent. If the atmosphere is much smaller than the radio galaxy (as in many cases), a decaying jet will still grow more and more slowly, allowing subsonically growing wings to keep up. This finding naturally explains the observations that XRG radio powers tend to lie near the FR I/II "break" (Cheung et al. 2009) while also possessing strong bridges associated with powerful FR II sources (Leahy & Williams 1984). Landt et al. (2010) argue that XRGs are the archetypal transition population between FR I and FR II sources, with about half the XRGs in their sample having weak emission lines from the AGN (weak-lined FR IIs are otherwise uncommon). This suggests that there is indeed an evolutionary progression in the AGN and jet luminosity of XRGs. Our models predict a fast-rise exponential-decay profile in which the XRG spends most of its lifetime as a weak FR II source (Figure 4.8). However, we note that Best (2009) find in an SDSS study that FR I and II sources are not as obviously separated as

in Ledlow & Owen (1996) and that FR II morphology occurs for a variety of radio powers and host galaxy masses.

Intermittency is another important prediction of our models for observed XRGs, but the action of intermittency in our simulations may represent a more complex underlying process. Intermittency on timescales similar to the e-folding time of a decaying jet (near the early passive phase) is effective in our simulations because it allows the jet to bypass the overpressured cocoon stage and form a bow shock within the radio lobe itself, thereby depositing a large amount of backflow into the wings from a very powerful jet close to the wing bases. Reinjection is effective in a relatively narrow window of time (3–10 Myr depending on the size of the radio galaxy, e.g. Figure 4.5) between the active and passive phases, but this may be plausible: the ripples in the Perseus cluster (Fabian et al. 2006) and Abell 2052 (Blanton et al. 2009) do imply an AGN duty cycle of about 10 Myr. This is consistent with our simulated sources between 50–100 kpc across. Thus, it is conceivable that regular intermittency is a viable mechanism for enhancing wings, although we note that if the intermittency is very rapid or very slow, it is ineffective (Section 4.3.2). On the other hand, intermittency could be replaced in our models by any mechanism which drives back-flows nearer the base of the wings such as the motion of denser ISM into the path of the jet. We note that intermittency may also be effective for wings attached to the primary lobes farther from the nucleus; a reinjected jet quickly re-establishes the cocoon and drives strong back-flows along its length as it rapidly reaches the prior hot spot. If the jet reinjected is similar to the outburst which initially formed the wings, we would still expect XRGs mostly to be weak FR II sources.

Wings should be fainter than the primary lobes The active lobes of XRGs typically have higher surface brightness than the wings. This behavior persists at lower (MHz) frequencies and is therefore not obviously attributable to spectral ageing, although spectral ageing may be in play for some XRGs (Lal & Rao 2007). Our models expect the wings to be fainter (lower surface brightness) because they are substantially wider than the collimated primary lobes yet contain (in most cases) less lobe material. We therefore suppose that the wing material spreads out and decreases the magnetic field energy density U_B.

Assuming that U_B decreases with increasing volume (i.e., assuming something like equipartition conditions, although precise equipartition is not required), the synchrotron emissivity in the wings will be substantially smaller than that in the lobes. In other words, "spherical" wings a factor of ~ 2 wider than the active lobes will have a factor of ~ 8 smaller U_B than in the lobes. In optically thin conditions (a good assumption), the surface brightness obtained from integrating through the wings only recovers a factor of ~ 2 in the wings, so we expect them to be a factor of ~ 4 dimmer than the active lobes (more generally, the square of the ratio between the wing width and the lobe width) for electrons of the same γ. Of course, in projection the wings may appear even dimmer since the lobes will tend to be shortened and therefore increase in surface brightness (ignoring relativistic dimming of the counterjet) whereas the wings will not.

Clearly, this prediction rests on a number of assumptions not included in our models and is therefore somewhat weak. Since the wings are filled with turbulent plasma, it is also possible that the magnetic field strength is increased by winding up of fields as the material mixes. Moreover, the jet power (and therefore the back-flow speed) is time dependent in our simulations, so the ratio between the surface brightness of the lobes and the wings would be time dependent in our model as

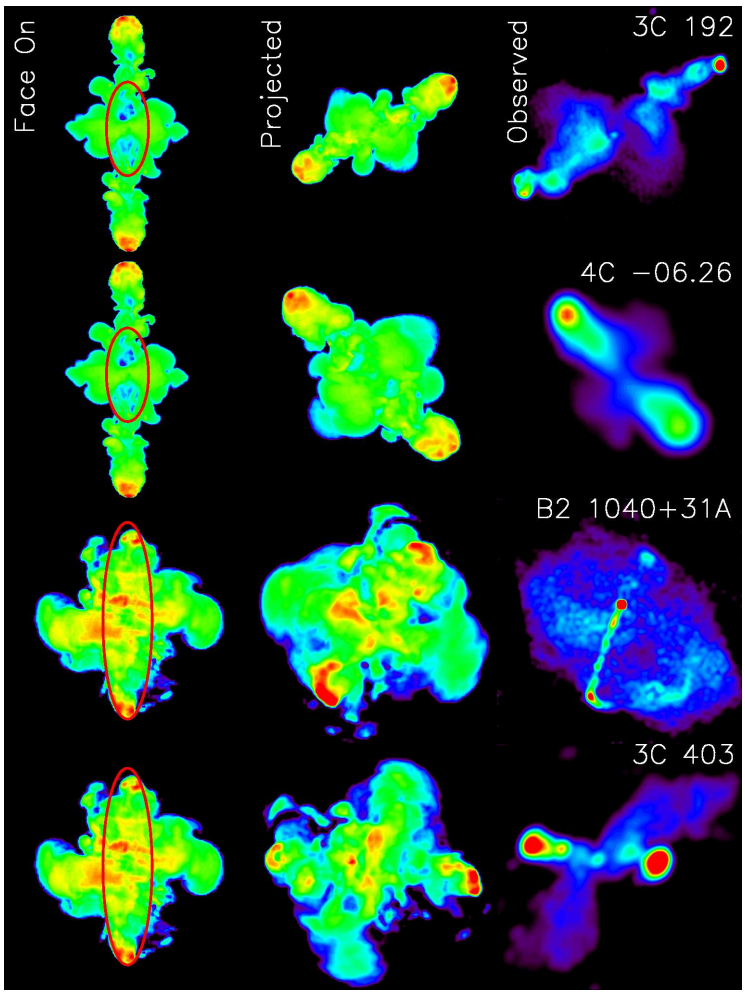

Figure 4.9 Gallery of false equipartition synchrotron maps ($j_\nu \propto p/\rho^{7/4}$) showing the resemblance between our winged sources and observed XRGs, and the importance of projection. Left: Face-on view showing intrinsic structure. The red ellipses show the core radius isobar of the model atmosphere. Center: Rotated and projected view. Right: XRG analog (various resolutions). We only show a few examples of simulations and note that any one simulation can reproduce several observed sources; more than 60 of the sources in Cheung (2007) can be plausibly reproduced by our simulations (in terms of appearance).

well. Nonetheless, the diffusion of material in the wings and the aforementioned projection effects seem likely to dim the wings in the backflow model.

Backflow follows existing channels Most of the wings in our simulated sources are seeded by the pressure-driven expansion of an overpressured cocoon early in the source's life. This cocoon expands asymmetrically because of the asymmetric pressure gradients and forms proto-wings which are later bolstered by the merger of laminar back-flows near the midplane sending material into the wings during the active phase. The laminar back-flows themselves are ineffective at drilling new channels. During the overpressured phase they acquire a vorticity near the terminal shocks that leads them to follow the contact discontinuity of the cocoon and ultimately flow back towards the AGN (Figure 4.3). During the active phase, they are mostly straight and flow towards the midplane.

Lobe material is also ineffective at producing channels because it follows the path of least resistance: in a confined ellipsoidal cocoon, it will simply spread out to increase the pressure throughout the cocoon rather than break out in a particular direction. This can be seen in the false synchrotron maps in Figure 4.2. These maps assume equipartition and are not indicative of what the sources would look like in the GHz bands. Rather, they effectively trace pressure in the cocoon, and it is easy to see that the pressure in the confined cocoon on the left side of the figure remains high relative to the X-shaped source (the false radio maps use the same scale).

Apart from proto-wings produced by the early pressure-driven expansions, Kelvin-Helmholtz and Rayleigh-Taylor instabilities produce channels which backflow reinforces. Given sufficient time and a powerful jet, these whorls and fingers can become wings in their own right, but likewise this is due to the growth of the instabilities and buoyancy rather than redirected laminar back-flows.

Notably, some sources exhibit wings which do *not* emanate from the center or are unlikely to have been produced via an overpressured cocoon (e.g. NGC 326). Because it is difficult to channel the back-flows, we hypothesize that if the backflow

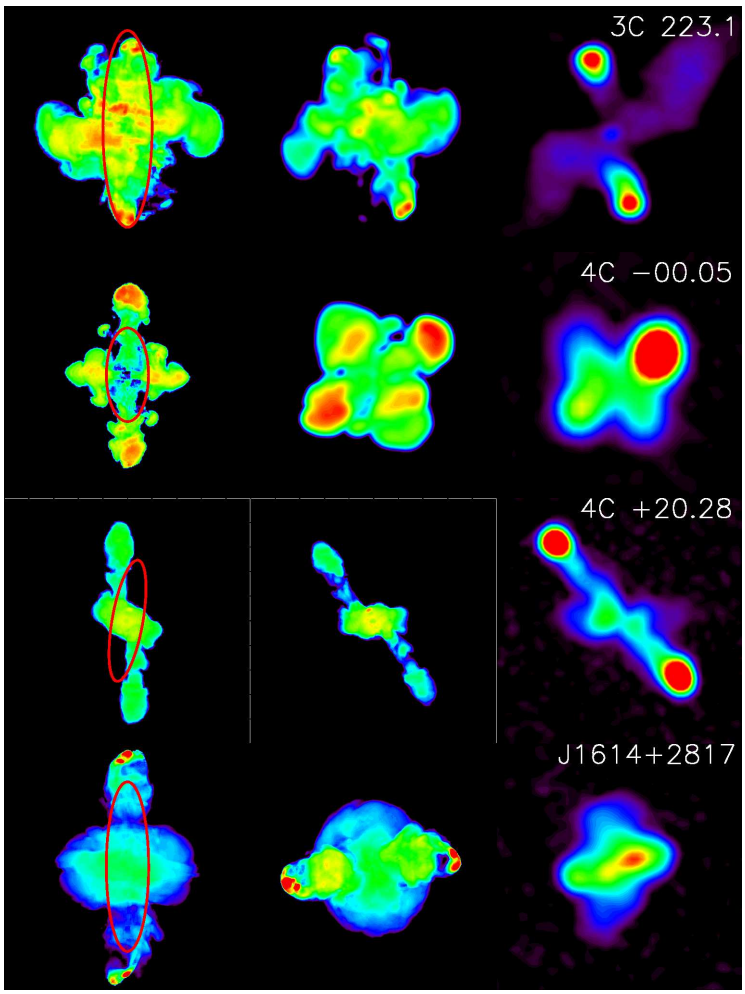

Figure 4.9 continued

model is correct, some seed proto-wing was necessary to produce such sources. The origin of these proto-wings is unclear.

Wings expand subsonically Related to the expectation that back-flows are not directly responsible for drilling channels is the prediction that the wings of radio galaxies expand subsonically for most of their lifetimes (Figures 4.3 and 4.4). This expectation is contrary to the Capetti et al. (2002) "overpressured cocoon" and Worrall et al. (1995) or Leahy & Williams (1984) "buoyant backflow" proposals in the literature (Section 4.1) and poses a serious problem for the backflow model

in terms of explaining long wings. We therefore discuss this point in some detail below.

The problem of subsonic expansion can be broken into two distinct objections: (1) If the wings grow subsonically while the primary lobes grow supersonically, how can wings be longer than the lobes? and (2) Subsonic expansion implies wing lifetimes of more than 100 Myr for sources hundreds of kpc across. The first objection is easier to reconcile with our models because our jets provide a natural mechanism for the subsonic expansion of the lobes, and it is not clear whether most radio galaxies (even powerful ones) really do expand very supersonically. Further, as we have noted, projection tends to enhance wings. However, the lifetimes of large sources are more difficult to explain.

To see this, consider that for a rich cluster atmosphere with $kT \sim 10$ keV (this corresponds to a $c_s \sim 1000$ km s^{-1} or, conveniently, 1.0 kpc Myr^{-1}), subsonic growth implies that wings 100 kpc from base-to-tip would be at least 100 Myr old. In group environments, where $c_s \lesssim 500$ km s^{-1} and monotonically declines at large radii (Sun et al. 2009), the longest observed wings (e.g. 3C 315 whose wings span ~ 400 kpc) could be almost 500 Myr old! Even if AGN activity persisted this long, synchrotron cooling might set in: if the bulk flows of replenishing backflow travel at a lobe sound speed $10c_s$, they would take between 20–100 Myr to replenish the leading edges of the wings. Depending on the break frequency and assuming magnetic fields in equipartition (B of a few μG) and a Lorentz factor γ of several$\times 10^3$, this may easily exceed the radiative cooling time.

To solve this problem, variations of the backflow model require that the wings actually do expand supersonically. In the "overpressured cocoon" model (Capetti et al. 2002), supersonic wing growth is achieved through sustained pressure-driven expansion, whereas in the "buoyant backflow" model (Worrall et al. 1995), wings are

driven by the nearly free expansion of diverted hypersonic back-flows. Our models reproduce overpressured cocoons and hypersonic back-flows, but the overall wing advance speed is subsonic.

For the overpressured cocoon model to produce long wings, a sustained overpressured state must be maintained to drive outflows. However, in our models the highly overpressured cocoon that forms soon after ignition quickly expands to reach pressure equilibrium: the supersonic expansion phase lasts at most around 15% of the lifetime of the radio galaxy regardless of the jet we inject (e.g. Figure 4.4). As the radius of the (isobaric) cocoon grows, its pressure falls much more rapidly than does that of the surrounding atmosphere at a similar radius (see also Zanni et al. 2003, Figure 2 in their paper), so the advance speed of the lateral cocoon expansion falls precipitously from a peak of about Mach 2. Thus, overpressured expansion appears to be relevant only very early in the life of the source and by itself can produce only short wings. Indeed, this conclusion is supported by earlier simulations (Zanni et al. 2003) where even in advantageous triaxial atmospheres, the overpressured cocoon produced at most an intrinsic W/L of ~ 0.5 (the jets in their work were held at constant velocity and W/L would thus decrease over time). Saripalli & Subrahmanyan (2009) suggest that the overpressured state may instead result from backflow piling up upon reaching the central (dense) region of the galaxy. Our models do not support this scenario, since the cocoon is contiguous and nearly isobaric throughout the active phase.

The buoyant backflow model argues that a combination of buoyancy forces and wings driven by hypersonic flows produce large X-shaped sources. For instance, Dennett-Thorpe et al. (2002) estimate that the current outburst in 3C 403 (Figure 4.1) started 16 Myr ago. If this outburst was solely responsible for generating the ~ 100 kpc wings hydrodynamically (as preferred by Kraft et al. 2005), the av-

erage expansion speed of the wings would have to be ~ 8000 km s^{-1} ($0.027c$). In contrast, a typical sound speed for galaxy groups is $c_s \lesssim 500$ km s^{-1}, a factor of 16 smaller. Likewise, Worrall et al. (1995) prefer hypersonic expansion. What could drive such wings? The answer invoked by these authors is redirected back-flows, which can be accelerated at the terminal hot spots up to a few percent of c (based on the spectral ageing–distance method of Alexander & Leahy 1987). The observational inference of high backflow speeds is consistent with our models and others (e.g. Antonuccio-Delogu & Silk 2010), which find back-flow speeds of about twice the lobe sound speed ($c_{s,\mathrm{lobe}} = 10c_s$). Further, Saripalli & Subrahmanyan (2009) argue that the collimated morphologies of some wings requires some driving force.

However, it is not evident that these laminar back-flows can be harnessed to drive wing expansion (see the prior prediction). Subsonic wing growth in our simulations is a natural consequence of the tendency of backflow (lobe material) to mix and expand. The fast back-flows from the terminal shocks merge near the midplane, dissipating their speed and driving flows into the wings which are subsonic relative to the low-density material in the lobes (Figure 4.3), although they are still supersonic relative to the background. These flows then expand and decelerate further in the wings, dissipating their thrust over a very large area. Hence, detection of $10^3 - 10^4$ km s^{-1} flows in the wings would be insufficient evidence for hypersonic wing expansion. Supersonic wing expansion would require collimation to prevent thrust dissipation.

Can a collimation mechanism be found? An obvious possibility we have not included is ordered magnetic fields, since particles can move along them much more easily than across, but (Huarte-Espinosa et al. 2011) find that in FR II sources, lobe magnetic fields become turbulent on timescales of ~ 10 Myr. More generally, we note that (weak) shocks found around double-lobed radio sources often imply cocoon expansion near Mach 1. If a powerful jet cannot drive highly supersonic

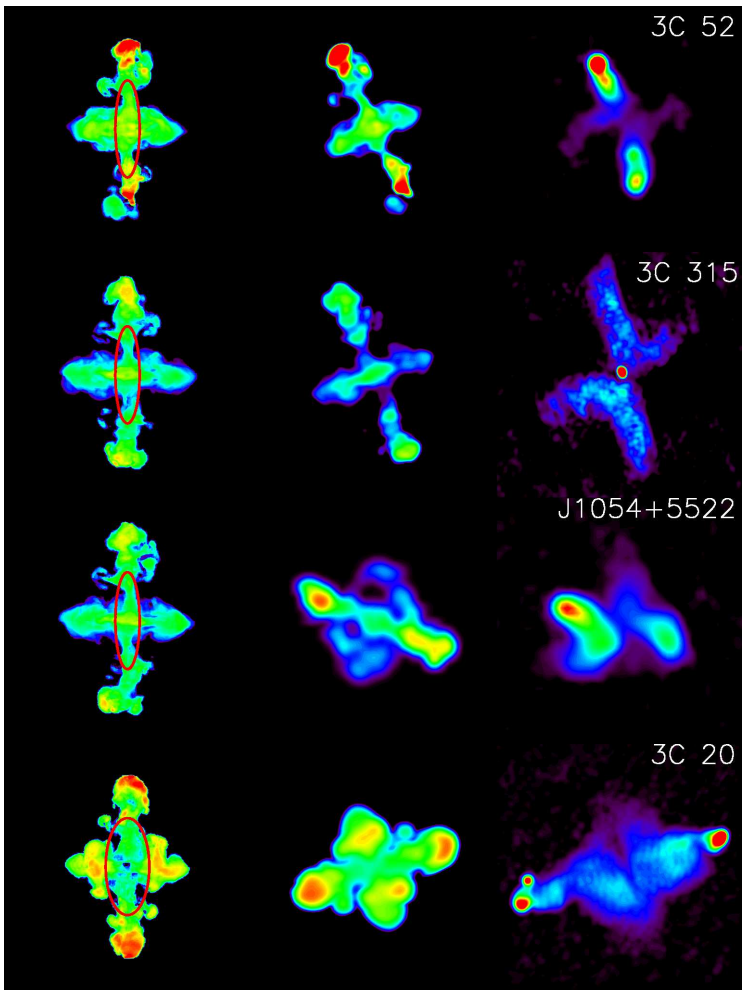

Figure 4.9 continued

expansion, it seems unlikely that less powerful, more disorganized backflow could do so.

Lastly, it is important to emphasize that subsonic expansion is only a serious problem for very large wings or very young AGN with a large W/L ratio. Our simulations can reproduce most winged and X-shaped sources with subsonic expansion if the AGN outburst is between 10–100 Myr old instead of 1–10 Myr. These simulations are also not the final word, as they only solve the equations of hydrodynamics in a relaxed, non-dynamic atmosphere.

4.5.2 Assessment

Our results, taken in context, strongly implicate a hydrodynamic origin for X-shaped sources and a common origin for winged and X-shaped sources. We can produce bona fide XRGs (i.e., with intrinsic $W/L > 0.8$) with a single outburst from a jet with a plausible time dependent kinetic luminosity on timescales broadly consistent with observed sources. The radio galaxies we produce are consistent with prior simulations, and faithful reproductions of observed radio galaxies can be generated by tuning the viewing angle (Figure 4.9). These sources are also consistent with most observed properties of the XRG population outlined above, and our simulations reproduce elements of the overpressured cocoon and buoyant backflow models while relying solely on the interaction of the radio lobe material with an anisotropic environment. Hence, the backflow model remains a strong contender for the origin of XRGs—it would be surprising if some XRGs were *not* produced in this manner.

However, our simulations also present new challenges to the proposals in the literature: we find that long wings require unusually elliptical atmospheres and expand subsonically, making very long wings difficult to explain. Having examined the deficiencies of our simulations, we cannot identify an obvious internal remedy; we note that pre-existing channels are necessary (in the backflow model) for some sources in the literature and may be generally important.

The final prediction of our simulations is therefore that the XRG population is heterogenous and *the backflow model works in tandem with other hydrodynamic models rather than solely on its own.* In short, this is because our models make it too difficult to produce XRGs given their observed frequency.

Consider that winged and X-shaped sources make up 5–10% of double-lobed radio sources. If, as in our models, X-shaped sources are produced by a fortunate

coincidence of jet geometry, ISM ellipticity, and jet power, we might imagine that the fraction of X-shaped sources is some function of each of these variables. In the simplest case, where each of these factors contribute independently to promoting wings, the fraction of XRGs might look like

$$f_{\rm XRG} \propto f_{\rm P.A.}^{\alpha} f_{\epsilon}^{\beta} f_{{\rm kin.}L}^{\gamma}, \tag{4.14}$$

where $f_{\rm XRG}$ is the fraction of double-lobed sources which are X-shaped and the other f values represent the fraction of sources for each variable which meet the threshold criterion for wings. The exponents are unknown measures of the relative importance of each variable. Obviously, the fraction of XRGs must be smaller than the fraction of sources which meet any one criterion.

Now, consider that virtually all double-lobed radio galaxies emanate from elliptical hosts, and have apparently random jet–major axis orientations (as opposed to the very weakest radio-emitting AGN whose jets seem to be pointed along the minor axis of their hosts; Browne & Battye 2010). Our models suggest that a jet within $\sim 15^{\circ}$ of the major axis of its host is required to produce wings. In a uniform distribution of radio jet position angles, we would thus expect that $f_{\rm P.A.} \sim 15/90 \approx 0.17$. Assuming all powerful jets have a kinetic luminosity function conducive to forming XRGs, we still require about half of all sources where the jet is co-aligned with the major axis to have high ellipticity (assuming the exponents are all equal to unity). Given that ellipticity is clearly a very sensitive parameter and that the peak ϵ of powerful radio galaxy hosts is far below the wing threshold (Smith & Heckman 1989), it is clear that our simulations (in this oversimplified formulation) underpredict the observed frequency of winged sources. In other words, wings are *too difficult* to make in our models.

To reconcile this result with the observations, either our models must be fundamentally deficient with respect to the behavior of backflow or they require alternate

mechanisms to form proto-wing channels such as the jet–stellar shell interaction model of Gopal-Krishna & Wiita (2010) or the jet–merging ISM explanation for Z-shaped sources in Zier (2005). As we have seen, backflowing material reinforces any proto-wings and can turn them into full-fledged wings if the original mechanism fails to do so; making the channels in the first place is what the backflow model cannot easily do.

Thus, we propose that the backflow model has a commensal relationship with other hydrodynamic mechanisms for forming wings by reinforcing and growing any pre-existing channels accessible to a jet pointed along the major axis of its host galaxy. These channels would naturally grow most easily along the steepest pressure gradient. In cases where the jet power and atmosphere size match appropriately, these channels would be produced by the expansion of an overpressured cocoon as in our simulations. In other cases, channels could be produced by the interaction of the jet with structure in the ISM or by minor mergers. In this scenario, we would still expect to see most of the predictions of our simulations listed above for the case of pure backflow in a relaxed atmosphere.

It is important to consider that the percentage of radio galaxies classified as XRGs is based on a flux-limited sample rather than a volume-limited one. There are many low-luminosity radio galaxies beyond the luminosity range in which XRGs appear, so the total fraction of XRGs is a gross upper limit. On the other hand, considering only powerful jets (at lower radio galaxy luminosity, jets are preferentially co-aligned with the minor axis of the host galaxy; Browne & Battye 2010), the arguments above still apply.

4.5.3 Distortions to the Canonical Double-Lobed FR II Radio Galaxy

At this point, it is worth revisiting the buoyant backflow model as phrased in Leahy & Williams (1984), where XRGs are unified with other distortions to the canonical FR II model (about two thirds of strongly bridged radio galaxies show central distortions) by the deflection of backflow around a denser medium. These distortions may also be related to radio galaxies with interrupted bridges by the "superdisk" model (Gopal-Krishna & Wiita 2009), in which gas displaced by a galaxy merger is believed responsible for docking the lobes in an asymmetric manner.

Because the backflow model as expressed in our simulations depends only on a fortuitous combination of atmosphere morphology and jet behavior to produce winged sources, we can indeed reproduce the basic bridge distortions of Leahy & Williams (1984). However, we cannot reproduce long Z-shaped sources and some asymmetric distortions which do not appear to be the result of bulk motion or cluster turbulence. These include sources with a single wing on one side, sources with wings which themselves bend dramatically, sources with one FR I lobe and one FR II lobe (HYMORs; Gopal-Krishna & Wiita 2000). Again, the main hindrance seems to be the inability to channel backflow; jets which bend may solve this problem. Although there are elements of the behavior of backflow which we do not presently understand, we come to the same conclusion as with X-shaped sources: the backflow model can account for other bridged distortions only in tandem with another hydrodynamic mechanism.

4.6 Summary and Conclusions

We have conducted a series of three-dimensional hydrodynamic simulations of light, hypersonic jets to study the viability of the backflow model for the formation of wings in X-shaped radio galaxies. The XRGs seem to be a population unto themselves, with characteristic environmental geometry, radio power, black hole mass, etc., and any successful model must account for these peculiarities. Our main results follow.

1. The jets, back-flows, and lobes in our simulations are similar to those in the recent literature, giving us confidence in the usefulness of our simulations as probes of the backflow model.

2. Wings in our models form in two stages: the establishment of channels or proto-wings and then buoyant (usually subsonic) expansion. Specifically, our models corroborate the overpressured cocoon model of Capetti et al. (2002) early on, but as cocoons quickly come to pressure equilibrium with their surroundings, most of the wing length represents subsonic expansion (Figure 4.3).

3. We have produced prominent wings by geometry and radio power alone, proving that the backflow model can, in principle, make X-shaped sources (Figure 4.2 and 4.9). Both the atmosphere and jet kinetic luminosity as a function of time are crucial to forming X-shaped sources.

4. Long wings are produced in a relatively small portion of parameter space, requiring galaxies with high ellipticity, decaying jets, proper jet orientation, and appropriate atmosphere size (Figures 4.7 and 4.8).

5. The main challenges to the backflow model are the requirement for high ellipticity and subsonic wing growth. Adding additional physics is not obviously

helpful. The backflow model seems to require an additional mechanism to make proto-wings which the backflow reinforces; in our models, we make these channels by the initial expansion of an overpressured cocoon in an anisotropic environment, but this cannot explain every XRG. We cannot form new channels solely by deflecting back-flows.

6. If the backflow model can overcome the issues noted above, it is a very strong candidate for explaining X-shaped and other disturbed radio galaxies. Our models naturally reproduce many of the characteristics of the XRG population (Table 4.4).

There are several natural extensions of this work which promise to be fruitful. First, adding magnetic fields and investigating other potential collimating mechanisms may rule out or boost the backflow model depending on the wing expansion speeds attained. Second, our models rely on the formation of channels misaligned with the jets; these have been proposed in several other contexts as well to explain radio galaxy morphology. The origin of these channels is not known, and identifying and testing candidates would be important for wing formation models. Third, more realistic jets could determine whether the backflow model can support both long wings and active FR II lobes with hot spots; the bending of the jets in particular is an important issue. Finally, models which produce the wings hydrodynamically but not explicitly by the deflection of backflow (e.g. the recently proposed stellar shell model Gopal-Krishna & Wiita 2010) are worth exploring by making the atmospheres more complex in tandem with more realistic jets.

Chapter 5

Summary & Future Work

5.1 Summary

This thesis project set out to answer two fundamental questions about the morphology of X-shaped radio galaxies:

1. Are XRGs and similar distortions *aware* of their hot atmospheres?

2. Can radio galaxies *respond* to their hot atmospheres in such a way to produce X-shaped morphology?

We addressed the first question from an observational standpoint, using the *Chandra* X-ray Observatory to image the hot atmospheres (both ISM and IGM/ICM) of nearby known and candidate XRGs (Cheung 2007) and comparing the results with optical and radio images. The second question is more difficult to answer from a purely observational standpoint, so we used three-dimensional hydrodynamic simulations to study the response of radio galaxies to anisotropic pressure gradients in the hot atmospheres. We summarize the main results presently:

1. XRGs tend to have jets co-aligned with the major axes of their hot atmospheres

and wings co-aligned with the minor axes, in agreement with the Capetti et al. (2002) and Saripalli & Subrahmanyan (2009) studies in the optical.

2. The ISM and IGM/ICM are separable in most observations of XRGs in which extended emission is detected. The ISM appears to generally follow the optical isophotes, as naively expected but challenged by Diehl & Statler (2007).

3. A deep X-ray observation of one XRG which disobeys this trend suggests that rapid jet reorientation is a more likely scenario in that case and demonstrates the power of X-ray observations to study all XRG formation hypotheses.

4. Hydrodynamic modeling of XRGs suggests that purely hydrodynamic effects can produce winged morphology in the presence of asymmetric pressure gradients. This morphology strongly resembles observed morphology in many cases.

5. However, in our models wings tend to expand subsonically and the backflows become disorganized. Long wings also require extreme asymmetry. Our models easily produce wings intrinsically shorter than the primary lobes, but the hydrodynamic hypotheses of XRG formation must account for very long wings.

This work makes a strong circumstantial case for the hydrodynamic models of XRG formation, but significant obstacles remain before these models can be accepted.

5.2 Future Work & Challenges

Like many problems in astronomy, discovering the origin of winged and X-shaped morphology is difficult primarily due to the lack of data—in this case, a way forward seems likely to come from low-frequency (MHz) radio observations, acquiring a larger sample of XRGs with high resolution soft X-ray data, or from the hard X-rays for those XRGs whose lobes cool via inverse Compton emission. Most of the radio galaxies have been observed in the GHz band, although at different resolutions and depths. We propose that in this band, the most important work is carrying on the efforts of Cheung (2007) to classify XRGs, determine what fraction of radio galaxies they represent, and look for distinctions between truly X-shaped sources and Z-shaped or other disturbed morphology. The absence of clear distinctions would indicate either that the secondary lobes in XRGs and other wing-like distortions to the classical double-lobed morphology have a common origin or that both fossil lobes and pressure-driven or buoyant wings behave similarly once formed. We shall return to the latter possibility below.

Despite the progress made on the X-ray front, the sample of XRGs with usable X-ray data is remarkably small—within $z < 0.2$, there are only ∼30 XRGs, 16 of which have some *Chandra* data. Of these, only about half are deep enough exposures to reveal a hot atmosphere. Since no upcoming soft X-ray detector will have the spatial resolution of *Chandra* and concurrent missions (such as XMM-*Newton*) have insufficient resolution, progress on this front requires further *Chandra* data. Given the relatively small sample of XRGs within $z < 0.2$ (where the spatial resolution and surface brightness are sufficient to isolate the ISM from the IGM/ICM), it is feasible to obtain shallow *Chandra* exposures for all XRGs (as in most of the sample in Chapter 2) and deep ones for the objects of interest. Upcoming missions such

as NuSTAR will likely detect many radio galaxies in the hard X-ray band because of inverse Compton scattering of the CMB or synchrotron seed photons. If some of these sources are XRGs, hard X-ray observations will be important to understanding the winged morphology and the age of plasma in the wings. As Lal & Rao (2007) found, some wing plasma appears to be "new" (i.e., replenished from the primary lobes) whereas other wings appear to have "old" plasma based on synchrotron ages. Hard X-ray imaging in tandem with low-frequency radio observations would provide additional age constraints. Optical data seem less likely to be useful, although as Mezcua et al. (2011) found, the black hole masses in XRG host galaxies tend to be larger than average for radio galaxies (all radio-loud objects have black hole masses above $10^8 M_\odot$; Chiaberge & Marconi 2011).

With regards to simulations, hydrodynamic models such as the ones presented in Chapter 4 are important as first approximations to radio galaxy evolution, but do not include much of the relevant physics. For instance, the action of viscosity may be important to bubble evolution, but due to the limitations in dynamic range, it is typically implemented in a formulaic way. It is unclear if this is sufficient for modeling unresolvable radio galaxy physics. Moreover, magnetic fields and special relativity are obviously important to radio galaxies even if, to first approximation, these objects act as light, hot fluids. On the other hand, models which attempt to add as much physics as possible are computationally expensive, even prohibitively so for searches of parameter space like the ones shown in Chapter 4. As our own modeling has proven, hydrodynamic explanations for XRG wings must go beyond plausibility arguments and may be very sensitive to ambient conditions.

There is no line of inquiry that will obviously pay large dividends in terms of explaining the origin of XRGs—sensitivity and time requirements limit the X-ray avenue, current radio and X-ray observations suggest a hybrid population, and nu-

merical modeling must be preceded by an understanding of what the most important physics is. However, as a population XRGs are interesting for another reason: observational tests of radio-mode AGN feedback theory.

One of the most surprising discoveries by *Chandra* is the ubiquity of X-ray cavities associated with radio galaxies, the presence of which has been used to demonstrate significant energy injection into the ICM by the AGN (Chapter 1). These cavities are surface brightness decrements blown by AGN outbursts in which the relativistic plasma of the radio lobes displaces the ICM. The energy injection is estimated by the volume of the cavity, since to displace the X-ray emitting gas, the AGN must have done approximately $4PV$ of work, where V is the cavity volume and P is the ambient pressure—typical values are on the order of 10^{58-60} erg. Despite these tremendous energies, it is unclear how the energy makes its way into the ICM, thereby heating the gas and preventing a cooling catastrophe in cool core clusters. There have been various models of the evolution of such cavities once the AGN turns off (for early work, see Reynolds et al. 2002), but as the bubbles buoyantly rise they become increasingly difficult to see with X-ray observations because the X-ray surface brightness declines with radius. The bubbles may, to some extent, be studied via their synchrotron emission at MHz frequencies, but at such long wavelengths it is difficult to achieve the high resolution necessary to determine the level of mixing between the bubble and its environs. Moreover, X-ray observations are required to measure local temperature and pressure. However, since X-ray observations of distant cavities are expensive, studies of cavities in the literature are predominantly concerned with active AGN outbursts near the cluster core.

Now consider that according to XRG formation scenarios, the wings are either fossil remnants or their propagation and morphology is determined by the structure of their environment. In either case, XRGs present an opportunity to study bubbles

of relativistic plasma that are *not* driven by jets but also happen to be near the cluster core where the X-ray surface brightness is high. The radio emission acts not only as a guide to where the cavities are located, but also as a probe of magnetic field structure (via polarization) and strength. Thus, high S/N X-ray observations of XRGs are one way to examine the behavior of bubbles once the jet has ceased. Even though most XRGs are *not* in rich cool core clusters, bubble evolution is a critical part of understanding AGN feedback; many cosmological simulations which incorporate AGN feedback simply assume that the energy injected into the cavity is isotropized in the ICM on some timescale.

As a proof of concept, we appeal to the only two deep *Chandra* exposures of XRGs in which an extended IGM is securely detected: 4C +00.58 and NGC 326. The former galaxy has been thoroughly studied in Chapter 3, and we only note that X-ray cavities have been detected along both of the wing axes. The archival data for NGC 326 (PI: D. Worrall) are unpublished except for a brief extraction of X-ray morphology in Hodges-Kluck et al. (2010a). Figure 5.1 shows the soft X-ray image ($0.3 - 3$ keV), harder $3 - 5$ keV image, and temperature and pressure maps (pressure is computed by assuming a radius for each bin in Figure 5.1 and using a spherical volume). In both 4C +00.58 and NGC 326, significant cavities associated with the wings are evident (Figure 5.2). We intend to follow up these detections by characterizing the cavities in the X-ray map and looking for additional insight from radio maps. A preliminary analysis of the NGC 326 data is under way. Further progress along this vein requires more deep *Chandra* exposures (XMM-*Newton* has sufficient spatial resolution to search for wing cavities in a few XRGs as well), and hence research proposals.

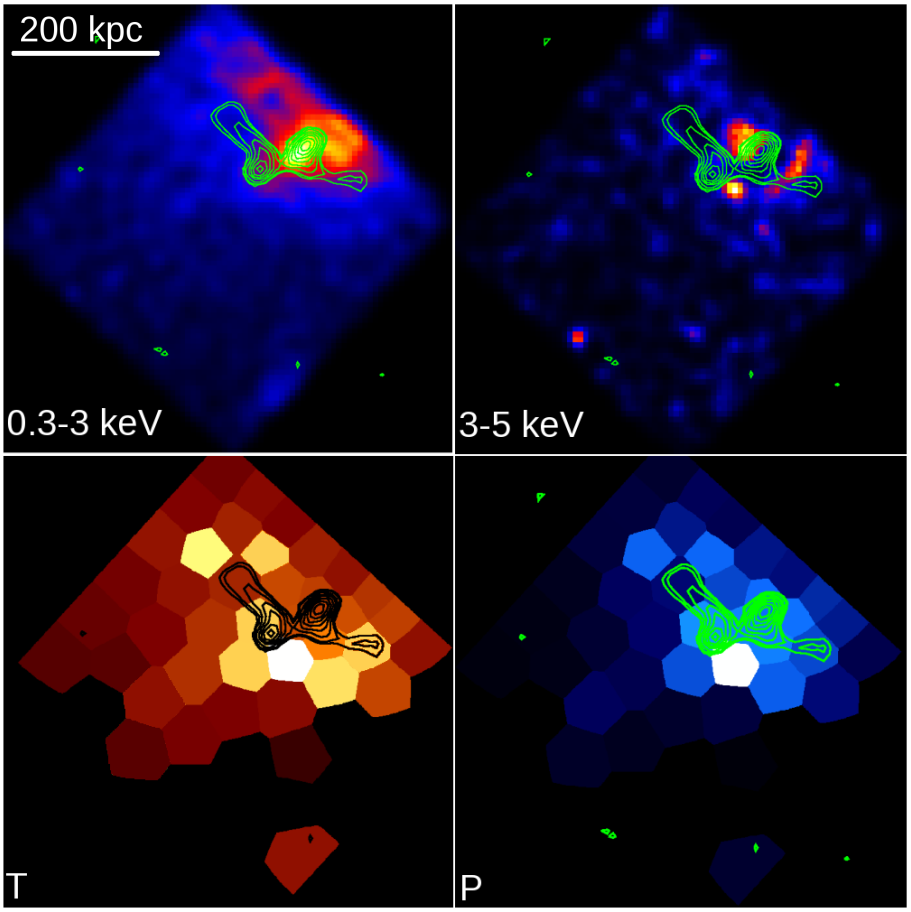

Figure 5.1 Maps of NGC 326 in $0.3 - 3$ keV (top left), $3 - 5$ keV (top right), temperature (bottom left), and pressure (bottom right). Temperature and pressure are computed from (single-temperature) spectral fits to regions defined by adaptively binning the surface brightness using weighted Voronoi tessellation. Black regions indicate insufficient photons to measure a temperature. Overlaid are the 1.4 GHz contours.

5.3 Conclusions

The work presented in this thesis represents a significant step forward in understanding the role of the hot atmospheres in the morphology of X-shaped radio galaxies, but even while generally validating the hydrodynamic models, our results demonstrate that these models cannot by themselves explain the observed XRGs. Crucially, our work also demonstrates the power of X-ray observations to probe other XRG for-

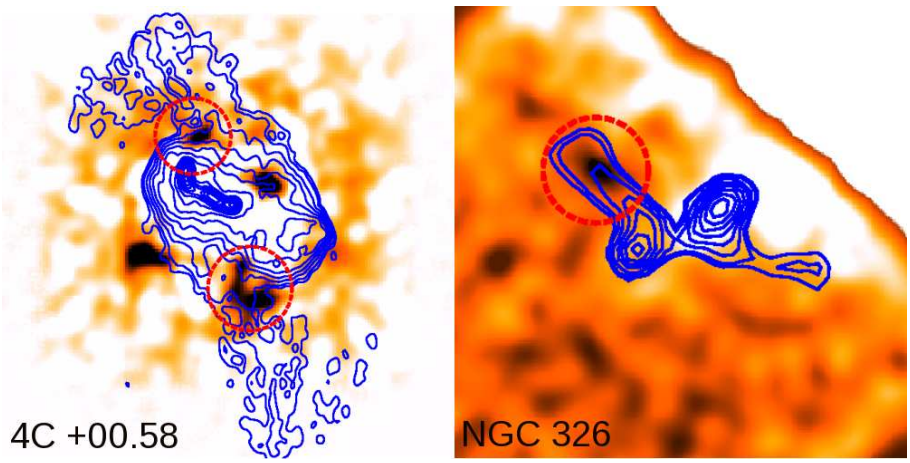

Figure 5.2 Unsharp masks of X-ray maps showing cavities associated with wings in 4C +00.58 and NGC 326 (dashed red circles). The unsharp mask is made by subtracting a smoothed version of the image from the raw image, thereby enhancing edges and asymmetric features. 4C +00.58 also has cavities along a different axis (Chapter 3). The edge at upper right in the map of NGC 326 is the edge of the ACIS-S3 chip.

mation mechanisms such as rapid jet reorientation. As discussed above, the best way forward is presently unclear. Generally, there seems to be a divide between astronomers interested in radio galaxies for their own sake and astronomers interested in radio-mode feedback. X-shaped radio galaxies are an excellent meeting ground for the two.

5.4 Acknowledgments

Support for this work was provided by the National Aeronautics and Space Administration through Chandra Award Numbers GO89109X, GO90111X, and GO011138A issued by the Chandra X-ray Observatory Center, which is operated by the Smithsonian Astrophysical Observatory for and on behalf of the National Aeronautics Space Administration under contract NAS8-03060.

This research has made use of the NASA/IPAC Extragalactic Database (NED)

which is operated by the Jet Propulsion Laboratory, California Institute of Technology, under contract with the National Aeronautics and Space Administration.

The Digitized Sky Surveys were produced at the Space Telescope Science Institute under U.S. Government grant NAG W-2166. The images of these surveys are based on photographic data obtained using the Oschin Schmidt Telescope on Palomar Mountain and the UK Schmidt Telescope. The plates were processed into the present compressed digital form with the permission of these institutions.

Funding for the SDSS and SDSS-II has been provided by the Alfred P. Sloan Foundation, the Participating Institutions, the National Science Foundation, the U.S. Department of Energy, the National Aeronautics and Space Administration, the Japanese Monbukagakusho, the Max Planck Society, and the Higher Education Funding Council for England. The SDSS Web Site is http://www.sdss.org/.

The SDSS is managed by the Astrophysical Research Consortium for the Participating Institutions. The Participating Institutions are the American Museum of Natural History, Astrophysical Institute Potsdam, University of Basel, University of Cambridge, Case Western Reserve University, University of Chicago, Drexel University, Fermilab, the Institute for Advanced Study, the Japan Participation Group, Johns Hopkins University, the Joint Institute for Nuclear Astrophysics, the Kavli Institute for Particle Astrophysics and Cosmology, the Korean Scientist Group, the Chinese Academy of Sciences (LAMOST), Los Alamos National Laboratory, the Max-Planck-Institute for Astronomy (MPIA), the Max-Planck-Institute for Astrophysics (MPA), New Mexico State University, Ohio State University, University of Pittsburgh, University of Portsmouth, Princeton University, the United States Naval Observatory, and the University of Washington.

Appendix A

Glossary

2MASS	Two-Micron All-Sky Survey (catalog of astronomical objects)
3C, 4C	3rd and 4th Cambridge Catalog of Radio Sources (catalog of astronomical obj
ACIS	AXAF CCD Imaging Spectrometer (*Chandra* instrument)
AGN	Active galactic nucleus/nuclei
AXAF	Advanced X-ray Astrophysics Facility (now *Chandra*)
CCD	Charged-couple device
Chandra or CXO	Chandra X-ray Observatory
CIAO	*Chandra* Interactive Analysis of Observations data reduction package
DRAGN	Double Radio-source AGN
DSS	Digital Sky Survey (catalog of astronomical objects)
EVLA	Expanded Very Large Array
Hubble or HST	Hubble Space Telescope
FIRST	Faint Images of the Radio Sky at Twenty-centimeters (catalog of astronomical
FR I/II	Fanaroff-Riley type I/II radio galaxy
FWHM	Full width at half maximum
GOATS	particularly emphatic form of "goats"
HRC	High Resolution Camera (*Chandra* instrument)
HRMA	High Resolution Mirror Assembly (*Chandra* mirrors)
HYMOR	Hybrid-morphology radio galaxy (FR I and FR II morphologies)
ICM	Intracluster Medium
IGM	Intergalactic Medium
ISM	Interstellar medium
LMXB	Low-mass X-ray binary consisting of a low-mass star and a compact object
MHD	Magnetohydrodynamic(s)
NED	NASA/IPAC Extragalactic Database
NGC	New General Catalogue (catalog of astronomical objects)
NRAO	National Radio Astronomy Observatory
NVSS	NRAO VLA Sky Survey (catalog of astronomical objects)
PKS	Parkes Radio Sources Catalog (catalog of astronomical objects)
PSF	Point Spread Function
ROSAT	ROentgen SATellite (X-ray observatory)
SED	Spectral Energy Distribution (as a function of frequency)
SDSS	Sloan Digital Sky Survey
SMBH	Supermassive black hole
VLA	Very Large Array
WMAP	Wilkinson Microwave Anisotropy Probe
XRB	X-ray binary
XMM-Newton	X-ray Multi-mirror Mission (X-ray observatory)
XRG	X-shaped Radio Galaxy

Sky Coordinates	
($''$)	arcsecond (unit of angular distance on sky)
($'$)	arcminute (unit of angular distance on sky)
Dec (δ)	Declination (used with Right Ascension to specify location on the sky)
RA (α)	Right Ascension (used with Declination to specify location on the sky)
P.A.	Position Angle (measured counter-clockwise from North)
Units of Distance & Time	
pc	parsec ("parallax-arcsecond"); 3.26 light years; $3.086 \times 10^1 8$ cm
kpc	kiloparsec (10^3 pc)
Mpc	Megaparsec (10^6 pc)
Myr	Megayear (10^6 yr)
z	Cosmological Redshift
Units of Detection & Energy	
Å	Angstrom (10^{-8} cm)
GHz	Gigahertz (10^9 Hz)
MHz	Megahertz (10^6 Hz)
eV	electron volt (1.602×10^{-12} erg)
keV	kilo-electron volt (10^3 eV; 1.602×10^{-9} erg)
mag	magnitude; a logarithmic form of flux in which $m_1 - m_2 = -2.5 \log(F_1/F_2)$
Timescales & Mathematical Shorthand	
c_s	Sound speed
kT	Temperature in units of energy
L_X	X-ray luminosity (isotropic)
N_H	Column density of neutral hydrogen (e.g., for Galactic absorption)
S/N	Signal-to-noise ratio
$t_{\rm ff}$	Free-free (thermal bremsstrahlung) cooling time
$t_{\rm sync}$	Synchrotron cooling time
$t_{\rm exp}$	Cavity expansion time

Appendix B

Synchrotron & Inverse Compton Radiation

B.1 Synchrotron Radiation

Charged particles moving in a magnetic field are subject to the $\vec{v} \times \vec{B}$ Lorentz force. This force accelerates the charge, producing radiation, and causes the charge to execute circular motion in the plane parallel to the magnetic field. The radiation emitted by this motion is *cyclotron radiation*. If the particles involved are moving at relativistic speeds, beaming of the radiation produced by the particle's gyration instead leads to *synchrotron radiation*.

Synchrotron radiation is ubiquitous in astrophysics and is one of the most prominent sources of "non-thermal" radiation (i.e., continuum radiation emitted by particles with a non-Maxwellian energy distribution). For instance, diffuse radio emission from our and other galaxies is synchrotron emission, where the particle acceleration is typically ascribed to supernova shock fronts and the magnetic fields are provided by the hot interstellar medium. The radio emission from radio galaxies is also syn-

chrotron emission, so a brief exposition of synchrotron radiation is important to this thesis.

In this section, we will briefly describe the synchrotron emission mechanism and the resultant spectrum from a power-law distribution of electrons, leaving the (substantial) formalism to standard textbooks such as Rybicki & Lightman (1979) or Pacholczyk (1970). Expressions in this section are given as guideposts for a qualitative discussion rather than derivations. The results important for this work are the synchrotron cooling time $t_{\rm sync}$, what is meant by the spectral index α, and the "steepening" of the spectrum with age for a cooling population of electrons.

B.1.1 Synchrotron Emission from a Single Electron

A particle in a constant magnetic field (with no electric field) has an equation of motion

$$\frac{d}{dt}(\gamma m\vec{v}) = \frac{q}{c}\vec{v}\times\vec{B}, \tag{B.1}$$

where $\gamma \equiv (1 - v^2/c^2)^{-1/2}$ is the Lorentz factor. Hereafter, we consider the case in which the particles are electrons. The electron's angular frequency about a field line ω_B is given by the familiar cyclotron frequency, but lower by a factor of γ due to the higher inertial mass of the electron:

$$\omega_B = \frac{\omega_c}{\gamma} = \frac{ecB}{\gamma m_e c^2}, \tag{B.2}$$

where the c in the numerator is left explicitly to show that the denominator is the mass-energy of the electron. If the particle has a velocity component along the field, the resulting motion is helical.

The power radiated by this electron is given by the general Larmor formula transformed to the observer's frame, resulting in a factor γ^4 more power than in the

non-relativistic case:

$$\frac{dE}{dt} = \frac{2}{3}\frac{e^2}{c^3}\gamma^4 a^2, \tag{B.3}$$

where a is the acceleration–in this case, the Lorentz force. After some manipulation, one obtains

$$\frac{dE}{dt} = 2\left(\frac{B^2}{8\pi}\right)\sigma_T \gamma^2 v^2 \sin^2\alpha, \tag{B.4}$$

where σ_T is the Thomson cross-section and α is the "pitch angle" between $\vec{v}$ and $\vec{B}$. The $B^2/8\pi$ term is the magnetic energy density u_B. Averaging over all possible pitch angles, the synchrotron power per electron is

$$\frac{dE}{dt} = \frac{4}{3}\sigma_T c \gamma^2 \beta^2 u_B, \tag{B.5}$$

where $\beta = v/c$.

When the electron is relativistic, the normal dipole radiation emitted in the frame of the electron is beamed in the frame of the observer (relativistic abberation), meaning that it is emitted into a narrow cone along the direction of motion. This means that emission is effectively visible only when the particle is directed towards the observer, and only for a very brief period of time (the opening angle of the cone θ is given by $\theta = \gamma^{-1}$). Hence, in the time domain, the observer sees a train of very narrow but widely separated pulses. The observed synchrotron spectrum in the frequency domain is the Fourier transform of this time series, so the relatively long delays between pulses become extremely short intervals in frequency space. Thus, the spectrum is approximately a series of very closely-spaced δ-functions up to a cut-off frequency corresponding to the time delay between pulses. In practice, electrons also emit at harmonics of the gyration frequency whose contributions become more important at large γ, and if there is a population of electrons instead of a single one (all with the same γ), the different pitch angles will broadedn the δ-functions in the pulse train. Hence, the synchrotron spectrum of electrons of a given energy

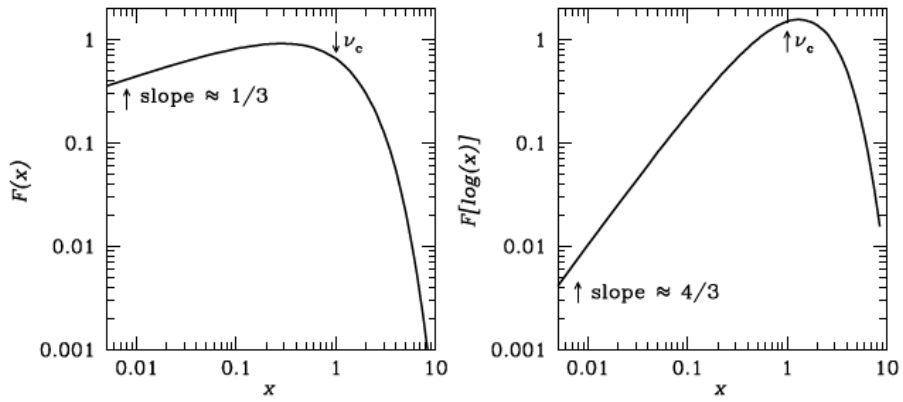

Figure B.1 Synchrotron spectrum of a single electron. Note the rise by $\nu^{1/3}$ at low frequencies and the steeper decline above $\nu_{\rm sync}$. Image taken from the "Essential Radio Astronomy" NRAO course by J. Condon & S. Ransom.

is continuous with some cutoff frequency. In fact, the spectrum is described by a modified Bessel function with a peak near the critical frequency $\nu_{\rm sync}$, given by

$$\nu_{\rm sync} = \frac{\gamma^2 eB}{2\pi m_e c} = \gamma^2 \nu_c, \tag{B.6}$$

where ν_c is the corresponding cyclotron (emitted) frequency. This spectrum is shown in Figure B.1. For $\nu \gg \nu_c$ (the peak emissivity is actually at about $0.3\nu_c$), the power radiated per frequency declines as $j_\nu \propto \nu^{1/2} e^{-\nu/\nu_c}$, whereas for $\nu \ll \nu_c$, $j_\nu \propto \nu^{1/3}$. Hence, above the critical frequency the spectrum has a much steeper decline than below.

Synchrotron emission is highly polarized. The circular motion of the electron in the plane perpendicular to the magnetic field appears like linear oscillations when viewed in that plane, so the emitted light in that plane is linearly polarized. When viewed out of the plane, typically the light has elliptical polarization.

B.1.2 Optically Thin Synchrotron Spectrum

Synchrotron emission from astrophysical sources does not come from a mono-energetic population of electrons, but rather from ensembles of electrons with some energy distribution in magnetic fields with some spatial energy density distribution and vectors pointing every which way. Hence, observed synchrotron spectra do not appear like Figure B.1. However, because the synchrotron spectrum of a single electron has a relatively sharp peak, to good approximation we can assume that all energy radiated by an electron of a given γ is emitted at the critical frequency $\nu_{\rm sync}$. Hence, a population of electrons produces a synchrotron spectrum which follows the distribution of electron energies.

A typical astronomical situation is one in which the emission is *optically thin* (picture a low-density plasma cloud where the observed emission along a line of sight is simply the integral of the plasma emissivity through the cloud), and where the electrons have a power-law energy distribution, i.e. where the number of electrons at a given energy is proportional to the energy: $N(E) \propto E^{-p}$. The emissivity as a function of frequency may then be written

$$J(\nu)d\nu = -\frac{dE}{dt}N(E)dE. \tag{B.7}$$

Since E is related to ν through the critical frequency,

$$E = \gamma m_e c^2 = (\nu/\nu_{\rm gyro})^{1/2} m_e c^2, \tag{B.8}$$

we have $dE/d\nu \propto \nu^{-1/2}$. The power $dE/dt \propto \gamma^2 B^2 \propto E^2 B^2 \propto \nu B^2$, so we obtain

$$J(\nu) \propto B^{(p+1)/2}\nu^{-(p-1)/2}. \tag{B.9}$$

Hence, the synchrotron spectrum of an ensemble of electrons with a power-law energy distribution $N(E) \propto E^{-p}$ is a power-law with a frequency dependence of

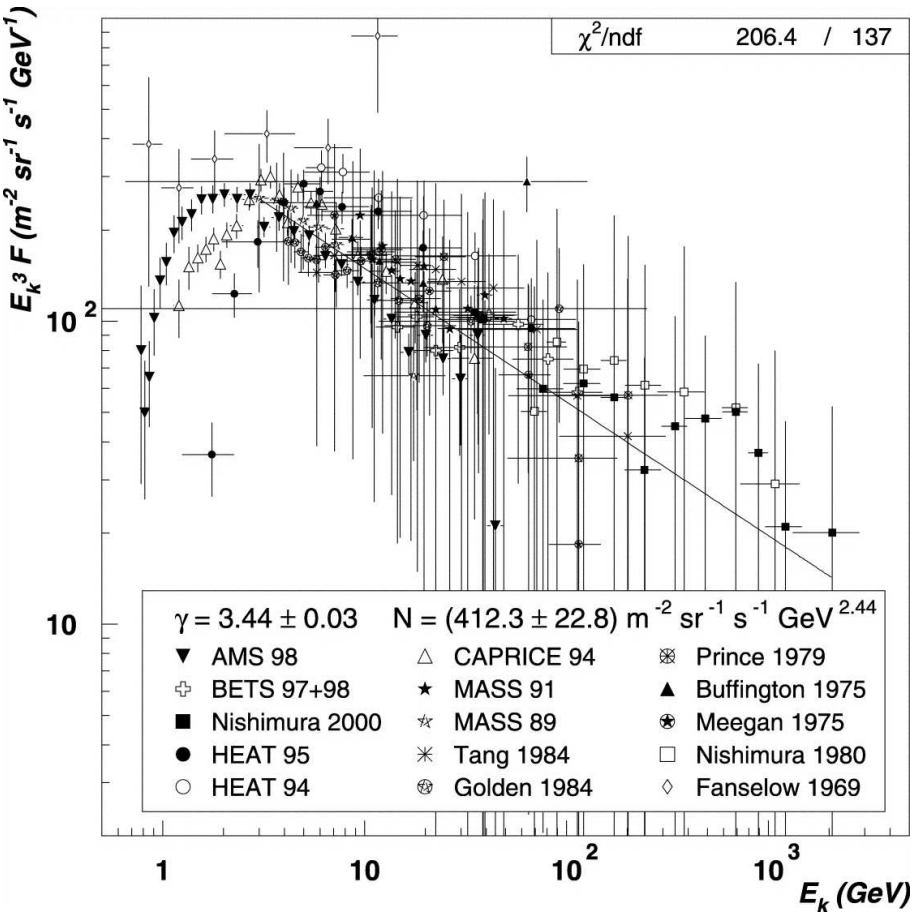

Figure B.2 Synchrotron spectrum of the ISM in our Galaxy. The best fit is a power-law electron energy distribution with some high and low-energy cutoff values and a spectral index of $\alpha \sim 0.7$ (Casadei & Bindi 2004).

$\nu^{-(p-1)/2}$. Defining the *spectral index* $\alpha \equiv (p-1)/2$,

$$J(\nu) \propto \nu^{-\alpha}. \tag{B.10}$$

Because the synchrotron spectrum follows $N(E)$, the synchrotron spectrum is likewise a power-law. Note that if one could produce a Maxwellian distribution of electron energies in the ultra-relativistic regime, the synchrotron spectrum would not be a power-law, but this is not observed.

A real synchrotron spectrum (Figure B.2) is still peaked, with the power-law behavior kicking in above some low-frequency cutoff. For an optically thin plasma, the contribution at very low frequencies is the $J(\nu) \propto \nu^{1/3}$ rise seen for individual

electrons (because this is always the behavior of individual electrons, α at low frequencies cannot be steeper than $-1/3$). The peak occurs because real power-law distributions have low and high-energy cutoff values. However, in the region of the spectrum where most observations occur, the synchrotron spectrum is a power-law. Interestingly, the typical spectral index of observed diffuse synchrotron radiation in galaxies is $\alpha = 0.7$, which is attributed to the fact that the power-law distribution of electrons accelerated in supernova shocks (the source of highly relativistic, diffuse electrons in the hot ISM) has the appropriate index. Values of α close to 0.7 are also observed in radio galaxies.

Typically, astronomers associate synchrotron emission with the radio part of the spectrum because this is where it is usually observed, indicating that electron energies and magnetic field strengths are insufficient to produce optical, UV, or X-ray synchrotron emission. However, one notable exception is in relativistic jets, where particles may be accelerated to sufficient energies that the jets appear in optical or even the X-ray bands. Another is pulsars, where γ-ray pulses have been observed and ascribed to electrons trapped very close to the pulsar surface. This has been seen, for instance, in the Crab Nebula.

B.1.3 Synchrotron Cooling and Spectral Ageing

Astronomers frequently want to estimate the synchrotron cooling time to compare it to other relevant timescales. An electron cooling by synchrotron radiation will radiate away its energy in the time

$$t_{\rm sync} \sim \frac{E}{\dot{E}} \propto \gamma B^2 \gamma^2 \propto B^{-2}\gamma^{-1}. \tag{B.11}$$

Thus, if we observe a known synchrotron source at a frequency ν, we may estimate how long the source will radiate at ν with some estimate for B and γ. Of course,

the source will fade faster at higher ν and slower at lower ν. Since the critical frequency $\nu_{\rm sync} \propto B\gamma^2$ and $\nu_{\rm observed} \sim \nu_{\rm sync}$ for electrons of a given γ, we only need to know either B or γ. Typically, B is estimated (when no better way is feasible) by a minimum-energy or equipartition argument. For instance, one may assume that the energy density of the emitting particles is equivalent to the energy density in the magnetic field. Hence, B may be estimated by observables and a few (relatively) safe assumptions. The expressions for this type of estimate require some unpacking, so we refer the interested reader to Blumenthal & Gould (1970) or Krolik (198?). Suffice it to say that while the actual field strength and distribution in the intracluster medium remain unknown, typical measured estimates are several μG. Thus, we may conveniently write $t_{\rm sync}$ as

$$t_{\rm sync} = \frac{\gamma m_e c^2}{\frac{4}{3}\sigma_T c \gamma^2 \beta^2 U_B} = 2400 \gamma_4^{-1} B_{\mu\rm G}^{-2} \text{ Myr}, \tag{B.12}$$

where γ_4 is γ in units of 10^4 and $B_{\mu\rm G}$ is B in units of 10^{-6} G. Assuming $B \sim 5\mu$G, the cooling time of electrons with $\gamma \sim 10^4$ is then $t_{\rm sync} \sim 100$ Myr. Since $\nu_{\rm sync} \sim 4 \times 10^6 B\gamma^2$ Hz, these electrons would radiate at $\nu \sim 2$ GHz. Suppose that these electrons were shock accelerated in a single event as part of a power-law distribution. Then a detection of the source at 2 GHz would place an upper limit on the age of the event whereas a non-detection would place a lower limit.

Because cooling is a function of γ, more energetic electrons cool faster, leading to a depletion at the high frequency end of a synchrotron spectrum of a cooling source. This depletion takes the form of a broken power-law, where electrons with cooling times longer than the time since the event produce a standard synchrotron spectrum. Above the knee, electrons with a high γ are rapidly depopulated (because there are many fewer of them, they do not significantly contribute to "bins" at lower γ as they cool). Hence, astronomers frequently refer to a *steep* spectrum at higher frequencies indicating cooling plasma, and by measuring the spectral index α at

several positions along a source (e.g., a radio galaxy), they can measure *spectral ageing*. For a detailed exposition, the reader is referred to Pacholczyk (1970) or Myers & Spangler (1985). The electron energy spectrum of a population subject to synchrotron cooling is given by

$$N(E, \theta, t) = N_0 E^{-p} [1 - C_2 B^2 \sin^2 \theta \times Et]^{(p-2)} \tag{B.13}$$

where C_2 is a constant given by Pacholczyk (1970), θ is the pitch angle, and t is the time since radiation began. One can see that at $t = 0$, the initial power law $N(E) \propto E^{-p}$ is recovered. The observed spectrum as a function of time can therefore be computed. However, since radio astronomers typically compare spectral indices α at several observed frequencies rather than obtaining the entire spectrum, it is usually the evolution of the spectral index which is required. Myers & Spangler (1985) define the synchrotron "maturity" parameter X_0:

$$X_0 = \frac{C_2^2}{C_1} \nu B^3 t^2 \tag{B.14}$$

where C_2 and C_1 are constants in Pacholczyk (1970). α is a function of X_0, so supposing that B is known or estimated from minimum-energy or equipartition arguments, the age of the source may be inferred when the present and original α are known (typically the original α is measured close to the particle acceleration sites).

Hence, synchrotron losses may be used to estimate the current age and lifetime of radio galaxies. However, in practice there are additional complications. For instance, radio galaxies also dissipate energy in the relativistic plasma via adiabatic expansion of the radio lobes. Further, the electrons may cool via inverse Compton emission (described below).

B.2 Inverse Compton Scattering

Compton scattering is the process whereby energetic photons dissipate their energy through random scattering interactions with electrons. Consider a photon of energy E traveling toward an electron at rest (Figure B.3). From a classical standpoint, when a photon collides with an electron it imparts some of its energy to the electron and continues in a new direction (the interaction is inelastic because of the recoil of the electron; the photon carries momentum as well as energy). The photon energy loss (wavelength shift) when the photon energy is much less than the rest mass energy of the electron is given by

$$\delta\lambda = \frac{h}{m_e c}(1 - \cos\theta), \tag{B.15}$$

where θ is the angle between the photon trajectory before and after the scattering. It turns out that if the photon energy $E < 4kT$, energy is lost by the photons at a rate

$$\frac{dE}{dt} = \frac{4}{3} c\sigma_T \gamma^2 \beta^2 u_{\rm rad}, \tag{B.16}$$

where $u_{\rm rad}$ is the initial energy density of the radiation field. Notably, this has the same form as for the power radiated by synchrotron emission except that in the synchrotron case, $u_{\rm rad}$ is replaced by the energy density in the magnetic field u_B. Hence,

$$\frac{P_{\rm sync}}{P_{\rm Comp}} = \frac{u_B}{u_{\rm rad}}. \tag{B.17}$$

Inverse Compton (IC) scattering is the opposite process, in which a photon of lower energy than the electron gains energy through scattering. Clearly, this requires hot (frequently relativistic) electrons, and therefore occurs in environments such as galaxy clusters, radio galaxies, AGN, etc. The power radiated by the *electrons* in IC scattering is the same as above, so the power is dependent on the energy distribution

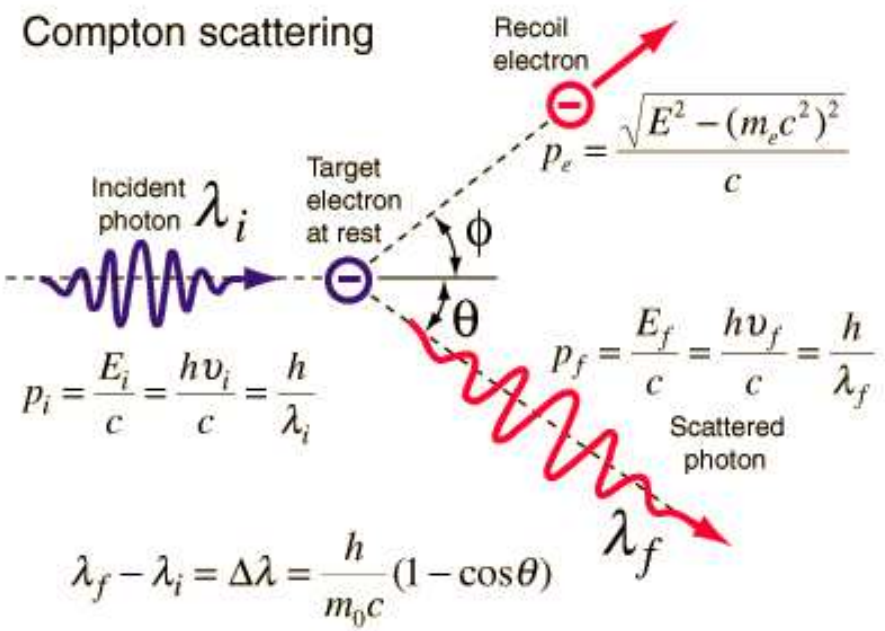

Figure B.3 A schematic diagram of Compton scattering in which an incident photon is inelastically scattered in some new direction by an encounter with an electron. Inverse Compton scattering occurs when the electron has more kinetic energy than the photon. Source: http://hyperphysics.phy-astr.gsu.edu

of the electrons through γ and β ($\gamma^2 - 1 = \gamma^2\beta^2$). If the electrons have a power-law distribution ($N(E) \propto E^{-p}$), the total power depends on the power-law index p and the upper and lower cutoff energies, whereas if the electrons have a thermal distribution the power is proportional to kT.

It turns out that regardless of the incident photon spectrum (blackbody, power-law, etc.), IC scattering off a power-law distribution of electrons with power-law index p produces a power-law spectrum with a spectral index α equivalent to the synchrotron case: $\alpha = (p-1)/2$. This is because the IC spectrum of a single (highly relativistic) electron in a uniform radiation field is sharply peaked with an average increase in frequency of

$$\frac{\nu}{\nu_0} \sim \frac{4}{3}\gamma^2 \tag{B.18}$$

and a maximum frequency of

$$\frac{\nu}{\nu_0} \sim 4\gamma^2. \tag{B.19}$$

Because the spectrum is so sharply peaked, electrons of a given energy contribute primarily at $\nu \sim 4/3\gamma^2$, so a power-law distribution of electrons produces a power-law frequency spectrum. Evidently, ultrarelativistic electrons may boost low-energy photons to frequencies a factor of 10^8 higher or more, elevating radio photons into the X-ray or γ-ray region of the spectrum. Note that the same process is called *inverse Compton* when describing the cooling electrons and *Comptonization* when describing the up-scattered photons. Hence, photons are Comptonized and electrons cool by IC emission.

B.2.1 The Cosmic Microwave Background

This process is relevant astrophysically because the Universe is suffused with the cosmic background radiation, a nearly perfect blackbody with a peak in the microwave region of the spectrum (hereafter the cosmic microwave background or CMB). The CMB is a radiation field left over from the epoch of recombination about 400,000 years after the Big Bang when the Universe cooled sufficiently to allow electrons and ions to form stable ions. Since this universal recombination involved the capture of unbound electrons with a Maxwellian energy distribution, the resultant radiation field has a blackbody spectrum and occurs everywhere in the Universe.

Since, by definition, the epoch of recombination occurred when the photons in the CMB could no longer ionize the newly-formed atoms, the Universe is optically thin to the CMB. Initially, the CMB was radiated by a plasma at $T \sim 10^4$ K, but as the Universe expanded the CMB cooled (one may think of this as the wavelength of the light expanding along with the Universe). The CMB is now a blackbody spectrum with a peak corresponding to about 3 K, so the photons are microwaves.

Hence, these CMB photons preferentially gain energy when scattering off hot plasmas such as those in galaxy cluster atmospheres or radio galaxy bubbles. Indeed, radio galaxy lobes have been observed in γ-rays as a result of the CMB up-scattering (Abdo et al. 2010). IC scattering of CMB photons traveling through galaxy clusters is also responsible for the *Sunyaev-Zeldovich effect* (SZ effect; Sunyaev & Zeldovich 1980), wherein at low frequencies the observed CMB coincident with the galaxy cluster has a decrement relative to the rest of the sky and at high frequencies is brighter than the rest of the sky. The SZ effect is now used as a way to probe the thermal pressure structure of clusters. Note that at higher redshift, the CMB energy density is higher, so when looking far away this becomes a substantially more important radiation field.

B.2.2 Inverse Compton Scattering and Radio Galaxies

The giant lobes that make up radio galaxies can be seen not only in the radio but also in the X-rays and even γ-rays (Figure B.4). The high-energy emission is attributed to IC scattering of photons by the same electrons which radiate in radio wavelengths via the synchrotron process. This conclusion is based on measured spectral indices (e.g. Isobe et al. 2002) in which the X-ray spectral index is comparable to that measured in the radio. Since in synchrotron emission the hottest electrons cool the fastest, the spectrum tends to be steeper at high energies than the power-law at the low energy end. Thus, the X-ray spectral indices tend to be higher than expected if the emission is synchrotron in origin. Another possibility for the X-ray emission cospatial with the lobes is shock compression of material by an expanding cocoon, but the observations are consistent with an IC origin. The seed photons for this IC emission may be the CMB, low-energy emission from the host galaxy, or the synchrotron emission of the lobes, depending on which field has the highest

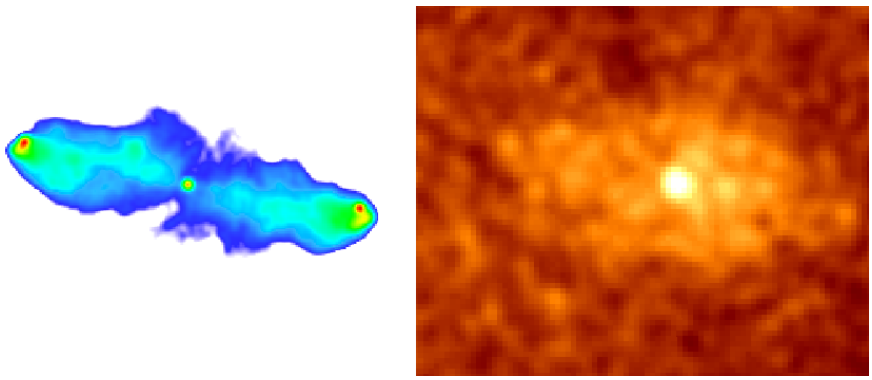

Figure B.4 The lobes of the radio galaxy 3C 452 as seen by (left) the VLA and (right) *Chandra* (Isobe et al. 2002). The lobes are visible in the X-rays thanks to IC scattering of CMB photons (the energy density of synchrotron self-Compton emission is too low in this case to explain the observed emission).

energy density in the lobes. As seen above, regardless of the origin of the emission, ultrarelativistic electrons will produce a power-law spectrum with the same spectral index as the synchrotron emission.

Radio jets are also frequently seen in the X-rays on kpc scales, but unlike in the case of the lobes, synchrotron emission *can* explain some of them. For instance, in 4C +00.58 (Chapter 3) we find that the spectral index in the X-rays is compatible with a synchrotron origin, similar to many other FR I X-ray jets. However, high-energy IC emission from jets must occur at some level because of the energetic electrons involved, and appears to be the dominant mechanism in FR II and quasar jets. The dominant radiation mechanism is determined by spectral index arguments; in some cases, the X-ray spectral index is so much flatter than the radio index (or even negative) that X-ray synchrotron emission is obviously impossible (the bow-tie problem; Harris & Krawczynski 2006).

On pc and sub-pc scales, the radio jets are unresolved (except in the case of very nearby jets such as M87) and it is impossible to separate radio and X-ray emission from the jet and from the core. IC emission produces X-rays very close to the black hole in an AGN because the inner accretion disk is thought to produce a

hot blackbody spectrum which then encounters an ultrarelativistic "corona" of hot electrons directly around the black hole. This encounter up-scatters the photons into a very high-energy power-law spectrum. Farther out (but still unresolved), the jet in a radio-loud AGN radiates via synchrotron emission. These photons are then up-scattered by the same electrons which produced them. The resultant radiation field is called *synchrotron self-Compton* radiation. Since the ratio of the power of IC and synchrotron emission is the ratio of energy in the radiation field (produced by the synchrotron emission) and the energy density of the magnetic field, doubling the density of electrons quadruples the power of synchrotron self-Compton radiation. When the synchrotron self-Compton contribution to $u_{\rm rad}$ is itself comparable to the purely synchrotron contribution, the electrons cool very rapidly. Hence, IC scattering is an important contributor to unresolved core AGN emission, but untangling the sources is beyond the scope of this work.

Appendix C

Notes on Individual Galaxies for the X-ray Study

This appendix refers to objects used in our X-ray study presented in Chapter 2.

C.1 XRGs

B2 1040+31A ($z = 0.036$): The radio galaxy emanates from the largest galaxy in a close triple system (Fanti et al. 1977) which itself is contained within a large region of intragroup medium. The larger IGM is in agreement with Worrall & Birkinshaw (2000), but for the relevant medium we use a smaller region of IGM which is bright against the large region and centered on the system. In the DSS image the host galaxy cannot be isolated from its companions, so we use the SDSS image alone. In the X-ray band, the host galaxy is bright; whether it is AGN emission is unclear based on the spectrum. Because the character of the emission does not change much outside the PSF, we assume we are seeing primarily thermal emission.

PKS 1422+26 ($z = 0.037$): This galaxy has striking wings and "warm" spots which occur about 50% of the distance between the lobe edge and the radio core. The radio galaxy defies easy Fanaroff-Riley classification and is here considered a hybrid FR I/II galaxy. Canosa et al. (1999) found radial asymmetry in the ROSAT image of the IGM which the *Chandra* image confirms. The radio hot spots coincide well with decrements in the X-ray image which must be cavities blown in the gas by the radio lobes. The surface brightness of the "ridge" this leaves in the middle is consistent with the hypothesis that the actual orientation of the IGM is elongated in the direction of the radio lobes. This is in contrast to 3C 285 or 3C 388, where cavities alone cannot explain the "excess" emission near the core. In addition, the spectrum of the AGN has a highly significant emission line-like feature at 4.0 keV which is presently unexplained.

NGC 326 ($z = 0.048$): NGC 326 is a double galaxy with the radio lobes emanating from the northern component; both galaxies show diffuse X-ray ISM emission, and the X-ray emission from the southern galaxy is exclusively thermal. The extent of the *Chandra* diffuse emission agrees well with the ROSAT data where there is overlap (Worrall et al. 1995). The long tails in the radio map appear to follow empty channels in the *Chandra* data, and the length of the tails relative to the active lobes provides constraints on backflow formation mechanisms (Gopal-Krishna et al. 2003). The ISM emission for the northern component is extracted excluding the central point source; the temperature of $kT = 0.68$ keV agrees precisely with the temperature of the thermal model included in the AGN emission, where a PL component is also required.

3C 403 ($z = 0.059$): This dataset was previously studied in detail by Kraft et al. (2005) who attempted to isolate the ISM emission from the nucleus by performing a spectral analysis in which the soft part of the spectrum was fit by an absorbed power law between $1.0 - 2.0$ keV, with a line-dominated thermal fit between $0.3 - 1.0$ keV. They then fit an elliptical profile to these thermal events. This line of reasoning is supported by the absence of a bright core corresponding to the PSF at $0.3 - 1.0$ keV. However, we find an acceptable fit in which an unabsorbed power law dominates between $0.3 - 2.0$ keV. This analysis is also complicated by the presence of a feature at 0.85 keV which is not fit by either Kraft et al. (2005) or ourselves. Since this feature accounts for $\sim 25\%$ of counts between $0.3 - 1.0$ keV (Figure 2.5; available online, we cannot distinguish between the thermal and power law models. It should be noted that the PA of the soft emission agrees well with the host galaxy; we are doubtless seeing *some* ISM. However, we do not know if it is the dominant component.

4C +00.58 ($z = 0.059$): The following text corresponds to our analysis of the 10 ks snapshot X-ray image; our analysis of the 110 ks data is presented in Chapter 3, but the text below is preserved as relevant to our work in Chapter 2: 4C +00.58 was classified as a candidate XRG (Cheung 2007) due to faint wings in the FIRST image. A new, higher resolution radio map reveals that the jet to the east of the core is bent toward the northwest and enclosed in a more symmetric radio lobe. We detect the inner part of this jet in the X-ray band (confirmed by line-fitting to determine the PA using the bootstrap resampling method). The PA of the jet was determined very well, so we masked it from our fit. It is unclear whether the diffuse emission represents the ISM or the IGM. $\epsilon_{\text{X-ray}}$ does not agree well with the host galaxy, but the PA does. There is likely some of both media represented in the

image, and deeper observations are required to separate the components. Notably, the jet appears to pass through the *minor* axis of the host galaxy. We include this galaxy in both the ISM and IGM X-ray—radio comparisons due to the ambiguity.

3C 192 ($z = 0.060$): 3C 192 is formally a "winged" galaxy (Cheung 2007), but the morphology is otherwise very similar to X-shaped radio galaxies. Enhanced emission is detected in an elliptical region encompassing the primary radio lobes, but a smaller enhancement we identify with the ISM exists near the AGN. It is also possible that this is the central region of the IGM, but it appears compact. Moreover, the "IGM" is consistent with being fit only by a power law ($\Gamma = 2.5$) and is in good spatial agreement with the primary lobes. It may also be fit by a thermal model with $kT \sim 0.9$ and $Z < 0.1$; if it is indeed thermal emission, the IGM is in perfect agreement with Capetti et al. (2002). However, a close inspection of the radio galaxy suggests that the X-ray emission may come from a bounding shock or otherwise have been influenced by the radio galaxy rather than a pre-existing highly eccentric IGM. In particular, even though the bright X-ray emission is not as large as the active lobes, the southwestern lobe appears to track enhanced X-ray emission to its hot spot. Notably, 3C 192 is in a very round host (Cheung & Springmann 2007; Smith & Heckman 1989). Capetti et al. (2002) found XRGs typically occur in galaxies with high projected ϵ, so the existence of similar morphology in round hosts bears investigation.

3C 433 ($z = 0.102$): The northern secondary lobe of 3C 433 is strikingly bent compared to the southern secondary (van Breugel et al. 1983). Miller & Brandt (2009) argue that the hybrid FR I/II lobe morphology is due to interaction with the surrounding IGM. In this scenario, the galaxy is a typical FR II source propagating into a very asymmetric environment. Miller & Brandt (2009) also include in their paper a *HST* image of the host galaxy whose PA is in good agreement with the parameters we derive from the DSS image. The X-ray emission near the southern lobe is consistent with either thermal emission (Miller & Brandt 2009) or power law emission. We assume the ISM is the relevant medium and attempt to isolate it, but we may also be incorporating some local IGM emission in the spectrum.

3C 315 ($z = 0.108$): The AGN is detected at a significance of 5.07σ (see Appendix A.3 for methods), but there are too few counts to make a spectrum. The diffuse IGM stands out against the background on large scales and is fit well by thermal models and not by power law models. No ISM is detected, but we can use the galaxy for comparison to the IGM independently. It is possible that this is not real IGM, as we suspect in 3C 192, but the alignment of the radio galaxy and the hot atmosphere is not as good as in 3C 192, nor is it quite as eccentric. Thus, there is no strong evidence that the radio galaxy created the observed X-ray morphology, but the exposure is very short.

C.2 Comparison Sample

3C 449 ($z = 0.017$): Both the ISM and IGM are bright in this 30 ks exposure, but the chip is somewhat smaller than the extent of the radio lobes. Notably, these lobes decollimate and show the characteristic FR I plumed structure near the edge of the intragroup medium; this structure and the hot atmospheres have been studied

with *XMM-Newton* in detail by Croston et al. (2003). Tremblay et al. (2007) find that the jet is parallel to a warped nuclear disk. The AGN was fit with the XSPEC models N_H(PL)+`apec`, but the an acceptable fit was also found for a PL+`apec` fit with no absorption and a smaller Γ.

3C 31 ($z = 0.017$): The X-ray jet (Hardcastle et al. 2002) is quite bright in the ACIS-S3 image and is readily distinguishable from other core X-ray emission, so we mask it in the analysis of the diffuse ISM. A weaker, nearby source to the southwest (visible in the optical light) may contaminate the ISM with a small amount of diffuse emission, but appears very weak in the X-ray.

3C 83.1B ($z = 0.018$): The *Chandra* data from this head-tail galaxy was published by Sun et al. (2005) who argue that there is a distinct southern edge to the X-ray emission which otherwise shares the ellipticity and position angle of the optical isophotes. They apply a deprojection analysis to the ISM data and find that the central ISM has a temperature of $kT = 0.45$ keV, in agreement with our non-deprojected fit to the central PSF emission with $kT = 0.48$ keV. Sun et al. (2005) also find that the LMXB contribution to the diffuse gas is on the order of $\sim 5\%$ and they show that the southern edge in the X-ray data cannot be produced by ICM pressure, but argue that the edge is a sign of ISM/ICM interaction and that if the galaxy is moving south very rapidly, the long twin tails to the north are naturally explained. The radio emission is likewise curtailed to the south.

3C 264 ($z = 0.021$): 3C 264 is a head-tail galaxy whose radio lobes both extend to the northeast, but there is a large envelope of radio emission around the AGN which is larger than the extent of the $2\sigma_{\rm sky}$ DSS optical isophotes. This data set is subarrayed to 1/8 of the ACIS-S3 area and suffers from a readout streak. We subtracted the streak and this removed a relatively small number of photons from the diffuse ISM. Both the host galaxy and the diffuse X-ray emission appear almost circular on the sky such that the position angle of the ellipses we fit (Table 2.5) are not well constrained.

3C 66B ($z = 0.022$): We detect strong ISM emission and the X-ray jet in this *Chandra* exposure. The IGM is detected and studied (with regards to its interaction with the radio lobes) using *XMM-Newton* data by Croston et al. (2003). In the *Chandra* exposure, however, the IGM is very weak and we cannot measure the morphology. The different character of the two lobes is attributed to interaction with the hot gas by Croston et al. (2003), with the western lobe being more confined. There is a small unresolved source to the southeast in the X-ray image which has an optical counterpart, but it is far enough from the ISM emission that our ellipse fitting is unaffected.

3C 296 ($z = 0.024$): Before fitting an ellipse we subtract a small companion to the northwest as well as the X-ray jet. The ISM is clearly detected (see also Diehl & Statler 2007, NGC 5532 in their paper) and the lobes begin expanding outside the IGM. The IGM has a similar shape and orientation to the ISM, but it is clearly distinct in temperature and where it is centered (in between 3C 296 and a companion to the southwest) even though it is relatively compact.

NGC 6251 ($z = 0.024$): The very large (Mpc-scale) radio lobes of this radio galaxy dwarf the entire ACIS array, and the 1/8-size S3 subarray contains emission only from the central core and along the jet (Evans et al. 2005). We detect some emission associated with the jet to the northwest of the galaxy along the chip. A bright readout streak has been removed, and we correct the spectrum of the central PSF for pileup. The spectrum of the AGN is fit well by either a power law with $\Gamma < 0.5$ and a thermal model or a slightly absorbed power law with $\Gamma = 1.5$ and a thermal model.

PKS 2153-69 ($z = 0.028$): This data has been published before with regard to interaction of the radio jet with a cloud of gas (Ly et al. 2005; Young et al. 2005). The gross morphology agrees well with the C02 geometric relation, although the surface brightness decrement to the north and south of the galaxy is due to the cavities blown out by the radio lobes, as is evident from the visible shocked bubbles of gas in the intragroup medium. Despite these cavities, the morphology of the larger IGM is easily measurable on larger scales, assuming the internal structure is entirely due to the radio galaxy activity.

3C 338 ($z = 0.030$): Unlike other extended sources for which deprojection is possible but which can be fit by an isothermal model to find an average temperature (most of the other galaxies in our sample), 3C 338 has sufficient signal to require at least a 2-T model to find average temperatures (signifying the presence of hotter and cooler gas) and these temperatures are roughly in line with the outer and inner temperatures of the Johnstone et al. (2002) deprojection analysis which also agrees with our own (we report the 2-T fit for consistency). Although the cluster gas is interacting with the radio galaxy, it is otherwise smooth and we take it to be a single large ellipsoid for the purpose of measuring ellipticity and position angle of the ICM.

Notably, we do not detect the AGN or the ISM amidst the very bright ICM. This observation is studied more thoroughly in Johnstone et al. (2002), including the unusual radio bridge parallel to the jets.

3C 98 ($z = 0.030$): The ISM of the galaxy in this ACIS-I observation is very close to the chip boundaries. However, it has clear ellipticity and is not contaminated by any companions, so we are able to fit an ellipse. There is diffuse thermal emission associated with the northern radio lobe that is similar to the ISM, but we see no evidence for such gas in the southern lobe. Notably, the orientation of the major axis of the HST image in Martel et al. (1999) disagrees with our DSS ellipse by $\sim 20°$. The HST image is more reliable, meaning that the radio jet is aligned close to the *major* axis of the host.

3C 465 ($z = 0.031$): 3C 465 is a wide-angle tail FR I radio galaxy located in cluster gas that has been well studied (both with *Chandra* and *XMM-Newton* by Hardcastle et al. 2005). The ICM covers most of the chip and is centered on the host of 3C 465. The ICM has clear ellipticity and the bright extended emission is comparable to the size of entire radio galaxy We fit ellipses to both the ISM and "local" ICM on a scale slightly smaller than half the size of the chip. Hardcastle et al. (2005) also present a radial profile which is in agreement with our average temperature for the cluster gas. The spectrum of the AGN can be fit well either by a power law with $\Gamma < 0.5$ and a thermal model or a slightly absorbed power law with $\Gamma = 2.4$ and a thermal model.

3C 293 ($z = 0.045$): The X-ray emission associated with the radio galaxy is quite weak, but the hot spots are distinct and there is a small amount of extended ISM emission. Unfortunately, the spatial extent of this diffuse emission is small compared to the optical isophotes, so the disagreement between the $\epsilon_{\text{X-ray}}$ and $\epsilon_{\text{DSS/SDSS}}$ (measured at a somewhat larger radius) is not especially surprising. Notably, the host galaxy has two nuclei and is in the process of merging (Martel et al. 1999).

Cyg A ($z = 0.056$): Cygnus A has been extensively studied in the X-rays thanks to its exceptionally bright filamentary structure and evident shock cocoon tracing the radio galaxy. This structure makes it impossible to measure the ellipse parameters of the ISM, but the larger ICM appears to have little structure beyond the cocoon and filaments (Young et al. 2002, show that the host galaxy has complex morphology as well). Therefore, we believe the directions of pressure and density gradients on large scales are likely to be similar to the ones the radio galaxy encounters.

3C 445 ($z = 0.056$): The bright nucleus of 3C 445 is far off-axis in this exposure; its brightness and high ellipticity make it impossible to measure the ellipse parameters of the diffuse ISM. Moreover, the Martel et al. (1999) *HST* image is dominated by the unresolved nucleus, so our DSS parameters may not be accurate. However, we include the galaxy in our sample because of the hot IGM surrounding the host.

3C 285 ($z = 0.079$): 3C 285 is currently experiencing a major merger, and instead of a well-defined ISM, we fit an ellipse to the "ridge" structure described in Hardcastle et al. (2007b). The ridge appears to be a unified structure (its X-ray properties do not differ along its length) and Hardcastle et al. (2007b) argue that it is *not* produced by the interaction of the radio galaxy with its environment. They reason that the agreement with the starlight (and, in 3C 442A, the flow of material from

tidal tails into a similar ridge) could not be generally predicted by the interaction of the radio galaxy with its environment. This is in agreement with our ISM–optical light correlation.

3C 452 ($z = 0.081$): This data set was studied in detail by Isobe et al. (2002) who find that the thermal and power law emission is well mixed throughout the region covered by the radio lobes. We attempt to isolate the two components using an analysis similar to Diehl & Statler (2007) in which the image is broken into hard and soft components. The thermal and power law emission each make up a certain percentage of the luminosity in each component, so a synthesized image of the thermal emission can be constructed by adding the correct percentage of each component to the final image. Although clearly the method will not be able to identify individual counts as thermal or nonthermal in origin, if the spatial distribution of nonthermal counts is significantly different from that of thermal ones, we would expect to see a difference in the synthesized images. In fact, we find general agreement with Isobe et al. (2002), although the nonthermal emission is dominant near the hot spots of the radio galaxy. If the thermal X-ray emission traces the physical boundaries of the IGM, then we would expect to see either an X- or Z-shaped galaxy, but the extremely good coincidence between X-ray and radio emission argues that this is instead a cocoon inside a larger (unseen) IGM.

3C 227 ($z = 0.087$): 3C 227 exhibits both core ISM and dimmer IGM emission near the host galaxy. The IGM morphology is difficult to study due to the chip boundary. The radio lobes appear to be ragged and bend around the major axis of the host galaxy, suggesting that strong backflows similar to those in the hydrodynamic XRG formation models are at work, but the IGM is too weak near these mini-wings to assess this hypothesis. The galaxy was included in the Hardcastle

et al. (2007a) study of particle acceleration in hot spots.

3C 388 ($z = 0.091$): 3C 388 is a radio galaxy oriented along the major axis of its host, but we detect no ISM in the X-ray exposure due to the strength of the surrounding ICM. The radio galaxy is comparable to the size of X-ray ICM isophotes elongated in its direction, which Kraft et al. (2006) attribute to the influence of the radio galaxy on its surroundings. The radio lobes have blown cavities in the X-ray emission, but near the core of the radio galaxy, the X-ray isophotes are elongated in a direction perpendicular to the radio lobes. Although much of this asymmetry is likely due to the cavities eating out the sides of a spheroid where the radio galaxy overlaps the core region (i.e. it is a physical structure but may not precede the radio galaxy), the western radio lobe seems to bend arounnd the ridge. Since the fainter portions of the radio lobes may be older plasma evolving buoyantly in the ICM (the jet in the western lobe is farther to the south), the ridge may also be influencing the shape of the radio galaxy.

C.3 Unused XRGs

Short observations of the more distant XRGs produced mixed results, with a number of sources exhibiting little-to-no diffuse emission. Where we cannot determine whether any diffuse emission is dominated by thermal emission or measure morphology, or where no diffuse emission corresponding to the relevant medium is detected, we cannot use the galaxy in our analysis. In the following short observations, the central point source is detected in all cases (with the weakest detection having a significance barely exceeding 3σ), and upper limits are given for the thermal luminosity. We use the methods of Ayres (2004) (Equations 3, 13, and 14 in his paper) to measure the detection significance and flux confidence limits. The measured number

of counts is given by

$$S = S_0 + \left(\frac{s^2+2}{3}\right) \pm \Delta S$$

where $S_0 = N - B$ is the detected number of counts in the cell, B is the expected background in the cell based on a much larger area elsewhere on the chip, and s is the significance; we choose $s = 1.645$ for 95% confidence intervals. The quantity ΔS is given by

$$\Delta S \equiv s\sqrt{\max[(N - \tfrac{1}{4}B), 0] + 1}$$

The detect cells we used were uniformly chosen to be circles with $3''$ in radius to enclose the *Chandra* PSF at most energies. The significance of the detection s was determined by solving the quadratic equation (Equation 3 in Ayres 2004):

$$\frac{\min[B^{0.1}, 1]}{7}s^2 + \sqrt{B}s + \left[B - N - \frac{2 \cdot \min[B^{0.1}, 1]}{7}\right] = 0$$

These values are reported for each galaxy. The thermal luminosity upper limits were computed by extracting a spectrum from a (large) region around the point source and increasing the strength of a thermal model in XSPEC until it was no longer a good fit. The temperature cannot be constrained and was thus fixed at $kT = 1.0$ keV. The unabsorbed luminosity was then computed at the upper bound of the model normalization and reported below.

4C +32.25 ($z = 0.053$): The point source is detected with a significance of 8.52σ with $S = 20.7^{+9.4}_{-6.3}$ counts in the detect cell. The diffuse emission within a $r = 24''$ region (much larger than the ISM) has an upper limit unabsorbed thermal luminosity of 4×10^{40} erg s^{-1} at ~ 1.0 keV, but it does not appear to be centrally concentrated on the chip. Our geometric analysis is not possible in this case, especially since the ISM is the medium of interest given the scale of the radio emission.

4C +48.29 ($z = 0.052$): We detect 19 counts in the detect cell (positioned around the core of radio emission) and detect the AGN with a significance of 7.56σ and $S = 17.6^{+8.9}_{-5.7}$ counts in a 95% confidence interval. The diffuse emission in a $r = 24''$ region is barely distinguishable from the background and we measure an unabsorbed thermal luminosity upper limit of $L = 5 \times 10^{40}$ erg s^{-1}. We attribute this to the faint IGM as opposed to the ISM due to the scale and lack of central concentration.

3C 136.1 ($z = 0.064$): This source has relatively high background, so we detect the AGN at a significance of only 3.3σ despite finding 11 counts in the detect cell. The number of counts is $S = 7.9^{+7.1}_{-3.9}$. Any diffuse emission is similarly buried in the background, and we measure an unabsorbed thermal luminosity upper limit of $L = 2 \times 10^{40}$ erg s^{-1} for a region with $r = 30''$.

J1101+1640 ($z = 0.068$): Unfortunately, this XRG was not positioned on any ACIS chip during the observation. The galaxy lies in a cluster (Abell 1145) and the radio lobes just extend onto part of the S3 chip, but no significant diffuse gas from the cluster is detected on the chip. The observation was mispointed due to an error in the primary literature and so cannot be used.

3C 223.1 ($z = 0.107$): 3C 223.1 actually has a bright AGN core where spectroscopy is possible, revealing a highly absorbed power law. The detection significance is 34.1σ and the number of counts detected $S = 206^{+25}_{-22}$. However, any diffuse emission is extremely faint, with an upper limit to unabsorbed thermal luminosity of $L = 8 \times 10^{40}$ erg s^{-1} in a region with $r = 30''$. We are therefore unable to use this galaxy in our XRG sample.

We also choose not to use the two *Chandra* observations of XRGs at higher redshift ($z = 0.128, 0.2854$) because of the requirement to simultaneously expand

the comparison sample (and 3C 197.1 is not included in the compilation of Cheung (2007)). We address these here:

3C 197.1 ($z = 0.128$): 3C 197.1 has a long northern wing which is comparable in spatial extent to the active lobe in a 1.5 GHz image (Neff et al. 1995), but there is no obvious southern wing which could be described as symmetric about the central AGN. In the 5 GHz image of Neff et al. (1995) extensions in the southern lobe appear to be essentially symmetric about the jet axis. 3C 197.1 is included in the Saripalli & Subrahmanyan (2009) list of XRGs, but its inclusion in our sample is questionable. We discuss it here because of the other "XRGs" listed in Saripalli & Subrahmanyan (2009) and not in Cheung (2007), 3C 197.1 bears the most similarity to the classical XRGs listed in Cheung (2007). We do not include it in our sample due to its relatively high redshift and ambiguity of classification. The *Chandra* exposure is a short 8 ks snapshot which clearly detects the AGN and some diffuse emission which may be the ISM or the IGM, but has insufficient counts to claim a spectroscopic detection of hot gas.

3C 52 ($z = 0.285$): 3C 52 is a classical XRG with highly collimated secondary lobes in the 1.5 GHz image (Alexander & Leahy 1987) and excluded from our sample on the basis of much higher redshift than our other sources. The *Chandra* image is an 8 ks snapshot which clearly detects the central point source and also a diffuse atmosphere larger than the radio galaxy itself (with a radius of about 50 arcsec centered on the galaxy). This atmosphere is in good agreement geometrically with the Capetti et al. (2002) relation (i.e. the major axis of the ellipsoidal atmosphere is coaligned with the active lobes), but proving the presence of a hot atmosphere spectroscopically is difficult. An isothermal `apec` model requires $T > 7$ keV and is otherwise poorly constrained; a power law with $\Gamma = 1.5$ fits the spectrum well.

Since the emission region is large compared to the radio galaxy, it seems likely this is hot gas, but a much deeper observation is necessary to establish this.

Bibliography

Abdo, A. A., Ackermann, M., Ajello, M., Atwood, W. B., Baldini, L., Ballet, J., Barbiellini, G., Bastieri, D., Baughman, B. M., Bechtol, K., Bellazzini, R., Berenji, B., Blandford, R. D., Bloom, E. D., Bonamente, E., Borgland, A. W., Bregeon, J., Brez, A., Brigida, M., Bruel, P., Burnett, T. H., Buson, S., Caliandro, G. A., Cameron, R. A., Caraveo, P. A., Casandjian, J. M., Cavazzuti, E., Cecchi, C., Çelik, Ö., Chekhtman, A., Cheung, C. C., Chiang, J., Ciprini, S., Claus, R., Cohen-Tanugi, J., Colafrancesco, S., Cominsky, L. R., Conrad, J., Costamante, L., Cutini, S., Davis, D. S., Dermer, C. D., de Angelis, A., de Palma, F., Digel, S. W., do Couto e Silva, E., Drell, P. S., Dubois, R., Dumora, D., Farnier, C., Favuzzi, C., Fegan, S. J., Finke, J., Focke, W. B., Fortin, P., Fukazawa, Y., Funk, S., Fusco, P., Gargano, F., Gasparrini, D., Gehrels, N., Georganopoulos, M., Germani, S., Giebels, B., Giglietto, N., Giordano, F., Giroletti, M., Glanzman, T., Godfrey, G., Grenier, I. A., Grove, J. E., Guillemot, L., Guiriec, S., Hanabata, Y., Harding, A. K., Hayashida, M., Hays, E., Hughes, R. E., Jackson, M. S., Jóhannesson G., Johnson, S., Johnson, T. J., Johnson, W. N., Kamae, T., Katagiri, H., Kataoka, J., Kawai, N., Kerr, M., Knödlseder, J., Kocian, M. L., Kuss, M., Lande, J., Latronico, L., Lemoine-Goumard, M., Longo, F., Loparco, F., Lott, B., Lovellette, M. N., Lubrano, P., Madejski, G. M., Makeev, A., Mazziotta, M. N., McConville, W., McEnery, J. E., Meurer, C., Michelson, P. F., Mitthumsiri, W., Mizuno, T.,

Moiseev, A. A., Monte, C., Monzani, M. E., Morselli, A., Moskalenko, I. V., Murgia, S., Nolan, P. L., Norris, J. P., Nuss, E., Ohsugi, T., Omodei, N., Orlando, E., Ormes, J. F., Paneque, D., Parent, D., Pelassa, V., Pepe, M., Pesce-Rollins, M., Piron, F., Porter, T. A., Rainò, S., Rando, R., Razzano, M., Razzaque, S., Reimer, A., Reimer, O., Reposeur, T., Ritz, S., Rochester, L. S., Rodriguez, A. Y., Romani, R. W., Roth, M., Ryde, F., Sadrozinski, H. F.-W., Sambruna, R., Sanchez, D., Sander, A., Saz Parkinson, P. M., Scargle, J. D., Sgrò, C., Siskind, J., Smith, D. A., Smith, P. D., Spandre, G., Spinelli, P., Starck, J.-L., Stawarz, L., Strickman, M. S., Suson, D. J., Tajima, H., Takahashi, H., Takahashi, T., Tanaka, T., Thayer, J. B., Thayer, J. G., Thompson, D. J., Tibaldo, L., Torres, D. F., Tosti, G., Tramacere, A., Uchiyama, T. L., Y. U., Vasileiou, V., Vilchez, N., Vitale, V., Waite, A. P., Wallace, E., Wang, P., Winer, B. L., Wood, K. S., Ylinen, T., Ziegler, M., Hardcastle, M. J., Kazanas, D., & Fermi-LAT Collaboration. 2010, Science, 328, 725

Adelman-McCarthy, J. K., Agüeros, M. A., Allam, S. S., Allende Prieto, C., Anderson, K. S. J., Anderson, S. F., Annis, J., Bahcall, N. A., Bailer-Jones, C. A. L., Baldry, I. K., Barentine, J. C., Bassett, B. A., Becker, A. C., Beers, T. C., Bell, E. F., Berlind, A. A., Bernardi, M., Blanton, M. R., Bochanski, J. J., Boroski, W. N., Brinchmann, J., Brinkmann, J., Brunner, R. J., Budavári, T., Carliles, S., Carr, M. A., Castander, F. J., Cinabro, D., Cool, R. J., Covey, K. R., Csabai, I., Cunha, C. E., Davenport, J. R. A., Dilday, B., Doi, M., Eisenstein, D. J., Evans, M. L., Fan, X., Finkbeiner, D. P., Friedman, S. D., Frieman, J. A., Fukugita, M., Gänsicke, B. T., Gates, E., Gillespie, B., Glazebrook, K., Gray, J., Grebel, E. K., Gunn, J. E., Gurbani, V. K., Hall, P. B., Harding, P., Harvanek, M., Hawley, S. L., Hayes, J., Heckman, T. M., Hendry, J. S., Hindsley, R. B., Hirata, C. M., Hogan, C. J., Hogg, D. W., Hyde, J. B., Ichikawa, S.-i., Ivezić, Ž., Jester, S.,

Johnson, J. A., Jorgensen, A. M., Jurić, M., Kent, S. M., Kessler, R., Kleinman, S. J., Knapp, G. R., Kron, R. G., Krzesinski, J., Kuropatkin, N., Lamb, D. Q., Lampeitl, H., Lebedeva, S., Lee, Y. S., Leger, R. F., Lépine, S., Lima, M., Lin, H., Long, D. C., Loomis, C. P., Loveday, J., Lupton, R. H., Malanushenko, O., Malanushenko, V., Mandelbaum, R., Margon, B., Marriner, J. P., Martínez-Delgado, D., Matsubara, T., McGehee, P. M., McKay, T. A., Meiksin, A., Morrison, H. L., Munn, J. A., Nakajima, R., Neilsen, Jr., E. H., Newberg, H. J., Nichol, R. C., Nicinski, T., Nieto-Santisteban, M., Nitta, A., Okamura, S., Owen, R., Oyaizu, H., Padmanabhan, N., Pan, K., Park, C., Peoples, Jr., J., Pier, J. R., Pope, A. C., Purger, N., Raddick, M. J., Re Fiorentin, P., Richards, G. T., Richmond, M. W., Riess, A. G., Rix, H.-W., Rockosi, C. M., Sako, M., Schlegel, D. J., Schneider, D. P., Schreiber, M. R., Schwope, A. D., Seljak, U., Sesar, B., Sheldon, E., Shimasaku, K., Sivarani, T., Smith, J. A., Snedden, S. A., Steinmetz, M., Strauss, M. A., SubbaRao, M., Suto, Y., Szalay, A. S., Szapudi, I., Szkody, P., Tegmark, M., Thakar, A. R., Tremonti, C. A., Tucker, D. L., Uomoto, A., Vanden Berk, D. E., Vandenberg, J., Vidrih, S., Vogeley, M. S., Voges, W., Vogt, N. P., Wadadekar, Y., Weinberg, D. H., West, A. A., White, S. D. M., Wilhite, B. C., Yanny, B., Yocum, D. R., York, D. G., Zehavi, I., & Zucker, D. B. 2008, ApJS, 175, 297

Alexander, P., & Leahy, J. P. 1987, MNRAS, 225, 1

Allen, S. W., Dunn, R. J. H., Fabian, A. C., Taylor, G. B., & Reynolds, C. S. 2006, MNRAS, 372, 21

Antonucci, R. 1993, ARA&A, 31, 473

Antonuccio-Delogu, V., & Silk, J. 2010, MNRAS, 405, 1303

Arnaud, K. A. 1996, in Astronomical Society of the Pacific Conference Series, Vol. 101, Astronomical Data Analysis Software and Systems V, ed. G. H. Jacoby &

J. Barnes, 17–+

Ayres, T. R. 2004, ApJ, 608, 957

Balmaverde, B., Capetti, A., & Grandi, P. 2006, A&A, 451, 35

Bardeen, J. M., & Petterson, J. A. 1975, ApJ, 195, L65+

Baum, S. A., Heckman, T. M., Bridle, A., van Breugel, W. J. M., & Miley, G. K. 1988, ApJS, 68, 643

Becker, R. H., White, R. L., & Helfand, D. J. 1995, ApJ, 450, 559

Begelman, M. C. 2001, in Astronomical Society of the Pacific Conference Series, Vol. 240, Gas and Galaxy Evolution, ed. J. E. Hibbard, M. Rupen, & J. H. van Gorkom, 363–+

Belan, M., de Ponte, S., Tordella, D., Massaglia, S., Mignone, A., Bodenschatz, E., & Ferrari, A. 2011, Ap&SS, 28

Best, P. N. 2009, Astronomische Nachrichten, 330, 184

Best, P. N., Röttgering, H. J. A., & Lehnert, M. D. 1999, MNRAS, 310, 223

Binney, J., & Merrifield, M. 1998, Galactic Astronomy, ed. Binney, J. & Merrifield, M.

Black, A. R. S., Baum, S. A., Leahy, J. P., Perley, R. A., Riley, J. M., & Scheuer, P. A. G. 1992, MNRAS, 256, 186

Blandford, R. D., & Payne, D. G. 1982, MNRAS, 199, 883

Blandford, R. D., & Znajek, R. L. 1977, MNRAS, 179, 433

Blanton, E. L., Randall, S. W., Douglass, E. M., Sarazin, C. L., Clarke, T. E., & McNamara, B. R. 2009, ApJ, 697, L95

Bliton, M., Rizza, E., Burns, J. O., Owen, F. N., & Ledlow, M. J. 1998, MNRAS, 301, 609

Bodo, G., Rossi, P., Massaglia, S., Ferrari, A., Malagoli, A., & Rosner, R. 1998, A&A, 333, 1117

Bogdanović, T., Reynolds, C. S., & Miller, M. C. 2007, ApJ, 661, L147

Braithwaite, J. 2010, MNRAS, 406, 705

Browne, I. W. A., & Battye, R. A. 2010, in Astronomical Society of the Pacific Conference Series, Vol. 427, Accretion and Ejection in AGN: a Global View, ed. L. Maraschi, G. Ghisellini, R. Della Ceca, & F. Tavecchio, 365–+

Canosa, C. M., Worrall, D. M., Hardcastle, M. J., & Birkinshaw, M. 1999, MNRAS, 310, 30

Capetti, A., Zamfir, S., Rossi, P., Bodo, G., Zanni, C., & Massaglia, S. 2002, A&A, 394, 39

Cappellari, M., & Copin, Y. 2003, MNRAS, 342, 345

Carvalho, J. C., & O'Dea, C. P. 2002a, ApJS, 141, 337

—. 2002b, ApJS, 141, 371

Casadei, D., & Bindi, V. 2004, ApJ, 612, 262

Cavaliere, A., & Fusco-Femiano, R. 1976, A&A, 49, 137

Cheung, C. C. 2007, AJ, 133, 2097

Cheung, C. C., Healey, S. E., Landt, H., Verdoes Kleijn, G., & Jordán, A. 2009, ApJS, 181, 548

Cheung, C. C., & Springmann, A. 2007, in Astronomical Society of the Pacific Conference Series, Vol. 373, The Central Engine of Active Galactic Nuclei, ed. L. C. Ho & J.-W. Wang, 259–+

Chiaberge, M., & Marconi, A. 2011, ArXiv e-prints

Churazov, E., Brüggen, M., Kaiser, C. R., Böhringer, H., & Forman, W. 2001, ApJ, 554, 261

Condon, J. J., Frayer, D. T., & Broderick, J. J. 1991, AJ, 101, 362

Croston, J. H., Birkinshaw, M., Conway, E., & Davies, R. L. 2003, MNRAS, 339, 82

David, L. P., Jones, C., & Forman, W. 1995, ApJ, 445, 578

De Young, D. S. 2010, ApJ, 710, 743

Dennett-Thorpe, J., Scheuer, P. A. G., Laing, R. A., Bridle, A. H., Pooley, G. G., & Reich, W. 2002, MNRAS, 330, 609

Diehl, S., & Statler, T. S. 2006, MNRAS, 368, 497

—. 2007, ApJ, 668, 150

Donato, D., Sambruna, R. M., & Gliozzi, M. 2004, ApJ, 617, 915

Dong, R., & Stone, J. M. 2009, ApJ, 704, 1309

Dotti, M., Volonteri, M., Perego, A., Colpi, M., Ruszkowski, M., & Haardt, F. 2010, MNRAS, 402, 682

Efron, B. 1982, The Jackknife, the Bootstrap and other resampling plans, ed. Efron, B.

Ekers, R. D., Fanti, R., Lari, C., & Parma, P. 1978, Nature, 276, 588

Evans, D. A., Fong, W., Hardcastle, M. J., Kraft, R. P., Lee, J. C., Worrall, D. M., Birkinshaw, M., Croston, J. H., & Muxlow, T. W. B. 2008, ApJ, 675, 1057

Evans, D. A., Hardcastle, M. J., Croston, J. H., Worrall, D. M., & Birkinshaw, M. 2005, MNRAS, 359, 363

Evans, D. A., Worrall, D. M., Hardcastle, M. J., Kraft, R. P., & Birkinshaw, M. 2006, ApJ, 642, 96

Fabian, A. C. 1994, ARA&A, 32, 277

Fabian, A. C. 2010, in IAU Symposium, Vol. 267, IAU Symposium, 341–349

Fabian, A. C., Sanders, J. S., Allen, S. W., Canning, R. E. A., Churazov, E., Crawford, C. S., Forman, W., GaBany, J., Hlavacek-Larrondo, J., Johnstone, R. M., Russell, H. R., Reynolds, C. S., Salome, P., Taylor, G. B., & Young, A. J. 2011, ArXiv e-prints

Fabian, A. C., Sanders, J. S., Taylor, G. B., Allen, S. W., Crawford, C. S., Johnstone,

R. M., & Iwasawa, K. 2006, MNRAS, 366, 417

Falceta-Gonçalves, D., Caproni, A., Abraham, Z., Teixeira, D. M., & de Gouveia Dal Pino, E. M. 2010, ApJ, 713, L74

Fanaroff, B. L., & Riley, J. M. 1974, MNRAS, 167, 31P

Fanti, C., Fanti, R., Gioia, I. M., Lari, C., Parma, P., & Ulrich, M. H. 1977, A&AS, 29, 279

Fosbury, R. A. E., Morganti, R., Wilson, W., Ekers, R. D., di Serego Alighieri, S., & Tadhunter, C. N. 1998, MNRAS, 296, 701

Gabuzda, D. C., Murray, É., & Cronin, P. 2004, MNRAS, 351, L89

Gaibler, V., Khochfar, S., & Krause, M. 2011, MNRAS, 411, 155

Gariel, J., MacCallum, M. A. H., Marcilhacy, G., & Santos, N. O. 2010, A&A, 515, A15+

Ge, J., & Owen, F. N. 1994, AJ, 108, 1523

Goldreich, P., & Julian, W. H. 1969, ApJ, 157, 869

Gopal-Krishna, Biermann, P. L., Gergely, L. Á., & Wiita, P. J. 2010, ArXiv e-prints

Gopal-Krishna, Biermann, P. L., & Wiita, P. J. 2003, ApJ, 594, L103

Gopal-Krishna, & Wiita, P. J. 2000, A&A, 363, 507

—. 2009, New Astronomy, 14, 51

—. 2010, New Astronomy, 15, 96

Hardcastle, M. J., Alexander, P., Pooley, G. G., & Riley, J. M. 1996, MNRAS, 278, 273

Hardcastle, M. J., Birkinshaw, M., & Worrall, D. M. 2001, MNRAS, 326, 1499

Hardcastle, M. J., Croston, J. H., & Kraft, R. P. 2007a, ApJ, 669, 893

Hardcastle, M. J., Evans, D. A., & Croston, J. H. 2006, MNRAS, 370, 1893

Hardcastle, M. J., Harris, D. E., Worrall, D. M., & Birkinshaw, M. 2004, ApJ, 612, 729

Hardcastle, M. J., Kraft, R. P., Worrall, D. M., Croston, J. H., Evans, D. A., Birkinshaw, M., & Murray, S. S. 2007b, ApJ, 662, 166

Hardcastle, M. J., & Sakelliou, I. 2004, MNRAS, 349, 560

Hardcastle, M. J., Sakelliou, I., & Worrall, D. M. 2005, MNRAS, 359, 1007

Hardcastle, M. J., Worrall, D. M., Birkinshaw, M., Laing, R. A., & Bridle, A. H. 2002, MNRAS, 334, 182

Harris, D. E., & Krawczynski, H. 2006, ARA&A, 44, 463

Hayes, J. C., Norman, M. L., Fiedler, R. A., Bordner, J. O., Li, P. S., Clark, S. E., ud-Doula, A., & Mac Low, M. 2006, ApJS, 165, 188

Heinz, S., Brüggen, M., Young, A., & Levesque, E. 2006, MNRAS, 373, L65

Hodges-Kluck, E. J., & Reynolds, C. S. 2011, ApJ, 733, 58

Hodges-Kluck, E. J., Reynolds, C. S., Cheung, C. C., & Miller, M. C. 2010a, ApJ, 710, 1205

Hodges-Kluck, E. J., Reynolds, C. S., Miller, M. C., & Cheung, C. C. 2010b, ApJ, 717, L37

Huarte-Espinosa, M., Krause, M., & Alexander, P. 2011, in IAU Symposium, Vol. 275, IAU Symposium, ed. G. E. Romero, R. A. Sunyaev, & T. Belloni, 170–171

Hudson, D. S., Mittal, R., Reiprich, T. H., Nulsen, P. E. J., Andernach, H., & Sarazin, C. L. 2010, A&A, 513, A37+

Isobe, N., Tashiro, M., Makishima, K., Iyomoto, N., Suzuki, M., Murakami, M. M., Mori, M., & Abe, K. 2002, ApJ, 580, L111

Jeltema, T. E., Binder, B., & Mulchaey, J. S. 2008, ApJ, 679, 1162

Johnstone, R. M., Allen, S. W., Fabian, A. C., & Sanders, J. S. 2002, MNRAS, 336, 299

Kalberla, P. M. W., Burton, W. B., Hartmann, D., Arnal, E. M., Bajaja, E., Morras, R., & Pöppel, W. G. L. 2005, A&A, 440, 775

Kawakatu, N., Kino, M., & Nagai, H. 2009, ApJ, 697, L173

Keppens, R., Meliani, Z., van der Holst, B., & Casse, F. 2008, A&A, 486, 663

Klein, U., Mack, K., Gregorini, L., & Parma, P. 1995, A&A, 303, 427

Komissarov, S. S., & Falle, S. A. E. G. 1996, in Astronomical Society of the Pacific Conference Series, Vol. 100, Energy Transport in Radio Galaxies and Quasars, ed. P. E. Hardee, A. H. Bridle, & J. A. Zensus, 173–+

Kraft, R. P., Azcona, J., Forman, W. R., Hardcastle, M. J., Jones, C., & Murray, S. S. 2006, ApJ, 639, 753

Kraft, R. P., Hardcastle, M. J., Worrall, D. M., & Murray, S. S. 2005, ApJ, 622, 149

Krause, M. 2003, A&A, 398, 113

—. 2005, A&A, 431, 45

Krolik, J. H. 1998, Active Galactic Nuclei: From the Central Black Hole to the Galactic Environment, ed. Krolik, J. H.

Laing, R. A., Riley, J. M., & Longair, M. S. 1983, MNRAS, 204, 151

Lal, D. V., & Rao, A. P. 2005, MNRAS, 356, 232

—. 2007, MNRAS, 374, 1085

Lambas, D. G., Maddox, S. J., & Loveday, J. 1992, MNRAS, 258, 404

Landt, H., Cheung, C. C., & Healey, S. E. 2010, MNRAS, 408, 1103

Landt, H., Padovani, P., Perlman, E. S., & Giommi, P. 2004, MNRAS, 351, 83

Leahy, J. P., Black, A. R. S., Dennett-Thorpe, J., Hardcastle, M. J., Komissarov, S., Perley, R. A., Riley, J. M., & Scheuer, P. A. G. 1997, MNRAS, 291, 20

Leahy, J. P., & Parma, P. 1992, in Extragalactic Radio Sources. From Beams to Jets, ed. J. Roland, H. Sol, & G. Pelletier, 307–308

Leahy, J. P., & Perley, R. A. 1991, AJ, 102, 537

Leahy, J. P., & Williams, A. G. 1984, MNRAS, 210, 929

Ledlow, M. J., & Owen, F. N. 1996, AJ, 112, 9

Ly, C., De Young, D. S., & Bechtold, J. 2005, ApJ, 618, 609

Lynden-Bell, D. 1969, Nature, 223, 690

Magdziarz, P. 1995, A&A, 299, 650

Martel, A. R., Baum, S. A., Sparks, W. B., Wyckoff, E., Biretta, J. A., Golombek, D., Macchetto, F. D., de Koff, S., McCarthy, P. J., & Miley, G. K. 1999, ApJS, 122, 81

Massaro, F., Harris, D., Axon, D., Balmaverde, B., Baum, S., Capetti, A., Chiaberge, M., Gilli, R., Giovannini, G., Grandi, P., Macchetto, D., O'Dea, C., Risaliti, G., & Sparks, W. 2008, in AAS/High Energy Astrophysics Division, Vol. 10, AAS/High Energy Astrophysics Division #10, 26.19–+

McKean, J., Ker, L., van Weeren, R. J., Batejat, F., Birzan, L., Bonafede, A., Conway, J., De Gasperin, F., Ferrari, C., Heald, G., Jackson, N., Macario, G., Orrù, E., Pizzo, R., Rafferty, D., Rottgering, H., Shulevski, A., Tasse, C., van der Tol, S., van Bemmel, I., van Diepen, G., van Zwieten, J. E., & for the LOFAR collaboration. 2011, ArXiv e-prints

McNamara, B. R., Nulsen, P. E. J., Wise, M. W., Rafferty, D. A., Carilli, C., Sarazin, C. L., & Blanton, E. L. 2005, Nature, 433, 45

Merritt, D., & Ekers, R. D. 2002, Science, 297, 1310

Mezcua, M., Lobanov, A. P., Chavushyan, V. H., & León-Tavares, J. 2011, A&A, 527, A38+

Mignone, A., Rossi, P., Bodo, G., Ferrari, A., & Massaglia, S. 2010, MNRAS, 402, 7

Miller, B. P., & Brandt, W. N. 2009, ApJ, 695, 755

Morsony, B. J., Heinz, S., Brüggen, M., & Ruszkowski, M. 2010, MNRAS, 407, 1277

Murgia, M., Parma, P., de Ruiter, H. R., Bondi, M., Ekers, R. D., Fanti, R., &

Fomalont, E. B. 2001, A&A, 380, 102

Myers, S. T., & Spangler, S. R. 1985, ApJ, 291, 52

Narayan, R., & Medvedev, M. V. 2001, ApJ, 562, L129

Narayan, R., & Quataert, E. 2005, Science, 307, 77

Neff, S. G., Roberts, L., & Hutchings, J. B. 1995, ApJS, 99, 349

Omma, H., & Binney, J. 2004, MNRAS, 350, L13

Omma, H., Binney, J., Bryan, G., & Slyz, A. 2004, MNRAS, 348, 1105

O'Neill, S. M., De Young, D. S., & Jones, T. W. 2009, ApJ, 694, 1317

O'Neill, S. M., & Jones, T. W. 2010, ApJ, 710, 180

O'Neill, S. M., Tregillis, I. L., Jones, T. W., & Ryu, D. 2005, ApJ, 633, 717

Ostriker, J. P., Choi, E., Ciotti, L., Novak, G. S., & Proga, D. 2010, ApJ, 722, 642

Owen, F. N., Ledlow, M. J., Morrison, G. E., & Hill, J. M. 1997, ApJ, 488, L15+

Pacholczyk, A. G. 1970, Radio astrophysics. Nonthermal processes in galactic and extragalactic sources, ed. Pacholczyk, A. G.

Penrose, R. 1969, Nuovo Cimento Rivista Serie, 1, 252

Perley, R. A., Dreher, J. W., & Cowan, J. J. 1984, ApJ, 285, L35

Perlman, E. S., Padgett, C. A., Georganopoulos, M., Worrall, D. M., Kastner, J. H., Franz, G., Birkinshaw, M., Dulwich, F., O'Dea, C. P., Baum, S. A., Sparks, W. B., Biretta, J. A., Lara, L., Jester, S., & Martel, A. 2010, ApJ, 708, 171

Perlman, E. S., & Wilson, A. S. 2005, ApJ, 627, 140

Peterson, J. R., & Fabian, A. C. 2006, Phys. Rep., 427, 1

Pope, E. C. D., Babul, A., Pavlovski, G., Bower, R. G., & Dotter, A. 2010, MNRAS, 406, 2023

Press, W. H., Teukolsky, S. A., Vetterling, W. T., & Flannery, B. P. 1992, Numerical recipes in C. The art of scientific computing, ed. Press, W. H., Teukolsky, S. A., Vetterling, W. T., & Flannery, B. P.

Quinn, P. J. 1984, ApJ, 279, 596

Randall, S. W., Forman, W. R., Giacintucci, S., Nulsen, P. E. J., Sun, M., Jones, C., Churazov, E., David, L. P., Kraft, R., Donahue, M., Blanton, E. L., Simionescu, A., & Werner, N. 2011, ApJ, 726, 86

Randall, S. W., Sarazin, C. L., & Ricker, P. M. 2002, ApJ, 577, 579

Rees, M. J. 1978, Nature, 275, 516

Rees, M. J., Begelman, M. C., Blandford, R. D., & Phinney, E. S. 1982, Nature, 295, 17

Reynolds, C. S., Heinz, S., & Begelman, M. C. 2002, MNRAS, 332, 271

Roettiger, K., Burns, J. O., Clarke, D. A., & Christiansen, W. A. 1994, ApJ, 421, L23

Rosario, D. J., Whittle, M., Nelson, C. H., & Wilson, A. S. 2010, ApJ, 711, L94

Rosati, P., Borgani, S., & Norman, C. 2002, ARA&A, 40, 539

Rosen, A., Hughes, P. A., Duncan, G. C., & Hardee, P. E. 1999, ApJ, 516, 729

Rottmann, H. 2001, PhD Thesis

Ruszkowski, M., Enßlin, T. A., Brüggen, M., Heinz, S., & Pfrommer, C. 2007, MNRAS, 378, 662

Ruszkowski, M., & Oh, S. P. 2010, ApJ, 713, 1332

Rybicki, G. B., & Lightman, A. P. 1979, Radiative processes in astrophysics, ed. Rybicki, G. B. & Lightman, A. P.

Sakelliou, I., & Merrifield, M. R. 2000, MNRAS, 311, 649

Sambruna, R. M., Gliozzi, M., Donato, D., Tavecchio, F., Cheung, C. C., & Mushotzky, R. F. 2004, A&A, 414, 885

Saripalli, L., & Subrahmanyan, R. 2009, ApJ, 695, 156

Saxton, C. J., Wu, K., Korunoska, S., Lee, K., Lee, K., & Beddows, N. 2010, MNRAS, 405, 1816

Simionescu, A., Roediger, E., Nulsen, P. E. J., Brüggen, M., Forman, W. R., Böhringer, H., Werner, N., & Finoguenov, A. 2009, A&A, 495, 721

Smith, D. A., Wilson, A. S., Arnaud, K. A., Terashima, Y., & Young, A. J. 2002, ApJ, 565, 195

Smith, E. P., & Heckman, T. M. 1989, ApJ, 341, 658

Smith, E. P., Heckman, T. M., Bothun, G. D., Romanishin, W., & Balick, B. 1986, ApJ, 306, 64

Spergel, D. N., Bean, R., Doré, O., Nolta, M. R., Bennett, C. L., Dunkley, J., Hinshaw, G., Jarosik, N., Komatsu, E., Page, L., Peiris, H. V., Verde, L., Halpern, M., Hill, R. S., Kogut, A., Limon, M., Meyer, S. S., Odegard, N., Tucker, G. S., Weiland, J. L., Wollack, E., & Wright, E. L. 2007, ApJS, 170, 377

Stone, J. M., & Norman, M. L. 1992a, ApJS, 80, 753

—. 1992b, ApJS, 80, 791

Sun, M., Jerius, D., & Jones, C. 2005, ApJ, 633, 165

Sun, M., Voit, G. M., Donahue, M., Jones, C., Forman, W., & Vikhlinin, A. 2009, ApJ, 693, 1142

Sunyaev, R. A., & Zeldovich, I. B. 1980, ARA&A, 18, 537

Sutherland, R. S., & Bicknell, G. V. 2007, ApJS, 173, 37

Tanaka, Y., Nandra, K., Fabian, A. C., Inoue, H., Otani, C., Dotani, T., Hayashida, K., Iwasawa, K., Kii, T., Kunieda, H., Makino, F., & Matsuoka, M. 1995, Nature, 375, 659

Tavecchio, F., Maraschi, L., Sambruna, R. M., Gliozzi, M., Cheung, C. C., Wardle, J. F. C., & Urry, C. M. 2006, ApJ, 641, 732

Thompson, A. R., Clark, B. G., Wade, C. M., & Napier, P. J. 1980, ApJS, 44, 151

Tremblay, G. R., Chiaberge, M., Donzelli, C. J., Quillen, A. C., Capetti, A., Sparks, W. B., & Macchetto, F. D. 2007, ApJ, 666, 109

Urry, C. M., & Padovani, P. 1995, PASP, 107, 803

van Breugel, W., Balick, B., Heckman, T., Miley, G., & Helfand, D. 1983, AJ, 88, 40

Veilleux, S., Cecil, G., & Bland-Hawthorn, J. 2005, ARA&A, 43, 769

Vernaleo, J. C., & Reynolds, C. S. 2006, ApJ, 645, 83

—. 2007, ApJ, 671, 171

Véron-Cetty, M. P., & Véron, P. 2001, A&A, 375, 791

Voigt, L. M., & Fabian, A. C. 2004, MNRAS, 347, 1130

Wald, R. M. 1974, Phys. Rev. D, 10, 1680

Williams, R. K. 2004, ApJ, 611, 952

Wirth, A., Smarr, L., & Gallagher, J. S. 1982, AJ, 87, 602

Worrall, D. M., & Birkinshaw, M. 2000, ApJ, 530, 719

Worrall, D. M., Birkinshaw, M., & Cameron, R. A. 1995, ApJ, 449, 93

Worrall, D. M., Birkinshaw, M., Kraft, R. P., & Hardcastle, M. J. 2007, ApJ, 658, L79

Wright, E. L. 2006, PASP, 118, 1711

Young, A. J., Wilson, A. S., Terashima, Y., Arnaud, K. A., & Smith, D. A. 2002, ApJ, 564, 176

Young, A. J., Wilson, A. S., Tingay, S. J., & Heinz, S. 2005, ApJ, 622, 830

Zanni, C., Massaglia, S., Bodo, G., Rossi, P., Capetti, A., & Ferrari, A. 2003, Memorie della Societa Astronomica Italiana Supplementi, 1, 155

Zier, C. 2005, MNRAS, 364, 583

Zier, C., & Biermann, P. L. 2001, A&A, 377, 23

Zuhone, J., & Markevitch, M. 2009, in American Institute of Physics Conference Series, Vol. 1201, American Institute of Physics Conference Series, ed. S. Heinz & E. Wilcots, 383–386